Homogenization of strain gradient continua: Constitutive parameter identification, size effects analysis, and brittle fracture propagation

vorgelegt von
M. Eng.
Hua Yang
ORCID: 0000-0003-2080-3452

an der Fakultät V - Verkehrs- und Maschinensysteme
der Technischen Universität Berlin
zur Erlangung des akademischen Grades

Doktor der Ingenieurwissenschaften
- Dr.-Ing. -

genehmigte Dissertation

Promotionsausschuss:

Vorsitzender: Prof. Dr.-Ing. Utz von Wagner
Gutachter: Prof. Dr. rer. nat. Wolfgang H. Müller
Gutachter: Prof. Dr. Victor Eremeyev

Tag der wissenschaftlichen Aussprache: 04. Oktober 2021

Berlin 2021

Homogenization of strain gradient continua: Constitutive parameter identification, size effects analysis, and brittle fracture propagation

Hua Yang
ORCID: 0000-0003-2080-3452

From the Faculty V – Mechanical Engineering and Transport Systems
of the Technische Universität Berlin
For the degree of
Doctor of Engineering Sciences

Subject area
Mechanics

Berlin 2021

Preface

With the development of additive manufacturing techniques metamaterials of any kind of complex geometries can be fabricated. With the aim of making successfully microstructural tailored metamaterials for desired properties, the accurate and efficient modeling techniques are of importance. A direct finite element modeling of metamaterials is usually not manageable due to millions of degrees of freedom. In order to find an equivalent homogeneous continuum with identified effective material parameters to substitute metamaterials is of practical significance. Motivated by this fact, in this thesis a homogenization tool is presented, which allows to homogenize metamaterials (heterogeneous Cauchy continua) to equivalent strain gradient continua. Size effects of metamaterials will be investigated by using the concept of strain gradient continua. Moreover, modeling and computation of brittle fracture propagation for strain gradient materials will be performed. This thesis is composed of two parts. In the first part a summary of the work including the background, state of the art, an overview of generalized continuum theories and asymptotic homogenization method, and main conclusions of this work is presented. The second part contains the main results which include four published journal articles [1] , [2] , [3] , [4] and one submitted manuscript [5].

A scientific product is never the work of a single individual. I would like to express my deep gratitude to my colleagues. First, I must say thank you to my supervisor Prof. Wolfgang H. Müller. I still remember it was a cold winter morning when I knocked at Prof. Müller's door for my application of doctoral study with a nervous and excited heart four years ago. Prof. Müller showed his interest in my CV and said "I think I have something you can do here...". Then the story began. Thanks to him for establishing such a wonderful environment to conduct scientific research. I am also grateful to his supervision and support. Furthermore, I would like to express my gratitude to Assoc. Prof. B. Emek Abali, who introduced this research topic to me. He has been a great mentor. I really appreciate his dedication and time awarded to

[1] H. Yang, D. Timofeev, B. E. Abali, B. Li, and W. H. Müller (2021). "Verification of strain gradient elasticity computation by analytical solutions." In: *ZAMM-Journal of Applied Mathematics and Mechanics/Zeitschrift für Angewandte Mathematik und Mechanik*, e202100023

[2] H. Yang, B. E. Abali, D. Timofeev, and W. H. Müller (2020). "Determination of metamaterial parameters by means of a homogenization approach based on asymptotic analysis." In: *Continuum Mechanics and Thermodynamics* 32, pp. 1251–1270

[3] H. Yang, D. Timofeev, I. Giorgio, and W. H. Müller (2020). "Effective strain gradient continuum model of metamaterials and size effects analysis." In: *Continuum Mechanics and Thermodynamics*, pp. 1–23

[4] E. Barchiesi, H. Yang, C. Tran, L. Placidi, and W. H. Müller (2021). "Computation of brittle fracture propagation in strain gradient materials by the FEniCS library." In: *Mathematics and Mechanics of Solids* 26.3, pp. 325–340

[5] H. Yang, B. E. Abali, W. H. Müller, S. Barboura, and J. Li (2021). "Verification of asymptotic homogenization method developed for periodic architected materials in strain gradient continuum." In: *Submitted*

me. He always made himself available to brainstorm with me, corrects manuscripts, gave me suggestions and invited me to some conferences. I also benefit from his rigorous attitude towards science, even the smallest of details. Part of this thesis was conducted during my productive visit to the International Research Center for the Mathematics and Mechanics of Complex Systems (MeMoCS). I am very thankful to Dr. Emilio Barchiesi for inspiration and fruitful discussions. I am also grateful to his warm host during my stay in Italy. That was my "Roman Holiday". I thank Prof. Victor Eremeyev for being the second referee of this thesis especially under the Corona situation. I express my gratitute to Prof. Utz von Wagner for being the chairman of the thesis committee.

Many thanks to my collaborators, Assoc. Prof. Ivan Giorgio, Assoc. Prof. Luca Placidi, Gregor Ganzosch, Chuong Anthony Tran, Dmitry Timofeev, Prof. Baotong Li. Many thanks to the colleagues in the LKM group, Dr. Christian Liebold, Dr. Felix A. Reich, Dr. Sebastian Glane, Dr. Oliver Stahn, Wilhelm Rickert, Dr. Aleksandr Morozov, Aleksei Sokolov, Arion Juritza, and Peter Sahlmann. Thanks to Asst. Prof. David Kamensky for the help given in tIGAr.

Last but not least, I thank all of my family members, especially my wife Dr. Yi Xia. Thanks to my little daughter Miduo, Your coming is the best gift in my life!

Zusammenfassung

Die Cauchy-Kontinuumstheorie ist nicht in der Lage, die absolute Größe der Mikrostruktur von Werkstoffen zu berücksichtigen. Daher kann sie das größenabhängige Materialverhalten nicht beschreiben. Die Dehnungsgradiententheorie ist in der Lage, sogenannte Größeneffekte zu erfassen. Der Engpass bei der Anwendung der Dehnungsgradiententheorie ist jedoch die Bestimmung zusätzlicher Materialparameter. In dieser Arbeit werden die zusätzlichen konstitutiven Parameter mit Hilfe der asymptotischen Homogenisierungsmethode bestimmt. Genauer gesagt werden heterogene Cauchy-Kontinua zu effektiven Dehnungsgradienten-Kontinua homogenisiert und die entsprechenden Materialparameter einschließlich der klassischen Steifigkeitstensoren sowie der Dehnungsgradienten-Steifigkeitstensoren mit Hilfe der Finite-Elemente-Methode ermittelt. Das sogenannte homothetische Verhältnis ϵ ist eine endliche Zahl, die $\epsilon < 1$ erfordert, aber nicht notwendigerweise $\epsilon \ll 1$. Es wird gefunden, dass die effektiven Parameter im Dehnungsgradiententensor alle verschwinden, wenn die Materialien rein homogen sind. Sowohl die klassischen als auch die Dehnungsgradienten-Steifigkeitsparameter sind unempfindlich gegenüber der Wiederholung von Repräsentative Volumenelemente. Die klassischen Steifigkeitsparameter sind unabhängig von den mikrostrukturellen Größen, die höherer Ordnung werden davon beeinflusst. Es wird eine Skalierungsregel für Dehnungsgradientenmodule angegeben. Es werden numerische 2D- und 3D-Beispiele durchgeführt und Materialparameter für Metamaterialien mit einer Gitter-Substruktur, Verbundwerkstoffe wie Epoxid-Kohlenstofffaser-Verbundwerkstoff, SiC/Al-Metallmatrix-Verbundwerkstoff und Aluminiumschaum identifiziert. Mit Hilfe der identifizierten Parameter werden Größeneffekte analysiert. Darüber hinaus werden die Berechnungen mit Hilfe der Dehnungsgradiententheorie für die Sprödbruchausbreitung dargestellt. Die Open-Source-Rechenplattform FEniCS wird in dieser Arbeit verwendet.

Abstract

Cauchy continuum theory is unable to account for the absolute size of microstructure of materials. Thus it fails to describe size dependent material behaviors. Strain gradient theory is capable of capturing so-called size effects. However, the bottleneck of the application of strain gradient theory is the determination of additional material parameters. In this thesis, the material parameters are determined by means of an asymptotic homogenization method. Specifically, heterogeneous Cauchy continua are homogenized towards effective strain gradient continua. The corresponding material parameters including classical stiffness tensors as well as strain gradient stiffness tensors are identified by using the finite element method. The so-called homothetic ratio ϵ is a finite number which requires $\epsilon < 1$ but not necessarily $\epsilon \ll 1$. It is found that the effective parameters in the strain gradient tensor all vanish when the materials are purely homogeneous. Both the classical and strain gradient stiffness parameters are insensitive to the repetition of representative volume elements. The classical stiffness parameters are independent of the microstructural sizes, the higher order ones are influenced by that. A scaling rule for strain gradient moduli is given. 2D and 3D numerical examples are conducted and materials parameters are identified for metamaterials including lattice structures, composite materials such as epoxy carbon fiber composite material, SiC/Al metal matrix composite, and aluminum foam. Size effects are analyzed by using the identified parameters in the case of a cantilever beam bending. Furthermore, computations for brittle fracture propagation of strain gradient materials are performed. The open source computing platform FEniCS is employed throughout this work.

Contents

Part I

Summary of the work

Chapter I

Introduction

1 Background

One of the predominant engineering activities over the decades has been the design, manufacture, and analysis of increasingly advanced engineering materials due to the requirements attributed to technological progress. Recently, the growing demands for improved properties of engineering parts have been partially resolved through the development of the so-called metamaterials. A key to the success of many modern structural parts is the achievement of desired behavior of metamaterials to given applications.

By means of design techniques such as topology optimization design method, metamaterials with desirable properties such as light weights, negative Poisson's ratio, or negative stiffness are possible to be devised. Analogous designs are of interest, such as in aerospace lightweight parts, controllable phononic/photonic modulators, energy absorbing bumpers for vehicles, as well as controlling and molding the flow of electromagnetic waves. The secrets of the exotic material behaviors are presumably hidden behind the underlying substructures. In other words, the microstructure characteristics such as size, shape, and spatial distribution of microstructures, enable the materials to provide fascinating properties. Examples of metamaterials include lattice materials, fiber-reinforced composites, and woven fabrics. Fig. I.1 shows the metamaterials designed by Coulais, Kettenis, and Hecke, 2018; S. Kumar, Tan, Zheng, and Kochmann, 2020; Barchiesi, Eugster, dell'Isola, and Hild, 2020. It should be mentioned that microstructural architectures are also one of the distinct features of natural materials, such as human muscle tissues, bamboo, and bone. Thanks to the rapid development of manufacturing techniques (known as 3D printing), metamaterials of complex morphology are possible to be generated.

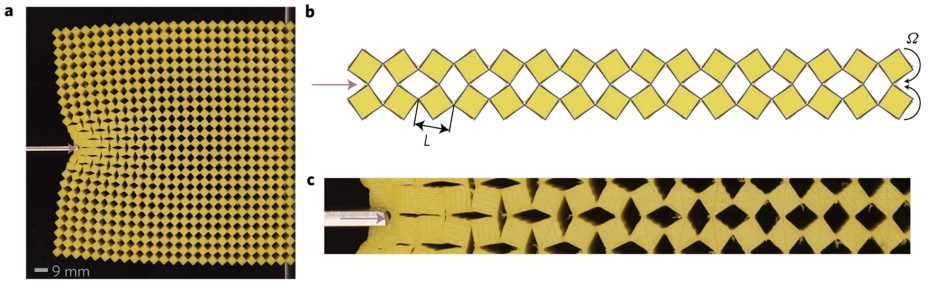

Indentation on a two-dimensional mechanical metamaterial in the work of Coulais, Kettenis, and Hecke 2017. Copyright 2017 Nature.

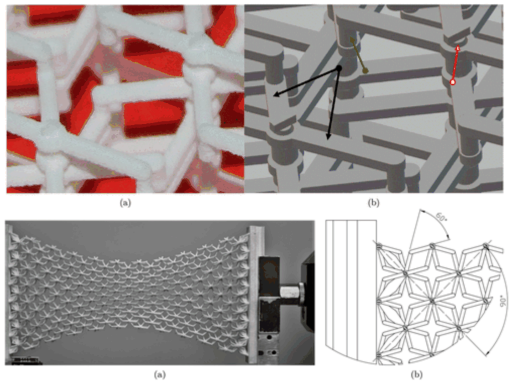

Bi-pantographic fabric and its extension test in Barchiesi, Eugster, dell'Isola, etal., 2019. Copyright 2017 Sage.

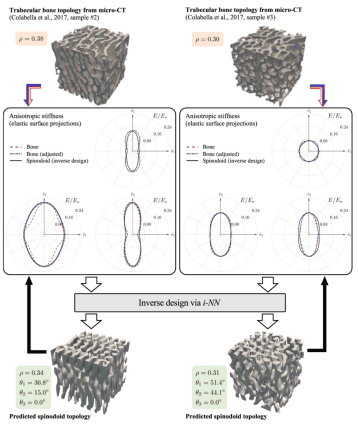

Biomimetic spinodoids in Kumar, etal., 2020. Copyright 2020 Nature.

Figure I.1: Examples of metamaterials.

The design of metamaterials is usually an iterative process, which requires heavy computational burdens in order to finish building up the system performing a given set of functions satisfactorily. For instance, comparing the static and dynamic responses of different designs and assessing the structural responses to variations of material and geometrical properties are needed. Since the microstructures are of complex morphologies and their sizes are usually one order magnitude smaller than macroscopic sizes, it is challenging to use a direct Finite Element Method (FEM) with a detailed mesh of substructures even by modern computer techniques. Consequently, as a remedy, continuum modeling of metamaterials, which uses homogenization methods to replace the actual metamaterials by a continuum model with identified effective properties, is of importance in engineering applications.

2 State of the art

In this section, the state of the art of homogenization methods, generalized continuum theories, parameters identification of generalized continua, and numerical implementations of strain gradient theory are presented.

2.1 Homogenization methods

The number of publications on homogenization methods has experienced a steady increase, see for instance the works in Hill, 1972; Hashin, 1991; Willis, 1977; Noor, 1988; Mishnaevsky and Schmauder, 2001; Zohdi and Wriggers, 2008; Kanoute, Boso, Chaboche, and Schrefler, 2009; V. P. Nguyen, Stroeven, and Sluys, 2011; dell'Isola, Seppecher, Alibert, et al., 2019. Various strategies including analytical and numerical approaches have been proposed in the literature.

Many investigations focus on the mechanics of materials approaches to calculate the effective properties of cellular materials. In Ashby and Medalist, 1983, effective mechanical properties (elastic, plastic, creep, and fracture) of cellular solids and foams were described by using simple formulae. In Masters and Evans, 1996; A.-J. Wang and D. McDowell, 2004; A.-J. Wang and D. McDowell, 2005, theoretical models to predict the effective properties of honeycombs were developed. In these works closed expressions of effective mechanical properties were provided. Such approaches establish direct relations between the effective properties and underlying microstructures, however, they present limitations when the topologies of the RVE (Representative Volume Element) are complex. It is also reported that the differences between the effective moduli calculated under different assumptions can be significant as mentioned in Hollister and Kikuchi, 1992.

The mean field homogenization method is a semi-analytical homogenization approach that uses formulations based on Eshelby's solution to predict effective properties of composite materials (V.-D. Nguyen and Noels, 2014). It is based on assumptions of interaction laws between different constituents of microstructures and gives macroscopic responses as well as basic information about the states of deformation within the constituents. The mean field homogenization method was first developed for linear elastic composite materials by extending Eshelby single inclusion solution (see Eshelby, 1957) to multiple inclusions in composite materials. Most common extensions of Eshelby's solution are the Mori–Tanaka scheme proposed by Mori and Tanaka, 1973 and the self-consistent approach, see Hill, 1965. Some works are dedicated to extend the mean field homogenization to account for non-linearity and damage as summarized in Pierard et al., 2006. However, the limitations of the mean field homogenization method may be that it is difficult to predict strain or stress localization phenomena and to take into account clustering, percolation, and size effects.

Another homogenization method is the asymptotic homogenization method, see Bensoussan, Lions, and Papanicolaou, 2011; A. L. Kalamkarov, Andrianov, and Danishevs'kyy, 2009. Two assumptions are made herein. First, there exists a scale separation which means that the size of macrostructure (L) is much larger than the characteristic size of the heterogeneity (l). In other words, the ratio $\epsilon = \frac{l}{L}$ is infinitesimal. Second, it is assumed that the microstructure is spatially periodic. Then asymptotic expansions are used to describe field quantities (such as displacement, strain, stress) and split them into separated microstructural and macrostructural problems, which allows to derive the effective properties under periodic boundary conditions. Asymptotic homogenization method can be applied to lattice structures or composite materials as long as their microstructures are periodically aligned. Various applications of the method have been reported in the literature. In Ghosh, Lee, and Moorthy, 1996, by combining asymptotic homogenization method with the Voronoi Cell finite element model, a multiple scale finite element analysis of heterogeneous elastic-plastic materials was done. In Challagulla, Georgiades, and A. Kalamkarov, 2007, effective elastic parameters of composite plates reinforced with orthotropic bars were obtained by means of asymptotic homogenization models. In Yu and T. Tang, 2007; Yu and T. Tang, 2007; T. Tang and Yu, 2008, variational asymptotic homogenization methods were developed to predict the effective properties of periodically heterogeneous materials and recover the local fields. In the works of Pinho-da-Cruz, Oliveira, and Teixeira-Dias, 2009; Pinho-da-Cruz, Oliveira, and Teixeira-Dias, 2009, mathematical formulation, finite element modeling of asymptotic homogenization method were presented, and effective mechanical properties of 3D periodic composite materials were identified.

There are also a number of computational homogenization methods proposed in the literature, as seen in the works of Yvonnet, 2019; Yuan and Fish, 2008; Fritzen, Forest, Böhlke, Kondo, and Kanit, 2012. Extensions of computational homogenization method to a large amount of problems have been done, such as large deformation in Takano, Ohnishi, Zako, and Nishiyabu, 2000, dynamics in Pham, Kouznetsova, and M. G. Geers, 2013, and multiphysics modeling in Patel and Zohdi, 2016; Javili, Chatzigeorgiou, and Steinmann, 2013; Özdemir, Brekelmans, and M. Geers, 2008.

A comprehensive overview of different homogenization methods may be found in Nemat-Nasser and Hori, 2013. It should be pointed out that most of the aforementioned methods are based on classical mechanics theories (also called Cauchy continuum theories), where the response at a material point depends only on the first gradients of the displacement field. Although Cauchy continuum theories have been of paramount importance, there is a growing number of evidence reporting the inadequacy of such theories in modeling metamaterials. Experimental investigations on cellular materials have presented size effects under different loads conditions, such as shear tests in Andrews, Gioux, P. Onck, and Gibson, 2001, bending tests in R. S. Lakes, 1983; R. Lakes, 1986, torsion tests in Anderson and R. Lakes, 1994, and indentation in Olurin, N. A. Fleck, and Ashby, 2000. The size effects cannot be captured

by using the homogenization techniques in the framework of Cauchy continuum theories. In Poncelet, Somera, Morel, Jailin, and Auffray, 2018, experimental evidence of the failure of Cauchy continuum theories for the overall modeling of a non-centrosymmetric lattice have been presented. In Boisse, Hamila, and Madeo, 2018, the difficulties of using the Cauchy continuum theories in modeling the mechanical behavior of textile composite reinforcements were highlighted. It was concluded that Cauchy continuum theories are not able to describe both the possibility of slippage between fibers and the bending stiffness of fibers. In Rosi, Auffray, and Combescure, 2020, it was found that the Cauchy continuum theories fail to predict elastic wave propagation in Gyroid lattices for very long wavelengths. Another example indicating failures of classical continuum theories is the so-called pantographic metamaterials (see the work of dell'Isola, Seppecher, Spagnuolo, et al., 2019). Such pantographic structures have non-negligible strain gradient terms in the formulation of deformation energy (Giorgio, N. Rizzi, and Turco, 2017; Nejadsadeghi et al., 2019; De Angelo, Spagnuolo, et al., 2019; Turco and Barchiesi, 2019), which are found in recent numerical and experimental evidences, for example, in shear tests (Barchiesi, Ganzosch, et al., 2019), three-point bending tests (Yildizdag, Barchiesi, and dell'Isola, 2020), compression tests (C. A. Tran, Gołaszewski, and Barchiesi, 2020), or torsion tests (Misra et al., 2018). In order to address the difficulties encountered, it is the so-called generalized continuum theories that are believed to be a proper tool to capture relevant deformation mechanisms. Readers are referred to W. H. Müller, 2020 for experimental evidences for generalized continuum theories.

2.2 Generalized continuum theories

The generalization of the classical continuum theory is not a new idea. The first attempt may be dated back to to the works of Cauchy, Piola and Voigt in the middle of the 19th century as described in dell'Isola, Corte, and Giorgio, 2017. In the early 20th century, Cosserat brothers enriched the kinematics of continua as the so-called "Cosserat continua" with not only the transnational displacements u_i but also microrotations ϕ_i (J. Altenbach, H. Altenbach, and Eremeyev, 2010; Eremeyev, Lebedev, and H. Altenbach, 2012). In this way, both stresses and couple stresses are fully taken into account in deformations. The Cosserat continua did not obtain enough attention until the early 1960s. During those years, the generalized continuum theories were developed by several pioneers including the celebrated works in R. Toupin, 1962; R. D. Mindlin, 1963; R. A. Toupin, 1964; R. D. Mindlin, 1965; Eringen, 1966; R. D. Mindlin and Eshel, 1968. The generalized continuum theories may be distinguished as two main types: The higher order theories and the higher grade theories (Tekoğlu and P. R. Onck, 2008; Forest, 2013). By enriching each material point with additional degrees of freedom, one may reach the higher order theories such as the micromorphic continuum theory (Eringen and Suhubi, 1964; R. D. Mindlin, 1963). Herein Mindlin distinguished the kinematic quantities on the macroscale and microscale. Besides the standard translational displacement u_i, of a material point on the macroscale, a micro-

volume is attached in the continuum, which can rotate and stretch independently from those on the marcoscale. As a result, a micro-deformation tensor ψ_{ij} is introduced to characterize nine additional degrees of freedom on the microscale. The micro-deformation can be described by deformable directors, one may refer to Fig. 9.2 in Liebold and W. H. Müller, 2015, and Fig. 2.2 in Hirschberger, 2008 for a visualization of the director triad. If the directors are "rigid", there are only three additional degrees of freedom ϕ_i accounting for micro-rotations, one arrives micropolar theory. Note that in the literature many authors use the names of micropolar theory and Cosserat theory interchangeably (Tekoğlu and P. R. Onck, 2008). Relating the micro-rotations to the macroscopic rotation vector $\phi_i = \frac{1}{2}e_{ijk}u_{k,j}$ with e_{ijn} the Levi-Civita symbol simplifies the micropolar to couple stress theory (Liebold and W. H. Müller, 2016).

Strain gradient theory belongs to the family of higher grade theories, where higher order gradients of the displacement field are added into the energy functional. It is noted that couple stress theory is not only a special case of micropolar but also strain gradient theory (Tekoğlu and P. R. Onck, 2008), where only the gradients of the rotation vector are considered in the strain energy density. Also by equating the ψ_{ij} to $u_{j,i}$, one simplifies the micromorphic theory to strain gradient theory. Indeed, mathematically speaking, the generalized continuum theories are closely connected and may be considered as special cases of a unified theory (Neff, Ghiba, Madeo, Placidi, and Rosi, 2014). Fig. I.2 gives a simple summary of the aforementioned theories. In the next chapter, detailed summaries of the more extensively studied micropolar theory and strain gradient theory will be presented.

Strain gradient theory has been widely used to model size effects (Abali, W. H. Müller, and Eremeyev, 2015; Abali, W. H. Müller, and dell'Isola, 2017; Abali, 2019). The employment of such theory allows one to investigate localization phenomena, regularize crack propagation (Placidi and Barchiesi, 2018; Shlyannikov, Martínez-Pañeda, Tumanov, and Tartygasheva, 2021), and resolve the dislocation core (Lazar, Maugin, and Aifantis, 2006). Moreover, the strain gradient continuum is able to accommodate points forces or force distributions along lines (Makvandi, Reiher, Bertram, and Juhre, 2018; Reiher, Giorgio, and Bertram, 2017), and the Cauchy continuum shows singularities when handling such issues. There are different versions of strain gradient elasticity theories including Mindlin's theory, modified strain gradient theory (Lam, F. Yang, Chong, J. Wang, and Tong, 2003), Aifantis' theory (Aifantis, 1992; Askes and Aifantis, 2011). The present work is devoted to Mindlin's strain gradient elasticity theory, since it is one of the more general ones. Mindlin (R. Mindlin and Tiersten, 1962) presented three formulations (Form I, Form II, and Form III) based on the second gradient of displacements, the first gradient of strain, and gradient of rotation, respectively. In R. D. Mindlin and Eshel, 1968, it was shown that these three formulations are equivalent. For isotropic strain gradient material there are five independent additional material parameters in 3D (Abali, H. Yang, and Papadopoulos, 2019), and 4 independent parameters in 2D cases (Placidi, Andreaus, Della Corte,

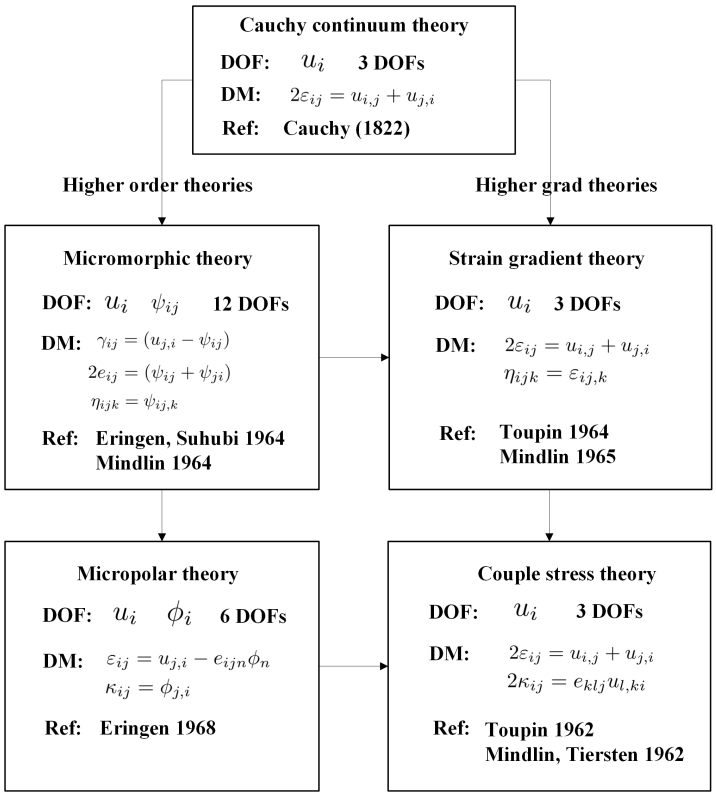

Figure I.2: Selected examples of generalized continuum theories. u_i is the displacement vector. ψ_{ij} represents the introduced additional degrees of freedom in the micromorphic continuum. ϕ_i is the micro-rotation vector. e_{ijn} is the Levi-Civita symbol. DOF: Degrees of freedom; DM: Deformation measure; Ref: Reference.

and Lekszycki, 2015). For anisotropic cases, readers may refer to the works of Auffray, Bouchet, and Brechet, 2009; Auffray, Le Quang, and Q.-C. He, 2013; Auffray, Dirrenberger, and Rosi, 2015, where explicit matrix representations of the strain gradient elastic tensor were derived and presented for 2D and 3D anisotropic cases in a compact way. Now determination of additional material parameters is needed.

2.3 Determination of the additional material parameters

Many debates exist in the literature for the determination of the additional material parameters. Although it is difficult to identify these parameters experimentally, there are some attempts in this respect. In R. Lakes and Drugan, 2015, bending tests on prismatic bars of square cross section composed of reticulated polyurethane foams were done. Experimental measurements were compared to the corresponding analytical solutions so that Cosserat parameters were found out. Réthoré, Kaltenbrunner, Dang, Chaudet, and Kuhn, 2015 determined strain gradient parameters for a honeycomb structure with a crack through the analysis of the displacement field measured by Digital Image Correlation (DIC) at two different scales. Real experiments are

usually too complex to implement, thus in the literature homogenization schemes aiming at identifications of additional material parameters are proposed. General homogenization schemes were shown in Trinh, Janicke, Auffray, Diebels, and Forest, 2012. Depending on the use of polynomial boundary conditions, overall Cosserat, strain gradient, and micromorphic effective continua were established and additional parameters were identified. In R. S. Kumar and D. L. McDowell, 2004, an energy equivalence assumption was made for lattice structure and its effective micropolar continuum. The material parameters were derived by equating two different continuous approximations of the strain energy function. Dos Reis and J. Ganghoffer, 2012; El Nady, Dos Reis, and J. Ganghoffer, 2017; Rahali, Assidi, Goda, Zghal, and J.-F. Ganghoffer, 2016 used the discrete asymptotic method, homogenized metamaterials to micropolar media, and identified material parameters for auxetic lattices and interlocks. An effective couple stress continuum model was built by Liu and Su, 2009, where the material parameters were obtained based on responses of an RVE under prescribed boundary conditions. Similarly, in Rahali, Goda, and J.-F. Ganghoffer, 2016; Goda and J.-F. Ganghoffer, 2015; Skrzat and Eremeyev, 2020, 3D woven textiles, 3D vertebral trabecular, and metal open-cell foams were homogenized to couple stress continua, classical and non-classical moduli were determined. In Hütter, 2017; Hütter, 2019; Biswas and Poh, 2017, homogenization of Cauchy continua towards micromorphic continua can be found.

There are also some efforts devoted to homogenization towards strain gradient continua. In Boutin, 1996, microstructural effects in elastic composites were studied by asymptotic homogenization method with higher order terms. Smyshlyaev and Cherednichenko, 2000 showed a rigorous mathematical derivation of strain gradient effects in the overall behavior periodic heterogeneous media by combining the variational approach and asymptotic homogenization method. Based on this study, in R. Peerlings and N. Fleck, 2004, a computational scheme was developed to evaluate strain gradient elasticity constants for periodic heterogeneous materials. The imposing of quadratic boundary conditions for the displacement of an RVE to identify the additional material parameters has been used by some researchers, see the works in Auffray, Bouchet, and Brechet, 2010; Bacigalupo, 2014; Monchiet, Auffray, and Yvonnet, 2020; Bacigalupo, Paggi, Dal Corso, and Bigoni, 2018. A body force correction has been introduced in Yvonnet, Auffray, and Monchiet, 2020, so that the strain gradient moduli are all zero when no microstructures exist. Some authors used energy density equivalency and the Cauchy-Born rule method to determine the strain gradient parameters as presented in Song and Wei, 2020. There are also some efforts on the analytical derivation of effective elastic parameters of strain gradient materials, see in the work of Ma and Gao, 2014 where Eshelby's equivalent inclusion method and Mori-Tanaka's averaging technique were used. In a very recent work of J. Ganghoffer and Reda, 2021, variational principle in linear elasticity with the extended Hill lemma was used to derive the closed form solutions of effective parameters. In dell'Isola, Giorgio, Pawlikowski, and N. L. Rizzi, 2016, the authors proposed a heuristic homogenization technique by considering a discrete spring model for extensible beams,

which leads to homogenized strain gradient deformation energies. The corresponding material parameters were identified in Giorgio, 2016; De Angelo, Barchiesi, Giorgio, and Abali, 2019; Shekarchizadeh, Abali, Barchiesi, and Bersani, 2021 by fitting the macro-constitutive parameters (in homogenized strain energy functional) using several numerical simulations performed with the micro-model (using a standard Cauchy first gradient theory). In Placidi, Andreaus, and Giorgio, 2017, gedanken experiments were used to identify the material parameters for pantographic structures. In Boutin, Giorgio, Placidi, et al., 2017, high-order continuum model was obtained for pantographic structures by means of a micro/macro-identification procedure based on the asymptotic homogenization method. In Li, 2011b; Li, 2011a; Li and X.-B. Zhang, 2013; Barboura and Li, 2018, a strain gradient constitutive law was established by homogenization of heterogeneous materials. The obtained strain gradient parameters are not dependent on the size of an RVE, but only relying on the intrinsic size of the materials. Following the methodology, in this thesis, a homogenization tool based on asymptotic analysis will be presented to determine the additional parameters.

2.4 Numerical implementations of strain gradient theory

Once the parameters are identified, a homogeneous continuum may be used as a replacement for metamaterials to study their mechanical behaviors, such as static or dynamic responses and crack propagation. Strain gradient elasticity theory leads to fourth order governing equations. Numerical experiments for strain gradient continua require C^1 continuity, which means that the unknowns and their spatial derivatives must be continuous. Meshless method, boundary element method can be employed to meet such requirements, see the works of Askes and Aifantis, 2002; Z. Tang, Shen, and Atluri, 2003; Tsepoura, Papargyri-Beskou, and Polyzos, 2002; Karlis, Tsinopoulos, Polyzos, and Beskos, 2008. Various finite element formulations have been proposed in the literature. Shu, King, and N. A. Fleck, 1999 developed mixed-type elements for strain gradient elasticity theory, where standard C^0 continuous shape functions were used. The nodal degrees of freedom include displacements and displacement gradients. The concept of the Lagrange multiplier was used to enforce kinematic constraints between displacement gradients. The mixed finite element formulation was extended to 3D in Zybell, Mühlich, Kuna, and Z. Zhang, 2012 and was implemented by means of commercial software Abaqus. In Phunpeng and Baiz, 2015, numerical implementation of such mixed-type finite element was carried out by an open source computing platform called FEniCS. C^1 elements were developed in Petera and Pittman, 1994; Zervos, Papanastasiou, and Vardoulakis, 2001; Papanicolopulos, Zervos, and Vardoulakis, 2009. In such elements displacements, first derivatives, and some second derivatives are interpolated. These elements are reported to be not competitive in three dimensions. For comparative studies of mixed-type elements and C^1 elements, it is referred to the works of Zervos, Papanicolopulos, and Vardoulakis, 2009; Fischer, Mergheim, and Steinmann, 2010. In Fischer, Klassen, Mergheim, Steinmann, and R. Müller, 2011; Rudraraju, Van der Ven, and Garikipati, 2014, IsoGeometric Analysis

(IGA) (Cottrell, Hughes, and Bazilevs, 2009) was extended to the numerical solution of the problems of gradient elasticity. The used shape functions in IGA naturally meet the requirements of higher order continuity. In Khakalo and Niiranen, 2017, isogeometric analysis of gradient elasticity by user element implementations within a commercial finite element software Abaqus was presented.

2.5 Crack propagation

Damage and fracture of materials are multiscale phenomena, which range from atomic level to crystal structures scale, from microstructure level (micro-voids or micro-cracks) to the macroscopic scale. At different scales, the mechanisms for crack initiation/formation and propagation are different. Although multiscale methods may be used, it depends on the descriptions of microstructures which are not easily obtained. Thus continuum modeling is believed to be a suitable way for the damage modeling of metamaterials (Placidi, Misra, and Barchiesi, 2018; Placidi, Misra, and Barchiesi, 2019).

From the computational viewpoint, FEM is often used to simulate the damage mechanics. Two main approaches are proposed in the literature within the framework of FEM: The discrete crack models (Moës, Dolbow, and Belytschko, 1999; Moës, Gravouil, and Belytschko, 2002) and the smeared/diffuse crack approach (Hillerborg, Modéer, and Petersson, 1976). The phase field method, as a case of the smeared/diffuse crack approach, has been gaining increasingly popularity among researchers due to its attracting features. It has been shown that a regularization through the inclusion of the gradient of damage in the phase field method alleviates the localization phenomena and mesh-dependency issue. Such a method allows to incorporates crack nucleation, branching, coalescence, and is able to predict complex crack paths. Remesh is avoided, element edges are not necessarily aligned with crack paths as shown in the works of Bourdin, Francfort, and Marigo, 2000; Francfort and Marigo, 1998; Natarajan, Annabattula, et al., 2019; Msekh, Sargado, Jamshidian, Areias, and Rabczuk, 2015; Bleyer and Alessi, 2018.

Strain gradient theory has been applied to the modeling of damaging process, see some recent works in Putar, Sorić, Lesičar, and Tonković, 2017; T. H. Nguyen and Niiranen, 2020; Makvandi, Duczek, and Juhre, 2019; Y. Yang and Misra, 2010; Abali, Klunker, Barchiesi, and Placidi, 2021. In Placidi and Barchiesi, 2018; Placidi, Misra, and Barchiesi, 2018; Placidi, Barchiesi, and Misra, 2018, an energy approach was used for the modeling of brittle fracture of materials by integrating strain gradient theory into phase field method. A variational inequality was used to yield the balance equations, boundary conditions, and the Karush–Kuhn–Tucker conditions. As such the regularization is realized by the introduced strain gradient instead of damage gradient. The microstructural effects may be taken into account by using such a formulation. The external boundary conditions of the damage introduced in the

damage gradient model are relieved. Based on the works of Placidi and Barchiesi, 2018, in this thesis a numerical tool for predicting the brittle fracture propagation of strain gradient materials will be developed.

3 Objectives of the thesis

The main objective of this thesis is to provide a computational homogenization tool in the framework of strain gradient elasticity, which can deliver effective parameters for metamaterials with periodic microstructures. The following research questions will be answered in the work:

- How to establish the connections between the material parameters at the microscale and macroscale?
- Can the asymptotic homogenization method be employed when the scale separation is not strictly fulfilled?
- Do the effective strain gradient moduli identified by the homogenization tool vanish for homogeneous materials where no substructures exist?
- Are the effective strain gradient moduli identified by the homogenization tool sensitive to the stack of RVEs?
- Do the identified parameters, particularly the strain gradient moduli organized in Voigt notation, match the forms of symmetry classes presented in the theoretical predictions for example in Auffray, Bouchet, and Brechet, 2009; Auffray, Le Quang, and Q.-C. He, 2013?
- How to validate the identified parameters? Can size effects be captured by using the identified parameters?

Moreover, this work also aims to provide a novel numerical implementation of strain gradient elasticity by isogeometric analysis and to provide novel numerical solutions for brittle crack propagation of strain gradient materials. It should be remarked that, in the following chapters, the word "macro" is attached to the length scale where phenomena are observed, "micro" is to the length scales used to build the architecture. No specific length scale is attached to the word "micro".

Chapter II

Generalized continuum theories

Generalized continuum theories are investigated in this thesis. Therefore an overview of selected generalized continuum theories is given in this chapter. Index notation is used: i, j, k, l, m, n is equal to $1, 2, 3$; Einstein's summation convention is used over repeated indices; a comma is for spatial derivatives in the Cartesian coordinate system $f_{,i} = \frac{\partial f}{\partial X_i}$; X_i is for the position vector in the reference configuration. All the equations are formulated under the assumption of small deformations.

1 Cauchy continuum theory

For a Cauchy continuum, the balance of linear momentum reads

$$\sigma_{ij,j} + f_i = 0 \ , \tag{II.1}$$

where σ_{ij} is the Cauchy stress, which is symmetric $\sigma_{ij} = \sigma_{ji}$. f_i is the specific volumetric force. The kinetic term is ignored in the above equation, since the static case is considered. The displacement and traction boundary conditions are given as

$$u_i = u_i^{\mathrm{P}} \ , \ n_i \sigma_{ij} = t_i^{\mathrm{P}} \ . \tag{II.2}$$

where u_i^{P}, and t_i^{P} are the prescribed displacement and traction with an outward unit normal vector n_i defined on the boundary. For the linear elastic material, the constitutive law can be given as

$$\sigma_{ij} = C_{ijkl} \varepsilon_{kl} \ , \tag{II.3}$$

where the linear strain tensor is used $\varepsilon_{ij} = \frac{1}{2}(u_{i,j} + u_{j,i})$. C_{ijkl} is the fourth order stiffness tensor. For an isotropic linear elastic material, there are two independent parameters, and C_{ijkl} can be expressed as

$$C_{ijkl} = \lambda\delta_{ij}\delta_{kl} + \mu(\delta_{ik}\delta_{jl} + \delta_{il}\delta_{jk}) \ , \tag{II.4}$$

such that

$$\sigma_{ij} = C_{ijkl}\varepsilon_{kl} = \lambda\varepsilon_{kk}\delta_{ij} + 2\mu\varepsilon_{ij} \ , \tag{II.5}$$

where λ and μ are two Lamé constants.

Although the Cauchy continuum theory is of crucial importance, it shows limitations when dealing with size dependent phenomena observed in the experiments of meta-materials, since there are no length scale related parameters in the constitutive law. A generalization of the Cauchy continuum theory allows to address this problem. As mentioned before, usually there are two paths for this purpose. In the following, the widely used micropolar theory and strain gradient theory are briefly summarized as examples for these two different types of generalized continuum theories.

2 Micropolar theory

A generalization of the Cauchy continuum theory by taking additional kinematical degrees of freedom (not only translational displacement) into account is possible. One example of such a generation is the micropolar theory. Fundamental equations in linear micropolar elasticity are summarized here. More details can be found in the works of Eremeyev, Lebedev, and H. Altenbach, 2012; Eringen, 2012. Compared to the Cauchy continuum theory, the kinematics in micropolar theory includes not only displacements u_i but also micro-rotations ϕ_i. The micro-rotations do not need to coincide with the macroscopic rotation of the continuum at the same point. For linear elastic micropolar solids, the governing equations are given by the balance of linear momentum and balance of angular momentum as:

$$\bar{\sigma}_{ij,i} + f_j = 0 \ , \quad e_{jmn}\bar{\sigma}_{mn} + m_{ij,i} + g_j = 0 \ \ , \tag{II.6}$$

where $\bar{\sigma}_{ij}$ is the stress tensor (not symmetric), m_{ij} is the couple stress tensor (not symmetric), f_i is the specific body force, g_i is the specific body couple, and e_{jmn} is the Levi-Civita tensor. The strain tensor and curvature tensor are given as:

$$\varepsilon_{ij} = u_{j,i} - e_{ijn}\phi_n \ , \quad \kappa_{ij} = \phi_{j,i} \ \ . \tag{II.7}$$

The stress tensor $\bar{\sigma}_{ij}$ and couple stress tensor m_{ij} are linked to strain tensor and curvature tensor by constitutive laws as:

$$\bar{\sigma}_{ij} = A_{ijkl}\varepsilon_{kl} + B_{ijkl}\kappa_{kl} \ , \quad m_{ij} = B_{klij}\varepsilon_{kl} + C_{ijkl}\kappa_{kl} \ \ , \tag{II.8}$$

where A_{ijkl}, B_{ijkl}, C_{ijkl} are fourth order stiffness tensors of micropolar materials. The tensor B_{ijkl} accounts for the coupling effects between the stress tensor and micro-curvature tensor and between the couple stress tensor and strain tensor. It vanishes when the materials are centro-symmetric. It should be noted that the tensors A_{ijkl} and C_{ijkl} have major symmetries $A_{ijkl} = A_{klij}$, $C_{ijkl} = C_{klij}$. The displacement and micro-rotation boundary conditions as well as traction boundary conditions are given by

$$\begin{aligned} u_i = u_i^{\mathrm{P}} \ , \ \phi_i = \phi_i^{\mathrm{P}} \ , \\ n_i \bar{\sigma_{ij}} = t_i^{\mathrm{P}} \ , \ n_i m_{ij} = c_i^{\mathrm{P}} \ , \end{aligned} \tag{II.9}$$

where u_i^{P} and ϕ_i^{P} represent the prescribed displacement and micro-rotation; t_i^{P} and c_i^{P} represent prescribed stress traction and couple stress traction, which are defined on the boundary with an outward unit normal vector n_i. For linear elastic isotropic micropolar materials, the constitutive laws can be written as (Eremeyev, Skrzat, and Stachowicz, 2016):

$$\begin{aligned} \bar{\sigma}_{ij} = \lambda \varepsilon_{kk} \delta_{ij} + (\mu + \kappa) \varepsilon_{ij} + \mu \varepsilon_{ji} \ , \\ m_{ij} = \alpha \kappa_{kk} \delta_{ij} + \beta \kappa_{ji} + \gamma \kappa_{ij} \ , \end{aligned} \tag{II.10}$$

where λ, μ, κ, α, β, γ are the elastic moduli.

3 Strain gradient theory

A generalization of Cauchy continuum by considering higher order gradient terms in the strain energy density results in strain gradient theory. In this section fundamental equations for strain gradient theory are recalled. R. Mindlin and Tiersten, 1962 gave three different forms (Form I, Form II, Form III) of strain energy density. In the version of Form II, the strain energy density, w, depends on both the strain tensors ε_{ij} and the first gradient of strains $\eta_{ijk} = \varepsilon_{ij,k}$

$$w = w(\varepsilon_{ij}, \eta_{ijk}) \ . \tag{II.11}$$

The stress σ_{ij} and the so-called hyperstress tensors τ_{ijk} are work-conjugated to ε_{ij} and η_{ijk}, which are shown as

$$\sigma_{ij} = \frac{\partial w}{\partial \varepsilon_{ij}} \ , \qquad \tau_{ijk} = \frac{\partial w}{\partial \eta_{ijk}} \ . \tag{II.12}$$

The variational of the internal energy functional in a domain Ω gives

$$\begin{aligned}\delta W^{\text{int}} = \int_\Omega \delta w \,\mathrm{d}V = \int_\Omega \Big(\sigma_{ij}\delta u_{i,j} + \tau_{ijk}\delta u_{i,jk}\Big)\,\mathrm{d}V = \int_\Omega \Big(-\sigma_{ij} + (\tau_{ijk})_{,k}\Big)_{,j}\delta u_i \,\mathrm{d}V \\ + \int_{\partial\Omega}\left(n_j\Big(\sigma_{ij} - (\tau_{ijk})_{,k}\Big) + n_k n_j \tau_{ijk}(D_p n_p) - D_j(n_k\tau_{ijk})\right)\delta u_i \,\mathrm{d}A \\ + \int_{\partial\Omega} n_k\tau_{ijk}n_j D(\delta u_i)\,\mathrm{d}A + \sum_m \oint_{\partial\partial\Omega_m} \Delta\Big(\nu_j n_k \tau_{ijk}\Big)\delta u_i \,\mathrm{d}l \ .\end{aligned} \tag{II.13}$$

where $\partial\Omega$ is the boundaries of Ω, and $\partial\partial\Omega_m$ represents the sharp edges. D and D_j are

$$D(\cdot) = n_k\frac{\partial(\cdot)}{\partial X_k} \ , \quad D_j(\cdot) = (\delta_{jk} - n_j n_k)\frac{\partial(\cdot)}{\partial X_k} \ ,$$

and n_i is the unit surface normal vector. Using the principle of virtual work leads to

$$\delta W^{\text{int}} - \delta W^{\text{ext}} = 0 \ . \tag{II.14}$$

The external work W^{ext} is assumed to be (Auffray, dell'Isola, Eremeyev, Madeo, and Rosi, 2015)

$$W^{\text{ext}} = \int_\Omega b_i u_i \,\mathrm{d}V + \int_{\partial\Omega}\Big(t_i u_i + r_i D(u_i)\Big)\,\mathrm{d}A + \sum_m \oint_{\partial\partial\Omega_m} f_i u_i \,\mathrm{d}l \ , \tag{II.15}$$

with b_i the specific body force, the so-called traction t_i, double traction r_i and wedge force f_k. By Eq. (II.13), Eq. (II.14), and Eq. (II.15), the governing equation, traction, double traction and, wedge forces are expressed as

$$\begin{gathered}(\sigma_{ij} - \tau_{ijk,k})_{,j} + b_i = 0 \ , \\ t_i = n_j(\sigma_{ij} - \tau_{ijk,k}) + n_k n_j \tau_{ijk}(D_p n_p) - D_j(n_k\tau_{ijk}) \ , \\ r_i = n_j n_k \tau_{ijk} \ , \\ f_i = \Delta\nu_j n_k \tau_{ijk} \ .\end{gathered} \tag{II.16}$$

For strain gradient materials, the strain energy density is given as:

$$w(\varepsilon_{ij}, \eta_{ijk}) = \frac{1}{2}\varepsilon_{ij}C_{ijkl}\varepsilon_{kl} + \frac{1}{2}\eta_{ijk}D_{ijklmn}\eta_{lmn} + \varepsilon_{ij}G_{ijklm}\eta_{klm} \ , \tag{II.17}$$

where C_{ijkl} and D_{ijklmn} are the classical fourth order stiffness tensor and the sixth order strain gradient elastic stiffness tensor, G_{ijklm} is the fifth order coupling tensor. For a linear elastic centro-symmetric strain gradient materials, the strain energy density is rewritten as

$$w(\varepsilon_{ij}, \eta_{ijk}) = \frac{1}{2}\varepsilon_{ij}C_{ijkl}\varepsilon_{kl} + \frac{1}{2}\eta_{ijk}D_{ijklmn}\eta_{lmn} \ . \tag{II.18}$$

In the case of isotropy, C_{ijkl} and D_{ijklmn} are expressed as

$$C_{ijkl} = \lambda\delta_{ij}\delta_{kl} + \mu(\delta_{ik}\delta_{jl} + \delta_{il}\delta_{jk}) \ , \tag{II.19}$$

$$\begin{aligned} D_{ijklmn} =& c_3(\delta_{ij}\delta_{kl}\delta_{mn} + \delta_{in}\delta_{jk}\delta_{lm} + \delta_{ij}\delta_{km}\delta_{ln} + \delta_{ik}\delta_{jn}\delta_{lm}) \\ &+ c_4\delta_{ij}\delta_{kn}\delta_{ml} + c_5(\delta_{ik}\delta_{jl}\delta_{mn} + \delta_{im}\delta_{jk}\delta_{ln} + \delta_{ik}\delta_{jm}\delta_{ln} + \delta_{il}\delta_{jk}\delta_{mn}) \\ &+ c_6(\delta_{il}\delta_{jm}\delta_{kn} + \delta_{im}\delta_{jl}\delta_{kn}) + c_7(\delta_{il}\delta_{jn}\delta_{mk} + \delta_{im}\delta_{jn}\delta_{lk} + \delta_{in}\delta_{jl}\delta_{km} + \delta_{in}\delta_{jm}\delta_{kl}) \ , \end{aligned} \tag{II.20}$$

λ and μ are the Lamé constants. c_3, c_4, c_5, c_6, and c_7 are five additional strain gradient parameters. By Eqs. (II.17)-(II.20), the stress and hyperstress tensors are given as

$$\sigma_{ij} = \frac{\partial w}{\partial \varepsilon_{ij}} = C_{ijkl}\varepsilon_{kl} = c_1\delta_{ij}\varepsilon_{kk} + 2c_2\varepsilon_{ij} \ , \tag{II.21}$$

$$\begin{aligned} \tau_{ijk} = \frac{\partial w}{\partial \eta_{ijk}} = D_{ijklmn}\eta_{lmn} =& c_3(\delta_{ij}\varepsilon_{km,m} + \delta_{jk}\varepsilon_{mm,i} + \delta_{ij}\varepsilon_{nk,n} + \delta_{ik}\varepsilon_{mm,j}) + c_4\delta_{ij}\varepsilon_{ll,k} \\ &+ c_5(\delta_{ik}\varepsilon_{jn,n} + \delta_{jk}\varepsilon_{li,l} + \delta_{ik}\varepsilon_{nj,n} + \delta_{jk}\varepsilon_{im,m}) \\ &+ c_6(\varepsilon_{ij,k} + \varepsilon_{ji,k}) + c_7(\varepsilon_{ik,j} + \varepsilon_{ki,j} + \varepsilon_{jk,i} + \varepsilon_{kj,i}) \ . \end{aligned} \tag{II.22}$$

4 Numerical implementation for strain gradient theory

In this work numerical experiments for strain gradient materials are conducted, which requires at least C^1 continuity as mentioned before. In order to address the issue two strategies are employed: The mixed finite element method and isogeometric analysis. A brief summary of the two methods is given in this section.

4.1 Mixed finite element formulation for strain gradient elasticity

A mixed finite element method guarantees weak C^1 continuity. It shows advantages when handling complex geometry and boundary conditions. Such a method will be used for the computations of crack propagation of strain gradient materials in this thesis.

The weak forms for strain gradient elasticity problems of mixed finite element formulation are shown in the works of Shu, King, and N. A. Fleck, 1999; Zybell, Mühlich,

Kuna, and Z. Zhang, 2012 as

$$\begin{aligned}\int_\Omega \Big(\sigma_{ij}\delta\varepsilon_{ij} - \rho_{jk}\delta u_{k,j}\Big)\mathrm{d}V &= \int_\Omega b_i\delta u_i \mathrm{d}V + \int_{\partial\Omega} t_i\delta u_i \mathrm{d}A \ , \\ \int_\Omega \Big(\tau_{ijk}\delta\eta_{ijk} + \rho_{jk}\delta\psi_{jk}\Big)\mathrm{d}V &= \int_{\partial\Omega} n_j r_k \delta\psi_{jk}\mathrm{d}A \ , \\ \int_\Omega \Big(-u_{k,j} + \psi_{jk}\Big)\delta\rho_{jk}\mathrm{d}V &= 0 \qquad \text{(no sum on } j \text{ and } k) \ ,\end{aligned} \tag{II.23}$$

where ψ_{ij} is the introduced additional degrees of freedom. It is the so-called relaxed strains, which are postulated to be equal to the displacement gradients in an approximate manner:

$$\psi_{ij} \approx u_{j,i} \ .$$

The relaxed strain gradients are then defined as:

$$\eta_{ijk} = \frac{1}{2}(\psi_{ij,k} + \psi_{ki,j}) \ .$$

ρ_{jk} is the introduced Lagrange multiplier with

$$\rho_{jk} = -\tau_{ijk,i} \ .$$

In Phunpeng and Baiz, 2015, an implementation of the above weak forms was given based on FEniCS [6]. The FEniCS library enables users to quickly transcribe mathematical models into efficient finite element codes through a domain-specific language, called UFL (Unified Form Language) embedded in Python. The assembly and the solution of the resulting system of equations are done automatically. Throughout the thesis, the FEniCS library is used. A finite element mesh can be generated by using an open source software SALOME [7]. Post-processing can be done by using the open source visualization application Paraview [8].

4.2 Isogeometric analysis

The other numerical method used in this thesis is IsoGeometric Analysis (IGA). In IGA, the so-called control mesh and physical mesh are defined. The control mesh is built by control points as indicated by red points in Fig. II.1. The physical mesh is the blue grid in Fig. II.1, which is built by knot spans (only a single patch exists herein). A knot vector $[\xi_1, \xi_2, \cdots, \xi_m]$ is a set of monotonically increasing points, where $\xi_i \in \mathbb{R}$ is referred to as i^{th} knot. A knot divides the interval $[\xi_1, \xi_m]$ into knot spans (similar to elements in FEM). For a given knot vector, the B-spline functions

[6] https://fenicsproject.org/
[7] https://www.salome-platform.org/
[8] https://www.paraview.org/

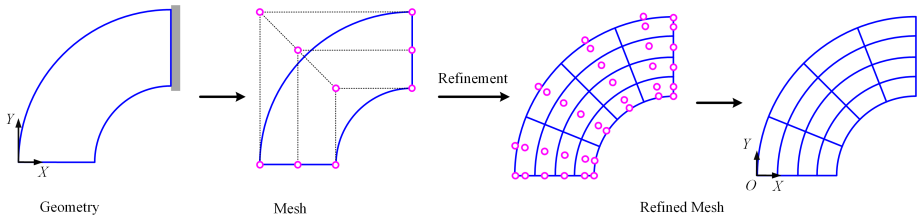

Figure II.1: Isogeometric analysis. Red points represent for control points. Blue grids are the physical elements.

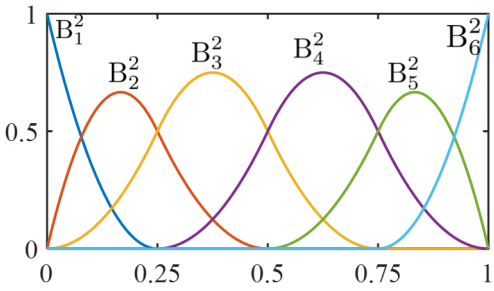

Figure II.2: B-spline basis function (p =2) constructed from the knot vector $\Xi = [0, 0, 0, 0.25, 0.5, 0.75, 1, 1, 1]$.

are defined recursively on $[\xi_1, \xi_m]$ by

$$B_i^p(\xi) = \frac{\xi - \xi_i}{\xi_{i+p} - \xi_i} B_i^{p-1}(\xi) + \frac{\xi_{i+p+1} - \xi}{\xi_{i+p+1} - \xi_{i+1}} B_{i+1}^{p-1}(\xi) \qquad \text{for} \quad p = 1, 2, 3... \tag{II.24}$$

with the zeroth order basis functions:

$$B_i^0(\xi) = \begin{cases} 1, & \text{if } \xi_i \leq \xi \leq \xi_{i+1} \ , \\ 0, & \text{otherwise} \ , \end{cases}$$

and $1 \leq i \leq n$, p being the polynomial degree, $n = m - p - 1$ being the number of B-splines. If an interior knot value repeats, it is referred to as a multiple knot. At a knot of multiplicity k the continuity is C^{p-k}. If the first or the last knots repeat $p+1$ times, the knot vector is said to be open. By means of a quadratic B-spline basis as shown in Fig. II.2, a C^1-continuous one dimensional NURBS (Non-Uniform Rational B-Spline) basis can be constructed as

$$N_i(\xi) = \frac{B_i^2(\xi) w_i}{\sum_{i=1}^n B_i^2(\xi) w_i} \ , \tag{II.25}$$

where w_i are the weights associated with each of the B-spline functions.

The weak form implemented by the IGA for strain gradient elasticity reads

$$\int_\Omega \left(\sigma_{ij}\delta u_{i,j} + \tau_{ijk}\delta u_{i,jk}\right) \mathrm{d}V = \int_\Omega b_i \delta u_i \,\mathrm{d}V + \int_{\partial\Omega} t_i \delta u_i \,\mathrm{d}A + \int_{\partial\Omega} r_i D(\delta u_i) \,\mathrm{d}A + \sum_m \oint_{\partial\partial\Omega_m} f_i \delta u_i \,\mathrm{d}l. \tag{II.26}$$

A library called tIGAr (Kamensky and Bazilevs, 2019) based on FEniCS software will be used to perform isogeometric analysis. It should be noted that only displacement degrees of freedom are required here, degrees of freedom that correspond to higher order gradients are not needed (Fischer, Klassen, Mergheim, Steinmann, and R. Müller, 2011).

Chapter III

Asymptotic homogenization method

The Asymptotic Homogenization (AH) method which is also known as Asymptotic Expansion Homogenization (AEH) or periodic homogenization or mathematical homogenization is one of the most rigorous homogenization approaches. It allows to describe physical phenomena of materials with periodic microstructures. By considering higher order terms in AH, a strain gradient constitutive law is possible to be established naturally. In this section, fundamental equations of AH are summarized.

1 Asymptotic homogenization method

As mentioned before, the main assumption of AH is the separation of scales: The macroscopic level $\boldsymbol{X}$ and the microscopic level $\boldsymbol{y}$. At the microscale the material associated to a material body Ω is heterogeneous with periodic microstructures. The purpose is to substitute it with a homogeneous counterpart at macroscale. In the framework of linear elasticity, the problem at microscale is given as

$$\begin{aligned}
&\sigma^{\mathrm{m}}_{ij,j} + f_i = 0 \qquad \text{in } \Omega \ , \\
&\varepsilon^{\mathrm{m}}_{ij} = \frac{1}{2}(u^{\mathrm{m}}_{i,j} + u^{\mathrm{m}}_{j,i}) \qquad \text{in } \Omega \ , \\
&\sigma^{\mathrm{m}}_{ij} = C^{\mathrm{m}}_{ijkl}\varepsilon^{\mathrm{m}}_{ij} \qquad \text{in } \Omega \ , \\
&u^{\mathrm{m}}_i = \bar{u}_i \qquad \text{on } \partial\Omega_u \ , \\
&\sigma^{\mathrm{m}}_{ij} n_j = \bar{t}_i \qquad \text{on } \partial\Omega_t \ ,
\end{aligned} \tag{III.1}$$

where the script "m" denotes the quantities at microscale (describing the high resolution of the heterogeneous materials), $\partial\Omega_u \cap \partial\Omega_t = 0$, $\partial\Omega_u \cup \partial\Omega_t = \partial\Omega$; $\bar{u}_i$ and $\bar{t}_i$

are prescribed displacement and traction; n_j is the outward unit vector normal to the boundary $\partial\Omega_t$. The displacement u_i^{m} can be approximated by using an asymptotic expansion:

$$u_i^{\mathrm{m}}(\boldsymbol{X}) = \overset{0}{u}_i(\boldsymbol{X}) + \epsilon \overset{1}{u}_i(\boldsymbol{X}, \boldsymbol{y}) + \dots \ , \tag{III.2}$$

where a small parameter ϵ is defined as $\epsilon = \frac{l}{L}$, with l the measurement of microscopic size and L the macroscopic size. $\overset{0}{u}_i(\boldsymbol{X})$ is the macroscopic solution for the homogenized body. The solution of $\overset{1}{u}_i$ is given as:

$$\overset{1}{u}_i = \varphi_{abi} \overset{0}{u}_{a,b} + \overset{1}{\bar{u}}_i(\boldsymbol{X}) \ , \tag{III.3}$$

where $\overset{1}{\bar{u}}_i = \overset{1}{\bar{u}}_i(\boldsymbol{X})$ are integration constants in $\boldsymbol{y}$; φ_{abi} is a $\boldsymbol{y}$-periodic function with zero average value. It is the solution of the following equation:

$$\frac{\partial}{\partial y_j}\left(C_{ijkl}^{\mathrm{m}} \left(\frac{\partial \varphi_{abk}}{\partial y_l} + \delta_{ak}\delta_{bl} \right) \right) = 0 \ . \tag{III.4}$$

After resolving φ_{abi} under periodic boundary condition, the homogenized stiffness tensor is obtained as

$$C_{abcd}^{\mathrm{M}} = \frac{1}{V} \int_{\Omega^P} C_{ijkl}^{\mathrm{m}} \left(\delta_{ia}\delta_{jb} + \frac{\partial \varphi_{abi}}{\partial y_j} \right) \left(\delta_{kc}\delta_{ld} + \frac{\partial \varphi_{cdk}}{\partial y_l} \right) \mathrm{d}V \ , \tag{III.5}$$

where the letter "M" denotes macroscopic homogenized quantities, Ω^P denotes an RVE of the heterogeneous materials with volume V. The formulation presented is indeed the AH in its most common form, first order form. It should be remarked that ϵ is not included in the expression of C_{abcd}^{M}, which means that the obtained parameters in C_{abcd}^{M} are size independent. A comment on AH was given in Chung, Tamma, and Namburu, 2001, "That is, the scale parameter ϵ is not contained in the equation. This precludes the exchange of length scale information across multiple scales...A paradox is therefore evident. If two points are selected arbitrarily close, both will have associated with it an entire unit cell that possesses some finite volume. The two unit cells can conceivably overlap. One might call this a *single-point* localization paradox." In order to capture the size dependent phenomena and attempt to overcome the mentioned paradox, in this thesis a homogenization tool based on AH with considering higher order terms will be presented. Such a formulation will link with strain gradient theory and allow to deliver the strain gradient parameters. The ϵ enters in the expression of the strain gradient stiffness tensor so that the length scale information is taken into account.

2 Numerical implementation of asymptotic homogenization

Different numerical implementation schemes of asymptotic homogenization are proposed in the literature such as finite element method (Oliveira, Pinho-da-Cruz, and Teixeira-Dias, 2009) and finite volume method (Z. He and Pindera, 2021). There are several ready-to-use codes in the framework of finite element method, such as Matlab codes in Andreassen and Andreasen, 2014; Dong, Y. Tang, and Zhao, 2019, FEniCS codes in Abali and Barchiesi, 2020; Bleyer, 2018, an Abaqus plug-in in Christoff, Brito-Santana, Talreja, and Tita, 2020.

In order to obtain the material parameters in Eq. (III.5), the solutions of the periodic fluctuation φ_{abi} must be resolved. The weak form of φ_{abi} reads

$$\int_{\Omega^P} \left(C^{\mathrm{m}}_{ijkl} \Big(\frac{\partial \varphi_{\underline{ab}k}}{\partial y_l} + \delta_{\underline{a}k} \delta_{\underline{b}l} \Big) \right) \frac{\partial \delta \varphi_{\underline{ab}i}}{\partial y_j} \, \mathrm{d}V = 0 \tag{III.6}$$

where no summation convention is applied over underlined indices. Such a weak form can be solved under the periodic boundary conditions. For a 2D square domain in $X_1 \in \left[-\frac{a}{2}, \frac{a}{2}\right]$ and $X_2 \in \left[-\frac{a}{2}, \frac{a}{2}\right]$, the boundary conditions are defined as

$$\begin{aligned} \varphi_{abi}(-\frac{a}{2}, X_2) &= \varphi_{abi}(\frac{a}{2}, X_2) \\ \varphi_{abi}(X_1, -\frac{a}{2}) &= \varphi_{abi}(X_1, \frac{a}{2}). \end{aligned} \tag{III.7}$$

A point at corner is fixed in order to make the solution unique in Oliveira, Pinho-da-Cruz, and Teixeira-Dias, 2009; Chung, Tamma, and Namburu, 2001. The magnitude of the restrictions can be any, because only the gradients of the solution of φ_{abi} matters in the expressions of C^{M}_{abcd} Chung, Tamma, and Namburu, 2001. Alternatively, it is also possible to introduce Lagrange multipliers to enforce the zero average of φ_{abi}, which will be presented in the following of the thesis.

Chapter IV

Discussions, conclusions, and outlook

1 Discussions and conclusions

The main goal of the thesis is to develop a homogenization tool for linear elastic materials with periodic substructures, which can be used to deliver not only the parameters in fourth order stiffness tensor but also those in fifth order and sixth order stiffness tensor. These identified parameters may be used to investigate the size dependent phenomena of metamaterials or crack propagation of strain gradient materials. There are five works contained in Part II in a didactic-structural systematic way.

Yang H., Timofeev D., Abali B. E., Li B., Müller W. H. (2021). "Verification of strain gradient elasticity computation by analytical solutions." In: *ZAMM-Journal of Applied Mathematics and Mechanics/Zeitschrift für Angewandte Mathematik und Mechanik*, e202100023. https://doi.org/10.1002/zamm.202100023

The objective of this chapter is to provide an accurate and reliable numerical implementation for strain gradient materials based on IGA, which will be used in the later chapters. The starting point is a recapitulation of the variational formulation of strain gradient elasticity theory. The constitutive relation proposed by Mindlin for 3D isotropic strain gradient solids has been employed. The strain energy is demonstrated to depend on 7 constitutive parameters: the 2 Lamé constants and other 5 length scale related parameters as shown in Eq. (II.19) and Eq. (II.20). The governing

equations and corresponding boundary conditions have been derived and shown in Eq. (II.16). The exotic so-called double forces and wedge forces appear in the formulation. Three cases of benchmark analytical solutions including extension, torsion, and non-conventional bending haven been considered. Furthermore, an isogeometric analysis implementation of strain gradient elasticity has been developed based on the tIGAr library using FEniCS. Verification of developed numerical implementation has been done by using the derived analytical solutions. Adequate agreements have been observed between numerical and analytical solutions. It is also found that the double forces and wedge forces are necessary to keep the equilibrium of strain gradient materials. The capability of accommodating line distributed forces (wedge forces) for strain gradient continua in 3D has been presented. The developed numerical tool is indeed general to investigate any geometries or boundary conditions for 2D and 3D strain gradient materials.

The 2nd work is the post-print version of the paper published as:
Yang H., Abali B. E., Timofeev D., Müller W. H. (2020). "Determination of metamaterial parameters by means of a homogenization approach based on asymptotic analysis." In: *Continuum Mechanics and Thermodynamics*, 32, pp, 1251–1270, Springer Nature. https://doi.org/10.1007/s00161-019-00837-4

Based on strain gradient elasticity theory, subsequently, in the second contribution, a homogenization method has been presented, which brings heterogeneous Cauchy continua with periodic substructures towards homogeneous strain gradient continua. Inspired by the works in Li, 2011b; Li and X.-B. Zhang, 2013; Barboura and Li, 2018, the departure is an assumption that the deformation energy for a selected RVE of metamaterials is equivalent at the microscale and at the macroscale. A linear elastic second order theory at the macroscale is used. Macroscopic displacement has been expressed by means of linear Taylor expansions up to quadratic terms in the spatial coordinates within the RVE. A linear elastic first order theory has been used at the microscale. Asymptotic analysis has been employed to approximate the microscopic displacement. By doing so, the microscopic displacement is decomposed into macroscopic displacement and periodic fluctuations. A connection of the material parameters has been established by expressing the macro- and microscopic energies in terms of the same quantity. It should be noted that the obtained expressions to determine material parameters are indeed the same as those in Li, 2011b; Li and X.-B. Zhang, 2013; Barboura and Li, 2018. However the mathematical formulation is different. One of the most distinct differences with the conventional AH method is that the homothetic ratio ϵ in the used asymptotic analysis is a finite number indicating the finite size of underlying microstructures. It is not necessarily infinitesimal. The ϵ enters the expression of strain gradient stiffness tensor such that the length scale information is taken into account. Finite element method has been used to determine the material parameters. Weak forms for obtaining the numerical solutions of the periodic fluctuations were derived and given.

The 3rd work is the paper in pre-print format submitted as:
Yang, H., Abali B. E., Müller W. H., Barboura S., Li J. (2021). "Verification of asymptotic homogenization method developed for periodic architected materials in strain gradient continuum." *Submitted*. https://arxiv.org/abs/2106.05158

In the third contribution, efforts were made to investigate the homogenization tool in 3D and verify it by means of various numerical experiments. It should be remarked that such a 3D study and numerical implementation of the homogenization tool were done in Abali and Barchiesi, 2020. In this chapter, different from Chapter II and Abali and Barchiesi, 2020, the effects of the material density of constitutions of microstructures are taken into account. In such a way, the identified material parameters are maybe dependent on densities of each constitution of microstructures. This was also discussed in Boutin, 1996. The numerical implementation was developed and based on the codes in Abali and Barchiesi, 2020. It should be emphasized that all of the parameters in the strain gradient elasticity theory have been determined, especially the rank five and rank six tensors. 2D and 3D numerical examples including composite materials and foams have been conducted to verify the homogenization method. It was found that the identified parameters in the strain gradient tensor all vanish when the materials are purely homogeneous. Both the classical and strain gradient stiffness parameters are insensitive to the repetition of RVEs. The stain gradient parameters are influenced by microstructural sizes. It should be remarked that conventional homogenization method can not take the effects of microstructural sizes into account due to the fact that length scale information is not contained. The classical stiffness tensor and strain gradient stiffness tensor in Voigt notation for microstructures with cubic material symmetry in 2D and 3D were given. The mathematical forms of materials of cubic symmetry match the predictions presented in Auffray, Bouchet, and Brechet, 2009; Weeger, 2021. Note that such a homogenization tool is applicable to any metamaterials with periodic substructures. To the author's best knowledge, such an identification of strain gradient parameters in 3D are presented for the first time in the literature. A scaling rule for strain gradient parameters was given, indicating that strain gradient parameters are proportional to the square of homothetic ratio when scaling a unit cell.

The 4th work is the publisher's version of the paper under a Creative Commons Attribution 4.0 International License (CC BY 4.0 (https://creativecommons.org/licenses/by/4.0/)):
Yang, H., Timofeev, D., Giorgio, I., Müller W. H. (2020). "Effective strain gradient continuum model of metamaterials and size effects analysis." In: *Continuum Mechanics and Thermodynamics*. pp, 1–23. https://doi.org/10.1007/s00161-020-00910-3

This work is devoted to validating the identified parameters generated by using mathematical formulations and codes developed in Chapter II. Comparisons with direct FEM computations where substructures were meshed have been done. Such comparisons were conducted in a cantilever beam bending case. It was found that the

homogenized strain gradient continua show good match with direct FEM solutions. It also showed that size effects of beams made of lattice or composite materials were captured with satisfactory accuracy in the homogenized strain gradient continua by using the identified parameters. That is to say: The homogenization tool captures the changes of macroscopic responses due to variations of microstructural sizes. If the microstructural size becomes negligible with respect to the macroscopic length scale, the results obtained coincide with the results from first order asymptotic homogenization method, and they both match the results of direct FEM solutions. The computations for the strain gradient continua were done by using the implementation proposed in the Chapter I of this part, where an isogeometric analysis based codes were provided.

The 5th work is the post-print version of the paper published as:
Barchiesi E., Yang H., Tran C. A., Placidi L., Müller W. H. (2020). "Computation of brittle fracture propagation in strain gradient materials by the FEniCS library." In: *Mathematics and Mechanics of Solids*. 26.3, pp, 325-340.
https://doi.org/10.1177/1081286520954513

In addition, an application of strain gradient modeling to quasi-static brittle fractures was presented within an approach based on a maximum energy-release rate principle. The features of regularizing singular stress fields of the strain gradient theory was used. By introducing strain gradient in the deformation energy functional, nonlocality is achieved without a damage gradient term in the dissipated energy. By using such a model, the normal part of the damage gradient is not constrained on boundaries, therefore, cracks can intersect boundaries non-orthogonally. The formulation is indeed proposed in Placidi and Barchiesi, 2018, the novelty here is the numerical implementation part where a staggered scheme based on FEniCS was used. The mixed FEM was used to solve the strain gradient elasticity problem, afterwards, the damage field is resolved analytically by using the obtained displacement and strain gradient solutions. A combination of the homogenization tool with the damage model is straight forward to investigate the crack propagation of metamaterials.

2 Scientific contributions of the thesis

The novelties and new features of the thesis are summarized as follows:

- A numerical implementation based on isogeometric analysis for strain gradient elasticity is provided in Python language. The code is built on an open source library tIGAr using FEniCS, which is applicable to 2D and 3D numerical analyses for strain gradient materials.

- The mathematical formulation of the homogenization method is presented. It serves as a mathematical justification for the homogenization tool. Such a homogenization tool is indeed quite general. It allows to determine all the material parameters in strain gradient elasticity theory for 2D or 3D metamaterials with periodic substructures.

- Material parameters are identified for lattice materials, composite materials, and foams. Examples include 2D or 3D cases, cubic material symmetry or transverse isotropic material symmetry, stiff or soft inclusions, cubic or spherical inclusions. The structures of the strain gradient stiffness tensor in Voigt notation are presented for cubic and transverse isotropic material symmetry.

- The homogenization tool can account for not only the volume fraction, morphology, but also the absolute size of the microstructures. In other words, it is applicable to a finite homothetic ratio case, which indicates a finite size of microstructure. Therefore, the presented method may allow to account for boundary effects of metamaterials (H. Yang and W. H. Müller, 2021). The aforementioned "*single-point* localization paradox" may be alleviated by including ϵ in the expression of $\boldsymbol{D}$ since the length scale information is contained. An interpretation of the homothetic ratio is made. A scaling rule for the strain gradient parameters is given.

- Benchmark tests for numerical validation of the identified strain gradient tensor in statics are addressed in the case of cantilever beam bending by comparing the homogenized strain gradient model to direct FEM computations where detailed mesh of substructures exists.

- A novel implementation scheme was provided which can be used to predict the crack propagation for strain gradient materials by means of mixed finite element method based on FEniCS computing platform. Results indicate that by using such a modeling, non-orthogonal and non-parallel intersections between cracks and boundaries can be observed.

3 Outlook

There are still many opportunities of improvements, applications, and extensions of the developed homogenization tool. Future work will focus on the following aspects:

- The homogenization tool is based on small strain assumptions. However, in reality, metamaterials can undergo large deformations. The first improvement is to introduce geometric non-linearity and material non-linearity into the homogenization method, for example to consider the Mooney Rivlin hyperelastic

model.

- A second improvement of the work is to verify the identified parameters further in 2D and 3D, not only in static but also in the aspects of dynamic responses, buckling, and wave propagation. An experimental validation of the identified parameters is important to further justify the method. For example, metmaterials can be 3D printed and a quasi-static measurement of displacements versus the mechanical response (reaction forces) under incremental loading may be implemented so that it can be used to compare with the corresponding responses of homogenized models.

- There are many negative values in the determined strain gradient stiffness tensor. Although the numerical solutions by using these parameters are resolved by means of IGA, existence and uniqueness of weak solutions need to be proved mathematically as those done in Eremeyev, Alzahrani, et al., 2019; Eremeyev, Lurie, Solyaev, and dell'Isola, 2020; Eremeyev, dell'Isola, Boutin, and Steigmann, 2018; Nazarenko, Glüge, and H. Altenbach, 2021.

- Comparisons of the proposed homogenization tool with those proposed in the literature (micromorphic homogenization in Rokoš, Ameen, R. H. Peerlings, and M. G. Geers, 2019; Biswas and Poh, 2017; Hütter, 2019; Hütter, 2017, computational second order homogenization method in Yvonnet, Auffray, and Monchiet, 2020, closed form solutions in J. Ganghoffer and Reda, 2021, couple stress homogenization method in Skrzat and Eremeyev, 2020) will be of benefit to highlight the pros and cons of different approaches.

- It should be noted that the homogenization tool is applicable to any periodic substructures. Thus it is interesting to investigate the material parameters of more complex materials, for example the pantographic structures and biomimetic spinodoids structures.

- A combination of the homogenization tool with topology optimization method is possible, which will possibly lead to a so-called multiscale topology optimization procedure (Hoang, P. Tran, Vu, and Nguyen-Xuan, 2020; Wu, Sigmund, and Groen, 2021).

Bibliography

Abali, B. E. (2019). "Revealing the physical insight of a length-scale parameter in metamaterials by exploiting the variational formulation." In: *Continuum Mechanics and Thermodynamics* 31.4, pp. 885–894.

Abali, B. E., Müller, W. H., and dell'Isola, F. (2017). "Theory and computation of higher gradient elasticity theories based on action principles." In: *Archive of Applied Mechanics* 87.9, pp. 1495–1510.

Abali, B. E., Müller, W. H., and Eremeyev, V. A. (2015). "Strain gradient elasticity with geometric nonlinearities and its computational evaluation." In: *Mechanics of Advanced Materials and Modern Processes* 1.1, pp. 1–11.

Abali, B. E. and Barchiesi, E. (2020). "Additive manufacturing introduced substructure and computational determination of metamaterials parameters by means of the asymptotic homogenization." In: *Continuum Mechanics and Thermodynamics*, pp. 1–17.

Abali, B. E., Klunker, A., Barchiesi, E., and Placidi, L. (2021). "A novel phase-field approach to brittle damage mechanics of gradient metamaterials combining action formalism and history variable." In: *ZAMM-Journal of Applied Mathematics and Mechanics/Zeitschrift für Angewandte Mathematik und Mechanik*, e202000289.

Abali, B. E., Yang, H., and Papadopoulos, P. (2019). "A Computational Approach for Determination of Parameters in Generalized Mechanics." In: *Higher Gradient Materials and Related Generalized Continua*. Springer, pp. 1–18.

Aifantis, E. C. (1992). "On the role of gradients in the localization of deformation and fracture." In: *International Journal of Engineering Science* 30.10, pp. 1279–1299.

Altenbach, J., Altenbach, H., and Eremeyev, V. A. (2010). "On generalized Cosserat-type theories of plates and shells: a short review and bibliography." In: *Archive of Applied Mechanics* 80.1, pp. 73–92.

Anderson, W. and Lakes, R. (1994). "Size effects due to Cosserat elasticity and surface damage in closed-cell polymethacrylimide foam." In: *Journal of Materials Science* 29.24, pp. 6413–6419.

Andreassen, E. and Andreasen, C. S. (2014). "How to determine composite material properties using numerical homogenization." In: *Computational Materials Science* 83, pp. 488–495.

Andrews, E., Gioux, G., Onck, P., and Gibson, L. (2001). "Size effects in ductile cellular solids. Part II: experimental results." In: *International Journal of Mechanical Sciences* 43.3, pp. 701–713.

Ashby, M. F. and Medalist, R. M. (1983). "The mechanical properties of cellular solids." In: *Metallurgical Transactions A* 14.9, pp. 1755–1769.

Askes, H. and Aifantis, E. C. (2002). "Numerical modeling of size effects with gradient elasticity-formulation, meshless discretization and examples." In: *International Journal of Fracture* 117.4, pp. 347–358.

Askes, H. and Aifantis, E. C. (2011). "Gradient elasticity in statics and dynamics: an overview of formulations, length scale identification procedures, finite element implementations and new results." In: *International Journal of Solids and Structures* 48.13, pp. 1962–1990.

Auffray, N., Bouchet, R., and Brechet, Y. (2010). "Strain gradient elastic homogenization of bidimensional cellular media." In: *International Journal of Solids and Structures* 47.13, pp. 1698–1710.

Auffray, N., Bouchet, R., and Brechet, Y. (2009). "Derivation of anisotropic matrix for bi-dimensional strain-gradient elasticity behavior." In: *International Journal of Solids and Structures* 46.2, pp. 440–454.

Auffray, N., dell'Isola, F., Eremeyev, V. A., Madeo, A., and Rosi, G. (2015). "Analytical continuum mechanics à la Hamilton–Piola least action principle for second gradient continua and capillary fluids." In: *Mathematics and Mechanics of Solids* 20.4, pp. 375–417.

Auffray, N., Dirrenberger, J., and Rosi, G. (2015). "A complete description of bidimensional anisotropic strain-gradient elasticity." In: *International Journal of Solids and Structures* 69, pp. 195–206.

Auffray, N., Le Quang, H., and He, Q.-C. (2013). "Matrix representations for 3D strain-gradient elasticity." In: *Journal of the Mechanics and Physics of Solids* 61.5, pp. 1202–1223.

Bacigalupo, A. (2014). "Second-order homogenization of periodic materials based on asymptotic approximation of the strain energy: formulation and validity limits." In: *Meccanica* 49.6, pp. 1407–1425.

Bacigalupo, A., Paggi, M., Dal Corso, F., and Bigoni, D. (2018). "Identification of higher-order continua equivalent to a Cauchy elastic composite." In: *Mechanics Research Communications* 93, pp. 11–22.

Barboura, S. and Li, J. (2018). "Establishment of strain gradient constitutive relations by using asymptotic analysis and the finite element method for complex periodic microstructures." In: *International Journal of Solids and Structures* 136, pp. 60–76.

Barchiesi, E., Eugster, S. R., dell'Isola, F., and Hild, F. (2020). "Large in-plane elastic deformations of bi-pantographic fabrics: asymptotic homogenization and experimental validation." In: *Mathematics and Mechanics of Solids* 25.3, pp. 739–767.

Barchiesi, E., Ganzosch, G., Liebold, C., Placidi, L., Grygoruk, R., and Müller, W. H. (2019). "Out-of-plane buckling of pantographic fabrics in displacement-controlled shear tests: experimental results and model validation." In: *Continuum Mechanics and Thermodynamics* 31.1, pp. 33–45.

Bensoussan, A., Lions, J.-L., and Papanicolaou, G. (2011). *Asymptotic analysis for periodic structures*. Vol. 374. American Mathematical Soc.

Biswas, R. and Poh, L. H. (2017). "A micromorphic computational homogenization framework for heterogeneous materials." In: *Journal of the Mechanics and Physics of Solids* 102, pp. 187–208.

Bleyer, J. (2018). *Numerical Tours of Computational Mechanics with FEniCS*. Zenodo.

Bleyer, J. and Alessi, R. (2018). "Phase-field modeling of anisotropic brittle fracture including several damage mechanisms." In: *Computer Methods in Applied Mechanics and Engineering* 336, pp. 213–236.

Boisse, P., Hamila, N., and Madeo, A. (2018). "The difficulties in modeling the mechanical behavior of textile composite reinforcements with standard continuum mechanics of Cauchy. Some possible remedies." In: *International Journal of Solids and Structures* 154, pp. 55–65.

Bourdin, B., Francfort, G. A., and Marigo, J.-J. (2000). "Numerical experiments in revisited brittle fracture." In: *Journal of the Mechanics and Physics of Solids* 48.4, pp. 797–826.

Boutin, C. (1996). "Microstructural effects in elastic composites." In: *International Journal of Solids and Structures* 33.7, pp. 1023–1051.

Boutin, C., Giorgio, I., Placidi, L., et al. (2017). "Linear pantographic sheets: asymptotic micro-macro models identification." In: *Mathematics and Mechanics of Complex Systems* 5.2, pp. 127–162.

Challagulla, K. S., Georgiades, A., and Kalamkarov, A. (2007). "Asymptotic homogenization modeling of thin composite network structures." In: *Composite structures* 79.3, pp. 432–444.

Christoff, B. G., Brito-Santana, H., Talreja, R., and Tita, V. (2020). "Development of an ABAQUS plug-in to evaluate the fourth-order elasticity tensor of a periodic material via homogenization by the asymptotic expansion method." In: *Finite Elements in Analysis and Design* 181, p. 103482.

Chung, P. W., Tamma, K. K., and Namburu, R. R. (2001). "Asymptotic expansion homogenization for heterogeneous media: computational issues and applications." In: *Composites Part A: Applied Science and Manufacturing* 32.9, pp. 1291–1301.

Cottrell, J. A., Hughes, T. J., and Bazilevs, Y. (2009). *Isogeometric analysis: toward integration of CAD and FEA*. John Wiley & Sons.

Coulais, C., Kettenis, C., and Hecke, M. van (2018). "A characteristic length scale causes anomalous size effects and boundary programmability in mechanical metamaterials." In: *Nature Physics* 14.1, pp. 40–44.

De Angelo, M., Barchiesi, E., Giorgio, I., and Abali, B. E. (2019). "Numerical identification of constitutive parameters in reduced-order bi-dimensional models for pantographic structures: Application to out-of-plane buckling." In: *Archive of Applied Mechanics*, pp. 1–26.

De Angelo, M., Spagnuolo, M., D'annibale, F., Pfaff, A., Hoschke, K., Misra, A., Dupuy, C., Peyre, P., Dirrenberger, J., and Pawlikowski, M. (2019). "The macroscopic behavior of pantographic sheets depends mainly on their microstructure: experimental evidence and qualitative analysis of damage in metallic specimens." In: *Continuum Mechanics and Thermodynamics* 31.4, pp. 1181–1203.

dell'Isola, F., Corte, A. D., and Giorgio, I. (2017). "Higher-gradient continua: The legacy of Piola, Mindlin, Sedov and Toupin and some future research perspectives." In: *Mathematics and Mechanics of Solids* 22.4, pp. 852–872.

dell'Isola, F., Giorgio, I., Pawlikowski, M., and Rizzi, N. L. (2016). "Large deformations of planar extensible beams and pantographic lattices: heuristic homogenization, experimental and numerical examples of equilibrium." In: *Proceedings of the Royal Society A: Mathematical, Physical and Engineering Sciences* 472.2185, p. 20150790.

dell'Isola, F., Seppecher, P., Alibert, J. J., Lekszycki, T., Grygoruk, R., Pawlikowski, M., Steigmann, D., Giorgio, I., Andreaus, U., Turco, E., et al. (2019). "Pantographic metamaterials: an example of mathematically driven design and of its technological challenges." In: *Continuum Mechanics and Thermodynamics* 31.4, pp. 851–884.

dell'Isola, F., Seppecher, P., Spagnuolo, M., Barchiesi, E., Hild, F., Lekszycki, T., Giorgio, I., Placidi, L., Andreaus, U., Cuomo, M., Eugster, S. R., Pfaff, A.,

Hoschke, K., Langkemper, R., Turco, E., Sarikaya, R., Misra, A., Angelo, M. D., D'Annibale, F., Bouterf, A., Pinelli, X., Misra, A., Desmorat, B., Pawlikowski, M., Dupuy, C., Scerrato, D., Peyre, P., Laudato, M., Manzari, L., Göransson, P., Hesch, C., Hesch, S., Franciosi, P., Dirrenberger, J., Maurin, F., Vangelatos, Z., Grigoropoulos, C., Melissinaki, V., Farsari, M., Müller, W., Abali, B. E., Liebold, C., Ganzosch, G., Harrison, P., Drobnicki, R., Igumnov, L., Alzahrani, F., and Hayat, T. (2019). "Advances in pantographic structures: design, manufacturing, models, experiments and image analyses." In: 31.4, pp. 1231–1282.

Dong, G., Tang, Y., and Zhao, Y. F. (2019). "A 149 line homogenization code for three-dimensional cellular materials written in matlab." In: *Journal of Engineering Materials and Technology* 141.1.

Dos Reis, F. and Ganghoffer, J. (2012). "Equivalent mechanical properties of auxetic lattices from discrete homogenization." In: *Computational Materials Science* 51.1, pp. 314–321.

El Nady, K., Dos Reis, F., and Ganghoffer, J. (2017). "Computation of the homogenized nonlinear elastic response of 2D and 3D auxetic structures based on micropolar continuum models." In: *Composite Structures* 170, pp. 271–290.

Eremeyev, V. A., Alzahrani, F. S., Cazzani, A., dell'Isola, F., Hayat, T., Turco, E., and Konopińska-Zmysłowska, V. (2019). "On existence and uniqueness of weak solutions for linear pantographic beam lattices models." In: *Continuum Mechanics and Thermodynamics* 31.6, pp. 1843–1861.

Eremeyev, V. A., dell'Isola, F., Boutin, C., and Steigmann, D. (2018). "Linear pantographic sheets: existence and uniqueness of weak solutions." In: *Journal of Elasticity* 132.2, pp. 175–196.

Eremeyev, V. A., Lebedev, L. P., and Altenbach, H. (2012). *Foundations of micropolar mechanics*. Springer Science & Business Media.

Eremeyev, V. A., Lurie, S. A., Solyaev, Y. O., and dell'Isola, F. (2020). "On the well posedness of static boundary value problem within the linear dilatational strain gradient elasticity." In: *Zeitschrift für angewandte Mathematik und Physik* 71.6, pp. 1–16.

Eremeyev, V. A., Skrzat, A., and Stachowicz, F. (2016). "On finite element computations of contact problems in micropolar elasticity." In: *Advances in Materials Science and Engineering* 2016.

Eringen, A. C. (1966). "Linear theory of micropolar elasticity." In: *Journal of Mathematics and Mechanics*, pp. 909–923.

Eringen, A. C. (2012). *Microcontinuum field theories: I. Foundations and solids*. Springer Science & Business Media.

Eringen, A. C. and Suhubi, E. (1964). "Nonlinear theory of simple micro-elastic solids—I." In: *International Journal of Engineering Science* 2.2, pp. 189–203.

Eshelby, J. D. (1957). "The determination of the elastic field of an ellipsoidal inclusion, and related problems." In: *Proceedings of the royal society of London. Series A. Mathematical and physical sciences* 241.1226, pp. 376–396.

Fischer, P., Mergheim, J., and Steinmann, P. (2010). "On the C1 continuous discretization of non-linear gradient elasticity: a comparison of NEM and FEM based on Bernstein–Bézier patches." In: *International journal for numerical methods in engineering* 82.10, pp. 1282–1307.

Fischer, P., Klassen, M., Mergheim, J., Steinmann, P., and Müller, R. (2011). "Isogeometric analysis of 2D gradient elasticity." In: *Computational Mechanics* 47.3, pp. 325–334.

Forest, S. (2013). "Micromorphic media." In: *Generalized continua from the theory to engineering applications*. Springer, pp. 249–300.

Francfort, G. A. and Marigo, J.-J. (1998). "Revisiting brittle fracture as an energy minimization problem." In: *Journal of the Mechanics and Physics of Solids* 46.8, pp. 1319–1342.

Fritzen, F., Forest, S., Böhlke, T., Kondo, D., and Kanit, T. (2012). "Computational homogenization of elasto-plastic porous metals." In: *International journal of plasticity* 29, pp. 102–119.

Ganghoffer, J. and Reda, H. (2021). "A variational approach of homogenization of heterogeneous materials towards second gradient continua." In: *Mechanics of Materials* 158, p. 103743.

Ghosh, S., Lee, K., and Moorthy, S. (1996). "Two scale analysis of heterogeneous elastic-plastic materials with asymptotic homogenization and Voronoi cell finite element model." In: *Computer methods in applied mechanics and engineering* 132.1-2, pp. 63–116.

Giorgio, I., Rizzi, N., and Turco, E. (2017). "Continuum modelling of pantographic sheets for out-of-plane bifurcation and vibrational analysis." In: *Proceedings of the Royal Society A: Mathematical, Physical and Engineering Sciences* 473.2207, p. 20170636.

Giorgio, I. (2016). "Numerical identification procedure between a micro-Cauchy model and a macro-second gradient model for planar pantographic structures." In: *Zeitschrift für angewandte Mathematik und Physik* 67.4, pp. 1–17.

Goda, I. and Ganghoffer, J.-F. (2015). "Identification of couple-stress moduli of vertebral trabecular bone based on the 3D internal architectures." In: *Journal of the mechanical behavior of biomedical materials* 51, pp. 99–118.

Hashin, Z. (1991). "The Spherical Inclusion With Imperfect Interface." In: *Journal of Applied Mechanics* 58.2, pp. 444–449.

He, Z. and Pindera, M.-J. (2021). "Finite volume based asymptotic homogenization theory for periodic materials under anti-plane shear." In: *European Journal of Mechanics-A/Solids* 85, p. 104122.

Hill, R. (1965). "A self-consistent mechanics of composite materials." In: *Journal of the Mechanics and Physics of Solids* 13.4, pp. 213–222.

Hill, R. (1972). "On constitutive macro-variables for heterogeneous solids at finite strain." In: *Proceedings of the Royal Society of London. A. Mathematical and Physical Sciences* 326.1565, pp. 131–147.

Hillerborg, A., Modéer, M., and Petersson, P.-E. (1976). "Analysis of crack formation and crack growth in concrete by means of fracture mechanics and finite elements." In: *Cement and concrete research* 6.6, pp. 773–781.

Hirschberger, C. B. (2008). "A Treatise on Micromorphic Continua. Theory, Homogenization, Computation." doctoralthesis. Technische Universität Kaiserslautern.

Hoang, V.-N., Tran, P., Vu, V.-T., and Nguyen-Xuan, H. (2020). "Design of lattice structures with direct multiscale topology optimization." In: *Composite Structures* 252, p. 112718.

Hollister, S. J. and Kikuchi, N. (1992). "A comparison of homogenization and standard mechanics analyses for periodic porous composites." In: *Computational mechanics* 10.2, pp. 73–95.

Hütter, G. (2017). "Homogenization of a Cauchy continuum towards a micromorphic continuum." In: *Journal of the Mechanics and Physics of Solids* 99, pp. 394–408.

Hütter, G. (2019). "On the micro-macro relation for the microdeformation in the homogenization towards micromorphic and micropolar continua." In: *Journal of the Mechanics and Physics of Solids* 127, pp. 62–79.

Javili, A., Chatzigeorgiou, G., and Steinmann, P. (2013). "Computational homogenization in magneto-mechanics." In: *International Journal of Solids and Structures* 50.25-26, pp. 4197–4216.

Kalamkarov, A. L., Andrianov, I. V., and Danishevs'kyy, V. V. (2009). "Asymptotic homogenization of composite materials and structures." In: *Applied Mechanics Reviews* 62.3.

Kamensky, D. and Bazilevs, Y. (2019). "tIGAr: Automating isogeometric analysis with FEniCS." In: *Computer Methods in Applied Mechanics and Engineering* 344, pp. 477–498.

Kanoute, P., Boso, D., Chaboche, J., and Schrefler, B. (2009). "Multiscale methods for composites: a review." In: *Archives of Computational Methods in Engineering* 16.1, pp. 31–75.

Karlis, G., Tsinopoulos, S., Polyzos, D., and Beskos, D. (2008). "2D and 3D boundary element analysis of mode-I cracks in gradient elasticity." In: *Computer Modeling in Engineering and Sciences* 26.3, p. 189.

Khakalo, S. and Niiranen, J. (2017). "Isogeometric analysis of higher-order gradient elasticity by user elements of a commercial finite element software." In: *Computer-Aided Design* 82, pp. 154–169.

Kumar, R. S. and McDowell, D. L. (2004). "Generalized continuum modeling of 2-D periodic cellular solids." In: *International Journal of solids and structures* 41.26, pp. 7399–7422.

Kumar, S., Tan, S., Zheng, L., and Kochmann, D. M. (2020). "Inverse-designed spinodoid metamaterials." In: *npj Computational Materials* 6.1, pp. 1–10.

Lakes, R. and Drugan, W. (2015). "Bending of a Cosserat elastic bar of square cross section: Theory and experiment." In: *Journal of Applied Mechanics* 82.9.

Lakes, R. S. (1983). "Size effects and micromechanics of a porous solid." In: *Journal of materials science* 18.9, pp. 2572–2580.

Lakes, R. (1986). "Experimental microelasticity of two porous solids." In: *International Journal of Solids and Structures* 22.1, pp. 55–63.

Lam, D. C., Yang, F., Chong, A., Wang, J., and Tong, P. (2003). "Experiments and theory in strain gradient elasticity." In: *Journal of the Mechanics and Physics of Solids* 51.8, pp. 1477–1508.

Lazar, M., Maugin, G. A., and Aifantis, E. C. (2006). "Dislocations in second strain gradient elasticity." In: *International Journal of Solids and Structures* 43.6, pp. 1787–1817.

Li, J. (2011a). "A micromechanics-based strain gradient damage model for fracture prediction of brittle materials–Part I: Homogenization methodology and constitutive relations." In: *International Journal of Solids and Structures* 48.24, pp. 3336–3345.

Li, J. (2011b). "Establishment of strain gradient constitutive relations by homogenization." In: *Comptes Rendus Mécanique* 339.4, pp. 235–244.

Li, J. and Zhang, X.-B. (2013). "A numerical approach for the establishment of strain gradient constitutive relations in periodic heterogeneous materials." In: *European Journal of Mechanics-A/Solids* 41, pp. 70–85.

Liebold, C. and Müller, W. H. (2015). "Are microcontinuum field theories of elasticity amenable to experiments? A review of some recent results." In: *Differential Geometry and Continuum Mechanics*, pp. 255–278.

Liebold, C. and Müller, W. H. (2016). "Comparison of gradient elasticity models for the bending of micromaterials." In: *Computational Materials Science* 116, pp. 52–61.

Liu, S. and Su, W. (2009). "Effective couple-stress continuum model of cellular solids and size effects analysis." In: *International Journal of Solids and Structures* 46.14-15, pp. 2787–2799.

Ma, H. and Gao, X.-L. (2014). "A new homogenization method based on a simplified strain gradient elasticity theory." In: *Acta Mechanica* 225.4, pp. 1075–1091.

Makvandi, R., Duczek, S., and Juhre, D. (2019). "A phase-field fracture model based on strain gradient elasticity." In: *Engineering Fracture Mechanics* 220, p. 106648.

Makvandi, R., Reiher, J. C., Bertram, A., and Juhre, D. (2018). "Isogeometric analysis of first and second strain gradient elasticity." In: *Computational Mechanics* 61.3, pp. 351–363.

Masters, I. and Evans, K. (1996). "Models for the elastic deformation of honeycombs." In: *Composite structures* 35.4, pp. 403–422.

Mindlin, R. D. (1963). *Microstructure in linear elasticity*. Tech. rep. Columbia Univ New York Dept of Civil Engineering and Engineering Mechanics.

Mindlin, R. D. (1965). "Second gradient of strain and surface-tension in linear elasticity." In: *International Journal of Solids and Structures* 1.4, pp. 417–438.

Mindlin, R. D. and Eshel, N. (1968). "On first strain-gradient theories in linear elasticity." In: *International Journal of Solids and Structures* 4.1, pp. 109–124.

Mindlin, R. and Tiersten, H. (1962). *Effects of couple-stresses in linear elasticity*. Tech. rep. COLUMBIA UNIV NEW YORK.

Mishnaevsky Leon L., J. and Schmauder, S. (2001). "Continuum Mesomechanical Finite Element Modeling in Materials Development: A State-of-the-Art Review." In: *Applied Mechanics Reviews* 54.1, pp. 49–67.

Misra, A., Lekszycki, T., Giorgio, I., Ganzosch, G., Müller, W. H., and dell'Isola, F. (2018). "Pantographic metamaterials show atypical Poynting effect reversal." In: *Mechanics Research Communications* 89, pp. 6–10.

Moës, N., Dolbow, J., and Belytschko, T. (1999). "A finite element method for crack growth without remeshing." In: *International journal for numerical methods in engineering* 46.1, pp. 131–150.

Moës, N., Gravouil, A., and Belytschko, T. (2002). "Non-planar 3D crack growth by the extended finite element and level sets—Part I: Mechanical model." In: *International journal for numerical methods in engineering* 53.11, pp. 2549–2568.

Monchiet, V., Auffray, N., and Yvonnet, J. (2020). "Strain-gradient homogenization: a bridge between the asymptotic expansion and quadratic boundary condition methods." In: *Mechanics of Materials* 143, p. 103309.

Mori, T. and Tanaka, K. (1973). "Average stress in matrix and average elastic energy of materials with misfitting inclusions." In: *Acta metallurgica* 21.5, pp. 571–574.

Msekh, M. A., Sargado, J. M., Jamshidian, M., Areias, P. M., and Rabczuk, T. (2015). "Abaqus implementation of phase-field model for brittle fracture." In: *Computational Materials Science* 96, pp. 472–484.

Müller, W. H. (2020). "The experimental evidence for higher gradient theories." In: *Mechanics of Strain Gradient Materials*. Springer, pp. 1–18.

Natarajan, S., Annabattula, R. K., et al. (2019). "A FEniCS implementation of the phase field method for quasi-static brittle fracture." In: *Frontiers of Structural and Civil Engineering* 13.2, pp. 380–396.

Nazarenko, L., Glüge, R., and Altenbach, H. (2021). "Positive definiteness in coupled strain gradient elasticity." In: *Continuum Mechanics and Thermodynamics* 33.3, pp. 713–725.

Neff, P., Ghiba, I.-D., Madeo, A., Placidi, L., and Rosi, G. (2014). "A unifying perspective: the relaxed linear micromorphic continuum." In: *Continuum Mechanics and Thermodynamics* 26.5, pp. 639–681.

Nejadsadeghi, N., De Angelo, M., Drobnicki, R., Lekszycki, T., dell'Isola, F., and Misra, A. (2019). "Parametric experimentation on pantographic unit cells reveals local extremum configuration." In: *Experimental Mechanics* 59.6, pp. 927–939.

Nemat-Nasser, S. and Hori, M. (2013). *Micromechanics: overall properties of heterogeneous materials*. Elsevier.

Nguyen, T. H. and Niiranen, J. (2020). "A second strain gradient damage model with a numerical implementation for quasi-brittle materials with micro-architectures." In: *Mathematics and Mechanics of Solids* 25.3, pp. 515–546.

Nguyen, V.-D. and Noels, L. (2014). "Computational homogenization of cellular materials." In: *International Journal of Solids and Structures* 51.11-12, pp. 2183–2203.

Nguyen, V. P., Stroeven, M., and Sluys, L. J. (2011). "Multiscale continuous and discontinuous modeling of heterogeneous materials: a review on recent developments." In: *Journal of Multiscale Modelling* 3.04, pp. 229–270.

Noor, A. K. (1988). "Continuum Modeling for Repetitive Lattice Structures." In: *Applied Mechanics Reviews* 41.7, pp. 285–296.

Oliveira, J., Pinho-da-Cruz, J., and Teixeira-Dias, F. (2009). "Asymptotic homogenisation in linear elasticity. Part II: Finite element procedures and multiscale applications." In: *Computational Materials Science* 45.4, pp. 1081–1096.

Olurin, O., Fleck, N. A., and Ashby, M. F. (2000). "Indentation resistance of an aluminium foam." In: *Scripta Materialia* 43.11, pp. 983–989.

Özdemir, I., Brekelmans, W., and Geers, M. (2008). "Computational homogenization for heat conduction in heterogeneous solids." In: *International journal for numerical methods in engineering* 73.2, pp. 185–204.

Papanicolopulos, S.-A., Zervos, A., and Vardoulakis, I. (2009). "A three-dimensional C1 finite element for gradient elasticity." In: *International journal for numerical methods in engineering* 77.10, pp. 1396–1415.

Patel, B. and Zohdi, T. I. (2016). "Numerical estimation of effective electromagnetic properties for design of particulate composites." In: *Materials & Design* 94, pp. 546–553.

Peerlings, R. and Fleck, N. (2004). "Computational evaluation of strain gradient elasticity constants." In: *International Journal for Multiscale Computational Engineering* 2.4.

Petera, J. and Pittman, J. (1994). "Isoparametric hermite elements." In: *International Journal for Numerical Methods in Engineering* 37.20, pp. 3489–3519.

Pham, K., Kouznetsova, V. G., and Geers, M. G. (2013). "Transient computational homogenization for heterogeneous materials under dynamic excitation." In: *Journal of the Mechanics and Physics of Solids* 61.11, pp. 2125–2146.

Phunpeng, V. and Baiz, P. (2015). "Mixed finite element formulations for strain-gradient elasticity problems using the FEniCS environment." In: *Finite Elements in Analysis and Design* 96, pp. 23–40.

Pierard, O. et al. (2006). "Micromechanics of inclusion-reinforced composites in elasto-plasticity and elasto-viscoplasticity: modeling and computation." In: *Universié Catholique de Louvain*.

Pinho-da-Cruz, J., Oliveira, J., and Teixeira-Dias, F. (2009). "Asymptotic homogenisation in linear elasticity. Part I: Mathematical formulation and finite element modelling." In: *Computational Materials Science* 45.4, pp. 1073–1080.

Placidi, L., Andreaus, U., Della Corte, A., and Lekszycki, T. (2015). "Gedanken experiments for the determination of two-dimensional linear second gradient elasticity coefficients." In: *Zeitschrift für angewandte Mathematik und Physik* 66.6, pp. 3699–3725.

Placidi, L., Andreaus, U., and Giorgio, I. (2017). "Identification of two-dimensional pantographic structure via a linear D4 orthotropic second gradient elastic model." In: *Journal of Engineering Mathematics* 103.1, pp. 1–21.

Placidi, L. and Barchiesi, E. (2018). "Energy approach to brittle fracture in strain-gradient modelling." In: *Proceedings of the Royal Society A: Mathematical, Physical and Engineering Sciences* 474.2210, p. 20170878.

Placidi, L., Barchiesi, E., and Misra, A. (2018). "A strain gradient variational approach to damage: a comparison with damage gradient models and numerical results." In: *Mathematics and Mechanics of Complex Systems* 6.2, pp. 77–100.

Placidi, L., Misra, A., and Barchiesi, E. (2018). "Two-dimensional strain gradient damage modeling: a variational approach." In: *Zeitschrift für angewandte Mathematik und Physik* 69.3, pp. 1–19.

Placidi, L., Misra, A., and Barchiesi, E. (2019). "Simulation results for damage with evolving microstructure and growing strain gradient moduli." In: *Continuum Mechanics and Thermodynamics* 31.4, pp. 1143–1163.

Poncelet, M., Somera, A., Morel, C., Jailin, C., and Auffray, N. (2018). "An experimental evidence of the failure of Cauchy elasticity for the overall modeling of a non-centro-symmetric lattice under static loading." In: *International Journal of Solids and Structures* 147, pp. 223–237.

Putar, F., Sorić, J., Lesičar, T., and Tonković, Z. (2017). "Damage modeling employing strain gradient continuum theory." In: *International Journal of Solids and Structures* 120, pp. 171–185.

Rahali, Y., Assidi, M., Goda, I., Zghal, A., and Ganghoffer, J.-F. (2016). "Computation of the effective mechanical properties including nonclassical moduli of 2.5 D and 3D interlocks by micromechanical approaches." In: *Composites Part B: Engineering* 98, pp. 194–212.

Rahali, Y., Goda, I., and Ganghoffer, J.-F. (2016). "Numerical identification of classical and nonclassical moduli of 3D woven textiles and analysis of scale effects." In: *Composite structures* 135, pp. 122–139.

Reiher, J. C., Giorgio, I., and Bertram, A. (2017). "Finite-element analysis of polyhedra under point and line forces in second-strain gradient elasticity." In: *Journal of Engineering Mechanics* 143.2, p. 04016112.

Réthoré, J., Kaltenbrunner, C., Dang, T. B. T., Chaudet, P., and Kuhn, M. (2015). "Gradient-elasticity for honeycomb materials: Validation and identification from full-field measurements." In: *International Journal of Solids and Structures* 72, pp. 108–117.

Rokoš, O., Ameen, M. M., Peerlings, R. H., and Geers, M. G. (2019). "Micromorphic computational homogenization for mechanical metamaterials with pattern-

ing fluctuation fields." In: *Journal of the Mechanics and Physics of Solids* 123, pp. 119–137.

Rosi, G., Auffray, N., and Combescure, C. (2020). "On the failure of classic elasticity in predicting elastic wave propagation in gyroid lattices for very long wavelengths." In: *Symmetry* 12.8, p. 1243.

Rudraraju, S., Van der Ven, A., and Garikipati, K. (2014). "Three-dimensional isogeometric solutions to general boundary value problems of Toupin's gradient elasticity theory at finite strains." In: *Computer Methods in Applied Mechanics and Engineering* 278, pp. 705–728.

Shekarchizadeh, N., Abali, B. E., Barchiesi, E., and Bersani, A. M. (2021). "Inverse analysis of metamaterials and parameter determination by means of an automatized optimization problem." In: *ZAMM-Journal of Applied Mathematics and Mechanics/Zeitschrift für Angewandte Mathematik und Mechanik*, e202000277.

Shlyannikov, V., Martínez-Pañeda, E., Tumanov, A., and Tartygasheva, A. (2021). "Crack tip fields and fracture resistance parameters based on strain gradient plasticity." In: *International Journal of Solids and Structures* 208, pp. 63–82.

Shu, J. Y., King, W. E., and Fleck, N. A. (1999). "Finite elements for materials with strain gradient effects." In: *International Journal for Numerical Methods in Engineering* 44.3, pp. 373–391.

Skrzat, A. and Eremeyev, V. A. (2020). "On the effective properties of foams in the framework of the couple stress theory." In: *Continuum Mechanics and Thermodynamics*, pp. 1–23.

Smyshlyaev, V. P. and Cherednichenko, K. D. (2000). "On rigorous derivation of strain gradient effects in the overall behaviour of periodic heterogeneous media." In: *Journal of the Mechanics and Physics of Solids* 48.6-7, pp. 1325–1357.

Song, J. and Wei, Y. (2020). "A method to determine material length scale parameters in elastic strain gradient theory." In: *Journal of Applied Mechanics* 87.3.

Takano, N., Ohnishi, Y., Zako, M., and Nishiyabu, K. (2000). "The formulation of homogenization method applied to large deformation problem for composite materials." In: *International Journal of Solids and Structures* 37.44, pp. 6517–6535.

Tang, T. and Yu, W. (2008). "Variational asymptotic micromechanics modeling of heterogeneous piezoelectric materials." In: *Mechanics of Materials* 40.10, pp. 812–824.

Tang, Z., Shen, S., and Atluri, S. (2003). "Analysis of materials with strain-gradient effects: A meshless local Petrov-Galerkin (MLPG) approach, with nodal displacements only." In: *Computer Modeling in Engineering and Sciences* 4.1, pp. 177–196.

Tekoğlu, C. and Onck, P. R. (2008). "Size effects in two-dimensional Voronoi foams: a comparison between generalized continua and discrete models." In: *Journal of the Mechanics and Physics of Solids* 56.12, pp. 3541–3564.

Toupin, R. (1962). "Elastic materials with couple-stresses." In: *Archive for rational mechanics and analysis* 11.1, pp. 385–414.

Toupin, R. A. (1964). "Theories of elasticity with couple-stress." In: *Archive for Rational Mechanics and Analysis* 17.2, pp. 85–112.

Tran, C. A., Gołaszewski, M., and Barchiesi, E. (2020). "Symmetric-in-Plane Compression of Polyamide Pantographic Fabrics—Modelling, Experiments and Numerical Exploration." In: *Symmetry* 12.5, p. 693.

Trinh, D. K., Janicke, R., Auffray, N., Diebels, S., and Forest, S. (2012). "Evaluation of generalized continuum substitution models for heterogeneous materials." In: *International Journal for Multiscale Computational Engineering* 10.6.

Tsepoura, K., Papargyri-Beskou, S., and Polyzos, D. (2002). "A boundary element method for solving 3D static gradient elastic problems with surface energy." In: *Computational mechanics* 29.4, pp. 361–381.

Turco, E. and Barchiesi, E. (2019). "Equilibrium paths of Hencky pantographic beams in a three-point bending problem." In: *Mathematics and Mechanics of Complex Systems* 7.4, pp. 287–310.

Wang, A.-J. and McDowell, D. (2004). "In-plane stiffness and yield strength of periodic metal honeycombs." In: *J. Eng. Mater. Technol.* 126.2, pp. 137–156.

Wang, A.-J. and McDowell, D. (2005). "Yield surfaces of various periodic metal honeycombs at intermediate relative density." In: *International Journal of Plasticity* 21.2, pp. 285–320.

Weeger, O. (2021). "Numerical homogenization of second gradient, linear elastic constitutive models for cubic 3D beam-lattice metamaterials." In: *International Journal of Solids and Structures* 224, p. 111037.

Willis, J. R. (1977). "Bounds and self-consistent estimates for the overall properties of anisotropic composites." In: *Journal of the Mechanics and Physics of Solids* 25.3, pp. 185–202.

Wu, J., Sigmund, O., and Groen, J. P. (2021). "Topology optimization of multi-scale structures: a review." In: *Structural and Multidisciplinary Optimization*, pp. 1–26.

Yang, H. and Müller, W. H. (2021). "Size effects of mechanical metamaterials: a computational study based on a second-order asymptotic homogenization method." In: *Archive of Applied Mechanics* 91.3, pp. 1037–1053.

Yang, Y. and Misra, A. (2010). "Higher-order stress-strain theory for damage modeling implemented in an element-free Galerkin formulation." In: *CMES-Computer modeling in engineering & sciences* 64.1, pp. 1–36.

Yildizdag, M. E., Barchiesi, E., and dell'Isola, F. (2020). "Three-point bending test of pantographic blocks: numerical and experimental investigation." In: *Mathematics and Mechanics of Solids*, p. 1081286520916911.

Yu, W. and Tang, T. (2007). "A variational asymptotic micromechanics model for predicting thermoelastic properties of heterogeneous materials." In: *International Journal of Solids and Structures* 44.22-23, pp. 7510–7525.

Yuan, Z. and Fish, J. (2008). "Toward realization of computational homogenization in practice." In: *International Journal for Numerical Methods in Engineering* 73.3, pp. 361–380.

Yvonnet, J., Auffray, N., and Monchiet, V. (2020). "Computational second-order homogenization of materials with effective anisotropic strain-gradient behavior." In: *International Journal of Solids and Structures* 191, pp. 434–448.

Yvonnet, J. (2019). *Computational homogenization of heterogeneous materials with finite elements*. Springer.

Zervos, A., Papanicolopulos, S.-A., and Vardoulakis, I. (2009). "Two finite-element discretizations for gradient elasticity." In: *Journal of engineering mechanics* 135.3, pp. 203–213.

Zervos, A., Papanastasiou, P., and Vardoulakis, I. (2001). "A finite element displacement formulation for gradient elastoplasticity." In: *International Journal for Numerical Methods in Engineering* 50.6, pp. 1369–1388.

Zohdi, T. I. and Wriggers, P. (2008). *An introduction to computational micromechanics*. Springer Science & Business Media.

Zybell, L., Mühlich, U., Kuna, M., and Zhang, Z. (2012). "A three-dimensional finite element for gradient elasticity based on a mixed-type formulation." In: *Computational materials science* 52.1, pp. 268–273.

Part II

Publications

Received: 16 January 2021 | Revised: 29 March 2021 | Accepted: 24 June 2021

DOI: 10.1002/zamm.202100023

ORIGINAL PAPER

ZAMM

Verification of strain gradient elasticity computation by analytical solutions

Hua Yang[1] | **Dmitry Timofeev**[2] | **B. Emek Abali**[3] | **Baotong Li**[4] | **Wolfgang H. Müller**[1]

[1] Technische Universität Berlin, Berlin, Germany

[2] Università degli Studi dell'Aquila, L'Aquila, Italy

[3] Uppsala University, Uppsala, Sweden

[4] Xi'an Jiaotong University, Xi'an, China

Correspondence
Hua Yang, Technische Universität Berlin, Berlin, Germany.
Email: hua.yang@campus.tu-berlin.de

As there are different computational methods for simulating problems in generalized mechanics, we present simple applications and their closed-form solutions for verifying a numerical implementation. For such a benchmark, we utilize these analytical solutions and examine three-dimensional numerical simulations by the finite element method (FEM) using IsoGeometric Analysis (IGA) with the aid of open source codes, called tIGAr, developed within the FEniCS platform. A study for the so-called wedge forces and double tractions help to comprehend their roles in the displacement solution as well as examine the significance by comparing to the closed form solutions for given boundary conditions. It is found that numerical results are in a good agreement with the analytical solutions if wedge forces and double tractions are considered. It is also presented how the wedge forces become necessary in order to maintain equilibrium in strain gradient materials.

KEYWORDS
analytical solutions, strain gradient elasticity, three-dimensional problems

1 | INTRODUCTION

Miniaturization of sensors and actuators, such as micro-electro mechanical systems (MEMS), necessitates an accurate modeling of materials at micrometer length scale (microscale). However, from experimental evidences [61] one can observe stiffening or softening material responses at the microscale when compared to a solution based on the Cauchy–Boltzmann continuum, that is, conventional elasticity theory. In order to capture these geometric length dependent phenomena, which are commonly referred to as size effects, a generalization of standard elasticity theory is required, such that the stored energy depends not only on strain but also on other primitive variables, for example, the spin or the strain gradient [5, 16, 37, 62]. Various theories of such a generalized mechanics are described in the literature. They are mathematically close and may be considered as particular cases of a unified theory [64]. For historical and philosophical remarks on the subject, we refer to [27, 29].

In the so-called strain gradient elasticity theory the stored energy is considered to be dependent on strains as well as strain gradients. Motivation for introducing higher order gradient of strains in the stored energy arises from various aspects, we refer to [1, 7, 11, 31, 36, 63, 86]. First, an investigation of highly localized phenomena, such as crack

formation and propagation, may be realized by involving higher order gradients in order to regularize the solution of cracks by penalizing the displacements, which are localized above a given threshold [17, 68, 71, 73, 78, 93]. Second, an accurate modeling of metamaterials is achieved in the framework of strain gradient theory [16, 26, 28, 35, 38, 40, 45, 89]. Indeed, the behaviors of metamaterials depend on the morphology of microstructures [23, 43, 53, 54] and show peculiar behaviors, such as size effects [3, 90–92] and band gaps [76, 80], which are not captured by the classical Cauchy continuum. Exotic material behaviors may be governed by internal or boundary layers of higher strain gradients [51]. As an example of metamaterials we refer to materials with pantographic substructures [32, 34] having non-negligible strain gradient terms in the formulation of deformation energy [24,25,41,65,88], which are found in recent numerical and experimental evidences, for example, in shearing tests [15], three-point bending tests [94], compression tests [87], or torsion tests [60]. A homogenization procedure of pantographic microstructures leading to second gradient materials is shown in [12–14, 84]. Generally speaking, generalized mechanics at the macroscale results in as a homogenization procedure from the Cauchy–Boltzmann continuum at the micrometer length-scale (microscale) [57]. Strain gradient theory is able to sustain the so-called wedge forces [9, 56, 77], which are acting on corners (point forces) in 2D and edges (force distributions along lines) in 3D, while the classical Cauchy continuum leads to singularities when handling such issues. From [8, 33, 48, 83], it becomes obvious that the reasons of inducing higher order strain gradient allows a continuum to sustain boundary conditions on vertices and edges of a body.

Strain gradient theory leads to higher order partial differential equations and requires an interpolation scheme for the finite element representation to guarantee a correspondingly higher order of continuity. For this reason, various numerical implementations of strain gradient theories are proposed in the literature, such as the mixed formulation [67, 85], C^1 continuous elements [42, 66, 95], and isogeometric analysis [39, 56,81]. The concept of IGA [46] is a mesh-based numerical approach using shape functions in FEM identical as the basic functions in CAD generated from NURBS (Non-Uniform Rational B-Splines). In the context of strain gradient elasticity, such a formulation serves the C^n continuity across the element boundaries. The NURBS interpolation requires only displacements as nodal degrees of freedom, and no derivatives of the displacement field are needed [39]. Some examples can be found in [19–21, 82]. From a general viewpoint, for verification purposes, a numerical solution have to be compared to analytical results [79]. Some analytical derivations were presented for 2D cases [22, 69, 74, 75, 95]. Obtaining results of this kind for 3D cases is rather challenging.

In this paper, closed-form analytical solutions [70, 72, 74] are presented for cases of three dimensional benchmark problems for a centro-symmetric and isotropic material modeled by strain gradient theory. The balance equations and the boundary terms (tractions, double tractions, and wedge forces on the boundaries) are derived by means of the variational method. Numerical implementations have been developed based on IGA (Iso-Geometric Analysis) for these classical cases in order to demonstrate the benchmarking procedure. The aim of the paper is to verify our implementation based on an IGA library called tIGAr [49, 50] provided on the FEniCS platform. Moreover, a comparative study allows us to understand the roles of wedge forces in maintaining equilibrium. The code uses open-source packages under GNU public license [44], and we make the codes publicly available in [2] in order to enable a scientific exchange. The paper is organized as follows: The variational formulation of strain gradient elasticity theory [1, 30] is outlined in Section 2. The formulation of three-dimensional problem is shown in Section 3. In Section 4 analytical and numerical results are compared for three different benchmark examples.

2 | STRAIN GRADIENT ELASTICITY

2.1 | Variational formulation

In this section, strain gradient elasticity as in [58, 59] will be revisited. Conventional continuum mechanics theories assume that stress at a material point is a function of state variables, such as strain, at the same point. This local assumption is adequate when the wavelength of a deformation field is orders in magnitude greater than the dominant micro-structural material length scale. However, when these two length scales are comparable, an extension becomes necessary, herein we use the strain gradient theory. Unlike the classical elasticity, in strain gradient theory the stored energy density depends on the strain, ε_{ij}, and on the strain gradient, η_{ijk}:

$$\varepsilon_{ij} = \frac{u_{i,j} + u_{j,i}}{2}, \quad \eta_{ijk} = \varepsilon_{ij,k} = \frac{u_{i,jk} + u_{j,ik}}{2}. \tag{1}$$

Here $\boldsymbol{u}$ denotes the displacement field and a comma means differentiation in space, $\boldsymbol{X}$, expressed in Cartesian coordinates,

$$u_{i,j} = \frac{\partial u_i}{\partial X_j}, \quad X_j \in \Omega \subset \mathbb{R}^3 \tag{2}$$

For strain gradient materials, the stored energy density, w, depends on the first and second gradients of the displacement field

$$w = w(\varepsilon_{ij}, \eta_{ijk}). \tag{3}$$

We compute the first variation of functional for the internal energy of the body W^{int}:

$$W^{\text{int}} = \int_\Omega w \, \mathrm{d}V, \tag{4}$$

such that we have

$$\delta W^{\text{int}} = \int_\Omega \delta w \, \mathrm{d}V = \int_\Omega \left(\frac{\partial w}{\partial u_{i,j}} \delta u_{i,j} + \frac{\partial w}{\partial u_{i,jk}} \delta u_{i,jk} \right) \mathrm{d}V, \tag{5}$$

where the variation of displacement δu_i is the test function in the finite element method to be used in simulations. After applying integration by parts, for the details we refer to the Appendix, we obtain

$$\begin{aligned} &\int_\Omega \left(\frac{\partial w}{\partial u_{i,j}} \delta u_{i,j} + \frac{\partial w}{\partial u_{i,jk}} \delta u_{i,jk} \right) \mathrm{d}V \\ &= \int_\Omega \left(-\frac{\partial w}{\partial u_{i,j}} + \left(\frac{\partial w}{\partial u_{i,jk}} \right)_{,k} \right)_{,j} \delta u_i \, \mathrm{d}V + \int_{\partial\Omega} n_j \left(\frac{\partial w}{\partial u_{i,j}} - \left(\frac{\partial w}{\partial u_{i,jk}} \right)_{,k} \right) \delta u_i \, \mathrm{d}A + \int_{\partial\Omega} n_k \frac{\partial w}{\partial u_{i,jk}} \delta u_{i,j} \, \mathrm{d}A. \end{aligned} \tag{6}$$

In the third integral of the right hand side of the equation above, on the boundary surface, the gradient of test function $\delta u_{i,j}$ can be decomposed into a gradient within and normal to the surface [10, 18, 47, 52]:

$$\delta u_{i,j} = D_j(\delta u_i) + n_j D(\delta u_i), \tag{7}$$

where the operators D and D_j read

$$D(\cdot) = n_k \frac{\partial(\cdot)}{\partial X_k}, \quad D_j(\cdot) = (\delta_{jk} - n_j n_k) \frac{\partial(\cdot)}{\partial X_k}, \tag{8}$$

and n_i is the unit surface normal vector. Considering Equation (7), the last integral in Equation (6) becomes

$$\int_{\partial\Omega} n_k \frac{\partial w}{\partial u_{i,jk}} \delta u_{i,j} \, \mathrm{d}A = \int_{\partial\Omega} n_k \frac{\partial w}{\partial u_{i,jk}} D_j(\delta u_i) \, \mathrm{d}A + \int_{\partial\Omega} n_k \frac{\partial w}{\partial u_{i,jk}} n_j D(\delta u_i) \, \mathrm{d}A. \tag{9}$$

The boundary surface is assumed to be divisible into a finite number of smooth parts, $\partial\Omega_m$, each bounded by an edge, $\partial\partial\Omega_m$. Using Stokes' divergence theorem by following [18] on each smooth surface, the following equation is obtained [52]

$$\int_{\partial\Omega_m} D_j \left(n_k \frac{\partial w}{\partial u_{i,jk}} \delta u_i \right) \mathrm{d}A = \int_{\partial\Omega_m} n_j n_k \frac{\partial w}{\partial u_{i,jk}} D_p(n_p) \delta u_i \, \mathrm{d}A + \oint_{\partial\partial\Omega_m} \nu_j n_k \frac{\partial w}{\partial u_{i,jk}} \delta u_i \, \mathrm{d}l, \tag{10}$$

where ν_j is the unit tangent vector and belongs to the tangent space to $\partial\Omega_m$. According to the chain rule, we have

$$\int_{\partial\Omega} D_j \left(n_k \frac{\partial w}{\partial u_{i,jk}} \delta u_i \right) \mathrm{d}A = \int_{\partial\Omega} D_j \left(n_k \frac{\partial w}{\partial u_{i,jk}} \right) \delta u_i \, \mathrm{d}A + \int_{\partial\Omega} D_j(\delta u_i) \left(n_k \frac{\partial w}{\partial u_{i,jk}} \right) \mathrm{d}A. \tag{11}$$

Then the first integral on the right hand side of Equation (9) is written as

$$\int_{\partial\Omega} n_k \frac{\partial w}{\partial u_{i,jk}} D_j(\delta u_i)\,\mathrm{d}A = \int_{\partial\Omega} n_i n_k \frac{\partial w}{\partial u_{i,jk}} (D_p n_p)\delta u_i\,\mathrm{d}A + \sum_m \oint_{\partial\partial\Omega_m} \Delta\left(\nu_j n_k \frac{\partial w}{\partial u_{i,jk}}\right)\delta u_i\,\mathrm{d}l - \int_{\partial\Omega} D_j\left(n_k \frac{\partial w}{\partial u_{i,jk}}\right)\delta u_i\,\mathrm{d}A. \tag{12}$$

By $\Delta(\cdot)$, we denote the difference between values of the expression in the parentheses, which are calculated at different sides of a sharp edge. Note that integration domain of the third integral in Equation (10) is the boundary of a smooth surface. The whole body is composed of several smooth surfaces. By $\sum_m$, the sharp edges of the body are summed up. We stress that every edge line enters twice since it belongs to two adjacent surface regions [18]. By inserting the latter into Equation (11), the last surface integral in Equation (6) becomes

$$\begin{aligned}\int_{\partial\Omega} n_k \frac{\partial w}{\partial u_{i,jk}} \delta u_{i,j}\,\mathrm{d}A = &\int_{\partial\Omega} n_i n_j \frac{\partial w}{\partial u_{i,jk}} (D_p n_p)\delta u_i\,\mathrm{d}A + \sum_m \oint_{\partial\partial\Omega_m} \Delta\left(\nu_j n_k \frac{\partial w}{\partial u_{i,jk}}\right)\delta u_i\,\mathrm{d}l \\ &- \int_{\partial\Omega} D_j\left(n_k \frac{\partial w}{\partial u_{i,jk}}\right)\delta u_i\,\mathrm{d}A + \int_{\partial\Omega} n_k \frac{\partial w}{\partial u_{i,jk}} n_j D\delta u_i\,\mathrm{d}A.\end{aligned} \tag{13}$$

Thus the final integral form reads

$$\begin{aligned}\int_\Omega \delta w\,\mathrm{d}V = &\int_\Omega \left(\frac{\partial w}{\partial u_{i,j}}\delta u_{i,j} + \frac{\partial w}{\partial u_{i,jk}}\delta u_{i,jk}\right)\mathrm{d}V = \int_\Omega \left(-\frac{\partial w}{\partial u_{i,j}} + \left(\frac{\partial w}{\partial u_{i,jk}}\right)_{,k}\right)_{,j} \delta u_i\,\mathrm{d}V \\ &+ \int_{\partial\Omega} \left(n_j\left(\frac{\partial w}{\partial u_{i,j}} - \left(\frac{\partial w}{\partial u_{i,jk}}\right)_{,k}\right) + n_k n_j \frac{\partial w}{\partial u_{i,jk}}(D_p n_p) - D_j\left(n_k \frac{\partial w}{\partial u_{i,jk}}\right)\right)\delta u_i\,\mathrm{d}A \\ &+ \int_{\partial\Omega} n_k \frac{\partial w}{\partial u_{i,jk}} n_j D(\delta u_i)\,\mathrm{d}A + \sum_m \oint_{\partial\partial\Omega_m} \Delta\left(\nu_j n_k \frac{\partial w}{\partial u_{i,jk}}\right)\delta u_i\,\mathrm{d}l.\end{aligned} \tag{14}$$

For a better analogy, we define stress and hyperstress as follows:

$$\sigma_{ij} = \frac{\partial w}{\partial u_{i,j}}, \qquad \tau_{ijk} = \frac{\partial w}{\partial u_{i,jk}}. \tag{15}$$

It is observed from the last two integrals in Equation (14) that second gradient continua can sustain external surface double forces and sustain external line forces [10].

According to the principle of virtual work,

$$\delta W^{\mathrm{int}} - \delta W^{\mathrm{ext}} = 0, \tag{16}$$

W^{ext} is the external work done on the body. It is assumed to have the form [10, 52]:

$$W^{\mathrm{ext}} = \int_\Omega b_i u_i\,\mathrm{d}V + \int_{\partial\Omega} (t_i u_i + r_i D(u_i))\,\mathrm{d}A + \sum_m \oint_{\partial\partial\Omega_m} f_i u_i\,\mathrm{d}l. \tag{17}$$

The first part, $b_i u_i$, is the energy density because of the specific force, b_i [4]. By Equations (14), (16), and (17), the so-called tractions t_i, double tractions r_i and wedge forces f_k are expressed as

$$\begin{aligned} t_i &= n_j(\sigma_{ij} - \tau_{ijk,k}) + n_k n_j \tau_{ijk}(D_p n_p) - D_j(n_k \tau_{ijk}), \\ r_i &= n_j n_k \tau_{ijk}, \\ f_i &= \Delta\nu_j n_k \tau_{ijk}. \end{aligned} \tag{18}$$

By inserting Equation (15), Equation (18) into Equation (16) with the aid of Equation (14), we find out the so-called governing equation:

$$(\sigma_{ij} - \tau_{ijk,k})_{,j} + b_i = 0. \tag{19}$$

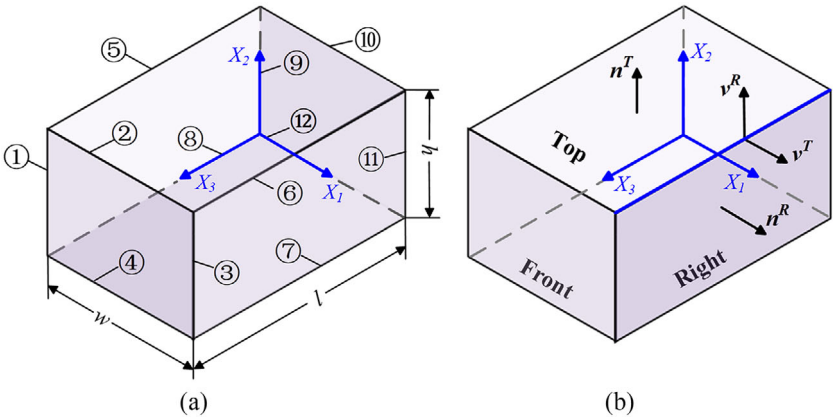

FIGURE 1 The schematic of a 3D block. A 3D block with numbered edges. (b) Unit tangential vector and unit normal vector

2.2 | Constitutive laws

Strain energy density in case of centrosymmetric materials reads

$$w(\varepsilon_{ij},\eta_{ijk}) = \frac{1}{2}\varepsilon_{ij}C_{ijkl}\varepsilon_{kl} + \frac{1}{2}\eta_{ijk}D_{ijklmn}\eta_{lmn}, \tag{20}$$

where C_{ijkl} and D_{ijklmn} are the first and the second gradient elastic stiffness tensors, respectively. For isotropic materials, they are given by

$$C_{ijkl} = c_1\delta_{ij}\delta_{kl} + c_2(\delta_{ik}\delta_{jl} + \delta_{il}\delta_{jk}), \tag{21}$$

$$\begin{aligned} D_{ijklmn} =& c_3(\delta_{ij}\delta_{kl}\delta_{mn} + \delta_{in}\delta_{jk}\delta_{lm} + \delta_{ij}\delta_{km}\delta_{ln} + \delta_{ik}\delta_{jn}\delta_{lm}) \\ &+ c_4\delta_{ij}\delta_{kn}\delta_{ml} + c_5(\delta_{ik}\delta_{jl}\delta_{mn} + \delta_{im}\delta_{jk}\delta_{ln} + \delta_{ik}\delta_{jm}\delta_{ln} + \delta_{il}\delta_{jk}\delta_{mn}) \\ &+ c_6(\delta_{il}\delta_{jm}\delta_{kn} + \delta_{im}\delta_{jl}\delta_{kn}) + c_7(\delta_{il}\delta_{jn}\delta_{mk} + \delta_{im}\delta_{jn}\delta_{lk} + \delta_{in}\delta_{jl}\delta_{km} + \delta_{in}\delta_{jm}\delta_{kl}). \end{aligned} \tag{22}$$

By c_1 and c_2 the Lamé constants are denoted. It is worth mentioning here that for a 3D case there are five additional parameters c_3, c_4, c_5, c_6, and c_7 in the second gradient stiffness tensor $\boldsymbol{D}$. By using Equations (20)–(22) we can rewrite Equation (15) as

$$\sigma_{ij} = \frac{\partial w}{\partial u_{i,j}} = c_1\delta_{ij}\varepsilon_{kk} + 2c_2\varepsilon_{ij}, \tag{23}$$

$$\begin{aligned} \tau_{ijk} = \frac{\partial w}{\partial u_{i,jk}} =& c_3(\delta_{ij}\varepsilon_{km,m} + \delta_{jk}\varepsilon_{mm,i} + \delta_{ij}\varepsilon_{nk,n} + \delta_{ik}\varepsilon_{mm,j}) + c_4\delta_{ij}\varepsilon_{ll,k} \\ &+ c_5(\delta_{ik}\varepsilon_{jn,n} + \delta_{jk}\varepsilon_{li,l} + \delta_{ik}\varepsilon_{nj,n} + \delta_{jk}\varepsilon_{im,m}) + c_6(\varepsilon_{ij,k} + \varepsilon_{ji,k}) \\ &+ c_7(\varepsilon_{ik,j} + \varepsilon_{ki,j} + \varepsilon_{jk,i} + \varepsilon_{kj,i}). \end{aligned} \tag{24}$$

3 | FORMULATION OF THE PROBLEM

A 3D block, as shown in Figure 1, is considered in the current section. The motivation for this selection is twofold. First, all surface boundaries are flat, consequently, the boundary conditions are simplified. Second, the presence of sharp edges would bring the wedge forces, and their importance will be demonstrated later on. We choose the length l, width w, and height h to be equal ($l = w = h$). Each of the 12 edges is characterized by a unique number, see Figure 1a. Unit tangential vectors and unit normal vectors for the right and top surfaces are presented in Figure 1b.

For the considered domain Ω its boundary $\partial\Omega$ is composed of flat surfaces leading to $D_p(n_p) = 0$ on $\partial\Omega$. Hence Equation (18) reads

$$\begin{aligned} t_i &= n_j\sigma_{ij} - n_j(\tau_{ijk,k} + \tau_{ihj,h}) + n_j n_h n_k \tau_{ijk,h}, \\ r_i &= n_j n_k \tau_{ijk}. \end{aligned} \tag{25}$$

Thus, expressions of tractions and double tractions as well for the left surface are the following:

$$\begin{aligned} t_1^L &= -\sigma_{11} + \tau_{111,1} + \tau_{112,2} + \tau_{113,3} + \tau_{121,2} + \tau_{131,3}, \\ t_2^L &= -\sigma_{21} + \tau_{211,1} + \tau_{212,2} + \tau_{213,3} + \tau_{221,2} + \tau_{231,3}, \\ t_3^L &= -\sigma_{31} + \tau_{311,1} + \tau_{312,2} + \tau_{313,3} + \tau_{321,2} + \tau_{331,3}, \\ r_1 &= \tau_{111}, \\ r_2 &= \tau_{211}, \\ r_3 &= \tau_{311}. \end{aligned} \tag{26}$$

According to Equation (18), the so-called wedge forces are

$$f_i = \Delta\nu_j n_k \tau_{ijk}. \tag{27}$$

There are 12 edges in total for the 3D block. Let us take the edge number 6, which is blue in Figure 1b, as an example. The unit normal vectors and tangent vectors for the right and top surfaces are

$$\begin{aligned} n_j^R &= \delta_{1j}, \quad n_j^T = \delta_{2j}, \\ \nu_i^R &= \delta_{i2}, \quad \nu_i^T = \delta_{i1}. \end{aligned} \tag{28}$$

The wedge force on the edge number 6 is then calculated by

$$\begin{aligned} f_1 &= \nu_j^R n_k^R \tau_{1jk} + \nu_j^T n_k^T \tau_{1jk} = \tau_{121} + \tau_{112}, \\ f_2 &= \nu_j^R n_k^R \tau_{2jk} + \nu_j^T n_k^T \tau_{2jk} = \tau_{221} + \tau_{212}, \\ f_3 &= \nu_j^R n_k^R \tau_{3jk} + \nu_j^T n_k^T \tau_{3jk} = \tau_{321} + \tau_{312}. \end{aligned} \tag{29}$$

Expressions for tractions, double tractions, and wedge forces on the remaining surfaces and edges respectively can be calculated analogously. Expressions for the stress tensor, the hyperstress tensor, and balance equations can be given explicitly in terms of the displacement by using Equations (23), (24), and (19) as shown in Appendix.

4 | ANALYTICAL AND NUMERICAL SOLUTIONS AND COMPARATIVE STUDIES OF A SECOND GRADIENT MODEL FOR A 3D BLOCK

Let us consider the deformation modes of a block corresponding to particular components of the strain gradient tensor as shown in Table 1 [6, 55]. We emphasize that for underlined indices no summation convention is applied. There are four distinct modes of deformations: Extension, torsion, non-conventional bending, and trapezoid [55, 72, 75]. These four modes correspond to specific non-zero strain gradient components, which will result in strain gradient effects of materials. For example, a trapezoid loading deforms the block to be trapezoid-shaped with non-zero strain gradient components η_{121} as shown in [55]. In this work, the extension, torsion, and non-conventional bending deformation modes are studied by considering specific displacement field solution corresponding to these non-zero strain gradient components as illustrated in Figure 2. The solutions of displacement fields are imposed, the corresponding boundary conditions (tractions, double tractions, and wedge forces) are found. This idea is based on the work in [9, 72, 75]. Numerical simulations are conducted

TABLE 1 Characterization of deformation patterns associated with $\boldsymbol{\eta}$. The summation convention is not applied over underlined indices. Unique indices are not equal ($i \neq j, j \neq k, i \neq k$)

Deformation patterns	Non-zero components of $\boldsymbol{\eta}$
Extension	$\eta_{\underline{iii}}$
Torsion	$\eta_{\underline{ijk}}$
Non-conventional bending	$\eta_{\underline{ijj}}$
Trapezoid	$\eta_{\underline{iji}}$

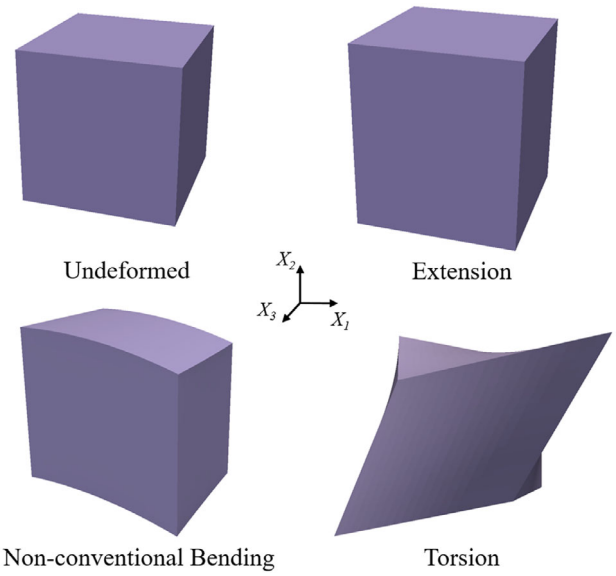

FIGURE 2 Deformation patterns associated with non-zero $\boldsymbol{\eta}$. Extension: η_{222}. Torsion: η_{123}. Non-conventional bending: η_{211}

based on the derived boundary conditions, and the calculated results are compared with the displacement fields. The weak form and its numerical implementation can be found in Appendix.

The geometry sizes and constitutive parameters of the block are shown in Table 2. The values of strain gradient related parameters may be possibly given as shown in Table 2 [9]. For defining the body forces, gravitational forces are implemented by the specific force g=10 N/kg. Three cases of different boundary conditions are investigated throughout this section.

4.1 | Extension

The following displacement fields leading to a non-zero η_{222} are considered:

$$u_1 = 0, \quad u_2 = \frac{\rho g(X_2 - l)(3l + X_2)}{2(c_1 + 2c_2)}, \quad u_3 = 0. \tag{30}$$

This solution of displacement fields can be achieved by the following body forces:

$$b_1 = 0, \quad b_2 = -\rho g, \quad b_3 = 0, \tag{31}$$

TABLE 2 Numerical data used for simulations

l m	ρ kg/m^3	E Pa	c_1 Pa	c_2 Pa	c_3 N	c_4 N	c_5 N	c_6N	c_7N
0.1	10^5	26×10^6	15×10^6	10×10^6	2600	2600	5200	2600	1300

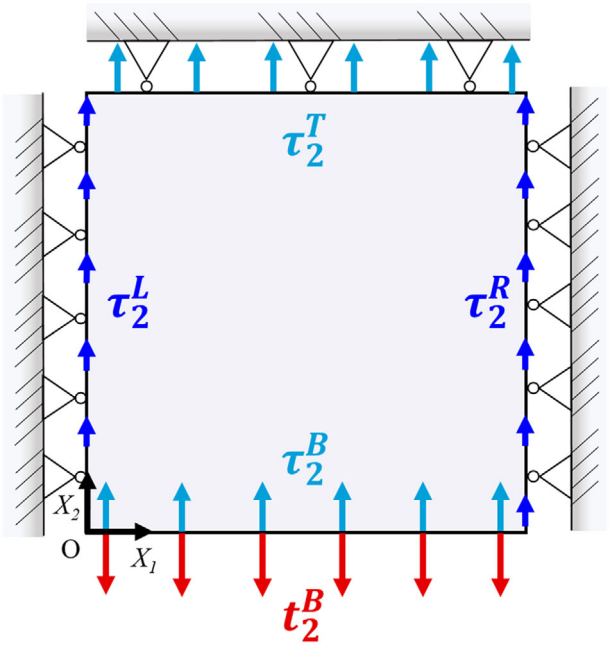

FIGURE 3 Graphical representation of the boundary conditions for the extension problem. It is visualized for a cut slice (z=0.05 m)

as well as the following surface boundary conditions:

$$
\begin{aligned}
&\text{Left surface:}\quad u_1^L = 0,\quad t_2^L = 0,\quad t_3^L = 0,\quad \tau_1^L = 0,\quad \tau_2^L = \tau_{211} = (c_3 + 2c_5)\frac{\rho g}{c_1 + 2c_2}, \tau_3^L = 0,\\
&\text{Right surface:}\quad u_1^R = 0,\quad t_2^R = 0,\quad t_3^R = 0,\quad \tau_1^R = 0,\quad \tau_2^R = \tau_{211} = (c_3 + 2c_5)\frac{\rho g}{c_1 + 2c_2},\quad \tau_3^R = 0,\\
&\text{Top surface:}\quad t_1^T = 0,\quad u_2^T = 0,\quad t_3^T = 0,\quad \tau_1^T = 0,\\
&\qquad\qquad \tau_2^T = (4c_3 + c_4 + 4c_5 + 2c_6 + 4c_7)\frac{\rho g}{c_1 + 2c_2},\quad \tau_3^T = 0,\\
&\text{Bottom surface:}\quad t_1^B = 0,\quad t_2^B = -\rho g(x_2 + l),\quad t_3^B = 0,\quad \tau_1^B = 0,\\
&\qquad\qquad \tau_2^B = (4c_3 + c_4 + 4c_5 + 2c_6 + 4c_7)\frac{\rho g}{c_1 + 2c_2},\quad \tau_3^B = 0,\\
&\text{Front surface:}\quad t_1^F = 0,\quad t_2^F = 0,\quad u_3^F = 0,\quad \tau_1^F = 0,\quad \tau_2^F = \tau_{233} = (c_3 + 2c_5)\frac{\rho g}{c_1 + 2c_2},\quad \tau_3^F = 0,\\
&\text{Back surface:}\quad t_1^K = 0,\quad t_2^K = 0,\quad u_3^K = 0,\quad \tau_1^K = 0,\quad \tau_2^K = \tau_{233} = (c_3 + 2c_5)\frac{\rho g}{c_1 + 2c_2},\quad \tau_3^K = 0.
\end{aligned}
\tag{32}
$$

Due to the kinematic restrictions, the wedge forces are not imposed in this case. The imposed kinematical constraints and boundary conditions are also shown in Figure 3 for a cut slice. Plots for numerically obtained total displacement are presented in Figure 4. In Figure 5, perfect overlap is observed between the analytical and numerical results. A difference is shown for numerical solutions if double tractions are not taken into account.

4.2 | Torsion

Lets now consider a torsion problem with the following displacement fields:

$$
u_1 = TX_2X_3,\quad u_2 = TX_1X_3,\quad u_3 = TX_1X_2,
\tag{33}
$$

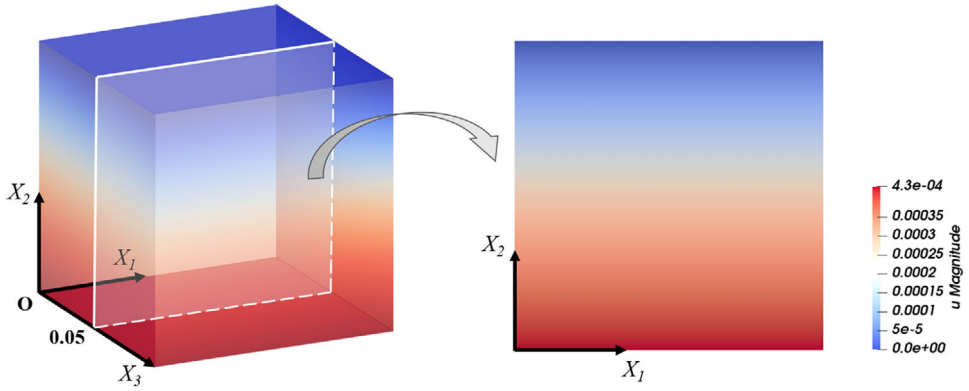

FIGURE 4 Total displacement of the extensional case

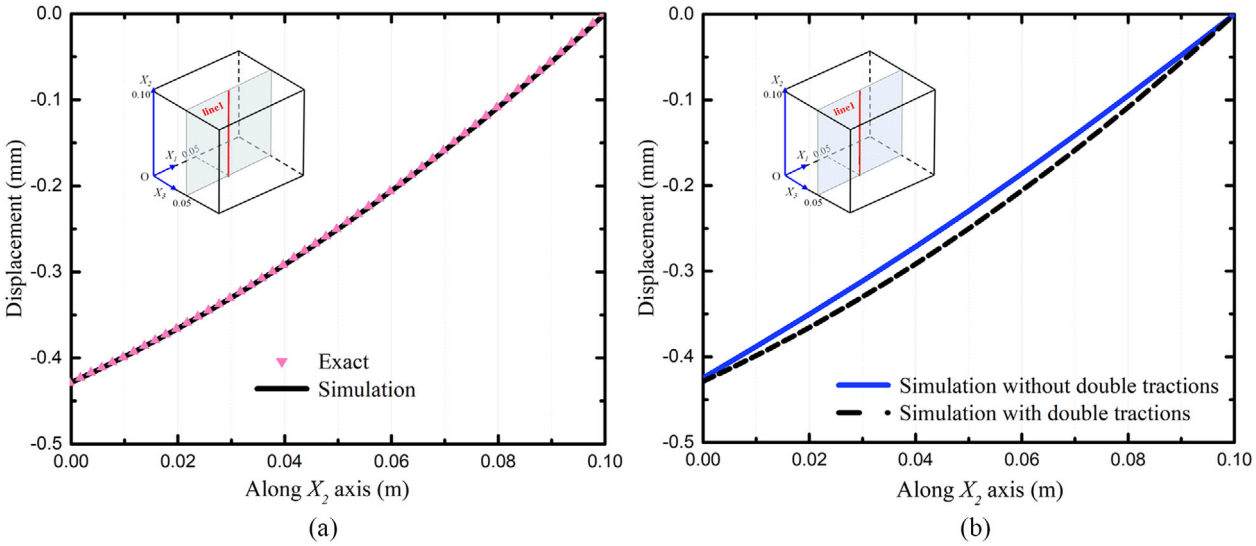

FIGURE 5 Comparisons for analytical solution and numerical ones. (a) Comparisons between the exact solution and the numerical one through a cut along X_2. (b) Comparisons between simulations through a cut along X_2

where T is a small constant with the physical dimension of the inverse of a length (T is set to be equal to 0.1 m^{-1}). The analytical solution is achieved by the following body forces:

$$b_1 = 0, \quad b_2 = 0, \quad b_3 = 0, \tag{34}$$

as well as the following boundary conditions:

$$\begin{aligned}
\text{Left surface:}\ & t_1^L = 0, u_2^L = 0, u_3^L = 0, \tau_1^L = 0, \tau_2^L = 0, \tau_3^L = 0,\\
\text{Right surface:}\ & t_1^R = 0, t_2^R = 2Tc_2X_3, t_3^R = 2Tc_2X_2, \tau_1^R = 0, \tau_2^R = 0, \tau_3^R = 0,\\
\text{Top surface:}\ & t_1^T = -2Tc_2X_3, t_2^T = 0, t_3^T = 2Tc_2X_1, \tau_1^T = 0, \tau_2^T = 0, \tau_3^T = 0,\\
\text{Bottom surface:}\ & u_1^B = 0, t_2^B = 0, u_3^B = 0, \tau_1^B = 0, \tau_2^B = 0, \tau_3^B = 0,\\
\text{Front surface:}\ & t_1^F = 2Tc_2X_2, t_2^F = 2Tc_2X_1, t_3^F = 0, \tau_1^F = 0, \tau_2^F = 0, \tau_3^F = 0,\\
\text{Back surface:}\ & u_1^K = 0, u_2^K = 0, t_3^K = 0, \tau_1^K = 0, \tau_2^K = 0, \tau_3^K = 0.
\end{aligned} \tag{35}$$

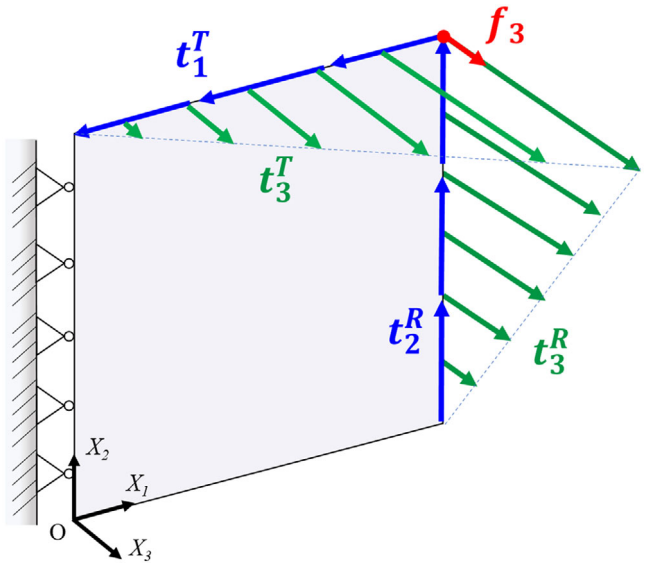

FIGURE 6 Graphical representation of the boundary conditions for the torsion problem. It is visualized for a cut slice (z = 0.05 m)

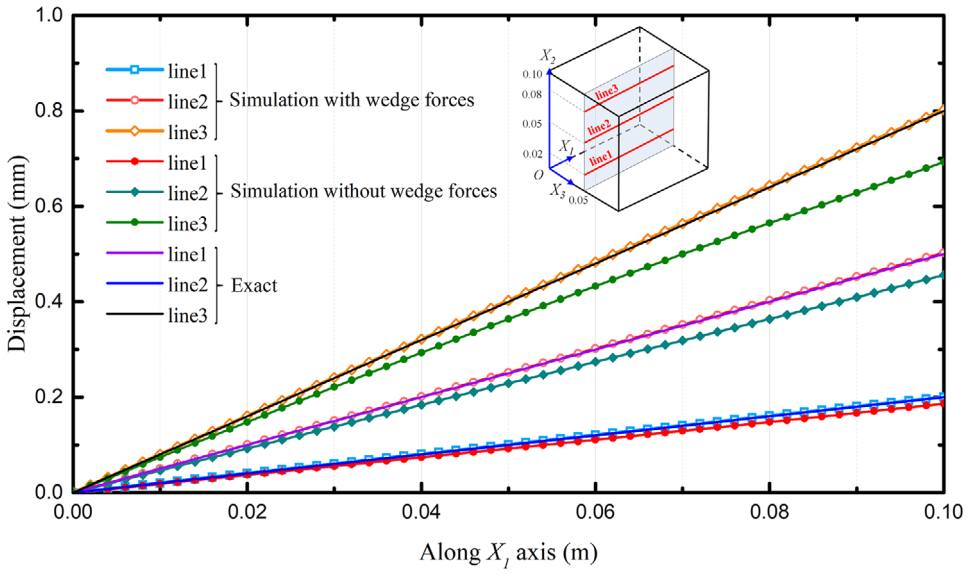

FIGURE 7 Comparisons between the exact solution and the numerical ones through three different cut

We emphasize that the double tractions on all of the surfaces are equal to zero. According to the kinematical restrictions, the imposed non-zero wedge forces are calculated by Equation (27)

$$\begin{aligned} &\text{Edge 2:}\quad f_1 = \tau_{132} + \tau_{123} = T(4c_6 + 8c_7),\\ &\text{Edge 3:}\quad f_2 = \tau_{213} + \tau_{231} = T(4c_6 + 8c_7),\\ &\text{Edge 6:}\quad f_3 = \tau_{321} + \tau_{312} = T(4c_6 + 8c_7). \end{aligned} \tag{36}$$

Figure 6 presents the imposed kinematical constraints and boundary conditions for a cut slice. Comparing the exact solution with the numerical outcomes on three different cuts (line1, line2, line3), see Figure 7, we observe that the plot for simulation incorporating wedge forces demonstrate an almost perfect overlapping with the plot of the analytical solution. Figure 8 indicates differences for total displacement plots for different boundary conditions. It is well known that a sin-

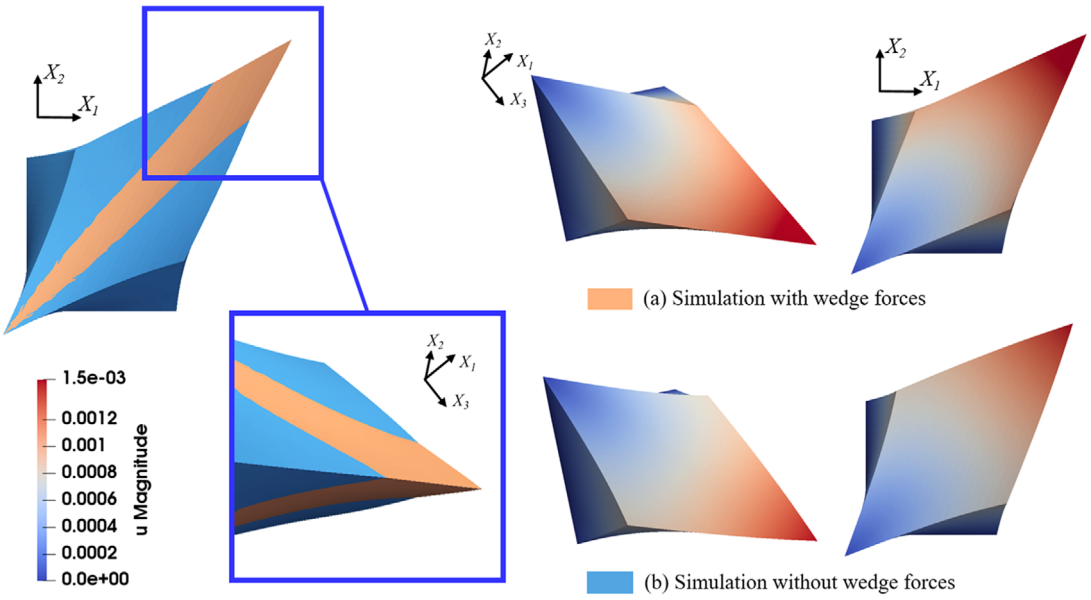

FIGURE 8 Comparisons between numerical solutions for the torsion tests (Scaling factor = 40). On the left hand side, the blocks are presented in the current configuration by two different colors for these two different numerical solutions

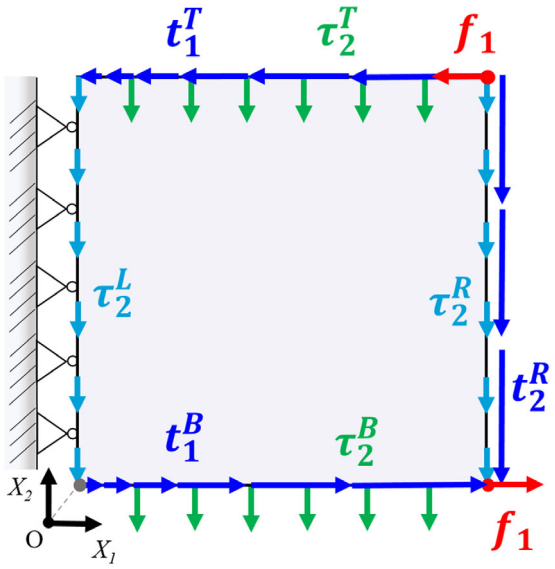

FIGURE 9 Graphical representation of the boundary conditions for the non-conventional bending problem. It is visualized for a cut slice (z=0.05 m)

gularity results under line loads for classical Cauchy continuum. However, the line loads (or wedge forces) in the strain gradient continuum are necessary and yield a continuous solution for the displacement fields.

4.3 | Non-conventional bending

The so-called non-conventional bending problem is considered. The displacement field equations are conceived as

$$u_1 = 0, \quad u_2 = -B\frac{X_1^2}{2}, \quad u_3 = 0, \tag{37}$$

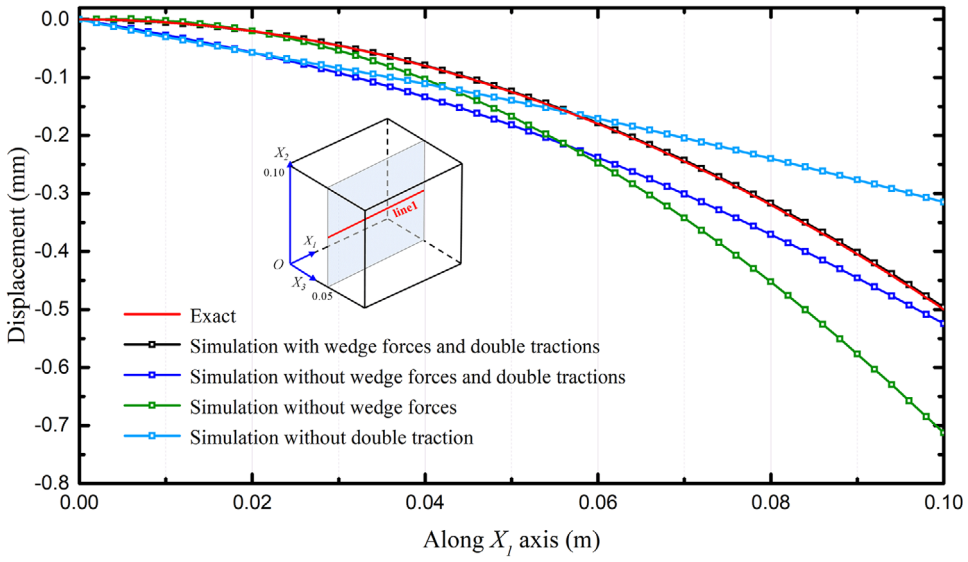

FIGURE 10 Comparisons between the exact solution and the numerical ones through a cut indicated as line 1

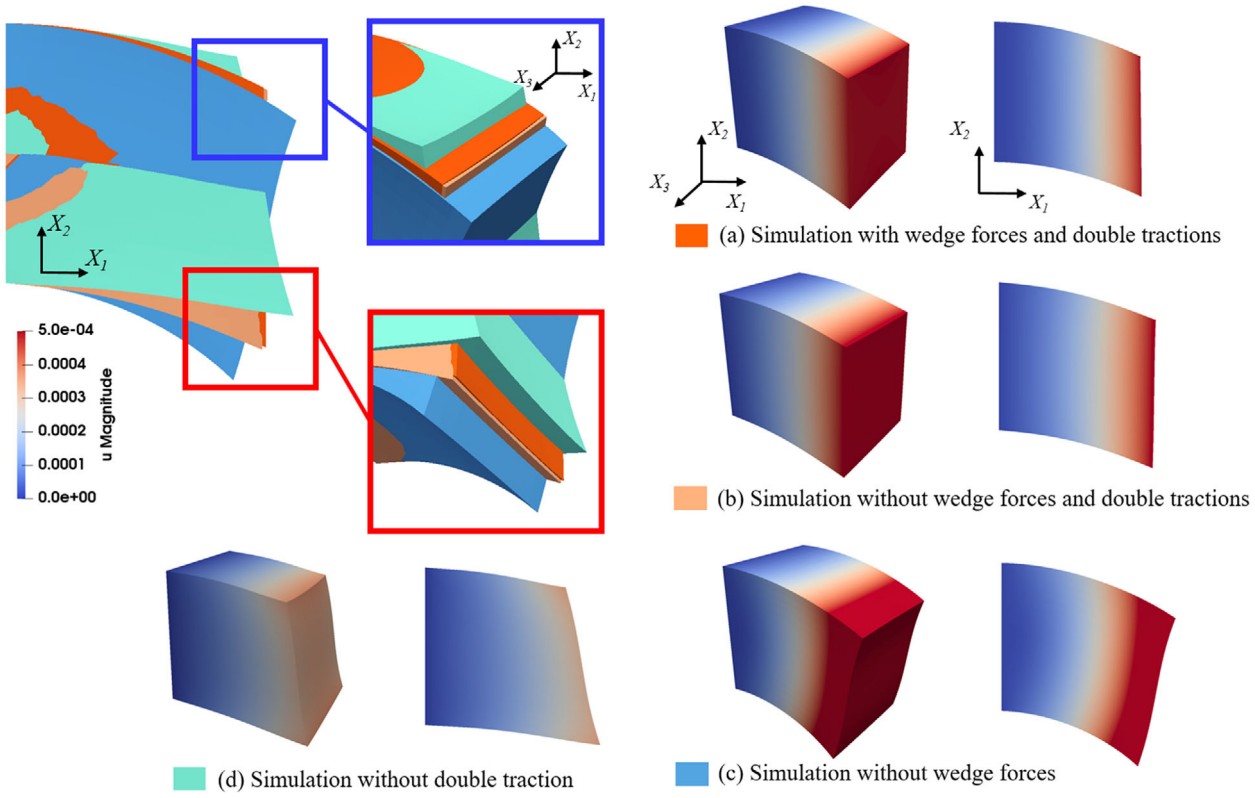

FIGURE 11 Total displacement for the non-conventional bending problem (scaling factor 50). Four different colors are used to demonstrate differences of the numerical solutions on the left hand side

where B is a small constant with the physical dimension of the inverse of a length (B is set to be equal to 0.1 m^{-1}). The solution of the displacement field is acquired by the following body forces:

$$b_1 = 0, \quad b_2 = Bc_2, \quad b_3 = 0, \tag{38}$$

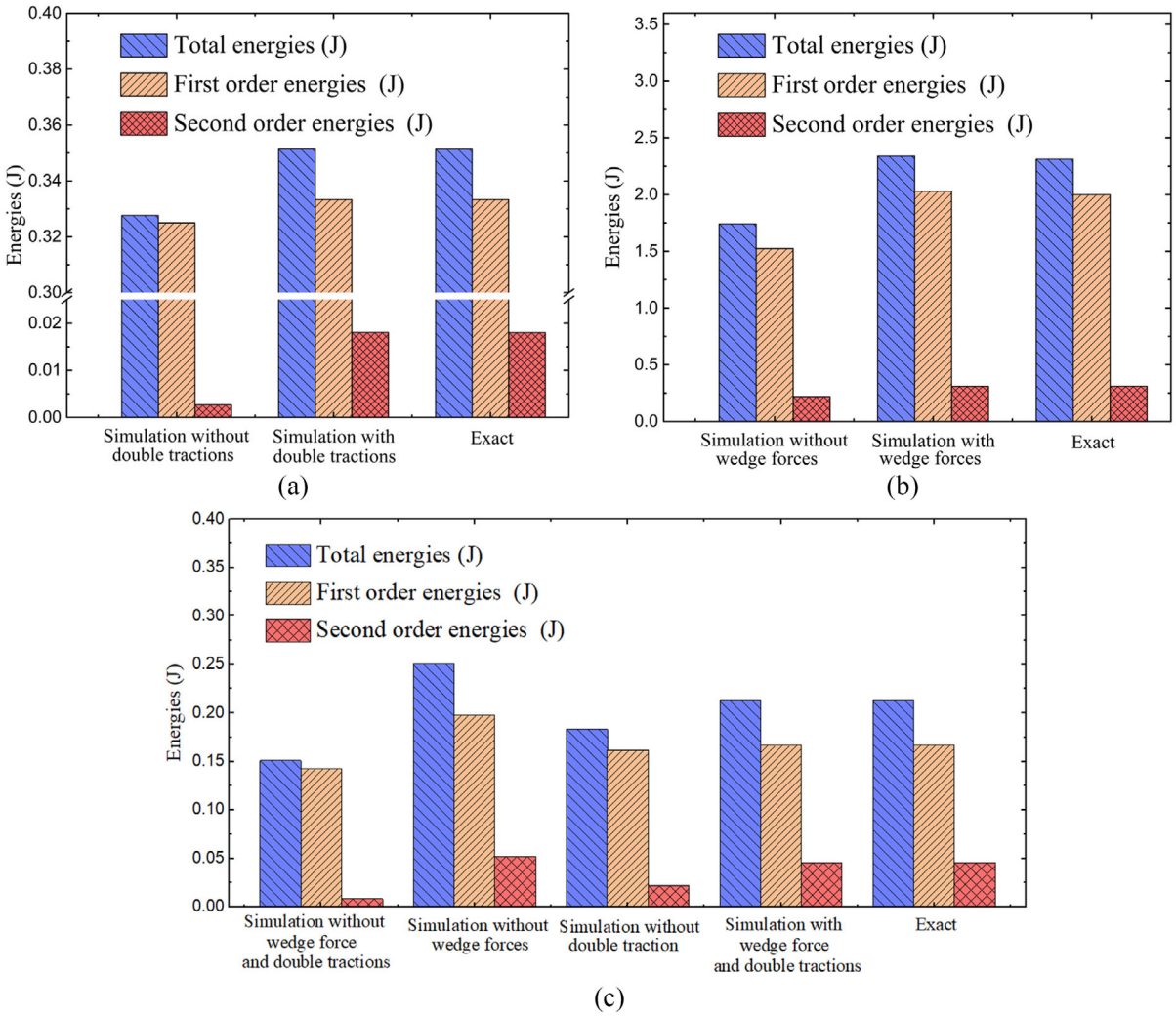

FIGURE 12 Comparisons for strain energies among analytical solutions and numerical ones. (a) Strain energies for the extensional case. (b) Strain energies for the torsion case. (c) Strain energies for the non-conventional bending case

as well as the following boundary conditions:

$$\begin{aligned}
\text{Left surface:}\quad & u_1^L = 0, u_2^L = 0, u_3^L = 0, \tau_1^L = 0, \tau_2^L = \tau_{211} = (-B)(c_5 + c_6 + c_7), \tau_3^L = 0,\\
\text{Right surface:}\quad & t_1^R = 0, t_2^R = -Bc_2X_1, t_3^R = 0, \tau_1^R = 0, \tau_2^R = (-B)(c_5 + c_6 + c_7), \tau_3^R = 0,\\
\text{Top surface:}\quad & t_1^T = -Bc_2X_1, t_2^T = 0, t_3^T = 0, \tau_1^T = 0, \tau_2^T = (-B)(c_3 + 2c_5), \tau_3^T = 0,\\
\text{Bottom surface:}\quad & t_1^B = Bc_2X_1, t_2^B = 0, t_3^B = 0, \tau_1^B = 0, \tau_2^B = (-B)(c_3 + 2c_5), \tau_3^B = 0,\\
\text{Front surface:}\quad & t_1^F = 0, t_2^F = 0, t_3^F = 0, \tau_1^F = 0, \tau_2^F = -Bc_5, \tau_3^F = 0,\\
\text{Back surface:}\quad & t_1^K = 0, t_2^K = 0, t_3^K = 0, \tau_1^K = 0, \tau_2^K = -Bc_5, \tau_3^K = 0.
\end{aligned} \tag{39}$$

The following wedge forces calculated by Equation (27) are imposed

$$\begin{aligned}
\text{Edge 2:}\quad & f_3 = \tau_{332} + \tau_{323} = (-B)(c_3 + c_5),\\
\text{Edge 4:}\quad & f_3 = \tau_{121} + \tau_{112} = B(c_3 + c_5),\\
\text{Edge 6:}\quad & f_1 = \tau_{121} + \tau_{112} = (-B)(c_3 + c_5 + c_6 + 3c_7),
\end{aligned}$$

$$\text{Edge 7:}\quad f_1 = -\tau_{121} - \tau_{112} = B(c_3 + c_5 + c_6 + 3c_7),$$
$$\text{Edge 10:}\quad f_3 = -\tau_{332} - \tau_{323} = (-B)(c_3 + c_5),$$
$$\text{Edge 12:}\quad f_3 = \tau_{332} + \tau_{323} = B(c_3 + c_5). \tag{40}$$

The imposed kinematical constraints and boundary conditions are presented in Figure 9 for a cut slice.

A comparison between the analytical solutions and the numerical ones along a line cut (line 1) are shown in Figure 10. Obviously, when the double tractions and wedge forces are both imposed, the numerical results are in good agreement with the analytical solutions.

The strain energies are calculated and presented here for the analytical and numerical solutions as shown in Figure 12. First order $\frac{1}{2}\varepsilon_{ij}C_{ijkl}\varepsilon_{kl}$ and second order $\frac{1}{2}\eta_{ijk}D_{ijklmn}\eta_{lmn}$ energies contribute differently in different cases. With the correctly imposed boundaries conditions the strain energies of the numerical solutions show an adequate agreement with the analytical solutions.

5 | CONCLUSIONS

In this paper, numerical simulations based on IGA are performed in order to be compared with an analytical solution obtained using the inverse method. Three exemplary cases of different boundary conditions were considered in 3D: Extension, torsion, and non-conventional bending. Numerical simulations were performed with and without taking the so-called wedge forces and double tractions into account. It was shown that the numerical results are in good agreement with the analytical solutions if the wedge forces and double tractions are considered. Besides that, we presented comparisons between the numerical simulations. Such a comparison helps to reveal and comprehend the roles of the wedge forces and double tractions in the solutions. The numerical implementation was conducted by means of an open source tool called tIGAr which is based on FEniCS library.

ACKNOWLEDGMENTS

Open access funding enabled and organized by Projekt DEAL.

ORCID

Hua Yang https://orcid.org/0000-0003-2080-3452
B. Emek Abali https://orcid.org/0000-0002-8735-6071

REFERENCES

[1] Abali, B.E.: Revealing the physical insight of a length-scale parameter in metamaterials by exploiting the variational formulation. Contin. Mech. Thermodyn. 31(4), 885–894 (2019)
[2] Abali, B.E.: Supply code for computations. http://bilenemek.abali.org/ (2020)
[3] Abali, B.E., Barchiesi, E.: Additive manufacturing introduced substructure and computational determination of metamaterials parameters by means of the asymptotic homogenization. Contin. Mech. Thermodyn. 33, 1–17 (2020)
[4] Abali, B.E., Müller, W.H., dell'Isola, F.: Theory and computation of higher gradient elasticity theories based on action principles. Arch. Appl. Mech. 87(9), 1495–1510 (2017)
[5] Abali, B.E., Müller, W.H., Eremeyev, V.A.: Strain gradient elasticity with geometric nonlinearities and its computational evaluation. Mech. Adv. Mater. Mod. Process. 1(1), 1–11 (2015)
[6] Abali, B.E., Yang, H., Papadopoulos, P.: A computational approach for determination of parameters in generalized mechanics. In Higher Gradient Materials and Related Generalized Continua, pp. 1–18. Springer (2019)
[7] Abdoul-Anziz, H., Seppecher, P.: Strain gradient and generalized continua obtained by homogenizing frame lattices. Math Mechanics Complex Systems 6(3), 213–250 (2018)
[8] Alibert, J.-J., Seppecher, P., dell'Isola, F.: Truss modular beams with deformation energy depending on higher displacement gradients. Math. Mech. Solids 8(1), 51–73 (2003)
[9] Andreaus, U., dell'Isola, F., Giorgio, I., Placidi, L., Lekszycki, T., Rizzi, N.L.: Numerical simulations of classical problems in two-dimensional (non) linear second gradient elasticity. Int. J. Eng. Sci. 108, 34–50 (2016)
[10] Auffray, N., dell'Isola, F., Eremeyev, V.A., Madeo, A., Rosi, G.: Analytical continuum mechanics à la Hamilton–Piola least action principle for second gradient continua and capillary fluids. Math. Mech. Solids 20(4), 375–417 (2015)
[11] Auffray, N., Dirrenberger, J., Rosi, G.: A complete description of bi-dimensional anisotropic strain-gradient elasticity. Int. J. Solids Struct. 69, 195–206 (2015)

[12] Barchiesi, E., dell'Isola, F., Hild, F., Seppecher, P.: Two-dimensional continua capable of large elastic extension in two independent directions: Asymptotic homogenization, numerical simulations and experimental evidence. Mech. Res. Commun. 103, 103466 (2020)
[13] Barchiesi, E., Eugster, S.R., dell'Isola, F., Hild, F.: Large in-plane elastic deformations of bi-pantographic fabrics: Asymptotic homogenization and experimental validation. Math. Mech. Solids 25(3), 739–767 (2020)
[14] Barchiesi, E., Eugster, S.R., Placidi, L., dell'Isola, F.: Pantographic beam: a complete second gradient 1d-continuum in plane. Z. Angew. Math. Phys. 70(5), 135 (2019)
[15] Barchiesi, E., Ganzosch, G., Liebold, C., Placidi, L., Grygoruk, R., Müller, W.H.: Out-of-plane buckling of pantographic fabrics in displacement-controlled shear tests: experimental results and model validation. Contin. Mech. Thermodyn. 31(1), 33–45 (2019)
[16] Barchiesi, E., Spagnuolo, M., Placidi, L.: Mechanical metamaterials: a state of the art. Math. Mech. Solids 24(1), 212–234 (2019)
[17] Barchiesi, E., Yang, H., Tran, C., Placidi, L., Müller, W.: Computation of brittle fracture propagation in strain gradient materials by the FEniCS library. Math. Mech. Solids 1081286520954513 (2020)
[18] Bertram, A.: Balance laws for gradient materials. In Mechanics of Strain Gradient Materials, pp. 19–35. Springer (2020)
[19] Cazzani, A., Malagù, M., Turco, E.: Isogeometric analysis: A powerful numerical tool for the elastic analysis of historical masonry arches. Contin. Mech. Thermodyn. 28(1-2), 139–156 (2016)
[20] Cazzani, A., Malagù, M., Turco, E.: Isogeometric analysis of plane-curved beams. Math. Mech. Solids 21(5), 562–577 (2016)
[21] Cazzani, A., Stochino, F., Turco, E.: An analytical assessment of finite element and isogeometric analyses of the whole spectrum of Timoshenko beams. ZAMM - J. Appl. Math. Mech./Z. Angew. Math. Mech. 96(10), 1220–1244 (2016)
[22] Charalambopoulos, A., Tsinopoulos, S.V., Polyzos, D.: Plane strain gradient elastic rectangle in bending. Arch. Appl. Mech. 1–20 (2020)
[23] Chen, Q., Chen, W., Wang, G.: Fully-coupled electro-magneto-elastic behavior of unidirectional multiphased composites via finite-volume homogenization. Mech. Mater. 103553 (2020)
[24] De Angelo, M., Barchiesi, E., Giorgio, I., Abali, B.E.: Numerical identification of constitutive parameters in reduced-order bi-dimensional models for pantographic structures: application to out-of-plane buckling. Arch. Appl. Mech. 89(7), 1333–1358 (2019)
[25] De Angelo, M., Spagnuolo, M., D'annibale, F., Pfaff, A., Hoschke, K., Misra, A., Dupuy, C., Peyre, P., Dirrenberger, J., Pawlikowski, M.: The macroscopic behavior of pantographic sheets depends mainly on their microstructure: experimental evidence and qualitative analysis of damage in metallic specimens. Contin. Mech. Thermodyn. 31(4), 1181–1203 (2019)
[26] Del, Vescovo, D., Giorgio, I.: Dynamic problems for metamaterials: review of existing models and ideas for further research. Int. J. Eng. Sci. 80, 153–172 (2014)
[27] dell'Isola, F., Andreaus, U., Luca, P.: At the origins and in the vanguard of peri-dynamics, non-local and higher gradient continuum mechanics. an underestimated and still topical contribution of Gabrio Piola. Math. Mech. Solids 20(8), 887–928 (2015)
[28] dell'Isola, F., Bucci, S., Battista, A.: Against the fragmentation of knowledge: the power of multidisciplinary research for the design of metamaterials. Adv. Methods Continuum Mechanics for Materials Struct. 523–545 (2016)
[29] dell'Isola, F., Della Corte, A., Giorgio, I.: Higher-gradient continua: The legacy of Piola, Mindlin, Sedov and Toupin and some future research perspectives. Math. Mech. Solids 22(4), 852–872 (2017)
[30] dell'Isola, F., Placidi, L.: Variational principles are a powerful tool also for formulating field theories. Variational models and methods in solid and fluid mechanics 1–15 (2012)
[31] dell'Isola, F., Sciarra, G., Vidoli, S.: Generalized Hooke's law for isotropic second gradient materials. In Proceedings of the Royal Society of London A: Mathematical, Physical and Engineering Sciences rspa–2008. The Royal Society (2009)
[32] dell'Isola, F., Seppecher, P., Alibert, J.J., Lekszycki, T., et al.: Pantographic metamaterials: An example of mathematically driven design and of its technological challenges. Contin. Mech. Thermodyn. 31(4), 851–884 (2019)
[33] dell'Isola, F., Seppecher, P., Madeo, A.: How contact interactions may depend on the shape of cauchy cuts in Nth gradient continua: Approach "á la D'Alembert". Z. Angew. Math. Phys. 63(6), 1119–1141 (2012)
[34] dell'Isola, F., Seppecher, P., Spagnuolo, M., Barchiesi, E., et al.: Advances in pantographic structures: design, manufacturing, models, experiments and image analyses. Contin. Mech. Thermodyn. 31(4), 1231–1282 (2019)
[35] dell'Isola, F., Steigmann, D., Della Corte, A.: Synthesis of fibrous complex structures: Designing microstructure to deliver targeted macroscale response. Appl. Mech. Rev. 67(6), 060804 (2015)
[36] Eremeyev, V.A., dell'Isola, F.: A note on reduced strain gradient elasticity. Generalized Models and Non-classical Approaches in Complex Materials 1, 301–310 (2018)
[37] Eremeyev, V.A., Lebedev, L.P., Altenbach, H.: Foundations of Micropolar Mechanics. Springer Science & Business Media (2012)
[38] Eugster, S., dell'Isola, F., Steigmann, D.: Continuum theory for mechanical metamaterials with a cubic lattice substructure. Mathematics and Mechanics of Complex Systems 7(1), 75–98 (2019)
[39] Fischer, P., Klassen, M., Mergheim, J., Steinmann, P., Müller, R.: Isogeometric analysis of 2D gradient elasticity. Computational Mechanics 47(3), 325–334 (2011)
[40] Giorgio, I.: Lattice shells composed of two families of curved kirchhoff rods: An archetypal example, topology optimization of a cycloidal metamaterial. Contin. Mech. Thermodyn. 1–20 (2020)
[41] Giorgio, I., Rizzi, N., Turco, E.: Continuum modelling of pantographic sheets for out-of-plane bifurcation and vibrational analysis. Proc. R. Soc. Lond. A, Math. Phys. Eng. Sci. 473(2207), 20170636 (2017)
[42] Glüge, R.: A for C strain 1 incompatible gradient mode elasticity element formulation. Higher Gradient Materials and Related Generalized Continua 120, 95 (2019)
[43] Glüge, R., Altenbach, H., Mahmood, N., Beiner, M.: On the difference between the tensile stiffness of bulk and slice samples of microstructured materials. Appl. Compos. Mater. 1–20 (2020)

[44] Gnu Public: Gnu general public license. http://www.gnu.org/copyleft/gpl.html (2007)
[45] Golaszewski, M., Grygoruk, R., Giorgio, I., Laudato, M., Di Cosmo, F.: Metamaterials with relative displacements in their microstructure: Technological challenges in 3d printing, experiments and numerical predictions. Contin. Mech. Thermodyn. 31(4), 1015–1034 (2019)
[46] Hughes, T.J., Cottrell, J.A., Bazilevs, Y.: Isogeometric analysis: CAD, finite elements, NURBS, exact geometry and mesh refinement. Comput. Methods Appl. Mech. Eng. 194(39-41), 4135–4195 (2005)
[47] Hutchinson, J., Fleck, N.: Strain gradient plasticity. Advances in Applied Mechanics 33, 295–361 (1997)
[48] Javii, A., Steinmann, P., dell'Isola, F.: Geometrically nonlinear higher-gradient elasticity with energetic boundaries. J. Mech. Phys. Solids (2013)
[49] Kamensky, D.: Open-source immersogeometric analysis of fluid–structure interaction using FEniCS and tIGAr. Comput. Math. Appl. (2020)
[50] Kamensky, D., Bazilevs, Y.: tIGAr: Automating isogeometric analysis with FEniCS. Comput. Methods Appl. Mech. Eng. 344, 477–498 (2019)
[51] Khakalo, S., Niiranen, J.: Anisotropic strain gradient thermoelasticity for cellular structures: Plate models, homogenization and isogeometric analysis. J. Mech. Phys. Solids 134, 103728 (2020)
[52] Lam, D.C., Yang, F., Chong, A., Wang, J., Tong, P.: Experiments and theory in strain gradient elasticity. J. Mech. Phys. Solids 51(8), 1477–1508 (2003)
[53] Liu, H., Li, B., Yang, Z., Hong, J.: Topology optimization of stiffened plate/shell structures based on adaptive morphogenesis algorithm. J. Manuf. Syst. 43, 375–384 (2017)
[54] Liu, H., Li, B., Zhang, L., Li, X.: Optimizing heat-absorption efficiency of phase change materials by mimicking leaf vein morphology. Appl. Energy 269, 114982 (2020)
[55] Luscher, D.J., McDowell, D.L., Bronkhorst, C.A.: A second gradient theoretical framework for hierarchical multiscale modeling of materials. Int. J. Plast. 26(8), 1248–1275 (2010)
[56] Makvandi, R., Reiher, J.C., Bertram, A., Juhre, D.: Isogeometric analysis of first and second strain gradient elasticity. Comput. Mech. 61(3), 351–363 (2018)
[57] Mandadapu, K.K., Abali, B.E., Papadopoulos, P.: On the polar nature and invariance properties of a thermomechanical theory for continuum-on-continuum homogenization. arXiv preprint arXiv:1808.02540 (2018)
[58] Mindlin, R.D.: Micro-structure in linear elasticity. Arch. Ration. Mech. Anal. 16(1), 51–78 (1964)
[59] Mindlin, R.D.: Second gradient of strain and surface-tension in linear elasticity. Int. J. Solids Struct. 1(4), 417–438 (1965)
[60] Misra, A., Lekszycki, T., Giorgio, I., Ganzosch, G., Müller, W.H., dell'Isola, F.: Pantographic metamaterials show atypical poynting effect reversal. Mech. Res. Commun. 89, 6–10 (2018)
[61] Müller, W.H.: The experimental evidence for higher gradient theories. In Mechanics of Strain Gradient Materials, pp. 1–18. Springer (2020)
[62] Müller, W.H., Rickert, W., Vilchevskaya, E.N.: Thence the moment of momentum. ZAMM - J. Appl. Math. Mech./Zeitschrift für Angewandte Mathematik und Mechanik 100(5), e202000117 (2020)
[63] Nazarenko, L., Glüge, R., Altenbach, H.: Positive definiteness in coupled strain gradient elasticity. Contin. Mech. Thermodyn. 1–13 (2020)
[64] Neff, P., Ghiba, I.-D., Madeo, A., Placidi, L., Rosi, G.: A unifying perspective: The relaxed linear micromorphic continuum. Contin. Mech. Thermodyn. 26(5), 639–681 (2014)
[65] Nejadsadeghi, N., De Angelo, M., Drobnicki, R., Lekszycki, T., dell'Isola, F., Misra, A.: Parametric experimentation on pantographic unit cells reveals local extremum configuration. Exp. Mech. 59(6), 927–939 (2019)
[66] Papanicolopulos, S.-A., Zervos, A., Vardoulakis, I.: A three-dimensional C1 finite element for gradient elasticity. Int. J. Numer. Methods Eng. 77(10), 1396–1415 (2009)
[67] Phunpeng, V., Baiz, P.: Mixed finite element formulations for strain-gradient elasticity problems using the FEniCS environment. Finite Elem. Anal. Des. 96, 23–40 (2015)
[68] Placidi, L.: A variational approach for a nonlinear one-dimensional damage-elasto-plastic second-gradient continuum model. Contin. Mech. Thermodyn. 28, 119–137 (2016)
[69] Placidi, L., Andreaus, U., Della Corte, A., Lekszycki, T.: Gedanken experiments for the determination of two-dimensional linear second gradient elasticity coefficients. Z. Angew. Math. Phys. 66(6), 3699–3725 (2015)
[70] Placidi, L., Andreaus, U., Giorgio, I.: Identification of two-dimensional pantographic structure via a linear D4 orthotropic second gradient elastic model. J. Eng. Math. 103(1), 1–21 (2017)
[71] Placidi, L., Barchiesi, E.: Energy approach to brittle fracture in strain-gradient modelling. Proc. R. Soc. Lond. A, Math. Phys. Eng. Sci. 474(2210), 20170878 (2018)
[72] Placidi, L., Barchiesi, E., Battista, A.: An inverse method to get further analytical solutions for a class of metamaterials aimed to validate numerical integrations. In: dell'Isola, F., Sofonea, M., Steigmann, D. (Eds) Mathematical Modelling in Solid Mechanics, volume 69 of Advanced Structured Materials, pp. 193–210. Springer Singapore (2017)
[73] Placidi, L., Barchiesi, E., Misra, A.: A strain gradient variational approach to damage: A comparison with damage gradient models and numerical results. Mathematics and Mechanics of Complex Systems 6(2), 77–100 (2018)
[74] Placidi, L., El Dhaba, A.R.: Semi-inverse method à la Saint-Venant for two-dimensional linear isotropic homogeneous second-gradient elasticity. Math. Mech. Solids 22(5), 919–937 (2017)
[75] Placidi, L., Rosi, G., Barchiesi, E.: Analytical solutions of 2-dimensional second gradient linear elasticity for continua with cubic D_4 microstructure. In: Abali, B., Altenbach, H., dell'Isola, F., Eremeyev, V., Öchsner, A. (Eds) New Achievements in Continuum Mechanics and Thermodynamics, volume 108 of Advanced Structured Materials, pp. 383–401. Springer, Cham (2019)

[76] Placidi, L., Rosi, G., Giorgio, I., Madeo, A.: Reflection and transmission of plane waves at surfaces carrying material properties and embedded in second-gradient materials. Math. Mech. Solids 19(5), 555–578 (2014)
[77] Reiher, J.C., Giorgio, I., Bertram, A.: Finite-element analysis of polyhedra under point and line forces in second-strain gradient elasticity. Journal of Engineering Mechanics 143(2), 04016112 (2017)
[78] Rinaldi, A., Placidi, L.: A microscale second gradient approximation of the damage parameter of quasi-brittle heterogeneous lattices. Z. Angew. Math. Mech. 94(10), 862–877 (2014)
[79] Roache, P.J.: Code verification by the method of manufactured solutions. J. Fluids Eng. 124(1), 4–10 (2002)
[80] Rosi, G., Auffray, N.: Anisotropic and dispersive wave propagation within strain-gradient framework. Wave Motion 63, 120–134 (2016)
[81] Rudraraju, S., Van der Ven, A., Garikipati, K.: Three-dimensional isogeometric solutions to general boundary value problems of Toupin's gradient elasticity theory at finite strains. Comput. Methods Appl. Mech. Eng. 278, 705–728 (2014)
[82] Schulte, J., Dittmann, M., Eugster, S., Hesch, S., Reinicke, T., dell'Isola, F., Hesch, C.: Isogeometric analysis of fiber reinforced composites using Kirchhoff–Love shell elements. Comput. Methods Appl. Mech. Eng. 362, 112845 (2020)
[83] Seppecher, P., Alibert, J.-J., dell'Isola, F.: Linear elastic trusses leading to continua with exotic mechanical interactions. Journal of Physics: Conference Series 319(1), 012018 (2011)
[84] Shekarchizadeh, N., Abali, B.E., Barchiesi, E., Bersani, A.M.: Inverse analysis of metamaterials and parameter determination by means of an automatized optimization problem. ZAMM - J. Appl. Math. Mech. / Zeitschrift für Angewandte Mathematik und Mechanik e202000277 (2021)
[85] Shu, J.Y., King, W.E., Fleck, N.A.: Finite elements for materials with strain gradient effects. Int. J. Numer. Methods Eng. 44(3), 373–391 (1999)
[86] Solyaev, Y., Lurie, S., Barchiesi, E., Placidi, L.: On the dependence of standard and gradient elastic material constants on a field of defects. Math. Mech. Solids 25(1), 35–45 (2020)
[87] Tran, C.A., Gołaszewski, M., Barchiesi, E.: Symmetric-in-plane compression of polyamide pantographic fabrics—modelling, experiments and numerical exploration. Symmetry 12(5), 693 (2020)
[88] Turco, E., Barchiesi, E.: Equilibrium paths of Hencky pantographic beams in a three-point bending problem. Mathematics and Mechanics of Complex Systems 7(4), 287–310 (2019)
[89] Turco, E., Barchiesi, E., Giorgio, I., dell'Isola, F.: A Lagrangian Hencky-type non-linear model suitable for metamaterials design of shearable and extensible slender deformable bodies alternative to Timoshenko theory. Int. J. Non-Linear Mech. 123, 103481 (2020)
[90] Yang, H., Abali, B.E., Timofeev, D., Müller, W.H.: Determination of metamaterial parameters by means of a homogenization approach based on asymptotic analysis. Contin. Mech. Thermodyn. 1–20 (2019)
[91] Yang, H., Müller, W.H.: Size effects of mechanical metamaterials: A computational study based on a second order asymptotic homogenization method. Arch. Appl. Mech. (2020)
[92] Yang, H., Timofeev, D., Giorgio, I., Müller, W.H.: Effective strain gradient continuum model of metamaterials and size effects analysis. Contin. Mech. Thermodyn. 1–23 (2020)
[93] Yang, Y., Ching, W.Y., Misra, A.: Higher-order continuum theory applied to fracture simulation of nano-scale intergranular glassy film. Journal of Nanomechanics and Micromechanics 1(2), 60–71 (2011)
[94] Yildizdag, M.E., Barchiesi, E., dell'Isola, F.: Three-point bending test of pantographic blocks: Numerical and experimental investigation. Math. Mech. Solids 1081286520916911 (2020)
[95] Zervos, A., Papanicolopulos, S.A., Vardoulakis, I.: Two finite-element discretizations for gradient elasticity. Journal of Engineering Mechanics 135(3), 203–213 (2009)

How to cite this article: Yang, H., Timofeev, D., Abali, B.E., Li, B., Müller, W.H. Verification of strain gradient elasticity computation by analytical solutions. Z Angew Math Mech. 2021; e202100023.
https://doi.org/10.1002/zamm.202100023

APPENDIX

A.1 | The weak form and its numerical implementation

According to Equations (4), (5), (16), and (17), the weak form is shown as

$$\int_\Omega \left(\sigma_{ij}\delta u_{i,j} + \tau_{ijk}\delta u_{i,jk}\right) \mathrm{d}V = \int_\Omega b_i \delta u_i \,\mathrm{d}V + \int_{\partial\Omega} t_i \delta u_i \,\mathrm{d}A + \int_{\partial\Omega} r_i D(\delta u_i)\,\mathrm{d}A + \sum_m \oint_{\partial\partial\Omega_m} f_i \delta u_i \,\mathrm{d}l, \tag{A.1}$$

where $r_i D(\delta u_i)$ is equal to $r_i n_j \frac{\partial \delta u_i}{\partial X_j}$, and n_j is the unit surface normal vector. For example, the n_j of the right surface in Figure 1(b) is equal to δ_{1j}.

In this work, the wedge forces are constants and uniformly distributed on each edge with the unit of N/m. The total force acting on each edge is equal to $f_i l$ in N. l in m is equal to the length of the corresponding edge. For example, in Section 4.2, the wedge forces on edge 2 is f_1. The total force acting on edge 2 is $f_1 l$. Instead of implementing the wedge forces directly, a traction with the amplitude of $\frac{f_1}{2l_m}$ in Pa is applied on a small region (area of the region is $2l_m l$) near edge 2 as shown in Figure A.1.

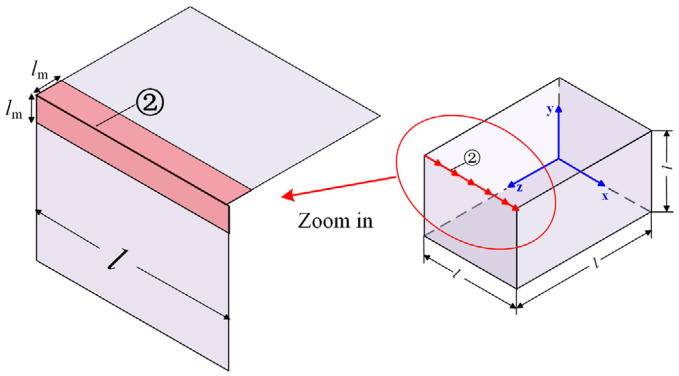

FIGURE A.1 The implementation of a wedge force on edge 2

For a detailed introduction of IGA we refer to [46]. In tIGAr, a self-contained implementation of single-patch explicit B-splines is realized by using a module called tIGAr.BSplines [50]. In this work, polynomial degree of the basis function has been chosen as 2 in order to acquire C^1-continuity for the formulation [39,81].

A.2 | The derivation of Equation (6)

The derivation of Equation (6) is shown here. Equation (6) reads

$$\int_\Omega \left(\frac{\partial w}{\partial u_{i,j}}\delta u_{i,j} + \frac{\partial w}{\partial u_{i,jk}}\delta u_{i,jk}\right) \mathrm{d}V = \int_\Omega \left(-\frac{\partial w}{\partial u_{i,j}} + \left(\frac{\partial w}{\partial u_{i,jk}}\right)_{,k}\right)_{,j} \delta u_i \,\mathrm{d}V + \int_{\partial\Omega} n_j \left(\frac{\partial w}{\partial u_{i,j}} - \left(\frac{\partial w}{\partial u_{i,jk}}\right)_{,k}\right)\delta u_i \,\mathrm{d}A + \int_{\partial\Omega} n_k \frac{\partial w}{\partial u_{i,jk}}\delta u_{i,j} \,\mathrm{d}A. \tag{A.2}$$

By using the divergence theorem, we can show that

$$\int_\Omega \left(\frac{\partial w}{\partial u_{i,j}}\delta u_i\right)_{,j} \mathrm{d}V = \int_{\partial\Omega} n_j \left(\frac{\partial w}{\partial u_{i,j}}\delta u_i\right) \mathrm{d}A. \tag{A.3}$$

With the help of the product rule we have

$$\int_\Omega \left(\frac{\partial w}{\partial u_{i,j}}\delta u_i\right)_{,j} \mathrm{d}V = \int_\Omega \left(\frac{\partial w}{\partial u_{i,j}}\right)_{,j} \delta u_i \,\mathrm{d}V + \int_\Omega \frac{\partial w}{\partial u_{i,j}}\delta u_{i,j} \,\mathrm{d}V. \tag{A.4}$$

Therefore, the first term in the left hand side in in Equation (6) is rewritten as

$$\int_\Omega \frac{\partial w}{\partial u_{i,j}}\delta u_{i,j} \,\mathrm{d}V = -\int_\Omega \left(\frac{\partial w}{\partial u_{i,j}}\right)_{,j} \delta u_i \,\mathrm{d}V + \int_{\partial\Omega} n_j \left(\frac{\partial w}{\partial u_{i,j}}\delta u_i\right) \mathrm{d}A. \tag{A.5}$$

Likewise, from the divergence theorem, we can show that

$$\int_\Omega \left(\frac{\partial w}{\partial u_{i,jk}}\delta u_{i,j}\right)_{,k} \mathrm{d}V = \int_{\partial\Omega} n_k \left(\frac{\partial w}{\partial u_{i,jk}}\delta u_{i,j}\right) \mathrm{d}A. \tag{A.6}$$

By using the product rule, we have

$$\int_\Omega \left(\frac{\partial w}{\partial u_{i,jk}}\delta u_{i,j}\right)_{,k} \mathrm{d}V = \int_\Omega \left(\frac{\partial w}{\partial u_{i,jk}}\right)_{,k} \delta u_{i,j}\,\mathrm{d}V + \int_\Omega \left(\frac{\partial w}{\partial u_{i,jk}}\right)\delta u_{i,jk}\,\mathrm{d}V. \tag{A.7}$$

Therefore, the second term in the left hand side in Equation (6) is rewritten as

$$\int_\Omega \left(\frac{\partial w}{\partial u_{i,jk}}\right)\delta u_{i,jk}\,\mathrm{d}V = \int_{\partial\Omega} n_k\left(\frac{\partial w}{\partial u_{i,jk}}\delta u_{i,j}\right)\mathrm{d}A - \int_\Omega \left(\frac{\partial w}{\partial u_{i,jk}}\right)_{,k}\delta u_{i,j}\,\mathrm{d}V \tag{A.8}$$

By using the divergence theorem and the product rule again,

$$\int_\Omega \left(\left(\frac{\partial w}{\partial u_{i,jk}}\right)_{,k}\delta u_i\right)_{,j} \mathrm{d}V = \int_{\partial\Omega} n_j\left(\left(\frac{\partial w}{\partial u_{i,jk}}\right)_{,k}\delta u_i\right)\mathrm{d}A, \tag{A.9}$$

$$\int_\Omega \left(\left(\frac{\partial w}{\partial u_{i,jk}}\right)_{,k}\delta u_i\right)_{,j} \mathrm{d}V = \int_\Omega \left(\left(\frac{\partial w}{\partial u_{i,jk}}\right)_{,k}\right)_{,j}\delta u_i\,\mathrm{d}V + \int_\Omega \left(\frac{\partial w}{\partial u_{i,jk}}\right)_{,k}\delta u_{i,j}\,\mathrm{d}V. \tag{A.10}$$

Therefore,

$$\int_\Omega \left(\frac{\partial w}{\partial u_{i,jk}}\right)_{,k}\delta u_{i,j}\,\mathrm{d}V = \int_{\partial\Omega} n_j\left(\left(\frac{\partial w}{\partial u_{i,jk}}\right)_{,k}\delta u_i\right)\mathrm{d}A - \int_\Omega \left(\left(\frac{\partial w}{\partial u_{i,jk}}\right)_{,k}\right)_{,j}\delta u_i\,\mathrm{d}V. \tag{A.11}$$

Consequently,

$$\int_\Omega \left(\frac{\partial w}{\partial u_{i,jk}}\right)\delta u_{i,jk}\,\mathrm{d}V = \int_{\partial\Omega} n_k\left(\frac{\partial w}{\partial u_{i,jk}}\delta u_{i,j}\right)\mathrm{d}A - \int_{\partial\Omega} n_j\left(\left(\frac{\partial w}{\partial u_{i,jk}}\right)_{,k}\delta u_i\right)\mathrm{d}A + \int_\Omega \left(\left(\frac{\partial w}{\partial u_{i,jk}}\right)_{,k}\right)_{,j}\delta u_i\,\mathrm{d}V \tag{A.12}$$

Therefore, we have

$$\begin{aligned}\int_\Omega \left(\frac{\partial w}{\partial u_{i,j}}\delta u_{i,j} + \frac{\partial w}{\partial u_{i,jk}}\delta u_{i,jk}\right)\mathrm{d}V = &\int_\Omega \left(-\frac{\partial w}{\partial u_{i,j}} + \left(\frac{\partial w}{\partial u_{i,jk}}\right)_{,k}\right)_{,j}\delta u_i\,\mathrm{d}V \\ &+ \int_{\partial\Omega} n_j\left(\frac{\partial w}{\partial u_{i,j}} - \left(\frac{\partial w}{\partial u_{i,jk}}\right)_{,k}\right)\delta u_i\,\mathrm{d}A + \int_{\partial\Omega} n_k\frac{\partial w}{\partial u_{i,jk}}\delta u_{i,j}\,\mathrm{d}A.\end{aligned} \tag{A.13}$$

A.3 | Components of stress, hyperstress, and balance equations

The expressions for stress component in terms of displacement is explicitly given by

$$\sigma_{11} = c_1(\varepsilon_{11} + \varepsilon_{22} + \varepsilon_{33}) + 2c_2\varepsilon_{11} = c_1(u_{1,1} + u_{2,2} + u_{3,3}) + 2c_2u_{1,1}, \tag{A.14}$$

and for hyperstress components

$$\begin{aligned}\tau_{111} = &c_3(4u_{1,11} + u_{1,22} + 3u_{2,12} + u_{1,33} + 3u_{3,13}) + c_4(u_{1,11} + u_{2,21} + u_{3,31}) \\ &+ c_5(4u_{1,11} + 2u_{1,22} + 2u_{2,12} + 2u_{1,33} + 2u_{3,13}) + 2c_6u_{1,11} + 4c_7u_{1,11}.\end{aligned} \tag{A.15}$$

The other components can be calculated in the same manner. Equation (19) together with Equations (23)–(24) gives us the system of partial differential equations. For example, the balance equation in X_1 direction is

$$\begin{aligned}(c_1+2c_2)u_{1,11}+(c_1+c_2)(u_{2,21}+u_{3,31})+c_2(u_{1,22}+u_{1,33})&=(3c_3+c_4+4c_5+2c_6+2c_7)\\ \times(u_{1,1111}+u_{2,2111}+u_{3,3111}+u_{1,1122}+u_{2,2122}+u_{3,3122}+u_{1,1133}+u_{3,3133}+u_{2,2133})&\\ +(c_3+2c_7)(u_{1,1111}+2u_{1,1122}+2u_{1,1133}+u_{1,2222}+2u_{1,2323}+u_{1,3333})-b_1.&\end{aligned} \tag{A.16}$$

Determination of Metamaterial Parameters by Means of a Homogenization Approach Based on Asymptotic Analysis

Hua Yang [a], B. Emek Abali [a], Dmitry Timofeev [*b] and Wolfgang H. Müller[a]

[a] *Technische Universität Berlin , Berlin (Germany)*
[b] *Università degli Studi dell'Aquila, L'Aquila (Italy)*

Abstract

By using modern additive manufacturing techniques a structure at the millimeter length scale (macroscale) can be produced showing a lattice substructure of micrometer dimensions (microscale). Such a system is called a metamaterial at the macroscale, because its mechanical characteristics deviate from the characteristics at the microscale. Cosnequently, a metamaterial is modeled by using additional parameters. These we intend to determine. A homogenization approach based on asymptotic analysis establishes a connection between these different characteristics at micro- and macroscales. A linear elastic first order theory at the microscale is related to a linear elastic second order theory at the macroscale. Small strains (and, correspondingly, small gradients) are assumed at both scales. A relation for the parameters at the macroscale is derived by using the equivalence of energy at macro- and microscales within a so-called Representative Volume Element (RVE). The determination of the parameters becomes possible by solving a boundary value problem within the framework of the Finite Element Method (FEM). The proposed approach guarantees that the additional parameters vanish if the material is purely homogeneous, in other words, it is fully compatible with conventional homogenization schemes based on spatial averaging techniques. Moreover, the proposed approach is reliable, because it ensures that the obtained additional parameters are insensitive to choices of the RVE consisting of a repetition of smaller RVEs depending upon the intrinsic size of the structure.

Keywords: Metamaterial, Homogenization, Strain gradient theory, Elasticity, Asymptotic analysis

1 Introduction

Periodic lattice type structures involving large number of repetitive substructures continue to attract the interest of many researchers because of their fascinating properties, such as relatively low manufacturing costs, high specific stiffness, etc. [46, 47, 19, 64, 48, 67]. The mechanical response of such a structure depends not only on the material, but also on the morphology of its substructure [63, 62]. Hence, an appropriate "metamaterial description" must be used for mimicking the dependence on its substructure.

In order to design and fabricate metamaterials for engineering applications, an accurate and efficient prediction of their mechanical performances is important [94, 28, 32, 98, 51]. Indeed, standard numerical techniques, such as the Finite Element Method (FEM), can be used for modeling a structure including every detail of its subunits [100, 101]. However, this requires the mesh size to be at least one order smaller than the geometric size of the substructure leading to very high computational costs. Hence, homogenization techniques are developed to upscale the mechanical response at the microscale—the presence of the substructure leads to a composite material, which can be seen as a heterogeneous material—to the macroscale by defining an appropriate constitutive equation. Especially in composite materials, with fibers embedded in a matrix building a periodic substructure, micro- and macroscale behaviors are modeled by the same linear elastic model, also a.k.a. Cauchy continuum. The homogenization of such periodic structures toward an equivalent Cauchy continuum has been investigated thoroughly [45, 57, 20, 72, 102, 68].

*Corresponding author: dima_timofeev@mail.ru

Many approaches in the literature assume that there exists a Representative Volume Element (RVE) with periodic boundary conditions that precisely captures the deformation behavior of the whole geometry. Such an approach utilizes the energy equivalence of the RVE at both macroscale and microscale, and it was also used in [52]. The effective properties of such homogenized continua is in good agreement with experiments [93] under the condition that $L \gg l$, where L represents the macroscopic length scale, *i.e.*, (mean value of) the geometric dimensions of the whole structure, and l represents the length scale of the microscale, namely, the geometric dimensions of the substructure. The quantity l will be used as the "length scale" of a basic cell of the structure, as indicated in Fig. 1. Note that the concept of a basic cell is different from that of an RVE. It is evident that a basic cell can be regarded as an RVE, and stacking or gathering several basic cells can construct an RVE as well. Classical homogenization encounters limitations [60, 10] when L is of a comparable order with respect to l.

Size effects fail to be captured by a standard homogenization having the same order theory at both scales. A feasible approach is to use a first order theory at the microscale and a second order one at the macroscale. This leads to additional parameters at the macroscale, which need to be determined. We refer to various formulations of a second order theory in [66, 95, 6, 2, 3, 33, 37, 86, 84, 81, 91, 8, 80, 83, 87, 7, 1, 70]. Higher order approaches are also referred to as *generalized continuum theories* and homogenization within that framework is a challenging task pursued by many scientists, among others by [40, 76, 49, 31, 85, 56, 17]. In most cases it is agreed that homogenization of an RVE by involving so-called higher gradient terms of the macroscopic field is a natural way to include a size effect [14, 60, 41, 44, 43, 42]. By using gamma-convergence homogenization results have been obtained in [5, 75, 4]. A remarkable class of structures described at the macroscale by using a second gradient elasticity theory are pantographic objects [18, 92, 89]. They have received a notable follow-up in the literature [30, 34, 82, 99, 97, 69], also from a mathematically rigorous standpoint regarding fundamental issues, such as well-posedness [36].

A possibly promising homogenization technique is asymptotic analysis, which has been used to obtain homogenized material parameters in [90]. This method decomposes the variables into their global variations and into local fluctuations. Such a decomposition was used to generate closed form equations to determine constitutive parameters in one-dimensional problems, for example in the analysis of composites [22, 16], while 2D problems [13, 15, 23, 78, 29] have been investigated numerically. FEM was applied in [73] demonstrating that higher-order terms start dominating when the difference between the parameters of the composite materials increases. A second-order asymptotic and computational homogenization technique is proposed by [13]. Here the boundary value problems generated by the asymptotic homogenization was solved with a quadratic ansatz. However, there are still two main issues that are not well addressed when trying to homogenize structures in the framework of generalized mechanics [96]:

- The first one concerns compatibility, in the sense that parameters of the strain gradient stiffness tensor should vanish when the structure is purely homogeneous.
- The second one concerns reliability, such that the strain gradient stiffness tensor has to be insensitive to a repetition of the basic cell.

A successful attempt is made in [59, 60] establishing a connection between microscale parameters and macroscale parameters (by using the strain gradient theory). A "correction" term was proposed, such that the strain gradient stiffness tensor satisfied compatibility and reliability requirements. Different numerical solution methods are used for this approach: Fast Fourier Technique (FFT) is employed in [61] and FEM was used in [15]. We follow their methodology and propose an alternative derivation for this "correction" term in Section 3 in a somewhat pedagogical manner. Furthermore, we apply and validate the method for simple yet general 2D metamaterials in Sections 4 and 5 by using FEM. In order to demonstrate its versatility, computations of the square lattice are performed in Section 6. The computations are performed with the aid of open-source codes developed by the FEniCS project [2]. The proposed method delivers all metamaterial parameters in 2D by using a linear elastic material model at the microscale after a computational procedure as investigated in what follows.

2 A preliminary remark on objective strain energy densities

The following analysis at the macro- and at the microscale is heavily based on expressions for the strain energy densities. In fact, in the end these will be formulated in terms of derivatives of the displacement, which puts the objectivity of these expressions at stake and makes us wonder what the limits of application of the proposed approach are. Let it be said here and now: The proposed approach holds for small deformations on the micro- as well as on the macroscale. However, the aforementioned pantographic structures can undergo large reversible deformations. It was also for this reason that the authors of [33], who are protagonists of this class of

metamaterials, decided to formulate the strain energy density such that it is ready for a mathematical treatment of isotropic second order gradient elastic materials at large deformations. We will use their results and specialize them to our case of interest, which is expressions for the strain energy density of a Cauchy material on the microscale and of a second order material on the macroscale subjected to small deformations. In this context the interested reader is also referred to Chapter 3 of [21], where the case of third order elastic continua for large deformations is examined.

In [33] the strain energy density is first expressed in terms of the deformation gradient and its gradient, $F_{\alpha i}$ and $F_{\alpha i,j}$, respectively. Following [33] we use small Latin indices to indicate Cartesian coordinates of the reference placement, $\boldsymbol{X}$. Later on we will depart from this nomenclature and also use a similar symbol for centers of mass. If required, Greek indices are used to characterize the current configuration. The principles of rational mechanics are now applied to arrive at the following (objective) form for the strain energy density:

$$w = \tfrac{1}{2}\left(E_{ij}C_{ijkl}E_{kl} + 2E_{ij}H_{ijklm}E_{kl,m} + E_{ij,k}D_{ijklmn}E_{lm,n}\right). \tag{1}$$

The (constant) stiffness tensors $\boldsymbol{C}$, $\boldsymbol{H}$, $\boldsymbol{D}$ are of forth, fifth, and sixth rank, respectively. They observe certain symmetry properties, which follow from the semi-positiveness of the strain energy density and from the symmetries of the Green-Lagrange tensor $\boldsymbol{E} = \frac{1}{2}\left(\boldsymbol{F}^{\top}\cdot\boldsymbol{F} - \mathbf{I}\right)$ and its derivative w.r.t. to the reference placement:

$$\begin{aligned} &C_{ijkl} = C_{jikl} = C_{ijlk} = C_{klij}\ , \quad H_{ijklm} = H_{jiklm} = H_{ijkml} = H_{lmijk} \\ &D_{ijklmn} = D_{jiklmn} = D_{ijkmln} = D_{lmnijk}. \end{aligned} \tag{2}$$

If the material is centrosymmetric then $\boldsymbol{H}$ vanishes and $\boldsymbol{C}$ and $\boldsymbol{D}$ can be expressed by sums of products of two and three unit tensors of second rank, respectively. This way $\boldsymbol{C}$ is reduced to two stiffness parameters (the two Lamé coefficients) and $\boldsymbol{D}$ to five:

$$\begin{aligned} C_{ijkl} &= \lambda\delta_{ij}\delta_{kl} + \mu\left(\delta_{ik}\delta_{jl} + \delta_{il}\delta_{jk}\right)\ , \quad H_{ijklp} = 0\ , \\ D_{ijklpq} &= c_1\left(\delta_{ij}\delta_{kl}\delta_{pq} + \delta_{ij}\delta_{kp}\delta_{lq} + \delta_{ik}\delta_{jq}\delta_{lp} + \delta_{iq}\delta_{jk}\delta_{lp}\right) + \\ &\quad c_2\delta_{ij}\delta_{kq}\delta_{lp} + c_3\left(\delta_{ij}\delta_{jl}\delta_{pq} + \delta_{ik}\delta_{jp}\delta_{lq} + \right. \\ &\quad\quad \left. \delta_{ik}\delta_{jq}\delta_{lp} + \delta_{il}\delta_{jk}\delta_{lp} + \delta_{ip}\delta_{jk}\delta_{lq}\right) + \\ &\quad c_4\left(\delta_{il}\delta_{jp}\delta_{kq} + \delta_{ip}\delta_{jl}\delta_{kq}\right) + \\ &\quad c_5\left(\delta_{il}\delta_{jq}\delta_{kp} + \delta_{ip}\delta_{jq}\delta_{kl} + \delta_{iq}\delta_{jl}\delta_{kp} + \delta_{iq}\delta_{jp}\delta_{kl}\right). \end{aligned} \tag{3}$$

It should be noted that in this form Eqns. (1) and (3) are the extension to what is known as the St. Venant-Kirchhoff generalization of Hooke's law for small strain linear elasticity to large strains, where the gradient of the Green-Lagrange tensor is not present ([53], pg. 250).

Recall that the Green-Lagrange tensor can be written in terms of displacement derivatives as follows:

$$E_{ij} = \tfrac{1}{2}\left(u_{i,j} + u_{j,i} + u_{k,i}u_{k,j}\right). \tag{4}$$

Consequently its derivative reads:

$$E_{ij,k} = \tfrac{1}{2}\left(u_{i,jk} + u_{j,ik} + u_{l,ik}u_{l,j} + u_{l,i}u_{l,jk}\right). \tag{5}$$

We define small strain second gradient theory such that we neglect all products of displacement derivatives and if no distinction needs to be made between current and reference placement. Then for an centrosymmetric material we arrive at:

$$w = \tfrac{1}{2}\left(C_{ijkl}u_{i,j}u_{k,l} + D_{ijklmn}u_{i,jk}u_{l,mn}\right). \tag{6}$$

By right, following [33], all indices should be in Greek letters, since it is the current configuration which is meant in the linear theory, but for convenience we refrain from doing so. Of course, if the classical Cauchy continuum of linear elasticity with small strains is concerned the second part in Eqn. (6) must be omitted. It should also be mentioned that this result is in agreement with Eqn. (16) of [65], if third order gradients in displacement are neglected, and Eqn. (19) of [58], where it is attempted to determine the seven stiffness coefficients experimentally. It should be pointed out that these authors do not address the issue of objectiveness of the strain energy and the small strain approximation, most likely because they were educated in the spirit of classical Hookean elasticity.

In order to formulate boundary value problems for the displacement and their gradients, equations of motions are required. They follow from the balance of momentum which will be reduced to the static case. Hence we need an expression for the stress tensor in terms of displacement gradients. The general theory for stresses and

the equations of motion of higher order gradient continua undergoing large deformations is outlined in [21], Chapters 1 and 2. We do not need such generality in the sequel. Hence we follow the way indicated in [65] and calculate hyperstresses of second and third rank, where according to Castigliano's principle, where the strain energy density (6) can be used as their potential:

$$\overset{(2)}{\sigma}_{ij} = \frac{\partial w}{\partial u_{i,j}} \ , \quad \overset{(3)}{\sigma}_{ijk} = \frac{\partial w}{\partial u_{ij,k}}. \tag{7}$$

Note that in the case of the traditional Cauchy continuum the hyperstress of second rank, $\overset{(2)}{\boldsymbol{\sigma}}$, becomes the ordinary Cauchy stress and the hyperstress of third rank, $\overset{(3)}{\boldsymbol{\sigma}}$, vanishes. The corresponding balance of momentum reads in the static case:

$$\overset{(2)}{\sigma}_{ij,j} - \overset{(3)}{\sigma}_{ijk,jk} + f_i = 0, \tag{8}$$

where f_i indicate the body forces.

3 Connection of micro- and macroscale parameters

Consider a continuum body occupying a domain Ω in two-dimensional space, $\Omega \in \mathbb{R}^2$. The metamaterial is embodied in an RVE, Ω^P, where periodically aligned RVEs constitute metamaterial domains,

$$\cup\, \Omega^P = \Omega \ , \quad \Omega^P \cap \Omega^Q = \emptyset \ , \qquad P, Q = 1, 2, 3, ...M, P \neq Q \ . \tag{9}$$

The RVE at the microscale represents the detailed substructure, such as the fibers and the matrix in a composite material. The same RVE at the macroscale is modeled as a homogeneous metamaterial. We assume that the corresponding stored energies are equal although the definitions at both scales differ. We use a first order theory for defining the volumetric energy (volume) density of an RVE at the microscale 'm,' and a second order theory at the macroscale, 'M,' for the energy density, *i.e.*, w^{m}, and w^{M}, respectively:

$$\begin{aligned} \int_{\Omega^P} w^{\mathrm{m}} \,\mathrm{d}V &= \int_{\Omega^P} w^{\mathrm{M}} \,\mathrm{d}V \ , \\ \int_{\Omega^P} \frac{1}{2} C^{\mathrm{m}}_{ijkl} u^{\mathrm{m}}_{i,j} u^{\mathrm{m}}_{k,l} \,\mathrm{d}V &= \int_{\Omega^P} \frac{1}{2} \left(C^{\mathrm{M}}_{ijkl} u^{\mathrm{M}}_{i,j} u^{\mathrm{M}}_{k,l} + D^{\mathrm{M}}_{ijklmn} u^{\mathrm{M}}_{i,jk} u^{\mathrm{M}}_{l,mn} \right) \mathrm{d}V \ . \end{aligned} \tag{10}$$

Note that all fields are expressed in Cartesian coordinates. The microscale stiffness tensor, C^{m}_{ijkl}, is a function in space. Consider a lattice substructure. Even if the trusses are made of a homogeneous material, the voids between the trusses generate a heterogeneous substructure at the microscale, such that the microscale stiffness tensor depends on space coordinates and possesses either the value of the truss material or is equal to zero due to the voids. In contrast to that, the macrocale material tensors, C^{M}_{ijkl} and D^{M}_{ijklmn}, are constant in space, because they are generated by the homogenization procedure to be explained in the following. The continuum body at the reference frame has particles at coordinates X_i, where they move to x_i under a mechanical loading. The displacement is the deviation from the reference frame and we emphasize that the microscale displacement, u^{m}_i, is different than the macroscale displacement, u^{M}_i,

$$\begin{aligned} u^{\mathrm{m}}_i &= x^{\mathrm{m}}_i - X_i \ , \\ u^{\mathrm{M}}_i &= x^{\mathrm{M}}_i - X_i \ , \end{aligned} \tag{11}$$

because the current positions of particles differ. This difference between x^{m}_i and x^{M}_i is illustrated in Fig. 1. For demonstrating the microscale deformation, the substructure is visualized as well. For simplicity, a well-known example is used, namely, composite materials with the red inclusion (fibers) embedded in the blue material (matrix). For the homogenized case, the same particle moves to x^{M}_i expressed at the macroscale without the substructure. We emphasize that micro- and macroscales are both expressed in the same coordinate system. Two different cases are examined, a heterogeneous one on the microscale with known material properties versus a homogeneous one on the macroscale with sought parameters. In order to identify the material parameters, strain energy expressions for macro- and microscales are derived in what follows.

3.1 The macroscale energy for an RVE

Consider the macroscale case for an RVE, Ω^P. As customary in spatial averaging, we define the geometric center $\overset{\mathrm{c}}{\boldsymbol{X}}$ of the RVE,

$$\overset{\mathrm{c}}{\boldsymbol{X}} = \frac{1}{V} \int_{\Omega} \boldsymbol{X} \,\mathrm{d}V \ , \tag{12}$$

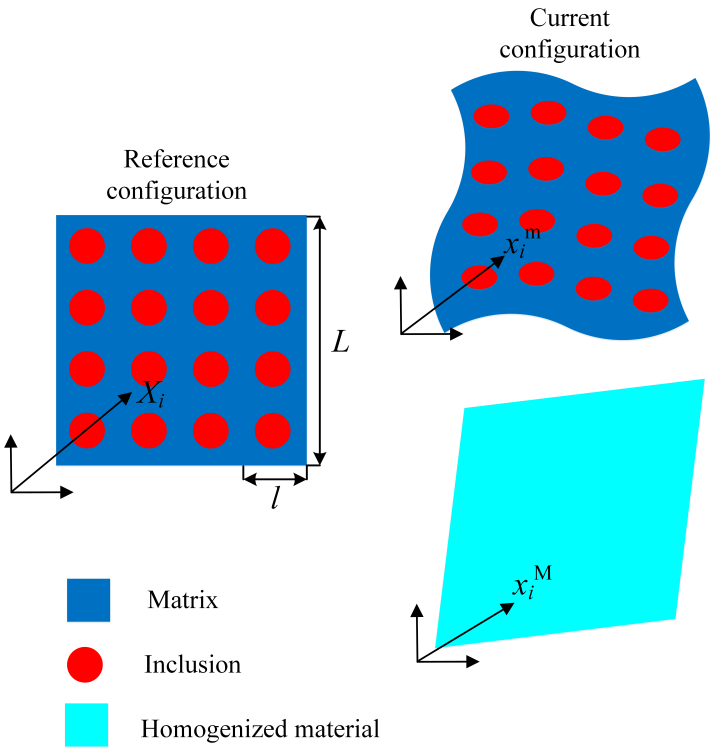

Figure 1: Left: Continuum body in the reference frame. Right top: Deformation at the microscale. Right bottom: Corresponding deformation at the macroscale.

approximate the macroscale displacement by a TAYLOR expansion around the value at the geometric center by truncating after quadratic terms (in order to account for the strain gradient effect), and calculate displacement gradients of this approximation

$$\begin{aligned} u_i^{\mathrm{M}}(\boldsymbol{X}) &= u_i^{\mathrm{M}}\Big|_{\overset{\mathrm{c}}{\boldsymbol{X}}} + u_{i,j}^{\mathrm{M}}\Big|_{\overset{\mathrm{c}}{\boldsymbol{X}}}(X_j - \overset{\mathrm{c}}{X}_j) + \frac{1}{2}u_{i,jk}^{\mathrm{M}}\Big|_{\overset{\mathrm{c}}{\boldsymbol{X}}}(X_j - \overset{\mathrm{c}}{X}_j)(X_k - \overset{\mathrm{c}}{X}_k) \ , \\ u_{i,l}^{\mathrm{M}}(\boldsymbol{X}) &= u_{i,j}^{\mathrm{M}}\Big|_{\overset{\mathrm{c}}{\boldsymbol{X}}}\delta_{jl} + \frac{1}{2}u_{i,jk}^{\mathrm{M}}\Big|_{\overset{\mathrm{c}}{\boldsymbol{X}}}(\delta_{jl}(X_k - \overset{\mathrm{c}}{X}_k) + (X_j - \overset{\mathrm{c}}{X}_j)\delta_{kl}) \ , \\ &= u_{i,l}^{\mathrm{M}}\Big|_{\overset{\mathrm{c}}{\boldsymbol{X}}} + u_{i,lk}^{\mathrm{M}}\Big|_{\overset{\mathrm{c}}{\boldsymbol{X}}}(X_k - \overset{\mathrm{c}}{X}_k) \ , \\ u_{i,lm}^{\mathrm{M}}(\boldsymbol{X}) &= u_{i,lk}^{\mathrm{M}}\Big|_{\overset{\mathrm{c}}{\boldsymbol{X}}}\delta_{km} = u_{i,lm}^{\mathrm{M}}\Big|_{\overset{\mathrm{c}}{\boldsymbol{X}}} \ . \end{aligned} \tag{13}$$

According to Eqn. (13), spatial averaging the gradient terms of the displacement field leads to

$$\begin{aligned} \langle u_{i,j}^{\mathrm{M}}\rangle &= \frac{1}{V}\int_{\Omega^P} u_{i,j}^{\mathrm{M}}\,\mathrm{d}V = u_{i,j}^{\mathrm{M}}\Big|_{\overset{\mathrm{c}}{\boldsymbol{X}}} + u_{i,jk}^{\mathrm{M}}\Big|_{\overset{\mathrm{c}}{\boldsymbol{X}}}\bar{I}_k \ , \quad \bar{I}_k = \frac{1}{V}\int_{\Omega^P}(X_k - \overset{\mathrm{c}}{X}_k)\,\mathrm{d}V \ , \\ \langle u_{i,jk}^{\mathrm{M}}\rangle &= \frac{1}{V}\int_{\Omega^P} u_{i,jk}^{\mathrm{M}}\,\mathrm{d}V = u_{i,jk}^{\mathrm{M}}\Big|_{\overset{\mathrm{c}}{\boldsymbol{X}}} \ . \end{aligned} \tag{14}$$

Since we require $\bar{I}_k = 0$ from Eqn. (12),

$$\langle u_{i,j}^{\mathrm{M}}\rangle = u_{i,j}^{\mathrm{M}}\Big|_{\overset{\mathrm{c}}{\boldsymbol{X}}} \ , \quad \langle u_{i,jk}^{\mathrm{M}}\rangle = u_{i,jk}^{\mathrm{M}}\Big|_{\overset{\mathrm{c}}{\boldsymbol{X}}} \ . \tag{15}$$

After inserting Eqn. (15) into Eqn. (13), we obtain

$$\begin{aligned} u_i^{\mathrm{M}}(\boldsymbol{X}) &= u_i^{\mathrm{M}}\Big|_{\overset{\mathrm{c}}{\boldsymbol{X}}} + \langle u_{i,j}^{\mathrm{M}}\rangle(X_j - \overset{\mathrm{c}}{X}_j) + \frac{1}{2}\langle u_{i,jk}^{\mathrm{M}}\rangle(X_j - \overset{\mathrm{c}}{X}_j)(X_k - \overset{\mathrm{c}}{X}_k) \ , \\ u_{i,j}^{\mathrm{M}}(\boldsymbol{X}) &= \langle u_{i,j}^{\mathrm{M}}\rangle + \langle u_{i,jk}^{\mathrm{M}}\rangle(X_k - \overset{\mathrm{c}}{X}_k) \ , \\ u_{i,jk}^{\mathrm{M}}(\boldsymbol{X}) &= \langle u_{i,jk}^{\mathrm{M}}\rangle \ . \end{aligned} \tag{16}$$

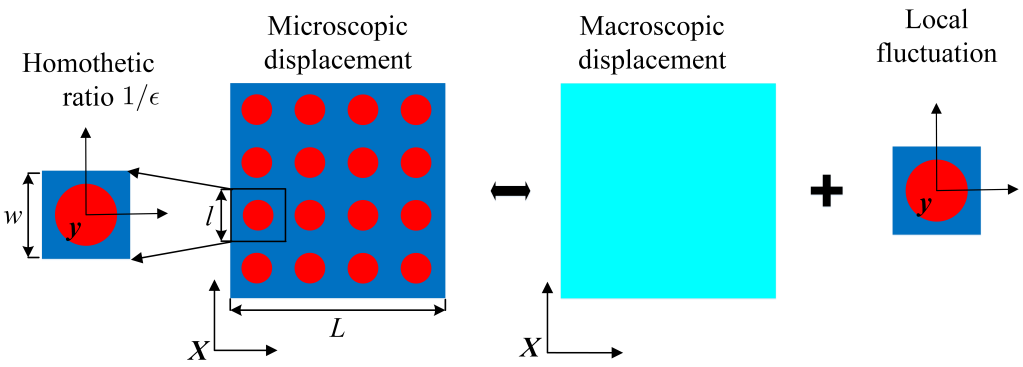

Figure 2: Illustration of the approximation of the asymptotic expansion.

Now, by using the last relation in Eqn. (16) on the right-hand side of Eqn. (10), the macroscale energy of an RVE reads as follows, because the macroscale stiffness tensors are constant in space,

$$\begin{aligned}
&\int_{\Omega^P} \frac{1}{2}\left(C^{\mathrm{M}}_{ijlm} u^{\mathrm{M}}_{i,j} u^{\mathrm{M}}_{l,m} + D^{\mathrm{M}}_{ijklmn} u^{\mathrm{M}}_{i,jk} u^{\mathrm{M}}_{l,mn}\right) \mathrm{d}V = \frac{1}{2} C^{\mathrm{M}}_{ijlm} \int_{\Omega^P} u^{\mathrm{M}}_{i,j} u^{\mathrm{M}}_{l,m} \,\mathrm{d}V + \\
&\frac{1}{2} D^{\mathrm{M}}_{ijklmn} \int_{\Omega^P} u^{\mathrm{M}}_{i,jk} u^{\mathrm{M}}_{l,mn} \,\mathrm{d}V = \frac{1}{2} C^{\mathrm{M}}_{ijlm} \int_{\Omega^P} \left(\langle u^{\mathrm{M}}_{i,j}\rangle + \langle u^{\mathrm{M}}_{i,jk}\rangle (X_k - \overset{\mathrm{c}}{X}_k)\right) \times \\
&\times \left(\langle u^{\mathrm{M}}_{l,m}\rangle + \langle u^{\mathrm{M}}_{l,mn}\rangle (X_n - \overset{\mathrm{c}}{X}_n)\right) \mathrm{d}V + \frac{1}{2} D^{\mathrm{M}}_{ijklmn} \int_{\Omega^P} \langle u^{\mathrm{M}}_{i,jk}\rangle \langle u^{\mathrm{M}}_{l,mn}\rangle \,\mathrm{d}V = \\
&= \frac{1}{2} V \left(C^{\mathrm{M}}_{ijlm} \langle u^{\mathrm{M}}_{i,j}\rangle \langle u^{\mathrm{M}}_{l,m}\rangle + (C^{\mathrm{M}}_{ijlm} \bar{I}_{kn} + D^{\mathrm{M}}_{ijklmn}) \langle u^{\mathrm{M}}_{i,jk}\rangle \langle u^{\mathrm{M}}_{l,mn}\rangle\right) ,
\end{aligned} \tag{17}$$

where

$$\bar{I}_{kn} = \frac{1}{V} \int_{\Omega^P} (X_k - \overset{\mathrm{c}}{X}_k)(X_n - \overset{\mathrm{c}}{X}_n) \,\mathrm{d}V \ . \tag{18}$$

Consequently, the macroscale energy of an RVE is expressed in terms of the gradient of macroscopic deformation. In what follows, it will be shown, by making use of asymptotic homogenization analysis, that the microscale energy can be formulated in terms of the gradient of macroscopic deformation as well leading to connections between the parameters.

3.2 The microscale energy for an RVE

Following the asymptotic homogenization method in [77] we reformulate the left-hand side of Eqn. (10). The asymptotic homogenization method separates length scales by using global coordinates, $\boldsymbol{X}$, for describing the global variation of the displacement, and by using local coordinates, $\boldsymbol{y}$, for describing the local fluctuation of the displacement. We refer to [74] and [35, Appendix B] for a more detailed investigation of the multiscale asymptotic analysis applied in this work. We introduce the local coordinates,

$$y_j = \frac{1}{\epsilon}(X_j - \overset{\mathrm{c}}{X}_j) \ , \tag{19}$$

where ϵ is a homothetic ratio scaling global and local coordinates. We stress that the dimensions of an RVE in local coordinates can be arbitrarily chosen by varying ϵ. For example, as depicted in Fig. 2, the size of an RVE is given by l in global coordinates, whereas it is denoted by w in local coordinates. If we choose $l = 0.001\,\mathrm{mm}$, as measured in global coordinates, $\boldsymbol{X}$, then it can be homothetically scaled to any dimension, such as $w = 0.001\,\mathrm{mm}$ or $w = 1000\,\mathrm{mm}$ in local coordinates, $\boldsymbol{y}$, by setting the homothetic ratio to $\epsilon = 1.0$ or $\epsilon = 10^{-6}$, in such a way that the size of the RVE is kept constant in the global coordinates. We remark that the homothetic ratio is used to describe the relationship for the sizes of an RVE between global and local coordinates, however, the ratio between macroscale and microscale remains the same, $L/l = \mathrm{const}$. We assume that the displacement field is a smooth function on the macroscopic level and $\boldsymbol{y}$-periodic in local coordinates resulting in vanishing mean local fluctuations within each RVE. Hence, the decomposition of the microscale displacement is additively decomposed into a macroscale displacement and into local fluctuations defined on different scales—they are independent.

Following [61] the displacement field of an RVE, Ω^P, at global coordinates $\boldsymbol{X}$ is expanded by using an asymptotic series with homothetic ratio ϵ, where, in general, the corresponding coefficients depend on global coordinates, $\boldsymbol{X}$, as well as on local coordinates, $\boldsymbol{y}$, which are related by Eqn. (19),

$$\boldsymbol{u}^{\mathrm{m}}(\boldsymbol{X}) = \overset{0}{\boldsymbol{u}}(\boldsymbol{X},\boldsymbol{y}) + \epsilon\overset{1}{\boldsymbol{u}}(\boldsymbol{X},\boldsymbol{y}) + \epsilon^2\overset{2}{\boldsymbol{u}}(\boldsymbol{X},\boldsymbol{y}) + \dots \ , \tag{20}$$

where $\overset{n}{\boldsymbol{u}}(\boldsymbol{X},\boldsymbol{y})$ $(n = 0,\, 1,\, 2,\, \dots)$ are assumed to be $\boldsymbol{y}$-periodic. We shall see later that the first term $\overset{0}{\boldsymbol{u}}(\boldsymbol{X},\boldsymbol{y})$ is independent of $\boldsymbol{y}$. We apply now the elasticity problem in statics (by using Eqn. (8) for a Cauchy continuum) as it needs to be fulfilled within the RVE,

$$\left(C^{\mathrm{m}}_{ijkl}u^{\mathrm{m}}_{k,l}\right)_{,j} + f_i = 0 \qquad \forall \boldsymbol{X} \in \Omega^P \ , \tag{21}$$

where the body force, $\boldsymbol{f}$, is a given function. By inserting Eqn. (20) as well as using the chain rule with the aid of the relation in Eqn. (19), we obtain

$$\begin{aligned} u^{\mathrm{m}}_{i,j} &= \left(\overset{0}{u}_i(\boldsymbol{X},\boldsymbol{y}) + \epsilon\overset{1}{u}_i(\boldsymbol{X},\boldsymbol{y}) + \epsilon^2\overset{2}{u}_i(\boldsymbol{X},\boldsymbol{y}) + \dots\right)_{,j} = \\ &= \overset{0}{u}_{i,j} + \frac{\partial\overset{0}{u}_i}{\partial y_k}\frac{\delta_{kj}}{\epsilon} + \epsilon\overset{1}{u}_{i,j} + \epsilon\frac{\partial\overset{1}{u}_i}{\partial y_k}\frac{\delta_{kj}}{\epsilon} + \epsilon^2\overset{2}{u}_{i,j} + \epsilon^2\frac{\partial\overset{2}{u}_i}{\partial y_k}\frac{\delta_{kj}}{\epsilon} + \dots \end{aligned} \tag{22}$$

Using the latter in Eqn. (21)

$$\begin{aligned} &\left(C^{\mathrm{m}}_{ijkl}\left(\overset{0}{u}_{k,l} + \frac{1}{\epsilon}\frac{\partial\overset{0}{u}_k}{\partial y_l} + \epsilon\overset{1}{u}_{k,l} + \frac{\partial\overset{1}{u}_k}{\partial y_l} + \epsilon^2\overset{2}{u}_{k,l} + \epsilon\frac{\partial\overset{2}{u}_k}{\partial y_l}\right)\right)_{,j} + \\ &+\frac{\partial}{\partial y_j}\left(C^{\mathrm{m}}_{ijkl}\left(\frac{1}{\epsilon}\overset{0}{u}_{k,l} + \frac{1}{\epsilon^2}\frac{\partial\overset{0}{u}_k}{\partial y_l} + \overset{1}{u}_{k,l} + \frac{1}{\epsilon}\frac{\partial\overset{1}{u}_k}{\partial y_l} + \epsilon\overset{2}{u}_{k,l} + \frac{\partial\overset{2}{u}_k}{\partial y_l}\right)\right) + f_i = 0 \end{aligned} \tag{23}$$

and then gathering terms having the same order in ϵ leads to the following terms:

- of the order ϵ^{-2},

$$\frac{\partial}{\partial y_j}\left(C^{\mathrm{m}}_{ijkl}\frac{\partial\overset{0}{u}_k}{\partial y_l}\right) = 0 \ , \tag{24}$$

- of the order ϵ^{-1},

$$\left(C^{\mathrm{m}}_{ijkl}\frac{\partial\overset{0}{u}_k}{\partial y_l}\right)_{,j} + \frac{\partial}{\partial y_j}\left(C^{\mathrm{m}}_{ijkl}\overset{0}{u}_{k,l}\right) + \frac{\partial}{\partial y_j}\left(C^{\mathrm{m}}_{ijkl}\frac{\partial\overset{1}{u}_k}{\partial y_l}\right) = 0 \ , \tag{25}$$

- and of the order ϵ^0,

$$\left(C^{\mathrm{m}}_{ijkl}\overset{0}{u}_{k,l}\right)_{,j} + \left(C^{\mathrm{m}}_{ijkl}\frac{\partial\overset{1}{u}_k}{\partial y_l}\right)_{,j} + \frac{\partial}{\partial y_j}\left(C^{\mathrm{m}}_{ijkl}\overset{1}{u}_{k,l}\right) + \frac{\partial}{\partial y_j}\left(C^{\mathrm{m}}_{ijkl}\frac{\partial\overset{2}{u}_k}{\partial y_l}\right) + f_i = 0 \ . \tag{26}$$

By solving these partial differential equations Eqn. (20) can be rewritten as

$$u^{\mathrm{m}}_i(\boldsymbol{X},\boldsymbol{y}) = \overset{0}{u}_i(\boldsymbol{X}) + \epsilon\varphi_{abi}(\boldsymbol{y})\overset{0}{u}_{a,b}(\boldsymbol{X}) + \epsilon^2\psi_{abci}(\boldsymbol{y})\overset{0}{u}_{a,bc}(\boldsymbol{X}) + \dots \ , \tag{27}$$

in which $\varphi_{abi}(\boldsymbol{y})$ and $\psi_{abci}(\boldsymbol{y})$ are both $\boldsymbol{y}$-periodic and they are the solutions of the following two partial differential equations,

$$\frac{\partial}{\partial y_j}\left(C^{\mathrm{m}}_{ijkl}\left(\frac{\partial\varphi_{abk}}{\partial y_l} + \delta_{ak}\delta_{bl}\right)\right) = 0 \ , \tag{28}$$

$$\frac{\partial}{\partial y_j}\left(C^{\mathrm{m}}_{ijkl}\left(\frac{\partial\psi_{abck}}{\partial y_l} + \varphi_{abk}\delta_{lc}\right)\right) + C^{\mathrm{m}}_{ickl}\left(\frac{\partial\varphi_{abk}}{\partial y_l} + \delta_{ka}\delta_{lb}\right) - C^{\mathrm{M}}_{icab} = 0 \ . \tag{29}$$

It should be noted that the choice of the indices of the third order tensor $\boldsymbol{\varphi}$ and fourth order tensor $\boldsymbol{\psi}$ differs from those in [61, 15]. Since $\boldsymbol{\varphi}$ and $\boldsymbol{\psi}$ are expressed in the Cartesian coordinates, we choose to use lower indices like φ_{abk} and ψ_{abck} here. They are mathematically and physically exactly identical to those in [61, 15]. We refer to the appendix for a derivation of Eqn. (27), Eqn. (28) and Eqn. (29). Since the first term $\overset{0}{u}_i(\boldsymbol{X})$ depends only

on the macroscopic coordinates, $\boldsymbol{X}$, it is assumed to be the known macroscopic displacement $\overset{0}{u}_i(\boldsymbol{X}) = u_i^{\mathrm{M}}(\boldsymbol{X})$ such that Eqn. (20) provides

$$u_i^{\mathrm{m}}(\boldsymbol{X},\boldsymbol{y}) = u_i(\boldsymbol{X})^{\mathrm{M}} + \epsilon\varphi_{abi}(\boldsymbol{y})u_{a,b}^{\mathrm{M}}(\boldsymbol{X}) + \epsilon^2\psi_{abci}(\boldsymbol{y})u_{a,bc}^{\mathrm{M}}(\boldsymbol{X}) + \dots \ . \tag{30}$$

We wish to express the energy on the microscale, thus, we need the gradient of the microscale displacement,

$$\begin{aligned} u_{i,j}^{\mathrm{m}} &= \left(u_i^{\mathrm{M}} + \epsilon\varphi_{abi}u_{a,b}^{\mathrm{M}} + \epsilon^2\psi_{abci}u_{a,bc}^{\mathrm{M}} + \dots\right)_{,j} \\ &= u_{i,j}^{\mathrm{M}} + \frac{\partial\varphi_{abi}}{\partial y_j}u_{a,b}^{\mathrm{M}} + \epsilon\varphi_{abi}u_{a,bj}^{\mathrm{M}} + \epsilon\frac{\partial\psi_{abci}}{\partial y_j}u_{a,bc}^{\mathrm{M}} + \epsilon^2\psi_{abci}u_{a,jbc}^{\mathrm{M}} + \dots, \end{aligned} \tag{31}$$

with the same accuracy, *i.e.*, after neglecting higher than second gradients and inserting Eqn. (16) with the aid of Eqn. (19) we write

$$\begin{aligned} u_{i,j}^{\mathrm{m}} &= \left(\delta_{ia}\delta_{jb} + \frac{\partial\varphi_{abi}}{\partial y_j}\right)u_{a,b}^{\mathrm{M}} + \epsilon u_{a,bc}^{\mathrm{M}}\left(\varphi_{abi}\delta_{jc} + \frac{\partial\psi_{abci}}{\partial y_j}\right) + \dots \\ &= \left(\delta_{ia}\delta_{jb} + \frac{\partial\varphi_{abi}}{\partial y_j}\right)\left(\langle u_{a,b}^{\mathrm{M}}\rangle + \epsilon y_c\langle u_{a,bc}^{\mathrm{M}}\rangle\right) + \epsilon\langle u_{a,bc}^{\mathrm{M}}\rangle\left(\varphi_{abi}\delta_{jc} + \frac{\partial\psi_{abci}}{\partial y_j}\right) + \dots \\ &= L_{abij}\langle u_{a,b}^{\mathrm{M}}\rangle + \epsilon M_{abcij}\langle u_{a,bc}^{\mathrm{M}}\rangle + \dots, \end{aligned} \tag{32}$$

where

$$\begin{aligned} L_{abij} &= \delta_{ia}\delta_{jb} + \frac{\partial\varphi_{abi}}{\partial y_j} \ , \\ M_{abcij} &= y_c\left(\delta_{ia}\delta_{jb} + \frac{\partial\varphi_{abi}}{\partial y_j}\right) + \left(\varphi_{abi}\delta_{jc} + \frac{\partial\psi_{abci}}{\partial y_j}\right) \ . \end{aligned} \tag{33}$$

By using the latter on the left-hand side of Eqn. (10) the microscale energy becomes

$$\begin{aligned} &\int_{\Omega^P}\frac{1}{2}C_{ijkl}^{\mathrm{m}}u_{i,j}^{\mathrm{m}}u_{k,l}^{\mathrm{m}}\,\mathrm{d}V = \frac{1}{2}\int_{\Omega^P}\Big(C_{ijkl}^{\mathrm{m}}L_{abij}L_{cdkl}\langle u_{a,b}^{\mathrm{M}}\rangle\langle u_{c,d}^{\mathrm{M}}\rangle + \\ &+\epsilon^2 C_{ijkl}^{\mathrm{m}}M_{abcij}M_{defkl}\langle u_{a,bc}^{\mathrm{M}}\rangle\langle u_{d,ef}^{\mathrm{M}}\rangle + 2\epsilon C_{ijkl}^{\mathrm{m}}L_{abij}M_{cdekl}\langle u_{a,b}^{\mathrm{M}}\rangle\langle u_{c,de}^{\mathrm{M}}\rangle\Big)\,\mathrm{d}V = \\ &= \frac{V}{2}\Big(\bar{C}_{abcd}\langle u_{a,b}^{\mathrm{M}}\rangle\langle u_{c,d}^{\mathrm{M}}\rangle + \bar{D}_{abcdef}\langle u_{a,bc}^{\mathrm{M}}\rangle\langle u_{d,ef}^{\mathrm{M}}\rangle + \bar{G}_{abcde}\langle u_{a,b}^{\mathrm{M}}\rangle\langle u_{c,de}^{\mathrm{M}}\rangle\Big) \end{aligned} \tag{34}$$

with

$$\begin{aligned} \bar{C}_{abcd} &= \frac{1}{V}\int_{\Omega^P}C_{ijkl}^{\mathrm{m}}L_{abij}L_{cdkl}\,\mathrm{d}V \ , \\ \bar{D}_{abcdef} &= \frac{\epsilon^2}{V}\int_{\Omega^P}C_{ijkl}^{\mathrm{m}}M_{abcij}M_{defkl}\,\mathrm{d}V \ , \\ \bar{G}_{abcde} &= \frac{2\epsilon}{V}\int_{\Omega^P}C_{ijkl}^{\mathrm{m}}L_{abij}M_{cdekl}\,\mathrm{d}V \ . \end{aligned} \tag{35}$$

Because we have assumed centro-symmetric materials, the rank 5 tensor vanishes, $\bar{\boldsymbol{G}} = 0$. We realize immediately by comparson with Eqn. (17) that

$$\begin{aligned} C_{ijlm}^{\mathrm{M}} &= \bar{C}_{ijlm} \ , \\ C_{ijlm}^{\mathrm{M}}\bar{I}_{kn} + D_{ijklmn}^{\mathrm{M}} &= \bar{D}_{ijklmn} \ , \end{aligned} \tag{36}$$

where

$$\bar{I}_{kn} = \int_{\Omega^P}(X_k - \overset{\mathrm{c}}{X}_k)(X_n - \overset{\mathrm{c}}{X}_n)\,\mathrm{d}V = \epsilon^2\int_{\Omega^P}y_k y_n\,\mathrm{d}V \ . \tag{37}$$

Therefore, we have generated an algorithm delivering effective parameters,

$$\begin{aligned} C_{abcd}^{\mathrm{M}} &= \frac{1}{V}\int_{\Omega^P}C_{ijkl}^{\mathrm{m}}L_{abij}L_{cdkl}\,\mathrm{d}V \ , \\ D_{abcdef}^{\mathrm{M}} &= \epsilon^2\left(\frac{1}{V}\int_{\Omega^P}C_{ijkl}^{\mathrm{m}}M_{abcij}M_{defkl}\,\mathrm{d}V - C_{abef}^{\mathrm{M}}\int_{\Omega^P}y_c y_d\,\mathrm{d}V\right) \ , \end{aligned} \tag{38}$$

after computing $\boldsymbol{\varphi}$ and $\boldsymbol{\psi}$ in an RVE.

4 Numerical solution of strain gradient homogenization problems

The final goal is to obtain the coefficients in the classical stiffness tensor C^{M}_{ijlm} and for the strain gradient stiffness tensor D^{M}_{ijklmn}. For their determination we need to solve Eqs. (28), (29). For the sake of simplicity we restrict the analysis to a 2D case, such that all indices are from $\{1, 2\}$. Within the RVE, which is the computational domain, Ω, Eqs. (28), (29) are solved by using the GALERKIN procedure in the FEM with continuous shape functions. All boundary conditions are assumed to be periodic, in other words, the values of ϕ_{abi}, ψ_{abci} are given by DIRICHLET boundary conditions.

Indeed, the solutions of Eqs. (28), (29) are determined for specific a, b indices (classical coefficients) as well as a, b, c indices (strain gradient coefficients). Consider the case where $a = 1$ and $b = 1$ leading to the weak form of Eqs. (28) after multiplying by an arbitrary test function vanishing on DIRICHLET boundaries and integrating by parts,

$$\int_\Omega \left(C^{\mathrm{m}}_{ijkl} \left(\frac{\partial \varphi_{11k}}{\partial y_l} + \delta_{1k}\delta_{1l} \right) \right) \frac{\partial \delta\varphi_{11i}}{\partial y_j} \, \mathrm{d}V = 0 \ , \tag{39}$$

from which we determine φ_{abi} after solving for $ab = 11, 12, 21, 22$. By knowing $\boldsymbol{\varphi}$, for example in the case of $a = 1$, $b = 1$, and $c = 2$, we then solve

$$\begin{aligned} \int_\Omega \Bigg(\Bigg(C^{\mathrm{m}}_{ijkl} \left(\frac{\partial \psi_{112k}}{\partial y_l} + \varphi_{11k}\delta_{l2} \right) \Bigg) \frac{\partial \delta\psi_{112i}}{\partial y_j} - \\ - C^{\mathrm{m}}_{i2kl} \left(\frac{\partial \varphi_{11k}}{\partial y_l} + \delta_{k1}\delta_{l1} \right) \delta\psi_{112i} + C^{\mathrm{M}}_{i211} \delta\psi_{112i} \Bigg) \mathrm{d}V = 0 \ . \end{aligned} \tag{40}$$

The result for $\boldsymbol{\psi}$ follows after solving for $abc = \{111, 112, 121, 122, 211, 212, 221, 222\}$. By inserting $\boldsymbol{\varphi}$ and $\boldsymbol{\psi}$ in Eqn. (33) and then applying Eqn. (38) we determine $\boldsymbol{C}^{\mathrm{M}}$ and $\boldsymbol{D}^{\mathrm{M}}$.

We have used the open-source software FEniCS for our computations. The CAD models of the RVE have been created on the open source platform SALOME 7.6, and FEM discretizations of the CAD models were realized by the mesh generator NetGen built in SALOME 7.6. Application of the periodic conditions and creating the matrices was done via Python. We emphasize that the generated mesh has to possess perfectly matching vertices on opposite (periodic) boundaries for consistency. Via NetGen this has been automatically fulfilled by mapping the meshes between periodic surfaces. The mesh is then transferred to FEniCS and the numerical solution of weak forms has been obtained by using the iterative solver *gmres* with the preconditioner *jacobi* with relative tolerance 10^{-5} and absolute tolerance 10^{-10} to ensure the accuracy of the calculations.

5 Identification of the classical and strain gradient stiffness tensors

In order to demonstrate the approach the classical and strain gradient stiffness tensors are identified for specific cases. First, consistency is examined by computing $\boldsymbol{C}^{\mathrm{M}}$ and $\boldsymbol{D}^{\mathrm{M}}$ for the case of a homogeneous material. As expected the approach delivers zero for $\boldsymbol{D}^{\mathrm{M}}$ (within the numerical tolerance). Concretely, the implementation leads to $\boldsymbol{D}^{\mathrm{M}}$ components 10^{-6} N or smaller for a material with a YOUNG's modulus, E, of 100 MPa and a POISSON's ratio, ν, of 0.3. This is consistent with the interpretation that for a homogeneous material all corresponding strain gradient material parameters must vanish.

Then a simple geometry, the so-called square lattice structure in 2D, is investigated. The square lattice structure has been widely used in engineering practice [9], as shown in Fig. 3, where gray lines build up a truss like structure. This inner structure is expected to deliver a D_4 invariant material symmetry group [11, 12, 79].

For the microscale material parameters of the lattice structure isotropic material properties are used:

$$\begin{aligned} C^{\mathrm{m}}_{ijkl} &= \lambda\delta_{ij}\delta_{kl} + \mu\delta_{ik}\delta_{jl} + \mu\delta_{il}\delta_{jk} \ , \\ \lambda &= \frac{E\nu}{(1+\nu)(1-2\nu)} \ , \ \mu = \frac{E}{2(1+\nu)} \ . \end{aligned} \tag{41}$$

VOIGT notation is used for representing the tensors, for convenience, we refer to Table 1 and Table 2 for the chosen convention based on the work by [12].

5.1 Parameter determination for the square lattice structure

In the case of the square lattice structure we assume that the material parameters of the inclusion are much smaller than those of the matrix. Simply stated, we consider a additively manufactured truss like structure

Table 1: VOIGT notation used for 2D strain tensors.

I	1	2	3
ij	11	22	12

Table 2: VOIGT notation used for 2D strain-gradient tensors.

I	1	2	3	4	5	6
ijk	111	221	122	222	112	121

with rods made out of a polymer and voids being the inclusions. By choosing material properties as compiled in Table 3 and the volume fraction of the inclusion to be 81%, we select different RVEs and determine the parameters. The RVEs are generated by repeating the corresponding basic cell, while the size of the basic cell is kept constant. Specifically the RVEs constitutes of one cell, four cells, and nine cells, as depicted in Fig. 3. The results for

$$\boldsymbol{C}^{\mathrm{M}} = \begin{pmatrix} C_{1111} & C_{1122} & 0 \\ & C_{1111} & 0 \\ \text{sym.} & & C_{1212} \end{pmatrix} ,$$

$$\boldsymbol{D}^{\mathrm{M}} = \begin{pmatrix} D_{111111} & D_{111221} & D_{111122} & 0 & 0 & 0 \\ & D_{221221} & D_{221122} & 0 & 0 & 0 \\ & & D_{122122} & 0 & 0 & 0 \\ & & & D_{111111} & D_{111221} & D_{111122} \\ & \text{sym.} & & & D_{221221} & D_{221122} \\ & & & & & D_{122122} \end{pmatrix} . \tag{42}$$

are compiled in Table 4.

In order to investigate how the size of the basic cell affects classical and strain gradient stiffness tensors different sizes of basic cells (0.2×0.2, 0.5×0.5) are selected and the corresponding results are compared with those obtained with the basic cells size 1×1, see Fig. 4 for the basic cells. Due to the fact that these three structures have the same topology, the same material properties, and the same inclusion volume fraction, the corresponding classical stiffness tensors are identical. However, this is not so in the case of the strain gradient stiffness tensors, as compiled in Table 5. All non-vanishing parameters approach zero as the size of basic cells is decreasing. We remark that this fact is intuitively correct. Indeed, when the size of basic cells vanishes, the material becomes homogeneous resulting in a vanishing $\boldsymbol{D}^{\mathrm{M}}$. This computation also illustrates the role of the homothetic ratio ϵ. To this end let us consider the parameter D_{221221} as shown in Table 5. In the case of a basic cell 1×1 this parameter is 4 times larger than that computed for the case of a basic cell 0.5×0.5, and it is 25 times larger than that computed for the case of a basic cell 0.2×0.2. The magnification factors (4 or 25) are equal to the square of homothetic ratios of these three basic cells as directly seen in Eqn. (35).

6 Computational validation of determined parameters

In order to verify and to validate the numerical values of the determined parameters, we perform three different computations: A computation on the microscale by incorporating the inner structure, a computation only with the determined classical stiffness tensor on the macroscale by using the homogenized structure, and another computation with both the determined classical stiffness tensor and the strain gradient tensor on the macroscale by using the homogenized structure.

As suggested in [71, 88, 39] the problem of strain gradient elasticity is solved by using a weak form that, in the linear setting, leads to an H^2 norm about the trial solutions as well as test functions. Hence, the

Table 3: Material properties used in lattice structures.

Type	E in MPa	ν
Matrix	100.0	0.3
Inclusion	10^{-30}	10^{-30}

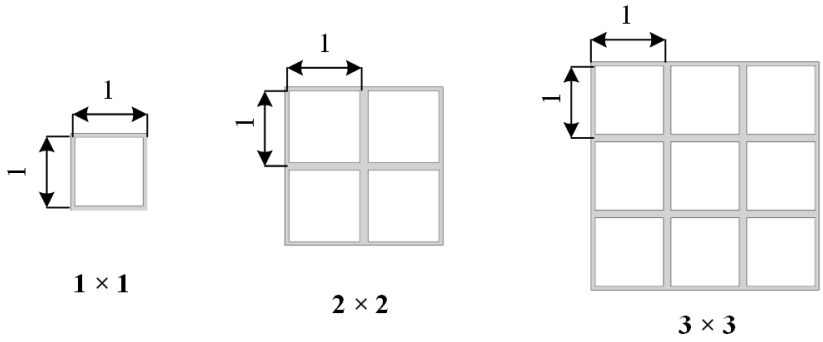

Figure 3: Geometry of square lattice structures and different selections of RVE.

Table 4: Parameters determined for the square lattice.

C_{1111} in MPa	C_{1122} in MPa	C_{1212} in MPa
11.177	0.555	0.060
D_{111111} in N	D_{111221} in N	D_{111122} in N
0.005379	0.042197	-0.047860
$D_{221221} inN$	D_{221122} in N	D_{122122} in N
1.597997	0.076341	0.033462

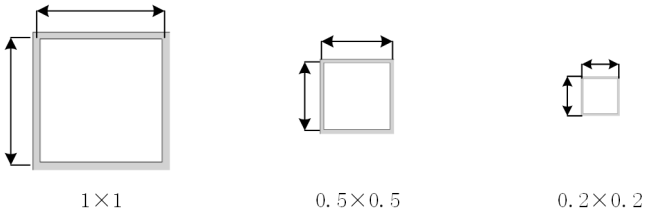

Figure 4: Different sizes of basic cell with the same volume ratio.

Table 5: Identified non-zero strain gradient stiffness parameters for the square lattice structure in units of N.

Type	D_{111111}	D_{111221}	D_{111122}	D_{221221}	D_{221122}	D_{122122}
1×1	0.005379	0.042197	-0.047860	1.597997	0.076341	0.033462
0.5×0.5	0.001344	0.010549	-0.011965	0.399499	0.019085	0.008365
0.2×0.2	0.000215	0.001688	-0.001914	0.063919	0.003054	0.001385

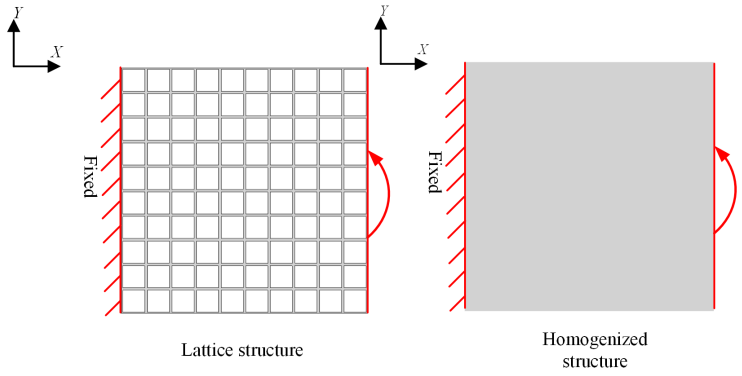

Figure 5: The boundary conditions for computations.

corresponding finite-dimensional approximations are guaranteed to lie in a function space that is at least of C^1 continuity. In order to obtain this property isogeometric FEM is employed with non-uniform rational Bezier splines (NURBS) based shape functions. The isogeometric FEM is able to ensure C^n continuity in one single patch, which is appropriate for 2D simple geometries as in the present case. A detailed discussion of the NURBS basis and isogeometric FEM as well as the weak formulation of strain gradient elasticity can be found in [54, 55, 24, 38, 25, 26, 27, 50]. The deformation energy that quantitatively describes the overall deformation behavior of the structures are used to compare the results.

The boundary conditions for the simulations are shown in Fig. 5. The left side of the structure is clamped and on the right side of the structure a rotation is prescribed along the center of the right edge. Two different types of computations are performed in the following subsections. In Section 6.1 the computations are done for the lattice structures with different macrosizes but the same sizes of basic cell, and in Section 6.2 we conduct computations for lattice structures with the same macrosizes but with different sizes of internal basic cells. The total volume remains the same in this case due to the fact that the ratio of the cell wall length to thickness of the basic cell is held constant with a ratio 1 to 10.

6.1 Computations for square lattices with the same basic cell sizes and varied macrosizes

In this section computations for the square lattice with the same sizes of the basic cell but with different macrosizes as shown in Fig. 6 are performed. The size of the basic cell is $1\,\text{mm} \times 1\,\text{mm}$, and the selected lattices are of the macrosizes

- $2\,\text{mm} \times 2\,\text{mm}$,
- $4\,\text{mm} \times 4$ mm,
- $6\,\text{mm} \times 6$ mm,
- $10\,\text{mm} \times 10\,\text{mm}$.

The results of the simulations are shown in Fig. 7, where the vertical axis stands for the strain energy of the structures (in mJ) and the horizontal axis stands for the prescribed rotation (in rad). The black solid lines in Fig. 7 represents the results on the microscale. We consider this solution to be the correct one. The blue dashed line with square markers represents the computations of the homogenized structure by using the classical stiffness tensor. The yellow dashed line with circle markers represents the simulations for the homogenized structure when taking the strain gradient effect into account.

The blue lines show a smaller strain energy with regard to the microscale due to the absence of the higher order strain gradient energy. We remark that while keeping the sizes of the basic cells unchanged, with increasing macrosizes of the structures, namely L/l becoming larger and larger, the computational results of the classical elasticity theory approach that on the microscale. We may say that in a large macroscale $L/l > 10$, classical elasticity is adequate to guarantee the accuracy of the computation. However, when the macroscopic length scale is of the same order of its sizes of the internal substructures, the strain gradient effect becomes significant. This phenomenon is also known as *size effect*.

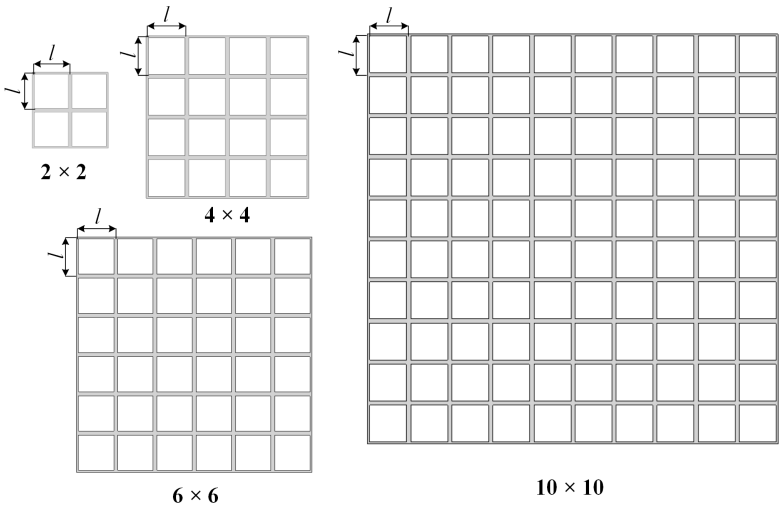

Figure 6: Selected simulations for square lattice with the same size micro-structure.

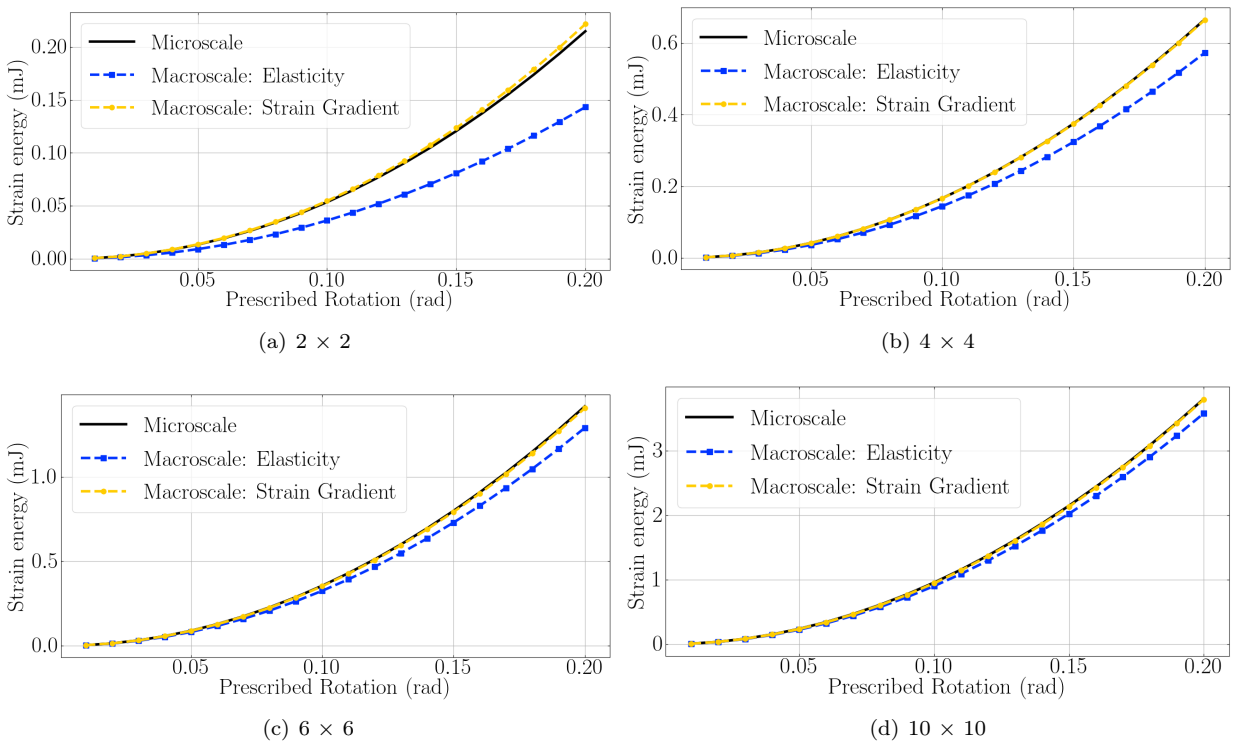

(a) 2 × 2

(b) 4 × 4

(c) 6 × 6

(d) 10 × 10

Figure 7: Comparison of strain energies for square lattice structures with different macroscale sizes.

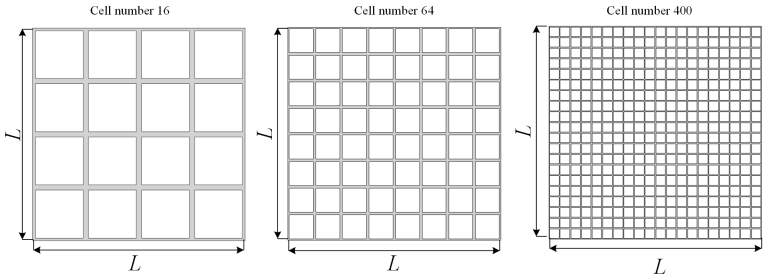

Figure 8: Selected simulations for square lattices with basic cells of varied sizes.

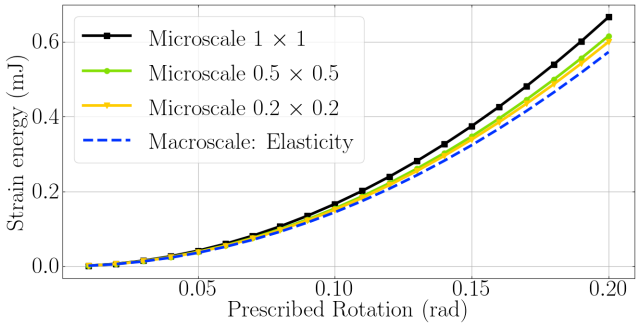

Figure 9: Comparative computations between microscale and macroscale of elasticity.

6.2 Computations for square lattices with varied basic cell sizes and the same macrosizes

In order to verify the identified parameters for square lattices with different basic cell sizes but the same macro sizes even further, computations are conducted in this section. Three square lattices are selected as shown in Fig. 8. These three lattices possess the same macrosizes 4 mm × 4 mm. Their basic cell sizes are 1 mm × 1 mm, 0.5 mm × 0.5 mm and 0.2 mm × 0.2 mm for the left, the middle and the right lattice in Fig. 8, respectively, which divides the macro domain into 16, 64 and 400 basic cells. The computations are shown in Fig. 9 and Fig. 10. Fig. 9 indicates that with increasing basic cell sizes, the strain energy at the rotation of 0.2 radian shows an increasing trend at the microscale. As it was mentioned above, this scale-dependent (depends on L/l) phenomenon is also know as size effect.

The computations on the macroscale of elasticity are identical for these three cases due to the fact that the ratio of the cell wall length to the thickness of the basic cell is fixed with a ratio 1 to 10. The computation on the macroscale of elasticity are independent of the scale ratio and they show a significant error compared with the microscale where the scale ratio (L/l) is getting smaller, and the size effect could not be ignored. When the scale ratio (L/l) is getting larger, which means the basic cell sizes is decreasing, the computations on the macroscale of elasticity are gradually approaching those of the microscale. In such a case, for example $L/l > 20$, the size effect can be ignored. It can be also observed from Fig. 10 (a), (b), (c) that the computations with strain gradient show a good quantitative match with the microscale, which means that by taking the strain gradient stiffness tensor into account, the size effect of the lattice structure is fully resolved.

7 Conclusions

A homogenization approach based on the asymptotic analysis has been exploited for developing a methodology in order to determine stiffness parameters of a metamaterial. Specifically, the strain gradient theory was used on the macroscale. The expressions of classical stiffness tensor and strain gradient stiffness tensor have been derived and the FEM has been successfully used to solve the partial differential equations generated from the homogenization procedure. The so-called square lattice structure has been investigated, and their material parameters are explicitly computed. The proposed approach guarantees that the parameters of strain gradient stiffness tensors vanish as the material becomes homogeneous. Moreover, it ensures that strain gradient related parameters are independent on the repetition of RVE, but dependent on the intrinsic size of the material. In order to validate the parameters determined by this methodology, additional numerical computations of the

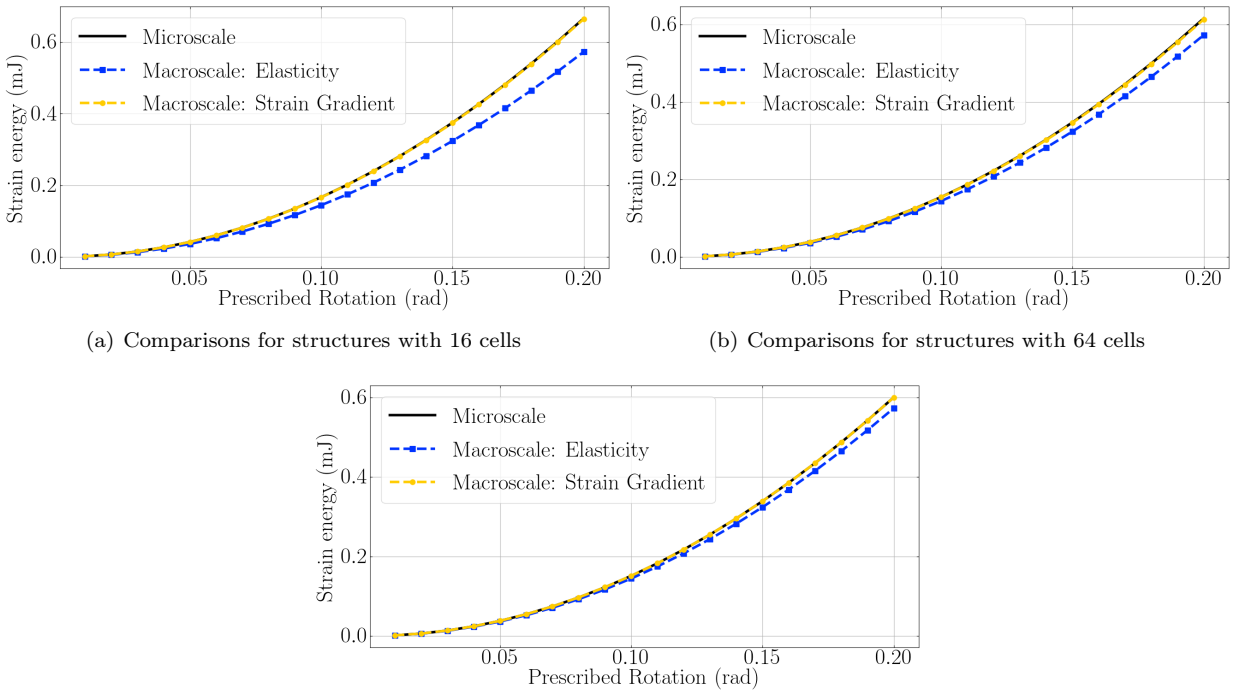

(a) Comparisons for structures with 16 cells

(b) Comparisons for structures with 64 cells

(c) Comparisions for structures with 400 cells

Figure 10: Comparisons between computations in microscale, macroscale of elascity, and macroscale of strain gradient for square lattice structures with different number of cells.

square lattice with different sizes have been performed. The numerical results show that the size effect of the lattice can be accurately captured by using the strain gradient theory with the parameters determined by the methodology applied herein. We emphasize that this methodology can be applied to any metamaterial made of a substructure with an RVE.

Appendix: Asymptotic solution for the displacement field

The asymptotic solution for an RVE are derived. Specifically the solutions of Eqn. (24), Eqn. (25) and Eqn. (26) are shown.

We start with Eqn. (24). Because C^{m}_{ijkl} is a function of $\boldsymbol{y}$, the only possible general solution of Eqn. (24) is to restrict $\overset{0}{u}_i(\boldsymbol{X})$, since it is $\boldsymbol{y}$-periodic and has a bounded gradient. The solution in the order of ϵ^{-2} can be given as

$$\overset{0}{u}_i = \overset{0}{u}_i(\boldsymbol{X}) \ . \tag{43}$$

Note that $\overset{0}{u}_i(\boldsymbol{X})$ depends only on the macroscopic coordinates. It is assumed to be the known macroscopic displacement $\overset{0}{u}_i(\boldsymbol{X}) = u^{\mathrm{M}}_i(\boldsymbol{X})$. By substituting Eqn. (43) into Eqn. (25), by introducing $\varphi_{abc} = \varphi_{abc}(\boldsymbol{y})$, for the inverse operation, we obtain

$$\begin{aligned}
&\frac{\partial C^{\mathrm{m}}_{ijab}}{\partial y_j}\frac{\partial \overset{0}{u}_a}{\partial X_b} = -\frac{\partial}{\partial y_j}\left(C^{\mathrm{m}}_{ijkl}\frac{\partial \overset{1}{u}_k}{\partial y_l}\right) \ , \\
&\frac{\partial C^{\mathrm{m}}_{ijab}}{\partial y_j} = -\frac{\partial}{\partial y_j}\left(C^{\mathrm{m}}_{ijkl}\frac{\partial \varphi_{abk}}{\partial y_l}\right) \ , \\
&\frac{\partial}{\partial y_j}\left(C^{\mathrm{m}}_{ijkl}\left(\frac{\partial \varphi_{abk}}{\partial y_l} + \delta_{ak}\delta_{bl}\right)\right) = 0 \ .
\end{aligned} \tag{44}$$

Then the general solution of Eqn. (25) can be given as

$$\overset{1}{u}_i = \varphi_{abi}\overset{0}{u}_{a,b} + \overset{1}{\bar{u}}_i(\boldsymbol{X}) \ , \tag{45}$$

where $\overset{1}{\bar{u}}_i = \overset{1}{\bar{u}}_i(\boldsymbol{X})$ are integration constants in $\boldsymbol{y}$.

Substitution of Eqn. (43) and Eqn. (45) (with $\overset{1}{\bar{u}}_i(\boldsymbol{X}) = 0$) into Eqn. (26) leads to

$$C^{\mathrm{m}}_{ijkl}\overset{0}{u}_{k,lj} + C^{\mathrm{m}}_{ijkl}\frac{\partial\varphi_{abk}}{\partial y_l}\overset{0}{u}_{a,bj} + \frac{\partial}{\partial y_j}\big(C^{\mathrm{m}}_{ijkl}\varphi_{abk}\big)\overset{0}{u}_{a,bl} + \frac{\partial}{\partial y_j}\Big(C^{\mathrm{m}}_{ijkl}\frac{\partial^2 u_k}{\partial y_l}\Big) + f_i = 0 \ . \tag{46}$$

Please note that the body force $\boldsymbol{f}$ keeps unchanged on the micro- and macroscales. We recall the governing equation in the macroscale which reads [3]

$$\begin{gathered}\left(\frac{\partial w^{\mathrm{M}}}{\partial u^{\mathrm{M}}_{i,j}} - \Big(\frac{\partial w^{\mathrm{M}}}{\partial u^{\mathrm{M}}_{i,jk}}\Big)_{,k}\right)_{,j} + f_i = 0 \ , \\ C^{\mathrm{M}}_{ijkl}u^{\mathrm{M}}_{k,lj} - D^{\mathrm{M}}_{ijklmn}u^{\mathrm{M}}_{l,mnkj} + f_i = 0 \ .\end{gathered} \tag{47}$$

By neglecting the fourth order term in Eqn. (47) and by using $\overset{0}{u}_i(\boldsymbol{X}) = u^{\mathrm{M}}_i(\boldsymbol{X})$, we obtain

$$f_i = -C^{\mathrm{M}}_{ijkl}u^{\mathrm{M}}_{k,lj} = -C^{\mathrm{M}}_{ijkl}\overset{0}{u}_{k,lj} \ . \tag{48}$$

on ofng Eqn. (48) into Eqn. (46) leads to

$$\frac{\partial}{\partial y_j}\Big(C^{\mathrm{m}}_{ijkl}\frac{\partial^2 u_k}{\partial y_l}\Big) = -\Big(C^{\mathrm{m}}_{icab} + C^{\mathrm{m}}_{ijkl}\frac{\partial\varphi_{abk}}{\partial y_l}\delta_{jc} + \frac{\partial}{\partial y_j}\big(C^{\mathrm{m}}_{ijkl}\varphi_{abk}\big)\delta_{lc} - C^{\mathrm{M}}_{icab}\Big)\overset{0}{u}_{a,bc} \ . \tag{49}$$

Because $\overset{0}{u}_{a,bc}$ is constant in $\boldsymbol{y}$, we can introduce ψ_{abci} depending on $\boldsymbol{y}$ and decompose as follows:

$$\overset{2}{u}_i = \psi_{abci}\overset{0}{u}_{a,bc} + \overset{2}{\bar{u}}_i(\boldsymbol{X}) \ . \tag{50}$$

where $\psi_{abcd} = \psi_{abcd}(\boldsymbol{y})$ and $\overset{2}{\bar{u}}_i(\boldsymbol{X})$ are integration constants in $\boldsymbol{y}$. By substituting Eqn. (50) (with $\overset{2}{\bar{u}}_i(\boldsymbol{X}) = 0$) into Eqn. (49), it is found that the tensor ψ_{abcd} must fulfill the following equation

$$\frac{\partial}{\partial y_j}\Big(C^{\mathrm{m}}_{ijkl}\Big(\frac{\partial\psi_{abck}}{\partial y_l} + \varphi_{abk}\delta_{lc}\Big)\Big) + C^{\mathrm{m}}_{ickl}\Big(\frac{\partial\varphi_{abk}}{\partial y_l} + \delta_{ka}\delta_{lb}\Big) - C^{\mathrm{M}}_{icab} = 0 \ , \tag{51}$$

such that Eqn. (20) provides

$$u^{\mathrm{m}}_i(\boldsymbol{X},\boldsymbol{y}) = \overset{0}{u}_i(\boldsymbol{X}) + \epsilon\varphi_{abi}(\boldsymbol{y})\overset{0}{u}_{a,b}(\boldsymbol{X}) + \epsilon^2\psi_{abci}(\boldsymbol{y})\overset{0}{u}_{a,bc}(\boldsymbol{X}) + \dots \ . \tag{52}$$

Acknowledgements

We express our gratitude to Emilio Barchiesi, Ivan Giorgio, and Francesco dell'Isola for valuable discussions. We also thank David Kamensky for the help of implementation of isogeometric FEM in FEniCS.

References

[1] B. E. Abali.
Revealing the physical insight of a length-scale parameter in metamaterials by exploiting the variational formulation.
Continuum Mechanics and Thermodynamics, 31:885–894, 2019.

[2] B. E. Abali, W. H. Müller, and F. dell'Isola.
Theory and computation of higher gradient elasticity theories based on action principles.
Archive of Applied Mechanics, 87(9):1495–1510, 2017.

[3] B. E. Abali, W. H. Müller, and V. A. Eremeyev.
Strain gradient elasticity with geometric nonlinearities and its computational evaluation.
Mechanics of Advanced Materials and Modern Processes, 1(4), 2015.

[4] J. Alibert and A. Della Corte.
Second-gradient continua as homogenized limit of pantographic microstructured plates: a rigorous proof.
Zeitschrift für angewandte Mathematik und Physik, 66(5):2855–2870, 2015.

[5] J.-J. Alibert, P. Seppecher, and F. dell'Isola.
Truss modular beams with deformation energy depending on higher displacement gradients.
Mathematics and Mechanics of Solids, 8(1):51–73, 2003.

[6] H. Altenbach and V. Eremeyev.
On the linear theory of micropolar plates.
ZAMM-Journal of Applied Mathematics and Mechanics/Zeitschrift für Angewandte Mathematik und Mechanik, 89(4):242–256, 2009.

[7] H. Altenbach and V. A. Eremeyev.
Direct approach-based analysis of plates composed of functionally graded materials.
Archive of Applied Mechanics, 78(10):775–794, 2008.

[8] U. Andreaus, M. Spagnuolo, T. Lekszycki, and S. R. Eugster.
A Ritz approach for the static analysis of planar pantographic structures modeled with nonlinear euler–bernoulli beams.
Continuum Mechanics and Thermodynamics, pages 1–21, 2018.

[9] S. Arabnejad and D. Pasini.
Mechanical properties of lattice materials via asymptotic homogenization and comparison with alternative homogenization methods.
International Journal of Mechanical Sciences, 77:249–262, 2013.

[10] H. Askes and E. C. Aifantis.
Gradient elasticity in statics and dynamics: an overview of formulations, length scale identification procedures, finite element implementations and new results.
International Journal of Solids and Structures, 48(13):1962–1990, 2011.

[11] N. Auffray, R. Bouchet, and Y. Brechet.
Derivation of anisotropic matrix for bi-dimensional strain-gradient elasticity behavior.
International Journal of Solids and Structures, 46(2):440–454, 2009.

[12] N. Auffray, J. Dirrenberger, and G. Rosi.
A complete description of bi-dimensional anisotropic strain-gradient elasticity.
International Journal of Solids and Structures, 69:195–206, 2015.

[13] A. Bacigalupo.
Second-order homogenization of periodic materials based on asymptotic approximation of the strain energy: formulation and validity limits.
Meccanica, 49(6):1407–1425, 2014.

[14] A. Bacigalupo, M. Paggi, F. Dal Corso, and D. Bigoni.
Identification of higher-order continua equivalent to a cauchy elastic composite.
Mechanics Research Communications, 93:11–22, 2018.

[15] S. Barboura and J. Li.
Establishment of strain gradient constitutive relations by using asymptotic analysis and the finite element method for complex periodic microstructures.
International Journal of Solids and Structures, 136:60–76, 2018.

[16] E. Barchiesi, F. dell'Isola, M. Laudato, L. Placidi, and P. Seppecher.
A 1D continuum model for beams with pantographic microstructure: Asymptotic micro-macro identification and numerical results.
In *Advances in Mechanics of Microstructured Media and Structures*, pages 43–74. Springer, 2018.

[17] E. Barchiesi, G. Ganzosch, C. Liebold, L. Placidi, R. Grygoruk, and W. H. Müller.
Out-of-plane buckling of pantographic fabrics in displacement-controlled shear tests: experimental results and model validation.
Continuum Mechanics and Thermodynamics, pages 1–13, 2018.

[18] E. Barchiesi and L. Placidi.
A review on models for the 3D statics and 2D dynamics of pantographic fabrics.
In *Wave Dynamics and Composite Mechanics for Microstructured Materials and Metamaterials*, pages 239–258. Springer, 2017.

[19] E. Barchiesi, M. Spagnuolo, and L. Placidi.
Mechanical metamaterials: a state of the art.
Mathematics and Mechanics of Solids, page 1081286517735695, 2018.

[20] A. Bensoussan, J.-L. Lions, and G. Papanicolaou.
Asymptotic analysis for periodic structures, volume 374.
American Mathematical Soc., 2011.

[21] A. Bertram.
Compendium on gradient materials including Solids and Fluids.
Magdeburg, Berlin, 2019.

[22] C. Boutin.
Microstructural effects in elastic composites.
International Journal of Solids and Structures, 33(7):1023–105, 1996.

[23] C. Boutin, F. dell'Isola, I. Giorgio, and L. Placidi.
Linear pantographic sheets: Asymptotic micro-macro models identification.
Mathematics and Mechanics of Complex Systems, 5(2):127–162, 2017.

[24] G. Capobianco and S. Eugster.
Time finite element based moreau-type integrators.
International Journal for Numerical Methods in Engineering, 114(3):215–231, 2018.

[25] A. Cazzani, M. Malagù, and E. Turco.
Isogeometric analysis of plane-curved beams.
Mathematics and Mechanics of Solids, 21(5):562–577, 2016.

[26] A. Cazzani, M. Malagù, E. Turco, and F. Stochino.
Constitutive models for strongly curved beams in the frame of isogeometric analysis.
Mathematics and Mechanics of Solids, 21(2):182–209, 2016.

[27] A. Cazzani, F. Stochino, and E. Turco.
An analytical assessment of finite element and isogeometric analyses of the whole spectrum of timoshenko beams.
ZAMM-Journal of Applied Mathematics and Mechanics/Zeitschrift für Angewandte Mathematik und Mechanik, 96(10):1220–1244, 2016.

[28] C. Chen and N. Fleck.
Size effects in the constrained deformation of metallic foams.
Journal of the Mechanics and Physics of Solids, 50(5):955–977, 2002.

[29] M. Cuomo, L. Contrafatto, and L. Greco.
A variational model based on isogeometric interpolation for the analysis of cracked bodies.
International Journal of Engineering Science, 80:173–188, 2014.

[30] M. De Angelo, M. Spagnuolo, F. D'Annibale, A. Pfaff, K. Hoschke, A. Misra, C. Dupuy, P. Peyre, J. Dirrenberger, and M. Pawlikowski.
The macroscopic behavior of pantographic sheets depends mainly on their microstructure: experimental evidence and qualitative analysis of damage in metallic specimens.
Continuum Mechanics and Thermodynamics, pages 1–23, 2019.

[31] F. dell'Isola, I. Giorgio, M. Pawlikowski, and N. Rizzi.
Large deformations of planar extensible beams and pantographic lattices: heuristic homogenization, experimental and numerical examples of equilibrium.
Proceedings of the Royal Society A: Mathematical, Physical and Engineering Sciences, 472(2185):20150790, 2016.

[32] F. dell'Isola and L. Placidi.
Variational principles are a powerful tool also for formulating field theories.
In *Variational models and methods in solid and fluid mechanics*, pages 1–15. Springer, 2011.

[33] F. dell'Isola, G. Sciarra, and S. Vidoli.
Generalized Hooke's law for isotropic second gradient materials.
In *Proceedings of the Royal Society of London A: Mathematical, Physical and Engineering Sciences*, pages rspa–2008. The Royal Society, 2009.

[34] F. dell'Isola, P. Seppecher, J. J. Alibert, T. Lekszycki, R. Grygoruk, M. Pawlikowski, D. Steigmann, I. Giorgio, U. Andreaus, E. Turco, M. Gołaszewski, N. Rizzi, C. Boutin, V. A. Eremeyev, A. Misra, L. Placidi, E. Barchiesi, L. Greco, M. Cuomo, A. Cazzani, A. Della Corte, A. Battista, D. Scerrato, I. Z. Eremeeva, Y. Rahali, J.-F. Ganghoffer, W. Müller, G. Ganzosch, M. Spagnuolo, A. Pfaff, K. Barcz, K. Hoschke, J. Neggers, and F. Hild.

Pantographic metamaterials: an example of mathematically driven design and of its technological challenges.
Continuum Mechanics and Thermodynamics, pages 1–34, 2018.

[35] Y. Efendiev and T. Y. Hou.
Multiscale finite element methods: theory and applications, volume 4.
Springer Science & Business Media, 2009.

[36] V. A. Eremeyev, F. dell'Isola, C. Boutin, and D. Steigmann.
Linear pantographic sheets: existence and uniqueness of weak solutions.
Journal of Elasticity, pages 1–22, 2017.

[37] V. A. Eremeyev and W. Pietraszkiewicz.
Material symmetry group of the non-linear polar-elastic continuum.
International Journal of Solids and Structures, 49(14):1993–2005, 2012.

[38] S. Eugster, C. Hesch, P. Betsch, and C. Glocker.
Director-based beam finite elements relying on the geometrically exact beam theory formulated in skew coordinates.
International Journal for Numerical Methods in Engineering, 97(2):111–129, 2014.

[39] P. Fischer, M. Klassen, J. Mergheim, P. Steinmann, and R. Müller.
Isogeometric analysis of 2D gradient elasticity.
Computational Mechanics, 47(3):325–334, 2011.

[40] S. Forest, R. Dendievel, and G. R. Canova.
Estimating the overall properties of heterogeneous cosserat materials.
Modelling and Simulation in Materials Science and Engineering, 7(5):829, 1999.

[41] S. Forest, F. Pradel, and K. Sab.
Asymptotic analysis of heterogeneous cosserat media.
International Journal of Solids and Structures, 38(26-27):4585–4608, 2001.

[42] P. Franciosi and A. El Omri.
Effective properties of fiber and platelet systems and related phase arrangements in n-phase heterogenous media.
Mechanics Research Communications, 38(1):38–44, 2011.

[43] P. Franciosi and G. Lormand.
Using the radon transform to solve inclusion problems in elasticity.
International Journal of Solids and Structures, 41(3-4):585–606, 2004.

[44] P. Franciosi, M. Spagnuolo, and O. U. Salman.
Mean green operators of deformable fiber networks embedded in a compliant matrix and property estimates.
Continuum Mechanics and Thermodynamics, pages 1–32, 2018.

[45] S. Ghosh, K. Lee, and S. Moorthy.
Two scale analysis of heterogeneous elastic-plastic materials with asymptotic homogenization and voronoi cell finite element model.
Computer methods in applied mechanics and engineering, 132(1-2):63–116, 1996.

[46] L. J. Gibson.
Biomechanics of cellular solids.
Journal of biomechanics, 38(3):377–399, 2005.

[47] L. J. Gibson and M. F. Ashby.
Cellular solids: structure and properties.
Cambridge university press, 1999.

[48] I. Giorgio, U. Andreaus, T. Lekszycki, and A. D. Corte.
The influence of different geometries of matrix/scaffold on the remodeling process of a bone and bioresorbable material mixture with voids.
Mathematics and Mechanics of Solids, 22(5):969–987, 2017.

[49] I. Giorgio, N. Rizzi, and E. Turco.
Continuum modelling of pantographic sheets for out-of-plane bifurcation and vibrational analysis.
Proceedings of the Royal Society A: Mathematical, Physical and Engineering Sciences, 473(2207):20170636, 2017.

[50] L. Greco and M. Cuomo.
B-spline interpolation of Kirchhoff-Love space rods.
Computer Methods in Applied Mechanics and Engineering, 256:251–269, 2013.

[51] C. R. Hendy and E. Turco.
Numerical validation of simplified theories for design rules of transversely stiffened plate girders.
Structural Engineer, 86:21, 2008.

[52] R. Hill.
On constitutive macro-variables for heterogeneous solids at finite strain.
Proceedings of the Royal Society of London. A. Mathematical and Physical Sciences, 326(1565):131–147, 1972.

[53] G. Holzapfel.
Nonlinear Solid Mechanics: A Continuum Approach for Engineering.
John Wiley & Sons, 2000.

[54] T. J. Hughes, J. A. Cottrell, and Y. Bazilevs.
Isogeometric analysis: Cad, finite elements, nurbs, exact geometry and mesh refinement.
Computer methods in applied mechanics and engineering, 194(39-41):4135–4195, 2005.

[55] D. Kamensky and Y. Bazilevs.
tigar: Automating isogeometric analysis with fenics.
Computer Methods in Applied Mechanics and Engineering, 344:477–498, 2019.

[56] V. Kouznetsova, M. G. Geers, and W. M. Brekelmans.
Multi-scale constitutive modelling of heterogeneous materials with a gradient-enhanced computational homogenization scheme.
International Journal for Numerical Methods in Engineering, 54(8):1235–1260, 2002.

[57] V. Kushnevsky, O. Morachkovsky, and H. Altenbach.
Identification of effective properties of particle reinforced composite materials.
Computational mechanics, 22(4):317–325, 1998.

[58] D. C. Lam, F. Yang, A. C. M. Chong, J. Wang, and P. Tong.
Experiments and theory in strain gradient elasticity.
Journal of the Mechanics and Physics of Solids, 51(8):1477–1508, 2003.

[59] J. Li.
Establishment of strain gradient constitutive relations by homogenization.
Comptes Rendus Mécanique, 339(4):235–244, 2011.

[60] J. Li.
A micromechanics-based strain gradient damage model for fracture prediction of brittle materials–part i: Homogenization methodology and constitutive relations.
International Journal of Solids and Structures, 48(24):3336–3345, 2011.

[61] J. Li and X.-B. Zhang.
A numerical approach for the establishment of strain gradient constitutive relations in periodic heterogeneous materials.
European Journal of Mechanics-A/Solids, 41:70–85, 2013.

[62] H. Liu, B. Li, and W. Tang.
Manufacturing oriented topology optimization of 3D structures for carbon emission reduction in casting process.
Journal of Cleaner Production, 2019.

[63] H. Liu, B. Li, Z. Yang, and J. Hong.
Topology optimization of stiffened plate/shell structures based on adaptive morphogenesis algorithm.
Journal of Manufacturing Systems, 43:375–384, 2017.

[64] Y. Lu and T. Lekszycki.
Modelling of bone fracture healing: influence of gap size and angiogenesis into bioresorbable bone substitute.
Mathematics and Mechanics of Solids, 22(10):1997–2010, 2017.

[65] R. D. Mindlin.
Second gradient of strain and surface-tension in linear elasticity.
International Journal of Solids and Structures, 1(4):417–438, 1965.

[66] R. D. Mindlin and N. Eshel.
On first strain-gradient theories in linear elasticity.
International Journal of Solids and Structures, 4(1):109–124, 1968.

[67] Z. Mróz and T. Lekszycki.
Optimal support reaction in elastic frame structures.
Computers & Structures, 14(3-4):179–185, 1981.

[68] L. Nazarenko, H. Stolarski, L. Khoroshun, and H. Altenbach.
Effective thermo-elastic properties of random composites with orthotropic components and aligned ellipsoidal inhomogeneities.
International Journal of Solids and Structures, 136:220–240, 2018.

[69] N. Nejadsadeghi, M. De Angelo, R. Drobnicki, T. Lekszycki, F. dell'Isola, and A. Misra.
Parametric experimentation on pantographic unit cells reveals local extremum configuration.
Experimental Mechanics, pages 1–13, 2019.

[70] N. Nejadsadeghi, L. Placidi, M. Romeo, and A. Misra.
Frequency band gaps in dielectric granular metamaterials modulated by electric field.
Mechanics Research Communications, 95:96–103, 2019.

[71] J. Niiranen, S. Khakalo, V. Balobanov, and A. H. Niemi.
Variational formulation and isogeometric analysis for fourth-order boundary value problems of gradient-elastic bar and plane strain/stress problems.
Computer Methods in Applied Mechanics and Engineering, 308:182–211, 2016.

[72] A. K. Noor.
Continuum modeling for repetitive lattice structures.
Applied Mechanics Reviews, 41(7):285–296, 1988.

[73] R. Peerlings and N. Fleck.
Computational evaluation of strain gradient elasticity constants.
International Journal for Multiscale Computational Engineering, 2(4), 2004.

[74] M. Peszynska and R. E. Showalter.
Multiscale elliptic-parabolic systems for flow and transport.
Electronic Journal of Differential Equations (EJDE), 147:1–30, 2007.

[75] C. Pideri and P. Seppecher.
A second gradient material resulting from the homogenization of an heterogeneous linear elastic medium.
Continuum Mechanics and Thermodynamics, 9(5):241–257, 1997.

[76] W. Pietraszkiewicz and V. Eremeyev.
On natural strain measures of the non-linear micropolar continuum.
International Journal of Solids and Structures, 46(3-4):774–787, 2009.

[77] J. Pinho-da Cruz, J. Oliveira, and F. Teixeira-Dias.
Asymptotic homogenisation in linear elasticity. part i: Mathematical formulation and finite element modelling.
Computational Materials Science, 45(4):1073–1080, 2009.

[78] L. Placidi, U. Andreaus, A. Della Corte, and T. Lekszycki.
Gedanken experiments for the determination of two-dimensional linear second gradient elasticity coefficients.
Zeitschrift für angewandte Mathematik und Physik, 66(6):3699–3725, 2015.

[79] L. Placidi, U. Andreaus, and I. Giorgio.
Identification of two-dimensional pantographic structure via a linear d4 orthotropic second gradient elastic model.
Journal of Engineering Mathematics, 103(1):1–21, 2017.

[80] L. Placidi, E. Barchiesi, and A. Battista.
An inverse method to get further analytical solutions for a class of metamaterials aimed to validate numerical integrations.
In *Mathematical Modelling in Solid Mechanics*, pages 193–210. Springer, 2017.

[81] L. Placidi, E. Barchiesi, and A. Misra.
A strain gradient variational approach to damage: a comparison with damage gradient models and numerical results.

Mathematics and Mechanics of Complex Systems, 6(2):77–100, 2018.

[82] L. Placidi, E. Barchiesi, E. Turco, and N. L. Rizzi.
A review on 2D models for the description of pantographic fabrics.
Zeitschrift für angewandte Mathematik und Physik, 67(5):121, 2016.

[83] L. Placidi, A. Misra, and E. Barchiesi.
Simulation results for damage with evolving microstructure and growing strain gradient moduli.
Continuum Mechanics and Thermodynamics, pages 1–21, 2018.

[84] L. Placidi, A. Misra, and E. Barchiesi.
Two-dimensional strain gradient damage modeling: a variational approach.
Zeitschrift für angewandte Mathematik und Physik, 69(3):56, 2018.

[85] Y. Rahali, I. Giorgio, J. Ganghoffer, and F. dell'Isola.
Homogenization à la Piola produces second gradient continuum models for linear pantographic lattices.
International Journal of Engineering Science, 97:148–172, 2015.

[86] G. Rosi, I. Giorgio, and V. A. Eremeyev.
Propagation of linear compression waves through plane interfacial layers and mass adsorption in second gradient fluids.
ZAMM-Journal of Applied Mathematics and Mechanics/Zeitschrift für Angewandte Mathematik und Mechanik, 93(12):914–927, 2013.

[87] G. Rosi, L. Placidi, and N. Auffray.
On the validity range of strain-gradient elasticity: a mixed static-dynamic identification procedure.
European Journal of Mechanics-A/Solids, 69:179–191, 2018.

[88] S. Rudraraju, A. Van der Ven, and K. Garikipati.
Three-dimensional isogeometric solutions to general boundary value problems of toupin's gradient elasticity theory at finite strains.
Computer Methods in Applied Mechanics and Engineering, 278:705–728, 2014.

[89] D. Scerrato, I. Giorgio, and N. L. Rizzi.
Three-dimensional instabilities of pantographic sheets with parabolic lattices: numerical investigations.
Zeitschrift für angewandte Mathematik und Physik, 67(3):53, 2016.

[90] V. P. Smyshlyaev and K. Cherednichenko.
On rigorous derivation of strain gradient effects in the overall behaviour of periodic heterogeneous media.
Journal of the Mechanics and Physics of Solids, 48(6-7):1325–1357, 2000.

[91] M. Spagnuolo, K. Barcz, A. Pfaff, F. dell'Isola, and P. Franciosi.
Qualitative pivot damage analysis in aluminum printed pantographic sheets: numerics and experiments.
Mechanics Research Communications, 83:47–52, 2017.

[92] D. Steigmann and F. dell'Isola.
Mechanical response of fabric sheets to three-dimensional bending, twisting, and stretching.
Acta Mechanica Sinica, 31(3):373–382, 2015.

[93] C. Sun and R. Vaidya.
Prediction of composite properties from a representative volume element.
Composites Science and Technology, 56(2):171–179, 1996.

[94] C. Tekoğlu and P. R. Onck.
Size effects in two-dimensional voronoi foams: a comparison between generalized continua and discrete models.
Journal of the Mechanics and Physics of Solids, 56(12):3541–3564, 2008.

[95] R. A. Toupin.
Elastic materials with couple-stresses.
Archive for Rational Mechanics and Analysis, 11(1):385–414, 1962.

[96] T.-H. Tran, V. Monchiet, and G. Bonnet.
A micromechanics-based approach for the derivation of constitutive elastic coefficients of strain-gradient media.
International Journal of Solids and Structures, 49(5):783–792, 2012.

[97] E. Turco, F. dell'Isola, N. L. Rizzi, R. Grygoruk, W. H. Müller, and C. Liebold.
Fiber rupture in sheared planar pantographic sheets: Numerical and experimental evidence.
Mechanics Research Communications, 76:86–90, 2016.

[98] E. Turco, M. Golaszewski, A. Cazzani, and N. L. Rizzi.
Large deformations induced in planar pantographic sheets by loads applied on fibers: experimental validation of a discrete lagrangian model.
Mechanics Research Communications, 76:51–56, 2016.

[99] E. Turco, M. Golaszewski, I. Giorgio, and F. D'Annibale.
Pantographic lattices with non-orthogonal fibres: Experiments and their numerical simulations.
Composites Part B: Engineering, 118:1–14, 2017.

[100] H. Yang, G. Ganzosch, I. Giorgio, and B. E. Abali.
Material characterization and computations of a polymeric metamaterial with a pantographic substructure.
Zeitschrift für angewandte Mathematik und Physik, 69(4):105, 2018.

[101] H. Yang and W. H. Müller.
Computation and experimental comparison of the deformation behavior of pantographic structures with different micro-geometry under shear and torsion.
Journal of Theoretical and Applied Mechanics, 57:421–434, 04 2019.

[102] T. I. Zohdi.
Homogenization methods and multiscale modeling.
Encyclopedia of Computational Mechanics Second Edition, pages 1–24, 2017.

Verification of asymptotic homogenization method developed for periodic architected materials in strain gradient continuum

Hua Yang[a], B. Emek Abali*[b], Wolfgang H. Müller[a],
Salma Barboura[c] and Jia Li[c]

[a] *Technische Universität Berlin, Berlin Germany*
[b] *Uppsala University, Uppsala, Sweden*
[c] *Sorbonne Paris North University, Paris, France*

Abstract

Strain gradient theory is an accurate model for capturing size effects and localization phenomena. However, the challenge in identification of corresponding constitutive parameters limits the practical application of such theory. We present and utilize asymptotic homogenization herein. All parameters in rank four, five, and six tensors are determined with the demonstrated computational approach. Examples for epoxy carbon fiber composite, metal matrix composite, and aluminum foam illustrate the effectiveness and versatility of the proposed method. The influences of volume fraction of matrix, the stack of RVEs, and the varying unit cell lengths on the identified parameters are investigated. The homogenization computational tool is applicable to a wide class materials and makes use of open-source codes in FEniCS.

Keywords: Strain gradient elasticity, Asymptotic homogenization method, Finite element method, Constitutive parameters identification

1 Introduction

Composite materials have been widely used in engineering practice. Due to the heterogeneous nature of composites, the mechanical properties of such materials are dependent on their substructures, for example, the material properties of matrix and reinforcements, the shape of inclusions, or the volume fraction of matrix, etc. An accurate determination of effective properties of these heterogeneous media plays an important role in the design and analysis of composites. Experiments could be conceived to evaluate their effective properties, but it is also possible to compute effective material parameters by means of homogenization methods [12, 42, 18, 24], which reduce the demands for experiments and enable to study microstructure of any complex geometries.

Homogenization techniques [8, 20, 72, 78, 26, 39, 46, 45] allow to represent a heterogeneous elastic material, at the microscale, as an equivalent homogeneous elastic material at the macroscale. Although of primary importance, the conventional homogenization fails to describe the mechanical responses when the heterogeneity of the material is of the same order of the macroscale. This is due to the fact that the conventional homogenization methods are based on a separation of scales, given by $\epsilon = l/L$, $l \ll L$. Here, l represents the typical length scale characteristic of the microstructural heterogeneity and L stands for the macroscopic length scale. If the microstructure consists of relatively small heterogeneity, or the macroscopic length is infinitely large, classical homogenization gives an adequate estimate of the average macroscopic properties [43, 77, 41]. However, if the size of heterogeneity is of the same order of magnitude as that of the macroscopic problem, conventional homogenization technique may fail. For example, size effects occur when the length scale of the macroscopic heterogeneous materials (L) tends to approach the length scale of the underlying heterogeneity (l). An upscaling of Cauchy theory indicates that additional terms are necessary in the constitutive equations [55] in order to predict size effects observed in experiments [60].

*Corresponding author: bilenemek@abali.org

In order to incorporate these additional terms, different homogenization techniques are proposed in the literature, for example in the framework of generalized mechanics [57, 32, 36, 34, 7] such as micropolar theory [50, 25, 76], couple stress [71], strain gradient theory [78, 48, 40, 4, 59, 73, 36], and micromorphic continuum [67, 44]. The task of obtaining homogenized constitutive equations for generalized continua is challenging and a number of debates are active in the literature [50, 25, 54, 28, 66, 37]. Many methods have been proposed to construct strain gradient continua by means of asymptotic homogenization approaches [18, 13, 19, 76], computational approaches [49], dynamic methods [61, 70, 68], and several other identification techniques [23, 22, 58, 3, 6, 5, 65]. Asymptotic homogenization method improves descriptions by exploiting higher order terms and considering their role in macroscopic behaviors [18]. In [52, 53, 14, 74, 2], an asymptotic homogenization based solution was provided to determine parameters of composite materials. Two issues were addressed therein. One is that the identified strain gradient parameters are all zero when structures are homogeneous. The other one is that these parameters are independent of stack of RVEs. In this paper, we briefly recall the homogenization method described in [74]. The method is used to determine 2D and 3D composite materials effective parameters, including epoxy carbon fiber composite material, SiC/Al metal matrix composite, and aluminum foam.

The remainder of this paper is structured as follows: In Section 2, the underlying method is briefly explained. In Section 3, the details of numerical implementation are demonstrated. In Section 4, effective parameters for 2D and 3D composite materials including epoxy-carbon fiber composites, metal matrix composite, and aluminum foam are identified. The homogenization computational tool is developed based on open-source codes in FEniCS. It allows for all kinds of 2D or 3D composite materials constructed by periodic microstructures.

2 Homogenization method

We start from an assertion that the deformation energy for the domain representing RVE, Ω_P, at the microscale is equal to the energy for the RVE at the macroscale, namely

$$\int_{\Omega_P} w^{\mathrm{m}}\,\mathrm{d}V = \int_{\Omega_P} w^{\mathrm{M}}\,\mathrm{d}V\ . \tag{1}$$

The superscripts "m" and "M" are used to denote microscopic and macroscopic quantities, respectively. At the microscale, detailed microstructures are present in the RVE. At the macroscale, the same domain is modeled by a homogeneous "metamaterial." We emphasize that an RVE can be different from a unit cell. A unit cell is the simplest repeating unit of heterogeneity. Spatial repetition of unit cells composes RVEs. At the microscale, the first order theory is used, and at the macroscale, second order theory is employed. Now by starting with a linear strain measure, for a quadratic deformation energy we obtain

$$\int_{\Omega_P} \frac{1}{2}C^{\mathrm{m}}_{ijkl}u^{\mathrm{m}}_{i,j}u^{\mathrm{m}}_{k,l}\,\mathrm{d}V = \int_{\Omega_P} \big(\frac{1}{2}C^{\mathrm{M}}_{ijkl}u^{\mathrm{M}}_{i,j}u^{\mathrm{M}}_{k,l} + G^{\mathrm{M}}_{ijklm}u^{\mathrm{M}}_{i,j}u^{\mathrm{M}}_{k,lm} + \frac{1}{2}D^{\mathrm{M}}_{ijklmn}u^{\mathrm{M}}_{i,jk}u^{\mathrm{M}}_{l,mn}\big)\,\mathrm{d}V\ . \tag{2}$$

C^{m}_{ijkl} is given in each material point of the RVE. We begin with the known microscale and search for its corresponding homogenized model parameters. The effective coefficients, C^{M}_{ijkl}, G^{M}_{ijklm}, and D^{M}_{ijklmn} are the unknowns that we are searching for. We point out that the minor symmetries $C^{\mathrm{m}}_{ijkl} = C^{\mathrm{m}}_{jikl} = C^{\mathrm{m}}_{ijlk}, C^{\mathrm{M}}_{ijkl} = C^{\mathrm{M}}_{jikl} = C^{\mathrm{M}}_{ijlk}$, $G^{\mathrm{M}}_{ijklm} = G^{\mathrm{M}}_{jiklm} = G^{\mathrm{M}}_{ijlkm}$, $D^{\mathrm{M}}_{ijklmn} = D^{\mathrm{M}}_{jiklmn} = D^{\mathrm{M}}_{ijkmln}$ and major symmetries $C^{\mathrm{m}}_{ijkl} = C^{\mathrm{m}}_{klij}$, $C^{\mathrm{M}}_{ijkl} = C^{\mathrm{M}}_{klij}$, $D^{\mathrm{M}}_{ijklmn} = D^{\mathrm{M}}_{lmnijk}$ of the classical and strain gradient stiffness tensors. In what follows, the connections between the microscopic material parameters and macroscopic ones are established.

Let us investigate the macroscopic case for an RVE, Ω_P. Firstly, the geometric center of the RVE is defined as $\overset{\mathrm{c}}{\boldsymbol{X}} = \frac{1}{V}\int_{\Omega_P}\boldsymbol{X}\,\mathrm{d}V$. The macroscopic energy of an RVE reads as follows (the detailed derivation can be found in [74]), as the macroscopic stiffness tensors are constant in space,

$$\begin{aligned}&\int_{\Omega_P} \big(\frac{1}{2}C^{\mathrm{M}}_{ijkl}u^{\mathrm{M}}_{i,j}u^{\mathrm{M}}_{k,l} + G^{\mathrm{M}}_{ijklm}u^{\mathrm{M}}_{i,j}u^{\mathrm{M}}_{k,lm} + \frac{1}{2}D^{\mathrm{M}}_{ijklmn}u^{\mathrm{M}}_{i,jk}u^{\mathrm{M}}_{l,mn}\big)\,\mathrm{d}V\ ,\\ &= \frac{V}{2}C^{\mathrm{M}}_{ijlm}\langle u^{\mathrm{M}}_{i,j}\rangle\langle u^{\mathrm{M}}_{l,m}\rangle + VG^{\mathrm{M}}_{ijklm}\langle u^{\mathrm{M}}_{i,j}\rangle\langle u^{\mathrm{M}}_{k,lm}\rangle + \frac{V}{2}(C^{\mathrm{M}}_{ijlm}\bar{I}_{kn} + D^{\mathrm{M}}_{ijklmn})\langle u^{\mathrm{M}}_{i,jk}\rangle\langle u^{\mathrm{M}}_{l,mn}\rangle\ ,\end{aligned} \tag{3}$$

$$\bar{I}_{kn} = \frac{1}{V}\int_{\Omega_P}(X_k - \overset{\mathrm{c}}{X}_k)(X_n - \overset{\mathrm{c}}{X}_n)\,\mathrm{d}V\ . \tag{4}$$

where

$$\langle u^{\mathrm{M}}_{i,j}\rangle = u^{\mathrm{M}}_{i,j}\Big|_{\overset{\mathrm{c}}{\boldsymbol{X}}}\ , \qquad \langle u^{\mathrm{M}}_{i,jk}\rangle = u^{\mathrm{M}}_{i,jk}\Big|_{\overset{\mathrm{c}}{\boldsymbol{X}}}\ . \tag{5}$$

At the microscale, the asymptotic homogenization method is used to approximate the deformation energy for the RVE. We introduce a small parameter ϵ, which is defined as $\epsilon = \frac{l}{L}$, where l is the characteristic length of the microstructure, L is the length of the macroscopic structure as shown in Fig. 1. We remark that ϵ is the so-called homothetic ratio, which shows the scaling law for strain gradient moduli. This property will be illustrated later. A local coordinate is then introduced as

$$y_j = \frac{1}{\epsilon}(X_j - \overset{\mathrm{c}}{X}_j) \ , \tag{6}$$

which is used to describe the local fluctuations caused by microscopic heterogeneity. Variable $\boldsymbol{X}$ is associated with the macroscopic scale. The displacement field for the RVE at the microscale is thus approximated with regard to ϵ as

$$\boldsymbol{u}^{\mathrm{m}}(\boldsymbol{X}) = \overset{0}{\boldsymbol{u}}(\boldsymbol{X},\boldsymbol{y}) + \epsilon \overset{1}{\boldsymbol{u}}(\boldsymbol{X},\boldsymbol{y}) + \epsilon^2 \overset{2}{\boldsymbol{u}}(\boldsymbol{X},\boldsymbol{y}) + \dots \ . \tag{7}$$

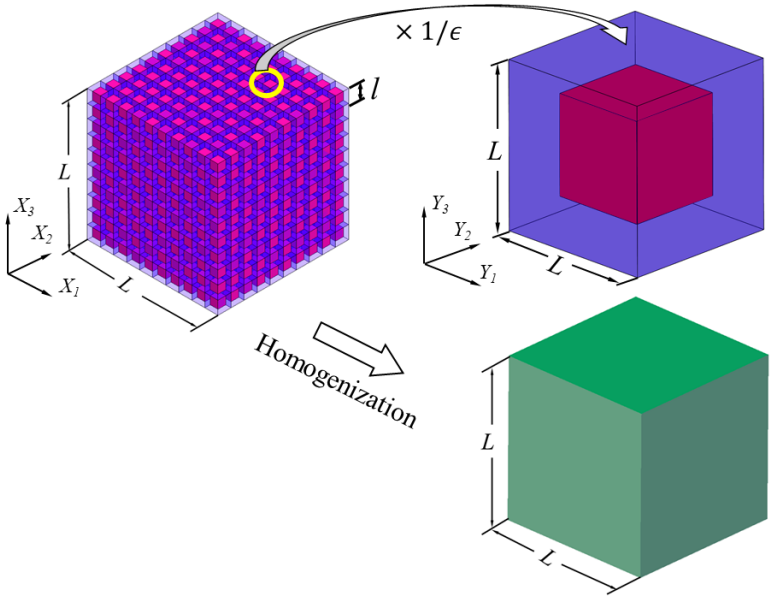

Figure 1: The heterogeneous continuum and its equivalent homogenized continuum.

For a linear elastostatics problem, the governing equation within the RVE is written as

$$\left(C^{\mathrm{m}}_{ijkl} u^{\mathrm{m}}_{k,l}\right)_{,j} + \rho^{\mathrm{m}} f_i = 0 \ , \tag{8}$$

where $\rho^{\mathrm{m}} f_i$ are volume forces, ρ^{m} is the mass density at the microscale, hence it is a function in $\boldsymbol{X}$ effected by the heterogeneous structure. By substituting Eqn. (7) to Eqn. (8) and gathering terms having the same order in ϵ leads to the following equations:

- in the order of ϵ^{-2}

$$\frac{\partial}{\partial y_j}\left(C^{\mathrm{m}}_{ijkl} \frac{\partial \overset{0}{u}_k}{\partial y_l}\right) = 0 \ ; \tag{9}$$

- in the order of ϵ^{-1}

$$\left(C^{\mathrm{m}}_{ijkl} \frac{\partial \overset{0}{u}_k}{\partial y_l}\right)_{,j} + \frac{\partial}{\partial y_j}\left(C^{\mathrm{m}}_{ijkl} \overset{0}{u}_{k,l}\right) + \frac{\partial}{\partial y_j}\left(C^{\mathrm{m}}_{ijkl} \frac{\partial \overset{1}{u}_k}{\partial y_l}\right) = 0 \ ; \tag{10}$$

- in the order of ϵ^{0}

$$\left(C^{\mathrm{m}}_{ijkl} \overset{0}{u}_{k,l}\right)_{,j} + \left(C^{\mathrm{m}}_{ijkl} \frac{\partial \overset{1}{u}_k}{\partial y_l}\right)_{,j} + \frac{\partial}{\partial y_j}\left(C^{\mathrm{m}}_{ijkl} \overset{1}{u}_{k,l}\right) + \frac{\partial}{\partial y_j}\left(C^{\mathrm{m}}_{ijkl} \frac{\partial \overset{2}{u}_k}{\partial y_l}\right) + \rho^{\mathrm{m}} f_i = 0 \ . \tag{11}$$

The only possible solution of Eqn. (9) is to restrict $\overset{0}{u}_i(\boldsymbol{X})$ as

$$\overset{0}{u}_i = \overset{0}{u}_i(\boldsymbol{X}) \ . \tag{12}$$

Because $\overset{0}{u}_i(\boldsymbol{X})$ is only dependent on the macroscopic coordinates, from Eqn. (7), it is assumed to be the macroscopic displacement $\overset{0}{u}_i(\boldsymbol{X}) = u_i^{\mathrm{M}}(\boldsymbol{X})$. After substituting Eqn. (12) into Eqn. (10), and introducing $\varphi_{abc} = \varphi_{abc}(\boldsymbol{y})$ which is $\boldsymbol{y}$-periodic with zero average value $\int_{\Omega^P} \varphi_{abi}\,\mathrm{d}V = 0$, we obtain

$$\frac{\partial}{\partial y_j}\left(C^{\mathrm{m}}_{ijkl}\left(\frac{\partial \varphi_{abk}}{\partial y_l} + \delta_{ak}\delta_{bl}\right)\right) = 0 \ . \tag{13}$$

Consequently, the solution of Eqn. (10) is given as

$$\overset{1}{u}_i = \varphi_{abi} u^{\mathrm{M}}_{a,b}(\boldsymbol{X}) + \overset{1}{\bar{u}}_i(\boldsymbol{X}) \ , \tag{14}$$

where $\overset{1}{\bar{u}}_i = \overset{1}{\bar{u}}_i(\boldsymbol{X})$ are integration constants.

By recalling the governing equation at the macroscale, we have

$$C^{\mathrm{M}}_{ijkl} u^{\mathrm{M}}_{k,lj} - D^{\mathrm{M}}_{ijklmn} u^{\mathrm{M}}_{l,mnkj} + \rho^{\mathrm{M}} f_i = 0 \ , \tag{15}$$

with $\rho^{\mathrm{M}} = \frac{1}{V}\int_{\Omega_P} \rho^{\mathrm{m}}\,\mathrm{d}V$ and the assumption that f_i keeps unchanged at the micro- and macroscales. By neglecting the fourth order term in Eqn. (15), we obtain

$$f_i = -\frac{C^{\mathrm{M}}_{ijkl} u^{\mathrm{M}}_{k,lj}}{\rho^{\mathrm{M}}} \ . \tag{16}$$

By plugging Eqn. (12), Eqn. (14) (with $\overset{1}{\bar{u}}_i(\boldsymbol{X}) = 0$), and Eqn. (16) into Eqn. (11) and introducing ψ_{abci} which is $\boldsymbol{y}$-periodic with zero average $\int_{\Omega^P} \psi_{abci}\,\mathrm{d}V = 0$, the solution of $\overset{2}{u}_i$ may be given as:

$$\overset{2}{u}_i = \psi_{abci} u^{\mathrm{M}}_{a,bc}(\boldsymbol{X}) + \overset{2}{\bar{u}}_i(\boldsymbol{X}) \ , \tag{17}$$

where $\overset{2}{\bar{u}}_i(\boldsymbol{X})$ are integration constants in $\boldsymbol{y}$. The fourth order tensor ψ_{abcd} must satisfy

$$\frac{\partial}{\partial y_j}\left(C^{\mathrm{m}}_{ijkl}\left(\frac{\partial \psi_{abck}}{\partial y_l} + \varphi_{abk}\delta_{lc}\right)\right) + C^{\mathrm{m}}_{ickl}\left(\frac{\partial \varphi_{abk}}{\partial y_l} + \delta_{ka}\delta_{lb}\right) - \frac{\rho^{\mathrm{m}}}{\rho^{\mathrm{M}}} C^{\mathrm{M}}_{icab} = 0 \ . \tag{18}$$

Therefore, the microscale displacement field is rewritten as

$$u^{\mathrm{m}}_i(\boldsymbol{X}, \boldsymbol{y}) = u^{\mathrm{M}}_i(\boldsymbol{X}) + \epsilon \varphi_{abi}(\boldsymbol{y}) u^{\mathrm{M}}_{a,b}(\boldsymbol{X}) + \epsilon^2 \psi_{abci}(\boldsymbol{y}) u^{\mathrm{M}}_{a,bc}(\boldsymbol{X}) + \dots \ . \tag{19}$$

By using Eqn. (19) and the latter on the left-hand side of Eqn. (2) the microscopic energy becomes

$$\begin{gathered}\int_{\Omega_P} \frac{1}{2} C^{\mathrm{m}}_{ijkl} u^{\mathrm{m}}_{i,j} u^{\mathrm{m}}_{k,l}\,\mathrm{d}V = \\ \frac{V}{2}\left(\bar{C}_{abcd}\langle u^{\mathrm{M}}_{a,b}\rangle\langle u^{\mathrm{M}}_{c,d}\rangle + \bar{G}_{abcde}\langle u^{\mathrm{M}}_{a,b}\rangle\langle u^{\mathrm{M}}_{c,de}\rangle + \bar{D}_{abcdef}\langle u^{\mathrm{M}}_{a,bc}\rangle\langle u^{\mathrm{M}}_{d,ef}\rangle\right) \ ,\end{gathered} \tag{20}$$

with

$$\begin{aligned}\bar{C}_{abcd} &= \frac{1}{V}\int_{\Omega_P} C^{\mathrm{m}}_{ijkl} L_{abij} L_{cdkl}\,\mathrm{d}V \ , \\ \bar{G}_{abcde} &= \frac{2\epsilon}{V}\int_{\Omega_P} C^{\mathrm{m}}_{ijkl} L_{abij} M_{cdekl}\,\mathrm{d}V \\ \bar{D}_{abcdef} &= \frac{\epsilon^2}{V}\int_{\Omega_P} C^{\mathrm{m}}_{ijkl} M_{abcij} M_{defkl}\,\mathrm{d}V \ ,\end{aligned} \tag{21}$$

The appearance of ϵ^2 is due to the fact that Eqn. (25) is expressed in the local coordinate $\boldsymbol{y}$ (The fifth order

tensor $\boldsymbol{M}$ is only related to $\boldsymbol{y}$).

$$\begin{aligned} L_{abij} &= \delta_{ia}\delta_{jb} + \frac{\partial \varphi_{abi}}{\partial y_j} \ , \\ M_{abcij} &= y_c\Big(\delta_{ia}\delta_{jb} + \frac{\partial \varphi_{abi}}{\partial y_j}\Big) + \Big(\varphi_{abi}\delta_{jc} + \frac{\partial \psi_{abci}}{\partial y_j}\Big) \ . \end{aligned} \tag{22}$$

Based on Eqn. (2) the effective parameters are calculated by

$$C^{\mathrm{M}}_{abcd} = \frac{1}{V}\int_{\Omega_P} C^{\mathrm{m}}_{ijkl} L_{abij} L_{cdkl}\,\mathrm{d}V \ , \tag{23}$$

$$G^{\mathrm{M}}_{abcde} = \frac{\epsilon}{V}\int_{\Omega_P} C^{\mathrm{m}}_{ijkl} L_{abij} M_{cdekl}\,\mathrm{d}V \ , \tag{24}$$

$$D^{\mathrm{M}}_{abcdef} = \frac{\epsilon^2}{V}\left(\int_{\Omega_P} C^{\mathrm{m}}_{ijkl} M_{abcij} M_{defkl}\,\mathrm{d}V - C^{\mathrm{M}}_{abde}\int_{\Omega_P} y_c y_f\,\mathrm{d}V\right) . \tag{25}$$

It should be remarked that the Eqn. (23) coincides with the conventional asymptotic homogenization method. The classical stiffness tensor is scale independent. However, as observed from the Eqn. (25), strain gradient stiffness parameters depend on ϵ^2. Indeed, these parameters emerge related to the substructure and vanish as $\epsilon = 0$ meaning that the substructure diminishes. We stress that this distinction is of importance and comes out of the proposed methodology quite naturally. As obvious in Eqn. (6), the homothetic ratio, ϵ, acts as a multiplier between the macroscopic length scale (in global coordinates, $\boldsymbol{X}$) and microscopic length scale (in local coordinates, $\boldsymbol{y}$). In this way, we acquire different $\boldsymbol{G}^{\mathrm{M}}$ and $\boldsymbol{D}^{\mathrm{M}}$ coefficients for the same RVE in larger structures. The role of ϵ will be further illustrated by using numerical examples.

3 Numerical implementation

In order to identify effective parameters, Eqn. (23) and Eqn. (25) need to be resolved, which requires $\boldsymbol{\varphi}$ and $\boldsymbol{\psi}$. The tensors $\boldsymbol{\varphi}$ and $\boldsymbol{\psi}$ are the solutions of Eqn. (13) and Eqn. (18), which are solved numerically by the finite element method. As shown in Figure 2, six cases $\varphi_{11i}, \varphi_{22i}, \varphi_{33i}, \varphi_{23i}, \varphi_{13i}, \varphi_{12i}$ in total in 3D need to be computed under periodic boundary conditions. After using integration by parts, considering the constraints of zero average for $\boldsymbol{\varphi}$, the following weak form for φ_{abk} is generated

$$\int_{\Omega^P}\left(C^{\mathrm{m}}_{ijkl}\Big(\frac{\partial \varphi_{\underline{ab}k}}{\partial y_l} + \delta_{\underline{a}k}\delta_{\underline{b}l}\Big)\right)\frac{\partial \delta\varphi_{\underline{ab}i}}{\partial y_j}\,\mathrm{d}V + \delta\int \lambda_{abi}\phi_{abi}\,\mathrm{d}V = 0 \tag{26}$$

and then immediately we have

$$\int_{\Omega^P}\left(C^{\mathrm{m}}_{ijkl}\Big(\frac{\partial \varphi_{\underline{ab}k}}{\partial y_l} + \delta_{\underline{a}k}\delta_{\underline{b}l}\Big)\right)\frac{\partial \delta\varphi_{\underline{ab}i}}{\partial y_j}\,\mathrm{d}V + \int_{\Omega^P}\lambda_{\underline{ab}i}\delta\varphi_{\underline{ab}i}\,\mathrm{d}V + \int_{\Omega^P}\delta\lambda_{\underline{ab}i}\varphi_{\underline{ab}i}\,\mathrm{d}V = 0 \ , \tag{27}$$

where over underlined indices, no summation convention is applied. All fields with a variational delta, δ, denote a corresponding test function such that $\boldsymbol{\varphi}$ and $\boldsymbol{\lambda}$ are unknowns. For each case of $\varphi_{11i}, \varphi_{22i}, \varphi_{33i}, \varphi_{23i}, \varphi_{13i}, \varphi_{12i}$, a corresponding LAGRANGE multiplier, $\lambda_{11i}, \lambda_{22i}, \lambda_{33i}, \lambda_{23i}, \lambda_{13i}, \lambda_{12i}$, is employed to enforce the zero average constrains of $\boldsymbol{\varphi}$ [16]. Likewise, the weak form for calculating ψ_{abci} reads

$$\begin{aligned} &\int_{\Omega^P}\Bigg(\Bigg(C^{\mathrm{m}}_{ijkl}\Big(\frac{\partial \psi_{\underline{abc}k}}{\partial y_l} + \varphi_{\underline{ab}k}\delta_{l\underline{c}}\Big)\Bigg)\frac{\partial \delta\psi_{\underline{abc}i}}{\partial y_j} - \\ &- C^{\mathrm{m}}_{i\underline{c}kl}\Big(\frac{\partial \varphi_{\underline{ab}k}}{\partial y_l} + \delta_{k\underline{a}}\delta_{l\underline{b}}\Big)\delta\psi_{\underline{abc}i} + \frac{\rho^{\mathrm{m}}}{\rho^{\mathrm{M}}}C^{\mathrm{M}}_{i\underline{cab}}\delta\psi_{\underline{abc}i}\Bigg)\,\mathrm{d}V + \\ &+ \int_{\Omega^P}\lambda_{\underline{abc}i}\delta\psi_{\underline{abc}i}\,\mathrm{d}V + \int_{\Omega^P}\delta\lambda_{\underline{abc}i}\psi_{\underline{abc}i}\,\mathrm{d}V = 0 \ . \end{aligned} \tag{28}$$

There are 18 weak forms in 3D to be solved for $\psi_{111i}, \psi_{112i}, \ldots \psi_{123i}$..

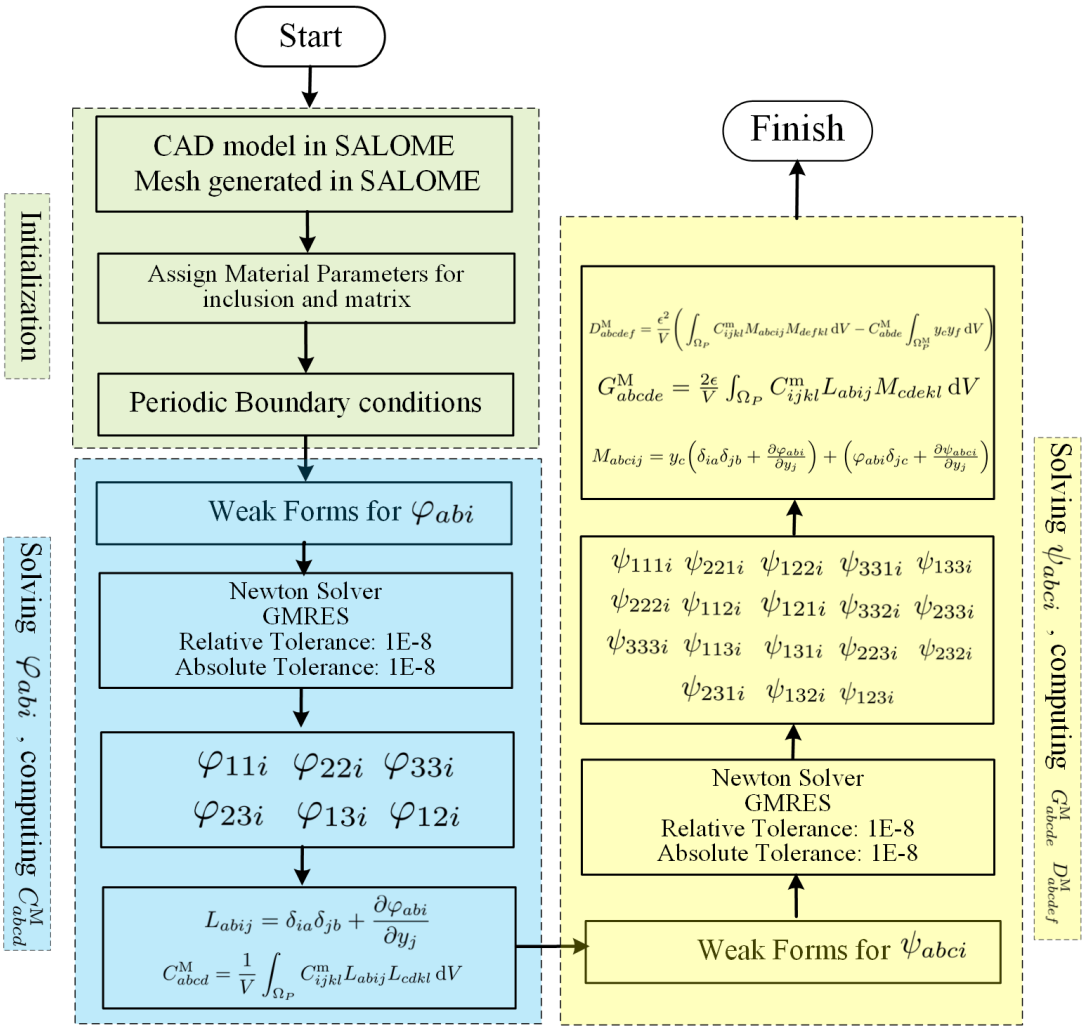

Figure 2: The flowchart of the numerical implementation.

The weak forms have been solved by the FEniCS platform. CAD model and mesh files are created by using an open-source software SALOME [1]. Triangle for surfaces elements and tetrahedron for volume elements are used to discretize the system. The same mesh is used such that the corresponding edges (in 2D) or surfaces (in 3D) are matching for nodes to be defined as the same degree of freedom in order to enforce the periodic boundary conditions as shown in Figure 3.

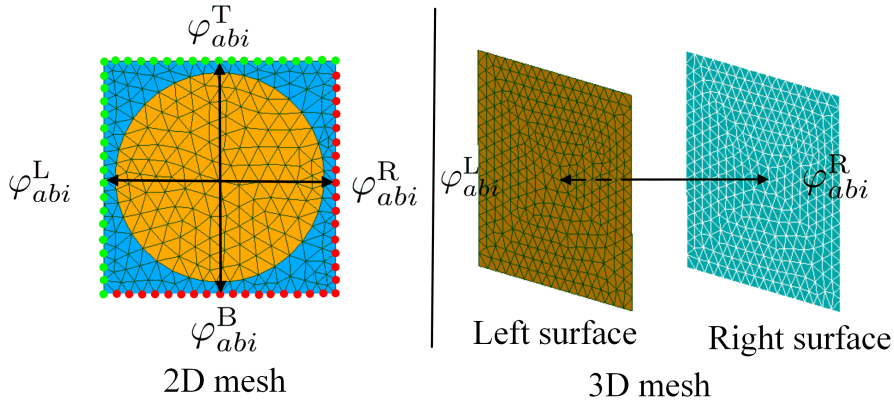

Figure 3: Periodic boundary conditions applied in FEM. Left: Right edge and green edge have the same mesh. Right: Only corresponding surfaces are shown, and so-called left surface and right surface have the same mesh. Same mesh is necessary for implementing periodic boundary conditions.

4 Numerical examples

The proposed homogenization method provides a unified analysis for general 2D and 3D composites. It can be used to homogenize fiber reinforced composites, particulate composites, and porous materials. In order to show the predictive capability of the proposed method, four examples are selected in the following.

4.1 2D epoxy-carbon fiber composite

A 2 dimensional carbon fibers reinforced epoxy composite structure is investigated. The material properties [1] for both constituents (matrix and inclusion) are shown in Table 1. The size of the unit cell is 1 mm. The fiber is of circular shape, its radius is 0.45 mm, thus, the volume fraction of matrix is 36.4%.

Table 1: Material properties used for 2D epoxy-carbon fiber composite. E Young's modulus, ν Poisson's ratio, and ρ mass density.

Type	E in GPa	ν	ρ in kg/m^3
Matrix (Epoxy)	17.3	0.35	1780
Inclusion (Carbon fiber)	35.9	0.30	1650

VOIGT notations as presented in Table 2, Table 3 are used to represent rank four, five, six tensors as matrices (analogous to VOIGT's notation).

Table 2: VOIGT notation used for 2D strain tensors.

A	1	2	3
ij	11	22	12

Table 3: VOIGT kind-notation used for 2D strain-gradient tensors.

θ	1	2	3	4	5	6
ijk	111	112	221	222	121	122

The convergence analysis is conducted as shown in Table 4. Due to the cubic material symmetry, it is expected the $C_{1111} = C_{2222}$, $D_{111111} = D_{222222}$. Therefore, when the ratios C_{1111}/C_{2222}, and D_{111111}/D_{222222} tend to be 1, the computation is converged.

Table 4: Convergence analysis. With the increasing of degrees of freedom, the ratios C_{1111}/C_{2222}, and D_{111111}/D_{222222} reach 1.

DOFs	C_{1111} GPa	C_{2222} GPa	C_{1111}/C_{2222}	D_{111111} N	D_{222222} N	D_{111111}/D_{222222}
1342	38.6	38.7	99.7 %	510.4	496.0	103.0 %
22362	38.9	38.9	100.0 %	505.3	506.1	100.0 %
90226	39.0	39.0	100.0 %	506.4	505.8	100.0 %

The solutions for $\boldsymbol{\varphi}$ and $\boldsymbol{\psi}$ are presented in Figure 4. It is observed that these fluctuations are all periodic. Furthermore, due to the fact that the material is cubic, rotating φ_{22}, ψ_{111}, ψ_{221}, ψ_{122} by 90 ° gives the same shapes as φ_{11}, ψ_{222}, ψ_{112}, ψ_{121}.

[1] Values of material properties are taken from matweb.com

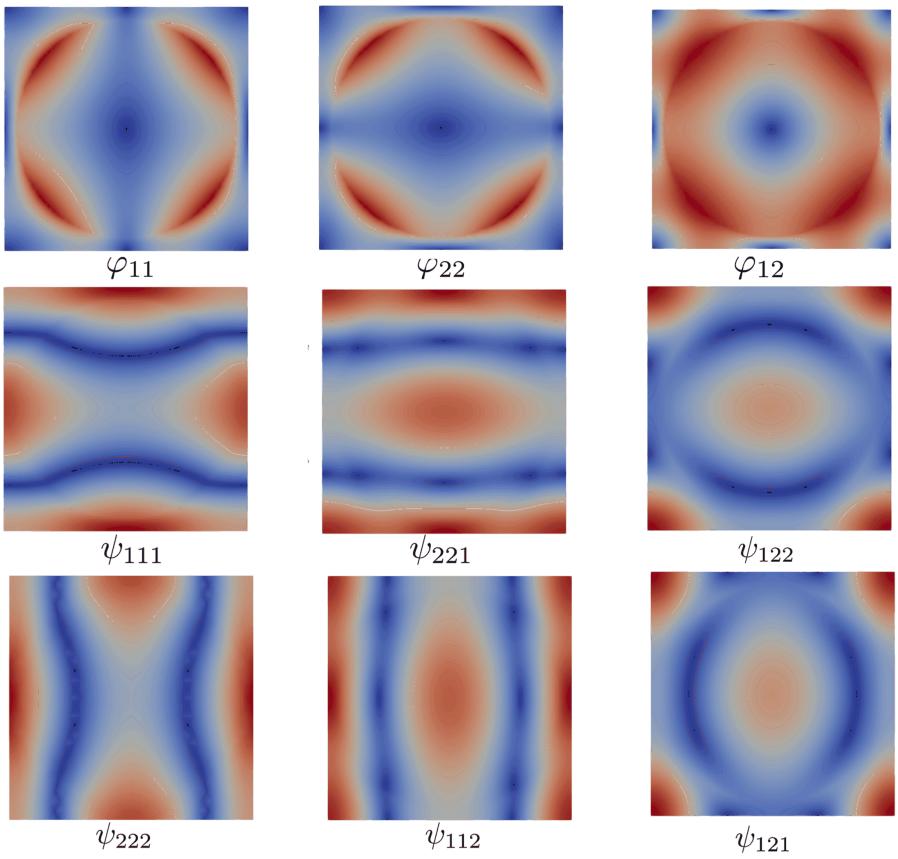

Figure 4: Solutions for $\boldsymbol{\varphi}$ and $\boldsymbol{\psi}$. Color distribution showing the cubic symmetry resulted local fluctuation in $\boldsymbol{\varphi}$ and $\boldsymbol{\psi}$ fields. Color bars are omitted since we analyze qualitatively.

The identified effective classical and stain gradient stiffness tensors are shown as follows:

$$C^{\mathrm{M}}_{AB} = \begin{pmatrix} 39.0 & 18.0 & 0.0 \\ 18.0 & 39.0 & 0.0 \\ 0.0 & 0.0 & 10.0 \end{pmatrix} \text{ GPa} ,$$

$$D^{\mathrm{M}}_{\theta\gamma} = \begin{pmatrix} 506.4 & 181.9 & 0.0 & -0.0 & 0.0 & -182.2 \\ 181.9 & -299.4 & 0.0 & 0.0 & 0.0 & -176.2 \\ 0.0 & 0.0 & 181.2 & -175.4 & -183.0 & 0.0 \\ 0.0 & 0.0 & -175.4 & -298.5 & 181.2 & 0.0 \\ 0.0 & 0.0 & -183.0 & 181.2 & 505.8 & 0.0 \\ -182.2 & -176.2 & 0.0 & 0.0 & 0.0 & 181.0 \end{pmatrix} \text{ N} .$$

It is found that there are three independent parameters in the stiffness tensor and six independent parameters in the strain gradient stiffness tensor. This observation is consistent with [10, 9] for cubic materials. By using the Voigt notation similar to the approach as in [10, 9, 11] in Table 5, the strain gradient stiffness matrix is made to be block-diagonal; each diagonal block matrix includes only non-zero parameters, and each diagonal block matrix is invariant under every cyclic permutation of $\boldsymbol{X}$ axis, $\boldsymbol{Y}$ axis, and $\boldsymbol{Z}$ axis [11]. Therefore, the Voigt notaion proposed in [11] will be used throughout the paper.

Table 5: Voigt notation used for 2D strain-gradient tensors proposed in [11].

α	1	2	3	4	5	6
ijk	111	221	122	222	112	121

$$D^{\mathrm{M}}_{\alpha\beta} = \begin{pmatrix} 506.4 & 181.9 & -182.2 & 0.0 & 0.0 & 0.0 \\ 181.9 & -299.4 & -176.2 & 0.0 & 0.0 & 0.0 \\ -182.2 & -176.2 & 181.0 & 0.0 & 0.0 & 0.0 \\ 0.0 & 0.0 & 0.0 & 505.8 & 181.2 & -183.0 \\ 0.0 & 0.0 & 0.0 & 181.2 & -298.5 & -175.4 \\ 0.0 & 0.0 & 0.0 & -183.0 & -175.4 & 181.2 \end{pmatrix} \mathrm{N}\ .$$

4.2 Interpretation of the homothetic ratio

When determining the strain gradient moduli, physical relevance of the so-called homothetic ratio, ϵ, is necessary for assessing the correct value. Let us consider specific cases as shown in Figure 5. In Figure 5 (a), the macroscopic length is $L = 4$ mm and the microscopic length is $l = 1$ mm. By using $\epsilon = \frac{l}{L} = \frac{1}{4}$, the 1 mm long RVE in global coordinates is magnified to 4 mm in the local coordinate. Since Eqn. (25) are expressed in the local coordinate $\boldsymbol{y}$, the parameters in D^{M}_{abcdef} are calculated in the local coordinate. Thus, the length of the computational domain in Eqn. (25) is 4 mm. Likewise, in Figure 5 (b), the length of integration domain is 2 times larger than that in Figure 5 (a). However $\epsilon = \frac{1}{8}$ is half of the former one. This leads to the equal values for strain gradient moduli. Consequently, in the last section, ϵ can be chosen as, for example, $\frac{1}{4}$ or $\frac{1}{8}$, as long as the corresponding length of integration domain is chosen accordingly.

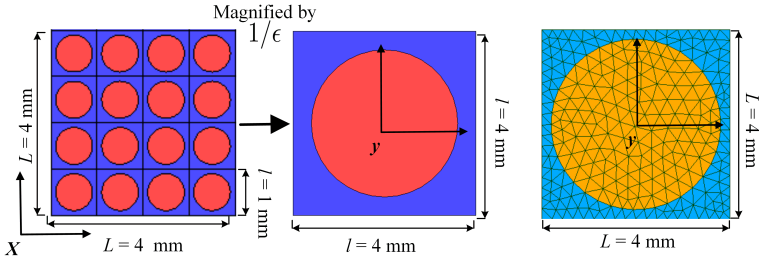

(a) The homothetic ratio $\epsilon = \frac{1}{4}$.

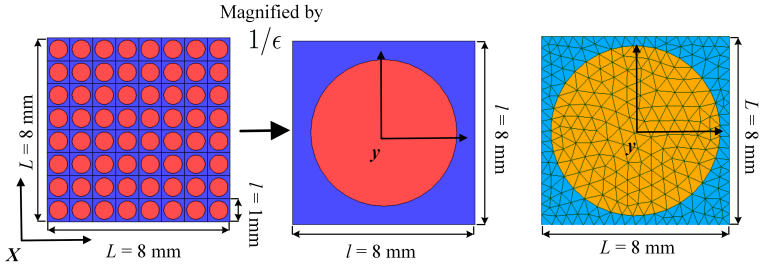

(b) The homothetic ratio $\epsilon = \frac{1}{8}$.

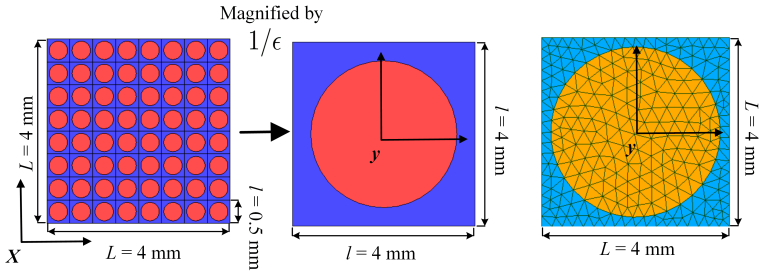

(c) The homothetic ratio $\epsilon = \frac{1}{8}$.

Figure 5: Visualization regarding the meaning of the homothetic ratio, ϵ, the local RVE remains the same, however, the ratio between micro- and macroscales varies.

Indeed, a scaling rule occurs for the strain gradient moduli. For example, in Figure 5 (c), the length of RVE is half of that in Figure 5 (a). The same macroscopic length equals in the calculated integrals in Eqn. (25).

The differences of the obtained strain gradient parameters originate from the ϵ^2 as presented in Eqn. (25). The strain gradient parameters for Figure 5 (a) are 4 times larger than those for Figure 5 (c). This scaling factor is calculated as the ratio between ϵ^2, also equal to the square of ratio of the unit cell lengths. Therefore, herein, we conclude that the strain gradient moduli is indeed not related to the macroscopic length but the microscopic length. This interpretation is indeed in coincidence with the well-known size effect in the literature. We emphasize that the substructure affects the values in C^{M}_{ijkl}, but not its ratio with respect to the macroscale. Therefore, for different substructures, C^{M}_{ijkl} needs to be recalculated. For the same substructure but different homothetic ratios, they remain the same.

4.3 3D cases

In the followings, we consider 3 dimensional cases. The effective parameters in the classical stiffness tensor and strain gradient stiffness tensor for a carbon fibers reinforced epoxy composite, a (hard) spherical particles reinforced (soft) matrix, a metal matrix composite, and an aluminum foam will be investigated. The used VOIGT notations for these 3 dimensional cases are displayed in Table 6 and Table 7.

Table 6: VOIGT notation used for 3D strain tensors.

A	1	2	3	4	5	6
ij	11	22	33	23	13	12

Table 7: VOIGT notation used for 3D strain-gradient tensors.

α	1	2	3	4	5	6	7	8	9	10	11	12	13	14	15	16	17	18
ijk	111	221	122	331	133	222	112	121	332	233	333	113	131	223	232	231	132	123

4.3.1 3D fiber reinforced composite

Carbon fiber is modeled by using a cylinder shaped inclusion in 3D. In order to compare and validate the results, the same material properties shown in Table 1 are used for inclusion and matrix. The radius of the cylinder is of 0.45 mm so that the volume fraction of matrix reads 36.4 %, which are both equal to the example shown in 2D. The calculated parameters are shown as follows:

$$C^{\mathrm{M}}_{AB} = \begin{pmatrix} 38.6 & 17.9 & 18.0 & 0.0 & 0.0 & 0.0 \\ 17.9 & 38.6 & 18.0 & 0.0 & 0.0 & 0.0 \\ 18.0 & 18.0 & 40.1 & 0.0 & 0.0 & 0.0 \\ 0.0 & 0.0 & 0.0 & 10.2 & 0.0 & 0.0 \\ 0.0 & 0.0 & 0.0 & 0.0 & 10.2 & 0.0 \\ 0.0 & 0.0 & 0.0 & 0.0 & 0.0 & 9.7 \end{pmatrix} \text{ GPa} ,$$

$$D^{\mathrm{M}}_{\alpha\beta} = \begin{pmatrix} 506.2 & 180.1 & -178.8 & 213.5 & 17.3 & 0.0 & 0.0 & 0.0 & 0.0 & 0.0 & 0.0 & 0.0 & 0.0 & 0.0 & 0.0 & 0.0 & 0.0 & 0.0 \\ 180.1 & -297.1 & -168.8 & -11.4 & -93.9 & 0.0 & 0.0 & 0.0 & 0.0 & 0.0 & 0.0 & 0.0 & 0.0 & 0.0 & 0.0 & 0.0 & 0.0 & 0.0 \\ -178.8 & -168.8 & 180.3 & -100.6 & -64.7 & 0.0 & 0.0 & 0.0 & 0.0 & 0.0 & 0.0 & 0.0 & 0.0 & 0.0 & 0.0 & 0.0 & 0.0 & 0.0 \\ 213.5 & -11.4 & -100.6 & -321.4 & -284.1 & 0.0 & 0.0 & 0.0 & 0.0 & 0.0 & 0.0 & 0.0 & 0.0 & 0.0 & 0.0 & 0.0 & 0.0 & 0.0 \\ 17.3 & -93.9 & -64.7 & -284.1 & 55.4 & 0.0 & 0.0 & 0.0 & 0.0 & 0.0 & 0.0 & 0.0 & 0.0 & 0.0 & 0.0 & 0.0 & 0.0 & 0.0 \\ 0.0 & 0.0 & 0.0 & 0.0 & 0.0 & 506.5 & 180.2 & -178.8 & 213.6 & 16.9 & 0.0 & 0.0 & 0.0 & 0.0 & 0.0 & 0.0 & 0.0 & 0.0 \\ 0.0 & 0.0 & 0.0 & 0.0 & 0.0 & 180.2 & -297.4 & -169.0 & -11.5 & -94.0 & 0.0 & 0.0 & 0.0 & 0.0 & 0.0 & 0.0 & 0.0 & 0.0 \\ 0.0 & 0.0 & 0.0 & 0.0 & 0.0 & -178.8 & -169.0 & 180.2 & -100.6 & -64.7 & 0.0 & 0.0 & 0.0 & 0.0 & 0.0 & 0.0 & 0.0 & 0.0 \\ 0.0 & 0.0 & 0.0 & 0.0 & 0.0 & 213.6 & -11.5 & -100.6 & -322.0 & -283.8 & 0.0 & 0.0 & 0.0 & 0.0 & 0.0 & 0.0 & 0.0 & 0.0 \\ 0.0 & 0.0 & 0.0 & 0.0 & 0.0 & 16.9 & -94.0 & -64.7 & -283.8 & 55.4 & 0.0 & 0.0 & 0.0 & 0.0 & 0.0 & 0.0 & 0.0 & 0.0 \\ 0.0 & 0.0 & 0.0 & 0.0 & 0.0 & 0.0 & 0.0 & 0.0 & 0.0 & 0.0 & 164.1 & 4.0 & -207.8 & 4.0 & -207.7 & 0.0 & 0.0 & 0.0 \\ 0.0 & 0.0 & 0.0 & 0.0 & 0.0 & 0.0 & 0.0 & 0.0 & 0.0 & 0.0 & 4.0 & 5.9 & 39.6 & -4.9 & -47.3 & 0.0 & 0.0 & 0.0 \\ 0.0 & 0.0 & 0.0 & 0.0 & 0.0 & 0.0 & 0.0 & 0.0 & 0.0 & 0.0 & -207.8 & 39.6 & 181.9 & -47.3 & -126.9 & 0.0 & 0.0 & 0.0 \\ 0.0 & 0.0 & 0.0 & 0.0 & 0.0 & 0.0 & 0.0 & 0.0 & 0.0 & 0.0 & 4.0 & -4.9 & -47.3 & 6.2 & 39.3 & 0.0 & 0.0 & 0.0 \\ 0.0 & 0.0 & 0.0 & 0.0 & 0.0 & 0.0 & 0.0 & 0.0 & 0.0 & 0.0 & -207.7 & -47.3 & -126.9 & 39.3 & 182.1 & 0.0 & 0.0 & 0.0 \\ 0.0 & 0.0 & 0.0 & 0.0 & 0.0 & 0.0 & 0.0 & 0.0 & 0.0 & 0.0 & 0.0 & 0.0 & 0.0 & 0.0 & 0.0 & -124.2 & -143.1 & -67.6 \\ 0.0 & 0.0 & 0.0 & 0.0 & 0.0 & 0.0 & 0.0 & 0.0 & 0.0 & 0.0 & 0.0 & 0.0 & 0.0 & 0.0 & 0.0 & -143.1 & -124.5 & -67.6 \\ 0.0 & 0.0 & 0.0 & 0.0 & 0.0 & 0.0 & 0.0 & 0.0 & 0.0 & 0.0 & 0.0 & 0.0 & 0.0 & 0.0 & 0.0 & -67.6 & -67.6 & 22.3 \end{pmatrix} \text{ N} .$$

We stress that the algorithm computes G as well, but as expected from the centro-symmetry in the substructure, all coefficients of G vanish. The unidirectional laminate carbon reinforced epoxy composite is a transverse

isotropic material. There are five independent parameters in the classical stiffness tensor, as shown below

$$C^{\mathrm{M}}_{AB} = \begin{pmatrix} c_1 & c_1-2c_5 & c_2 & 0.0 & 0.0 & 0.0 \\ c_1-2c_5 & c_1 & c_2 & 0.0 & 0.0 & 0.0 \\ c_2 & c_2 & c_3 & 0.0 & 0.0 & 0.0 \\ 0.0 & 0.0 & 0.0 & c_4 & 0.0 & 0.0 \\ 0.0 & 0.0 & 0.0 & 0.0 & c_4 & 0.0 \\ 0.0 & 0.0 & 0.0 & 0.0 & 0.0 & c_5 \end{pmatrix}.$$

We stress that the computed parameters are matching this relation within a tolerance of ±6.7%. After investigating the strain gradient stiffness tensor, we find the relations between higher order parameters as shown in Figure 6.

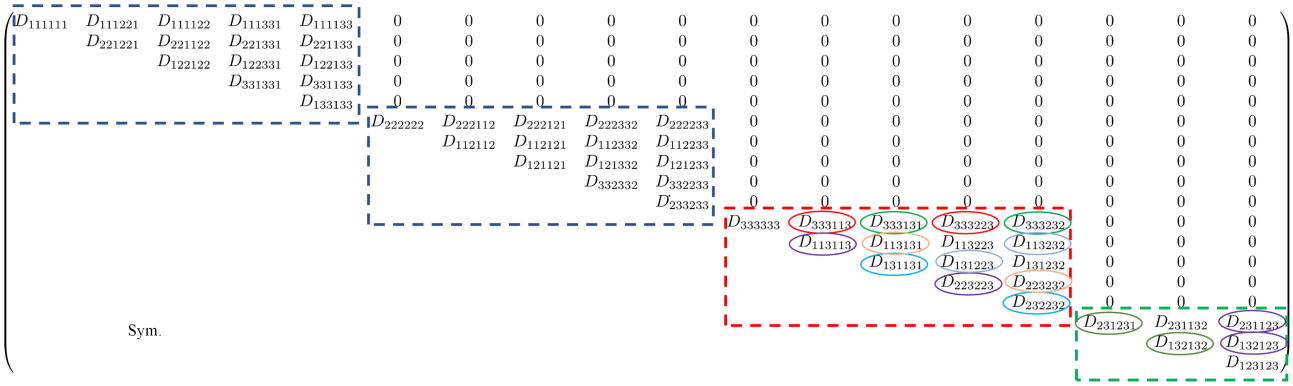

Figure 6: The structure of strain gradient stiffness tensor for transverse isotropic materials. It is found that the first two 5×5 matrices in the diagonal are equal, for example, $D_{111111} = D_{222222}$. In the third 5×5 matrix in the diagonal, it is also observed that $D_{333113} = D_{333223}$, $D_{333131} = D_{333232}$, $D_{113113} = D_{223223}$, $D_{113131} = D_{223232}$, $D_{113232} = D_{131223}$, $D_{131131} = D_{232232}$. In the 3×3 matrix, $D_{231231} = D_{132132}$, $D_{231123} = D_{132123}$.

Excluding the parameters of the same value, there are 28 parameters in $\boldsymbol{D}$ for this transverse isotropic material

$$D^{\mathrm{M}}_{\alpha\beta} = \begin{pmatrix} d_1 & d_2 & d_3 & d_4 & d_5 & 0 & 0 & 0 & 0 & 0 & 0 & 0 & 0 & 0 & 0 & 0 & 0 & 0 \\ & d_6 & d_7 & d_8 & d_9 & 0 & 0 & 0 & 0 & 0 & 0 & 0 & 0 & 0 & 0 & 0 & 0 & 0 \\ & & d_{10} & d_{11} & d_{12} & 0 & 0 & 0 & 0 & 0 & 0 & 0 & 0 & 0 & 0 & 0 & 0 & 0 \\ & & & d_{13} & d_{14} & 0 & 0 & 0 & 0 & 0 & 0 & 0 & 0 & 0 & 0 & 0 & 0 & 0 \\ & & & & d_{15} & 0 & 0 & 0 & 0 & 0 & 0 & 0 & 0 & 0 & 0 & 0 & 0 & 0 \\ & & & & & d_1 & d_2 & d_3 & d_4 & d_5 & 0 & 0 & 0 & 0 & 0 & 0 & 0 & 0 \\ & & & & & & d_6 & d_7 & d_8 & d_9 & 0 & 0 & 0 & 0 & 0 & 0 & 0 & 0 \\ & & & & & & & d_{10} & d_{11} & d_{12} & 0 & 0 & 0 & 0 & 0 & 0 & 0 & 0 \\ & & & & & & & & d_{13} & d_{14} & 0 & 0 & 0 & 0 & 0 & 0 & 0 & 0 \\ & & & & & & & & & d_{15} & 0 & 0 & 0 & 0 & 0 & 0 & 0 & 0 \\ & & & & & & & & & & d_{16} & d_{17} & d_{18} & d_{17} & d_{18} & 0 & 0 & 0 \\ & & & & & & & & & & & d_{19} & d_{20} & d_{21} & d_{22} & 0 & 0 & 0 \\ & & & & & & & & & & & & d_{23} & d_{22} & d_{24} & 0 & 0 & 0 \\ & & & & & & & & & & & & & d_{19} & d_{20} & 0 & 0 & 0 \\ & & & & & & & & & & & & & & d_{23} & 0 & 0 & 0 \\ & & & & & & & & & & & & & & & d_{25} & d_{27} & d_{28} \\ & & & & & & & & & & & & & & & & d_{25} & d_{28} \\ \text{Sym.} & & & & & & & & & & & & & & & & & d_{26} \end{pmatrix}.$$

We emphasize that some of the 28 parameters could be linearly dependent which leads to a reduction of independent coefficients. Moreover, the corresponding parameters in 2D and 3D stiffness tensors are equal within a tolerance of ±4.4%, for example, C_{1111} or D_{111111} in the 2D stiffness tensors are equal to those in the 3D tensors. This verifies the calculated results. In order to further test the homogenization method, computations for different volume fraction of matrix are conducted as presented in Figure 7.

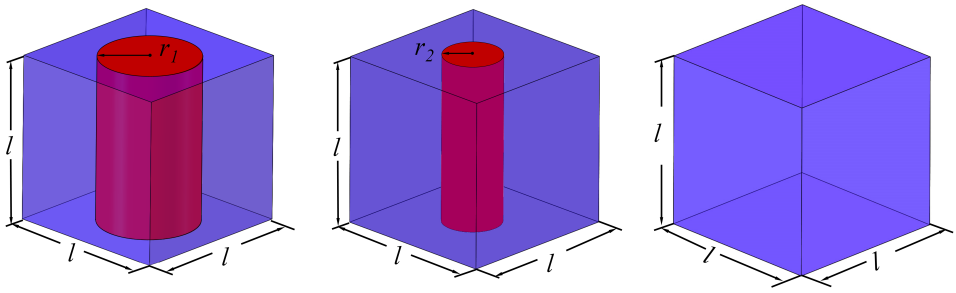

Figure 7: Different volume fraction of matrix. $l = 1$ mm, $r_1 = 0.45$ mm, $r_2 = 0.35$ mm.

The results are shown in Figure 8. It is observed that with the increasing of the volume fraction of matrix, absolute values of most of effective parameters decrease. This is due to the fact that matrix (epoxy) is softer than inclusion (carbon). It should be emphasized that when the volume fraction of matrix is 1, namely the material is purely homogeneous, the higher order parameters vanish as expected.

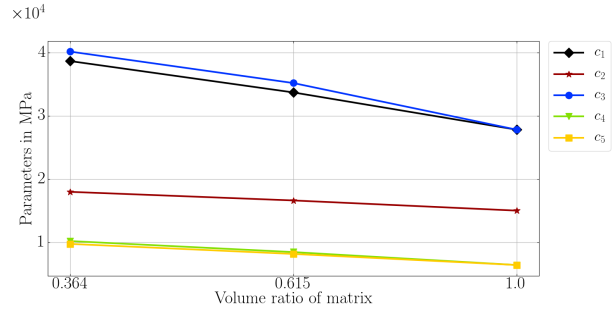

(a) Effective classical stiffness parameters.

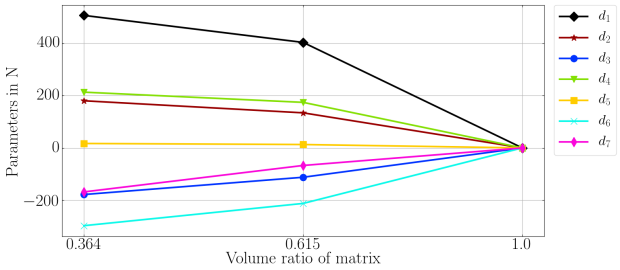

(b) Effective strain gradient stiffness parameters (d_1 - d_7).

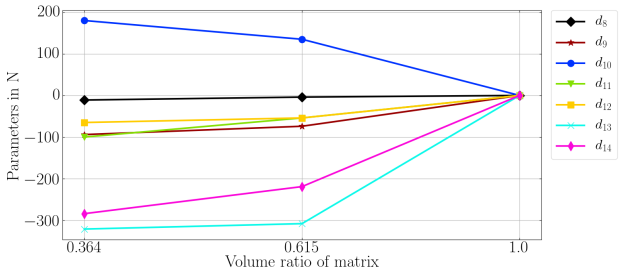

(c) Effective strain gradient stiffness parameters (d_8 - d_{14}).

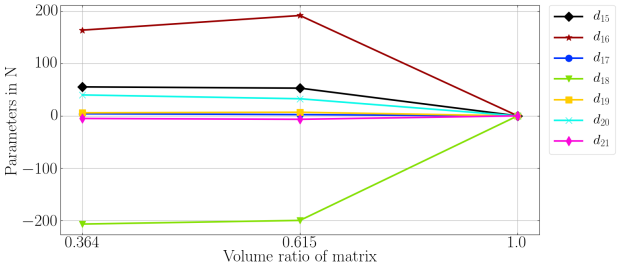

(d) Effective strain gradient stiffness parameters (d_{15} - d_{21}).

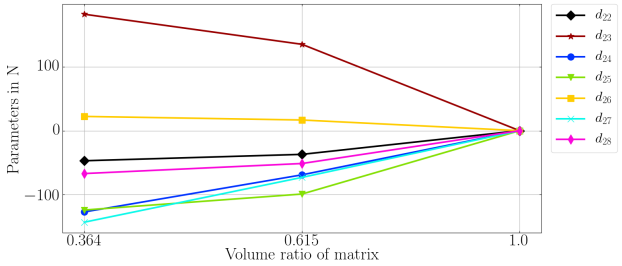

(e) Effective strain gradient stiffness parameters (d_{22} - d_{28}).

Figure 8: Effective material parameters with the changing of volume fraction of matrix. It should be noted that when the material is purely homogeneous (volume fraction of matrix is 1), all higher order parameters vanish.

Further investigations are carried out for RVEs by varying their sizes (1 mm×1 mm×1 mm, 2 mm×2 mm×2 mm, 3 mm×3 mm×3 mm) as shown in Figure 9 and Figure 10. It is found that all coefficients remain constant, which indicates that the obtained parameters are independent of the repetition of RVEs.

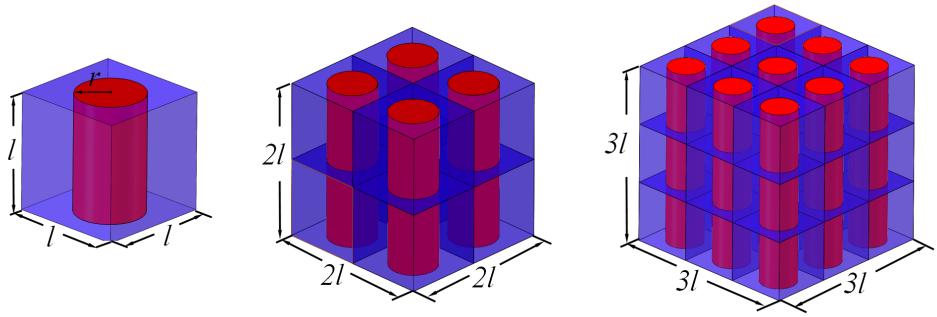

Figure 9: RVEs constructed by 1 unit cell, 8 unit cells, 27 unit cells. $l = 1$ mm, the radius of fiber is 0.45 mm.

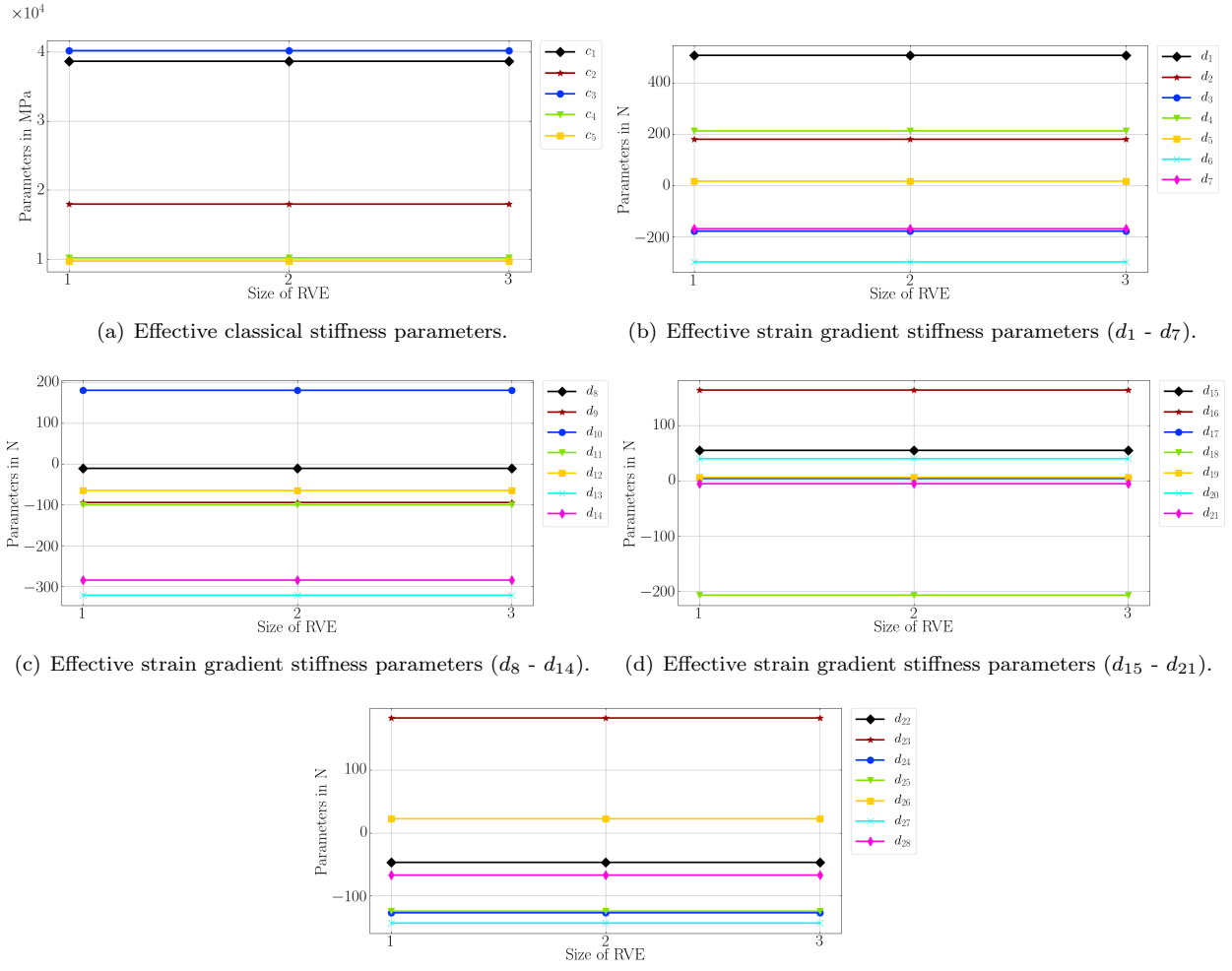

(a) Effective classical stiffness parameters.

(b) Effective strain gradient stiffness parameters (d_1 - d_7).

(c) Effective strain gradient stiffness parameters (d_8 - d_{14}).

(d) Effective strain gradient stiffness parameters (d_{15} - d_{21}).

(e) Effective strain gradient stiffness parameters (d_{22} - d_{28}).

Figure 10: Effective material parameters with the repetition of RVEs (1 mm×1 mm×1 mm, 2 mm×2 mm×2 mm, 3 mm×3 mm×3 mm).

Effective parameters are studied for unit cells with varying sizes as displayed in Figure 11. The smaller unit cells are generated by homothetically scaling the larger one. Therefore, the volume fraction of matrix are identical in these cases. It is found in Figure 12 that the parameters in the classical stiffness tensor remain the same, but the ones in the strain gradient stiffness tensor vary with the changing of the unit cell lengths. This fact is because of C^{M}_{ijkl} being invariant regarding the microstructural size. However the effective strain gradient ones are sensitive to the homothetic ratio ϵ. These higher order parameters follow a scaling rule. For example, the parameters can be obtained for the unit cell size of 0.5 mm ×0.5 mm ×0.5 mm by multiplying a scaling factor with the effective parameters of the unit cell size of 1 mm ×1 mm ×1 mm. The scaling factor is the

square of homothetic ratio ϵ^2 which is numerically equal to the square of ratio of the unit cell lengths herein.

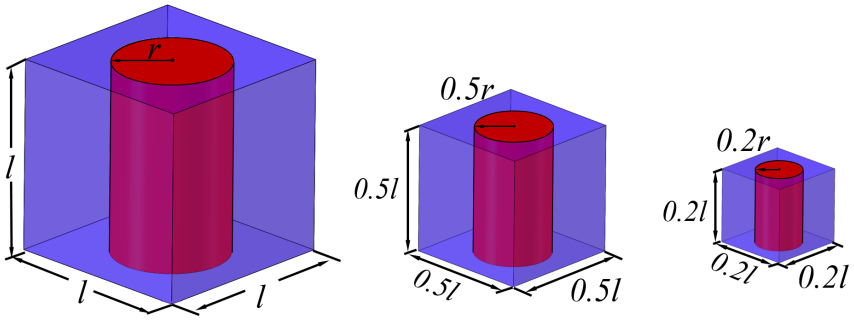

Figure 11: Unit cells with the changing sizes. $l = 1$ mm The volume fraction of matrix are kept equal.

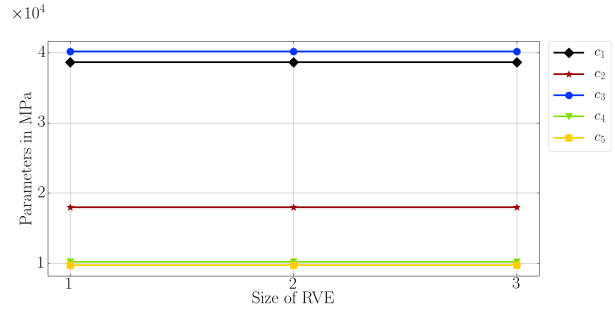

(a) Effective classical stiffness parameters.

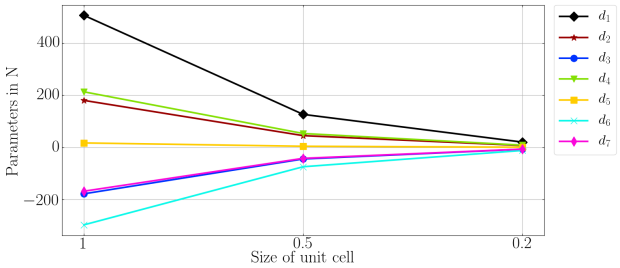

(b) Effective strain gradient stiffness parameters (d_1 - d_7).

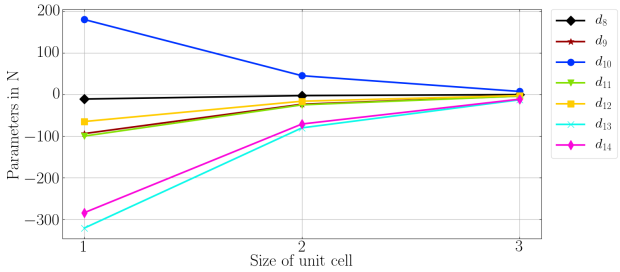

(c) Effective strain gradient stiffness parameters (d_8 - d_{14}).

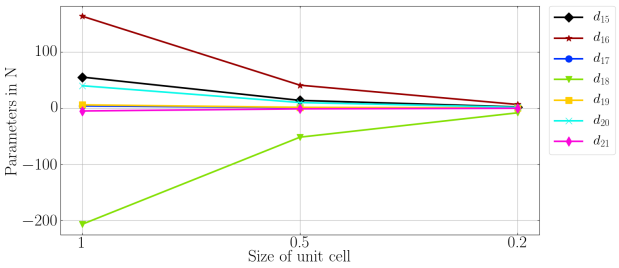

(d) Effective strain gradient stiffness parameters (d_{15} - d_{21}).

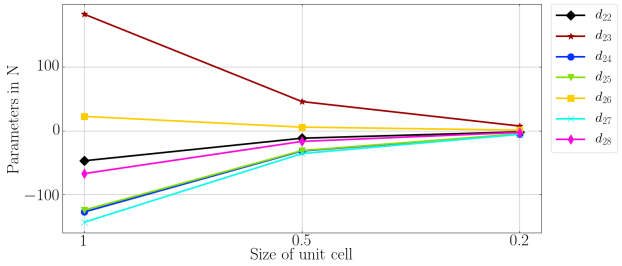

(e) Effective strain gradient stiffness parameters (d_{22} - d_{28}).

Figure 12: Effective material parameters with the changing lengths of unit cells, we emphasize that the sub-structure remains the same.

4.3.2 SiC/Al Metal Matrix Composite (MMC)

Aluminum-based MMCs have gained interest in engineering over the past few decades. The insertion of a ceramic material into a aluminum matrix leads to an fascinating mechanical properties. In this section, the effective properties of SiC/Al metal matrix composite are investigated. RVE models have been created for

three-dimensional spherical particles embedded into the metal matrix. Filler is used as a reinforcement. Their volume ratios within the MMC vary from 0% to 38.2 % by volume. The material parameters taken from [17] are compiled in Table 8.

Table 8: Material properties used for SiC/Al metal matrix composite material. E Young's modulus, ν Poisson's ratio, and ρ density.

Type	E in GPa	ν	ρ in kg/m^3
Matrix (Al2618-T4)	70	0.3	2900
Inclusion (SiC)	450	0.17	3100

The identified parameters for 61.8% volume ratio of matrix are found as follows

$$C^{\mathrm{M}}_{AB} = \begin{pmatrix} 163.3 & 50.5 & 50.5 & 0.0 & 0.0 & 0.0 \\ 50.5 & 163.5 & 50.5 & 0.0 & 0.0 & 0.0 \\ 50.5 & 50.5 & 163.6 & 0.0 & 0.0 & 0.0 \\ 0.0 & 0.0 & 0.0 & 46.4 & 0.0 & 0.0 \\ 0.0 & 0.0 & 0.0 & 0.0 & 46.3 & 0.0 \\ 0.0 & 0.0 & 0.0 & 0.0 & 0.0 & 46.3 \end{pmatrix} \text{ GPa} ,$$

$$D^{\mathrm{M}}_{\alpha\beta} = \begin{pmatrix}
7120.6 & 1075.0 & -844.4 & 1077.8 & -836.6 & 0.0 & 0.0 & 0.0 & 0.0 & 0.0 & 0.0 & 0.0 & 0.0 & 0.0 & 0.0 & 0.0 & 0.0 & 0.0 \\
1075.0 & -2517.5 & -788.5 & -48.3 & -275.8 & 0.0 & 0.0 & 0.0 & 0.0 & 0.0 & 0.0 & 0.0 & 0.0 & 0.0 & 0.0 & 0.0 & 0.0 & 0.0 \\
-844.4 & -788.5 & 1914.3 & -276.5 & -347.3 & 0.0 & 0.0 & 0.0 & 0.0 & 0.0 & 0.0 & 0.0 & 0.0 & 0.0 & 0.0 & 0.0 & 0.0 & 0.0 \\
1077.9 & -48.3 & -276.5 & -2515.1 & -789.7 & 0.0 & 0.0 & 0.0 & 0.0 & 0.0 & 0.0 & 0.0 & 0.0 & 0.0 & 0.0 & 0.0 & 0.0 & 0.0 \\
-836.6 & -275.8 & -347.3 & -789.7 & 1915.1 & 0.0 & 0.0 & 0.0 & 0.0 & 0.0 & 0.0 & 0.0 & 0.0 & 0.0 & 0.0 & 0.0 & 0.0 & 0.0 \\
0.0 & 0.0 & 0.0 & 0.0 & 0.0 & 7130.6 & 1070.6 & -850.1 & 1076.5 & -840.1 & 0.0 & 0.0 & 0.0 & 0.0 & 0.0 & 0.0 & 0.0 & 0.0 \\
0.0 & 0.0 & 0.0 & 0.0 & 0.0 & 1070.6 & -2504.4 & -781.2 & -48.1 & -276.2 & 0.0 & 0.0 & 0.0 & 0.0 & 0.0 & 0.0 & 0.0 & 0.0 \\
0.0 & 0.0 & 0.0 & 0.0 & 0.0 & -850.1 & -781.2 & 1915.4 & -275.8 & -347.6 & 0.0 & 0.0 & 0.0 & 0.0 & 0.0 & 0.0 & 0.0 & 0.0 \\
0.0 & 0.0 & 0.0 & 0.0 & 0.0 & 1076.5 & -48.1 & -275.8 & -2513.8 & -790.7 & 0.0 & 0.0 & 0.0 & 0.0 & 0.0 & 0.0 & 0.0 & 0.0 \\
0.0 & 0.0 & 0.0 & 0.0 & 0.0 & -840.1 & -276.2 & -347.6 & -790.8 & 1917.1 & 0.0 & 0.0 & 0.0 & 0.0 & 0.0 & 0.0 & 0.0 & 0.0 \\
0.0 & 0.0 & 0.0 & 0.0 & 0.0 & 0.0 & 0.0 & 0.0 & 0.0 & 0.0 & 7141.0 & 1072.0 & -848.8 & 1072.0 & -849.8 & 0.0 & 0.0 & 0.0 \\
0.0 & 0.0 & 0.0 & 0.0 & 0.0 & 0.0 & 0.0 & 0.0 & 0.0 & 0.0 & 1072.0 & -2490.1 & -783.5 & -47.5 & -276.5 & 0.0 & 0.0 & 0.0 \\
0.0 & 0.0 & 0.0 & 0.0 & 0.0 & 0.0 & 0.0 & 0.0 & 0.0 & 0.0 & -848.8 & -783.5 & 1915.3 & -275.4 & -350.4 & 0.0 & 0.0 & 0.0 \\
0.0 & 0.0 & 0.0 & 0.0 & 0.0 & 0.0 & 0.0 & 0.0 & 0.0 & 0.0 & 1072.0 & -47.5 & -275.4 & -2506.2 & -786.2 & 0.0 & 0.0 & 0.0 \\
0.0 & 0.0 & 0.0 & 0.0 & 0.0 & 0.0 & 0.0 & 0.0 & 0.0 & 0.0 & -849.8 & -276.5 & -350.4 & -786.2 & 1915.4 & 0.0 & 0.0 & 0.0 \\
0.0 & 0.0 & 0.0 & 0.0 & 0.0 & 0.0 & 0.0 & 0.0 & 0.0 & 0.0 & 0.0 & 0.0 & 0.0 & 0.0 & 0.0 & -596.3 & -711.0 & -709.6 \\
0.0 & 0.0 & 0.0 & 0.0 & 0.0 & 0.0 & 0.0 & 0.0 & 0.0 & 0.0 & 0.0 & 0.0 & 0.0 & 0.0 & 0.0 & -711.0 & -593.9 & -708.1 \\
0.0 & 0.0 & 0.0 & 0.0 & 0.0 & 0.0 & 0.0 & 0.0 & 0.0 & 0.0 & 0.0 & 0.0 & 0.0 & 0.0 & 0.0 & -709.6 & -708.1 & -589.7
\end{pmatrix} \text{ N} .$$

Due to the cubic material symmetry of the RVE, there are three independent parameters in the classical stiffness tensor,

$$C^{\mathrm{M}}_{AB} = \begin{pmatrix} c_1 & c_2 & c_2 & 0 & 0 & 0 \\ c_2 & c_1 & c_2 & 0 & 0 & 0 \\ c_2 & c_2 & c_1 & 0 & 0 & 0 \\ 0 & 0 & 0 & c_3 & 0 & 0 \\ 0 & 0 & 0 & 0 & c_3 & 0 \\ 0 & 0 & 0 & 0 & 0 & c_3 \end{pmatrix} .$$

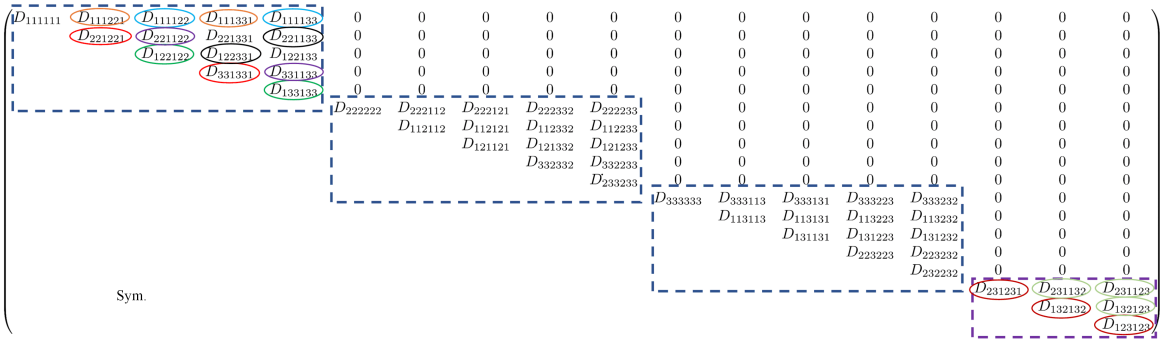

Figure 13: The structure of the strain gradient stiffness tensor for cubic materials. Three 5 × 5 matrices in the diagonal are equal, For example, $D_{111111} = D_{222222}$. In the first 5 × 5 matrix, it is also observed that $D_{111221} = D_{111331}$, $D_{111122} = D_{111133}$, $D_{221221} = D_{331331}$, $D_{122122} = D_{133133}$, $D_{221122} = D_{331133}$, $D_{221133} = D_{122331}$. In the 3 × 3 matrix, $D_{231231} = D_{132132} = D_{123123}$, $D_{231132} = D_{231123} = D_{132123}$.

As shown in Figure 13, excluding the parameters of the same value, there are 11 parameters found in the strain gradient stiffness tensor,

$$D^{\mathrm{M}}_{\alpha\beta} =$$

$$\begin{pmatrix}
d_1 & d_2 & d_3 & d_2 & d_3 & 0 & 0 & 0 & 0 & 0 & 0 & 0 & 0 & 0 & 0 & 0 & 0 & 0 \\
 & d_4 & d_5 & d_6 & d_7 & 0 & 0 & 0 & 0 & 0 & 0 & 0 & 0 & 0 & 0 & 0 & 0 & 0 \\
 & & d_8 & d_7 & d_9 & 0 & 0 & 0 & 0 & 0 & 0 & 0 & 0 & 0 & 0 & 0 & 0 & 0 \\
 & & & d_4 & d_5 & 0 & 0 & 0 & 0 & 0 & 0 & 0 & 0 & 0 & 0 & 0 & 0 & 0 \\
 & & & & d_8 & 0 & 0 & 0 & 0 & 0 & 0 & 0 & 0 & 0 & 0 & 0 & 0 & 0 \\
 & & & & & d_1 & d_2 & d_3 & d_2 & d_3 & 0 & 0 & 0 & 0 & 0 & 0 & 0 & 0 \\
 & & & & & & d_4 & d_5 & d_6 & d_7 & 0 & 0 & 0 & 0 & 0 & 0 & 0 & 0 \\
 & & & & & & & d_8 & d_7 & d_9 & 0 & 0 & 0 & 0 & 0 & 0 & 0 & 0 \\
 & & & & & & & & d_4 & d_5 & 0 & 0 & 0 & 0 & 0 & 0 & 0 & 0 \\
 & & & & & & & & & d_8 & 0 & 0 & 0 & 0 & 0 & 0 & 0 & 0 \\
 & & & & & & & & & & d_1 & d_2 & d_3 & d_2 & d_3 & 0 & 0 & 0 \\
 & & & & & & & & & & & d_4 & d_5 & d_6 & d_7 & 0 & 0 & 0 \\
 & & & & & & & & & & & & d_8 & d_7 & d_9 & 0 & 0 & 0 \\
 & & & & & & & & & & & & & d_4 & d_5 & 0 & 0 & 0 \\
 & & & & & & & & & & & & & & d_8 & 0 & 0 & 0 \\
 & & & & & & & & & & & & & & & d_{10} & d_{11} & d_{11} \\
 & & & & & & & & & & & & & & & & d_{10} & d_{11} \\
\text{Sym.} & & & & & & & & & & & & & & & & & d_{10}
\end{pmatrix}.$$

Please note, among these 11 parameters, some of them might be linearly dependent. Further investigations are conducted for different volume fraction of matrix, different sizes of selected RVE, and different sizes of unit cells as indicated in Figures 14, 16, 18. Results are displayed in Figures 15, 17, 19. It is observed that the higher order parameters are zero when materials are homogeneous; they are independent of the stack of RVEs, and they are sensitive to microstructural sizes as well as following the scaling rule.

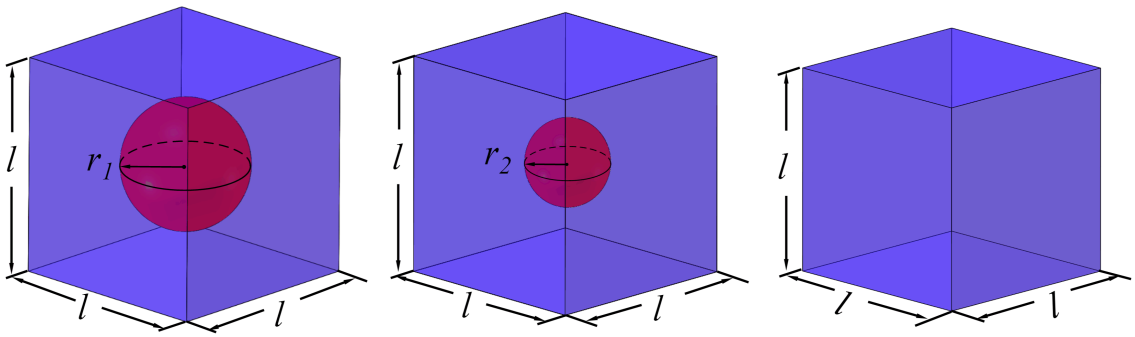

Figure 14: Changing volume fraction of matrix.

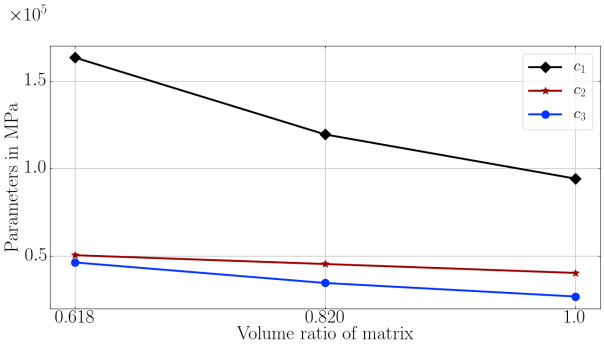

(a) Effective classical stiffness parameters.

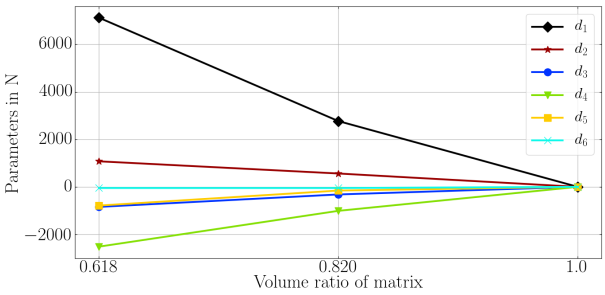

(b) Effective strain gradient stiffness parameters (d_1 - d_6).

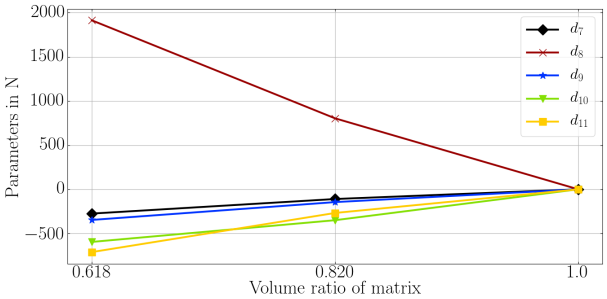

(c) Effective strain gradient stiffness parameters (d_7 - d_{11}).

Figure 15: Effective material parameters with the changing of volume fraction of matrix.

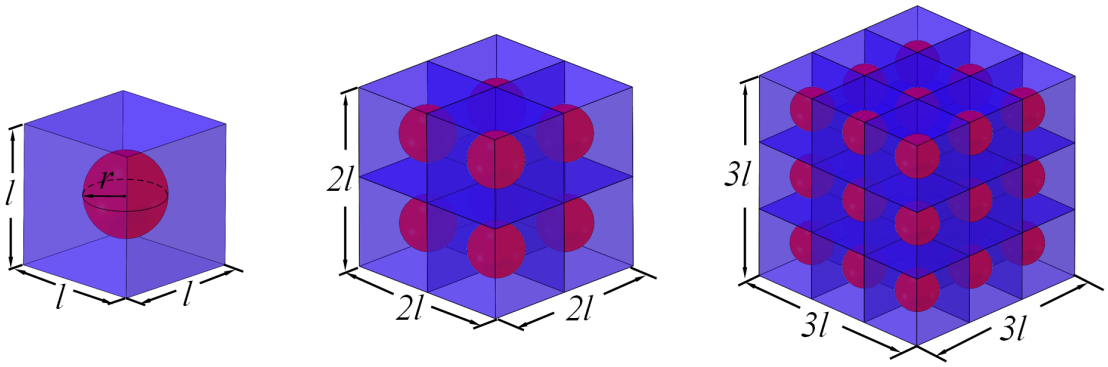

Figure 16: RVEs constructed by 1 unit cell, 8 unit cells, 27 unit cells.

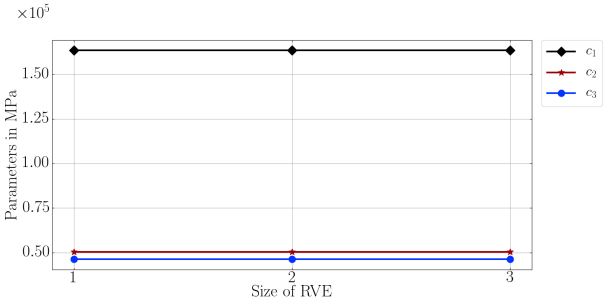

(a) Effective classical stiffness parameters.

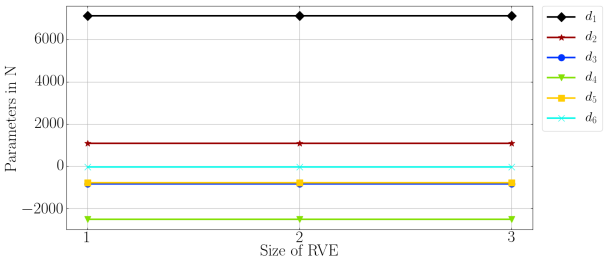

(b) Effective strain gradient stiffness parameters (d_1 - d_6).

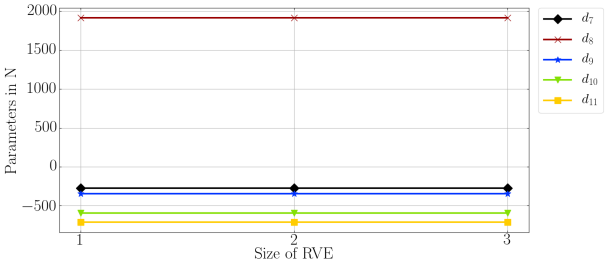

(c) Effective strain gradient stiffness parameters (d_7 - d_{11}).

Figure 17: Effective material parameters with the changing RVE sizes ($1 \times 1 \times 1$, $2 \times 2 \times 2$, $3 \times 3 \times 3$).

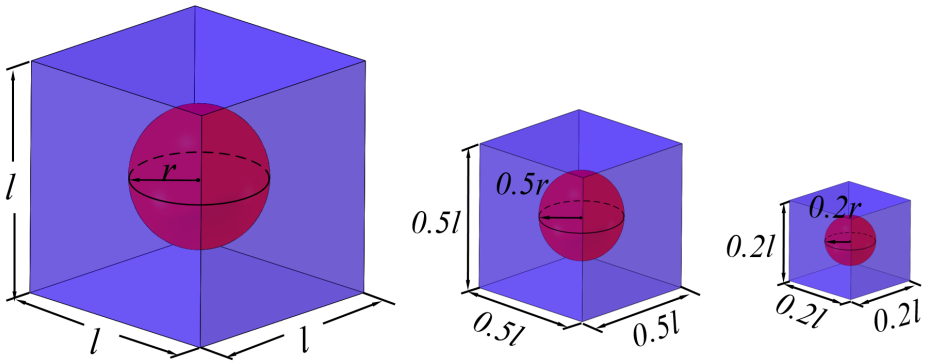

Figure 18: Unit cells with changing lengths.

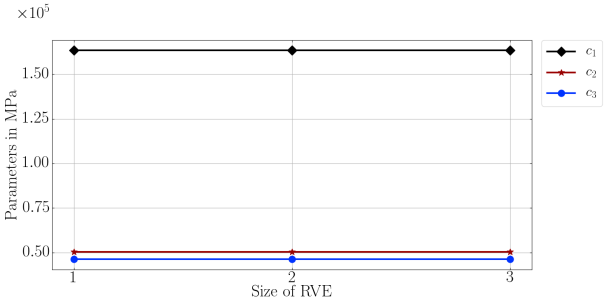

(a) Effective classical stiffness parameters.

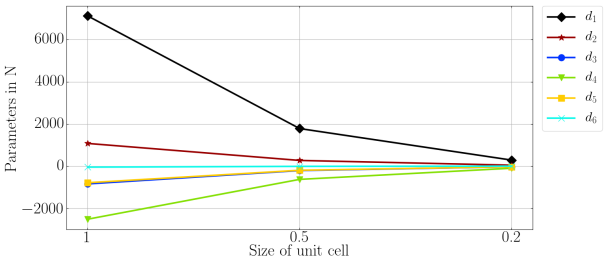

(b) Effective strain gradient stiffness parameters (d_1 - d_6).

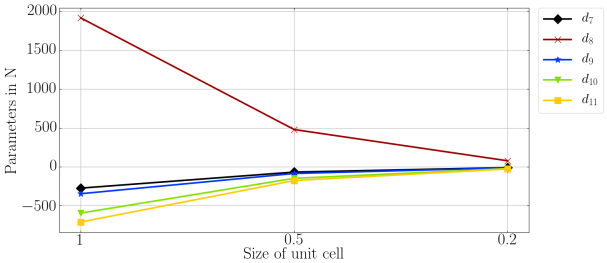

(c) Effective strain gradient stiffness parameters (d_7 - d_{11}).

Figure 19: Effective material parameters with the changing lengths of unit cells.

4.3.3 Aluminum foam

Aluminum foam is a highly porous metallic material with a cellular substructure. The RVEs of the aluminum foam are modeled by using a cubic inclusion which are technically voids embedded in a matrix made of aluminum. In order to avoid numerical problems, a small number is assigned to the Young's modulus of voids. The material properties used for aluminum foam is found in Table 9.

Table 9: Material properties used for aluminum foam. E Young's modulus, ν Poisson's ratio, and ρ mass density.

Type	E in GPa	ν	ρ in kg/m^3
Matrix (Aluminum)	70	0.3	2700
Inclusion (Voids)	1e-10	0.0	0.0

The identified parameters are found as follows:

$$C^{\mathrm{M}}_{AB} = \begin{pmatrix} 15.1 & 3.0 & 3.0 & 0.0 & 0.0 & 0.0 \\ 3.0 & 15.1 & 3.0 & 0.0 & 0.0 & 0.0 \\ 3.0 & 3.0 & 15.1 & 0.0 & 0.0 & 0.0 \\ 0.0 & 0.0 & 0.0 & 2.9 & 0.0 & 0.0 \\ 0.0 & 0.0 & 0.0 & 0.0 & 2.9 & 0.0 \\ 0.0 & 0.0 & 0.0 & 0.0 & 0.0 & 2.9 \end{pmatrix} \text{ GPa} ,$$

$$D^{\mathrm{M}}_{\alpha\beta} = \begin{pmatrix}
1130.3 & 185.4 & 288.8 & 184.8 & 288.6 & 0.0 & 0.0 & 0.0 & 0.0 & 0.0 & 0.0 & 0.0 & 0.0 & 0.0 & 0.0 & 0.0 & 0.0 & 0.0 \\
185.4 & 1080.6 & 114.9 & 328.0 & 74.6 & 0.0 & 0.0 & 0.0 & 0.0 & 0.0 & 0.0 & 0.0 & 0.0 & 0.0 & 0.0 & 0.0 & 0.0 & 0.0 \\
288.8 & 114.9 & −42.8 & 74.5 & 160.7 & 0.0 & 0.0 & 0.0 & 0.0 & 0.0 & 0.0 & 0.0 & 0.0 & 0.0 & 0.0 & 0.0 & 0.0 & 0.0 \\
184.8 & 328.0 & 74.5 & 1080.3 & 114.9 & 0.0 & 0.0 & 0.0 & 0.0 & 0.0 & 0.0 & 0.0 & 0.0 & 0.0 & 0.0 & 0.0 & 0.0 & 0.0 \\
288.6 & 74.6 & 160.7 & 114.9 & −42.6 & 0.0 & 0.0 & 0.0 & 0.0 & 0.0 & 0.0 & 0.0 & 0.0 & 0.0 & 0.0 & 0.0 & 0.0 & 0.0 \\
0.0 & 0.0 & 0.0 & 0.0 & 0.0 & 1139.1 & 187.6 & 290.6 & 186.9 & 290.2 & 0.0 & 0.0 & 0.0 & 0.0 & 0.0 & 0.0 & 0.0 & 0.0 \\
0.0 & 0.0 & 0.0 & 0.0 & 0.0 & 187.6 & 1081.0 & 114.7 & 328.4 & 75.0 & 0.0 & 0.0 & 0.0 & 0.0 & 0.0 & 0.0 & 0.0 & 0.0 \\
0.0 & 0.0 & 0.0 & 0.0 & 0.0 & 290.6 & 114.7 & −42.8 & 74.9 & 161.0 & 0.0 & 0.0 & 0.0 & 0.0 & 0.0 & 0.0 & 0.0 & 0.0 \\
0.0 & 0.0 & 0.0 & 0.0 & 0.0 & 186.9 & 328.4 & 74.9 & 1080.4 & 115.4 & 0.0 & 0.0 & 0.0 & 0.0 & 0.0 & 0.0 & 0.0 & 0.0 \\
0.0 & 0.0 & 0.0 & 0.0 & 0.0 & 290.2 & 75.0 & 161.0 & 115.4 & −42.5 & 0.0 & 0.0 & 0.0 & 0.0 & 0.0 & 0.0 & 0.0 & 0.0 \\
0.0 & 0.0 & 0.0 & 0.0 & 0.0 & 0.0 & 0.0 & 0.0 & 0.0 & 0.0 & 1171.8 & 194.3 & 296.5 & 194.5 & 296.9 & 0.0 & 0.0 & 0.0 \\
0.0 & 0.0 & 0.0 & 0.0 & 0.0 & 0.0 & 0.0 & 0.0 & 0.0 & 0.0 & 194.3 & 1082.3 & 115.6 & 329.8 & 76.3 & 0.0 & 0.0 & 0.0 \\
0.0 & 0.0 & 0.0 & 0.0 & 0.0 & 0.0 & 0.0 & 0.0 & 0.0 & 0.0 & 296.5 & 115.6 & −42.1 & 76.3 & 162.0 & 0.0 & 0.0 & 0.0 \\
0.0 & 0.0 & 0.0 & 0.0 & 0.0 & 0.0 & 0.0 & 0.0 & 0.0 & 0.0 & 194.5 & 329.8 & 76.3 & 1082.1 & 115.8 & 0.0 & 0.0 & 0.0 \\
0.0 & 0.0 & 0.0 & 0.0 & 0.0 & 0.0 & 0.0 & 0.0 & 0.0 & 0.0 & 296.9 & 76.3 & 162.0 & 115.8 & −42.0 & 0.0 & 0.0 & 0.0 \\
0.0 & 0.0 & 0.0 & 0.0 & 0.0 & 0.0 & 0.0 & 0.0 & 0.0 & 0.0 & 0.0 & 0.0 & 0.0 & 0.0 & 0.0 & 406.8 & 19.6 & 19.9 \\
0.0 & 0.0 & 0.0 & 0.0 & 0.0 & 0.0 & 0.0 & 0.0 & 0.0 & 0.0 & 0.0 & 0.0 & 0.0 & 0.0 & 0.0 & 19.6 & 406.7 & 19.8 \\
0.0 & 0.0 & 0.0 & 0.0 & 0.0 & 0.0 & 0.0 & 0.0 & 0.0 & 0.0 & 0.0 & 0.0 & 0.0 & 0.0 & 0.0 & 19.9 & 19.8 & 406.9
\end{pmatrix} \mathrm{N}\,.$$

Three independent parameters and eleven parameters are observed in the classical stiffness tensor and the strain gradient stiffness tensor, respectively. This is consistent to the cubic material symmetry as mentioned before. Investigations on the different volume fraction of matrix, repetition of RVEs, changing sizes of unit cells are conducted as displayed in Figures 20, 22, 24. Corresponding outcomes are presented in Figures 21, 23, 25.

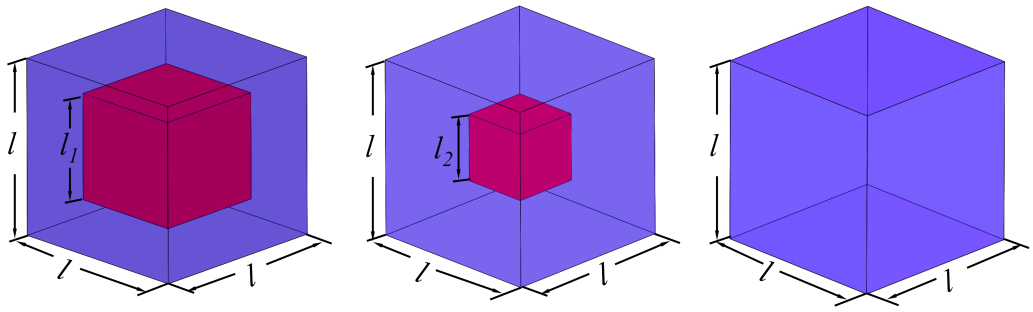

Figure 20: Different volume fraction of matrix for the aluminum foam.

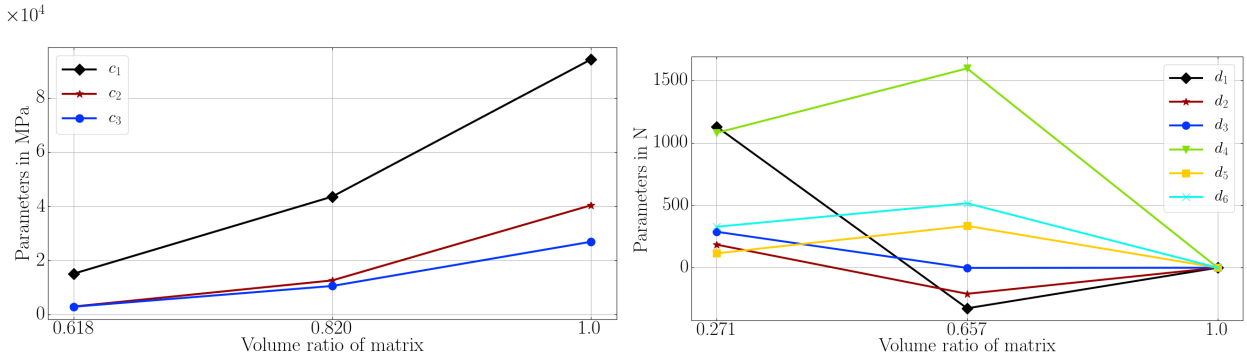

(a) Effective classical stiffness parameters.

(b) Effective strain gradient stiffness parameters (d_1 - d_6).

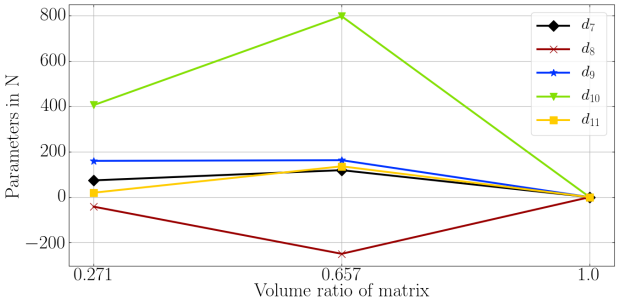

(c) Effective strain gradient stiffness parameters (d_7 - d_{11}).

Figure 21: Effective material parameters with changing of volume fraction of matrix.

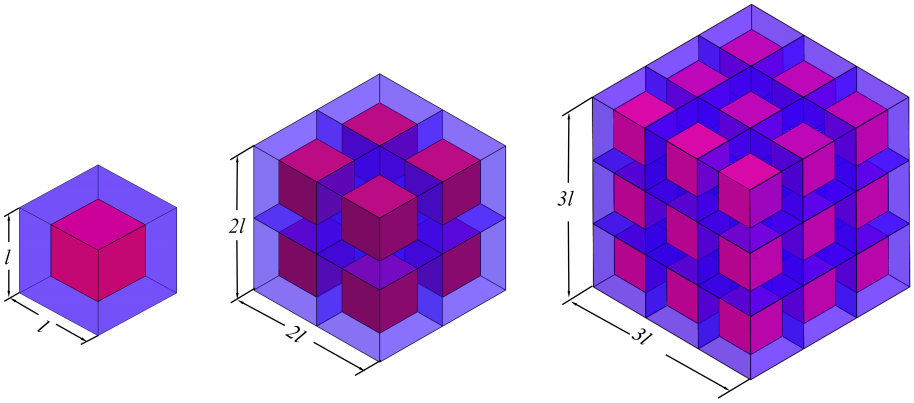

Figure 22: RVEs constructed by 1 unit cell, 8 unit cells, 27 unit cells.

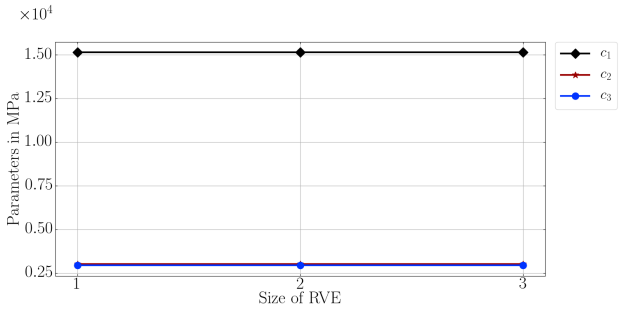

(a) Effective classical stiffness parameters.

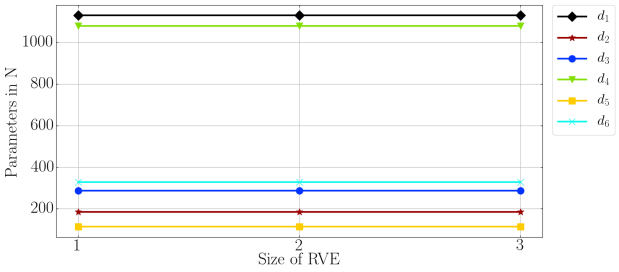

(b) Effective strain gradient stiffness parameters (d_1 - d_6).

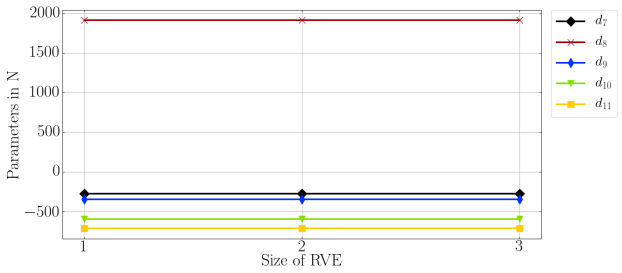

(c) Effective strain gradient stiffness parameters (d_7 - d_{11}).

Figure 23: Effective material parameters with changing RVE sizes ($1 \times 1 \times 1$, $2 \times 2 \times 2$, $3 \times 3 \times 3$).

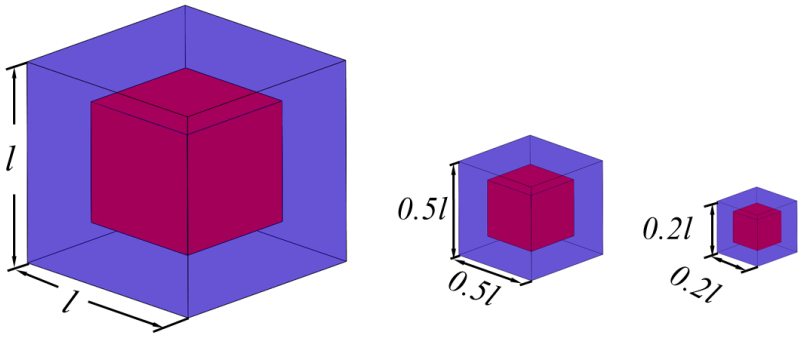

Figure 24: Unit cells with changing lengths.

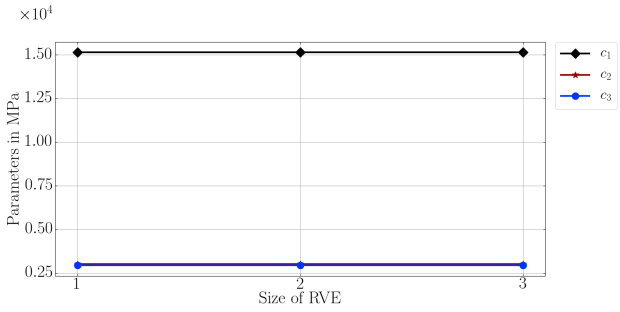

(a) Effective classical stiffness parameters.

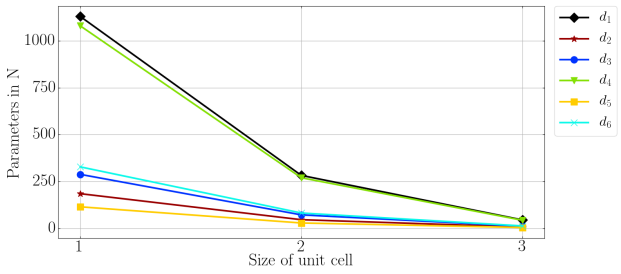

(b) Effective strain gradient stiffness parameters (d_1 - d_6).

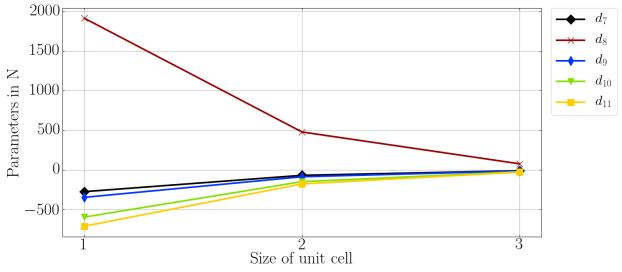

(c) Effective strain gradient stiffness parameters (d_7 - d_{11}).

Figure 25: Effective material parameters with changing lengths of unit cells.

5 Remark on positive definiteness

As observed from the previous sections, negative values appear in strain gradient stiffness tensors. This fact may raise concerns regarding the positive definiteness of the strain energy function. In [57, 21, 63, 30], the issue of positive definiteness of the strain energy function for strain gradient materials is addressed and bounds on material parameters are provided. The bounds on strain gradient constants consider the continuum to be purely local, which means that the strain energy function is convex with respect to every material point [57]. However, when homogenizing the microstructures of composite materials with an equivalent strain gradient continuum, we have a limited non-locality. The non-locality originates from the energy equivalence as shown in Eqn. (1). We emphasize that the ϵ is a finite number, $\epsilon < 1$ but not necessarily $\epsilon \ll 1$, which means that the studied composite material has a finite macroscopic and microscopic sizes. Therefore, the strain energy function averaged over this microstructure size should be positive definite and not the pointwise local strain

energy function. Thus coefficients in the strain gradient stiffness tensor could be negative as long as the strain energy density function integrated over the periodic unit cell is positive definite. This interpretation is aligned with in [50, 14, 53].

6 Conclusions

Asymptotic homogenization method was employed to homogenize composite material into effective homogeneous strain gradient continua. Main conclusions are summarized as follows:

- Purely computational analysis determines all the parameters in the strain gradient theory. In particular, the parameters in the rank five tensor and the rank six tensor.
- Numerical examples for 2D and 3D, stiff and soft inclusions, cubic and transverse material symmetry cases were conducted.
- In both 2D and 3D numerical examples, the effective strain gradient parameters vanish when materials are purely homogeneous, they are independent of repetitions of RVEs and sensitive to microstructural sizes.
- Without assuming a specific symmetry group, in the case of cubic symmetry, all expected relations have been captured by the proposed formalism.
- Physical meaning of the homothetic ratio ϵ is interpreted, a so-called scaling rule for effective strain gradient parameters has been discussed. The method is valid when ϵ is a finite value. $\epsilon < 1$ is required but not necessarily $\epsilon \ll 1$.

The homogenization tool is applicable to any composite materials with a periodic substructure at the microscale. Such multiscale are nowadays possible to manufacture by 3D printers. Therefore, effective parameters determination is of interest for a possible topology optimization. Further investigations will focus on the following aspects:

- To validate the identified parameters not only in statics [75] but also in vibration responses, buckling critical loads [47], and wave propagation [69, 31].
- To apply the homogenization method to the analysis of 3D composite materials with finite thickness. This may be achieved by by modeling the full thickness unit cell model and relieving the out-of-plane periodicity of the unit cell [62].
- To explore the possibility of studying more sophisticated metamaterials such as the so-called pantographic structures [23, 22, 38, 15] or the biomimetic spinodoids metamaterials [64, 51] by the homogenization method.
- To extend the homogenization method to non-linear regime [35, 27, 33] and multiphysics fields [12, 56, 29].

References

[1] B. E. Abali.
Computational Reality, volume 55 of *Advanced Structured Materials*.
Springer Nature, Singapore, 2017.

[2] Bilen Emek Abali and Emilio Barchiesi.
Additive manufacturing introduced substructure and computational determination of metamaterials parameters by means of the asymptotic homogenization.
Continuum Mechanics and Thermodynamics, pages 1–17, 2020.

[3] Houssam Abdoul-Anziz and Pierre Seppecher.
Strain gradient and generalized continua obtained by homogenizing frame lattices.
Mathematics and mechanics of complex systems, 6(3):213–250, 2018.

[4] Houssam Abdoul-Anziz, Pierre Seppecher, and Cédric Bellis.
Homogenization of frame lattices leading to second gradient models coupling classical strain and strain-gradient terms.
Mathematics and Mechanics of Solids, 24(12):3976–3999, 2019.

[5] A Aghaei, N Bochud, G Rosi, and S Naili.
Assessing the effective elastic properties of the tendon-to-bone insertion: a multiscale modeling approach.
Biomechanics and Modeling in Mechanobiology, 20(2):433–448, 2021.

[6] Jean-Jacques Alibert and Alessandro Della Corte.
Homogenization of nonlinear inextensible pantographic structures by γ-convergence.
Mathematics and Mechanics of Complex Systems, 7(1):1–24, 2019.

[7] Holm Altenbach and Samuel Forest.
Generalized continua as models for classical and advanced materials.
Springer, 2016.

[8] Sajad Arabnejad and Damiano Pasini.
Mechanical properties of lattice materials via asymptotic homogenization and comparison with alternative homogenization methods.
International Journal of Mechanical Sciences, 77:249–262, 2013.

[9] Nicolas Auffray, Regis Bouchet, and Yves Brechet.
Derivation of anisotropic matrix for bi-dimensional strain-gradient elasticity behavior.
International Journal of Solids and Structures, 46(2):440–454, 2009.

[10] Nicolas Auffray, Justin Dirrenberger, and Giuseppe Rosi.
A complete description of bi-dimensional anisotropic strain-gradient elasticity.
International Journal of Solids and Structures, 69:195–206, 2015.

[11] Nicolas Auffray, Hung Le Quang, and Qi-Chang He.
Matrix representations for 3D strain-gradient elasticity.
Journal of the Mechanics and Physics of Solids, 61(5):1202–1223, 2013.

[12] Jean-Louis Auriault, Claude Boutin, and Christian Geindreau.
Homogenization of coupled phenomena in heterogenous media, volume 149.
John Wiley & Sons, 2010.

[13] Andrea Bacigalupo, Marco Paggi, F Dal Corso, and D Bigoni.
Identification of higher-order continua equivalent to a Cauchy elastic composite.
Mechanics Research Communications, 93:11–22, 2018.

[14] Salma Barboura and Jia Li.
Establishment of strain gradient constitutive relations by using asymptotic analysis and the finite element method for complex periodic microstructures.
International Journal of Solids and Structures, 136:60–76, 2018.

[15] Emilio Barchiesi, Francesco dell'Isola, and François Hild.
On the validation of homogenized modeling for bi-pantographic metamaterials via digital image correlation.
International Journal of Solids and Structures, 208:49–62, 2021.

[16] Jeremy Bleyer.
Numerical Tours of Computational Mechanics with FEniCS, 2018.

[17] Helmut J Böhm, Anton Eckschlager, and W Han.
Multi-inclusion unit cell models for metal matrix composites with randomly oriented discontinuous reinforcements.
Computational materials science, 25(1-2):42–53, 2002.

[18] Claude Boutin.
Microstructural effects in elastic composites.
International Journal of Solids and Structures, 33(7):1023–1051, 1996.

[19] Claude Boutin, Francesco dell'Isola, Ivan Giorgio, and Luca Placidi.
Linear pantographic sheets: Asymptotic micro-macro models identification.
Mathematics and Mechanics of Complex Systems, 5(2):127–162, 2017.

[20] Qiang Chen, George Chatzigeorgiou, and Fodil Meraghni.
Extended mean-field homogenization of viscoelastic-viscoplastic polymer composites undergoing hybrid progressive degradation induced by interface debonding and matrix ductile damage.
International Journal of Solids and Structures, 210:1–17, 2020.

[21] Francesco dell'Isola, Giulio Sciarra, and Stefano Vidoli.
Generalized Hooke's law for isotropic second gradient materials.

Proceedings of the Royal Society A: Mathematical, Physical and Engineering Sciences, 465(2107):2177–2196, 2009.

[22] Francesco dell'Isola, Pierre Seppecher, Jean Jacques Alibert, Tomasz Lekszycki, Roman Grygoruk, Marek Pawlikowski, David Steigmann, Ivan Giorgio, Ugo Andreaus, Emilio Turco, Maciej Gołaszewski, Nicola Rizzi, Claude Boutin, Victor A. Eremeyev, Anil Misra, Luca Placidi, Emilio Barchiesi, Leopoldo Greco, Massimo Cuomo, Antonio Cazzani, Alessandro Della Corte, Antonio Battista, Daria Scerrato, Inna Zurba Eremeeva, Yosra Rahali, Jean-François Ganghoffer, Wolfgang Müller, Gregor Ganzosch, Mario Spagnuolo, Aron Pfaff, Katarzyna Barcz, Klaus Hoschke, Jan Neggers, and François Hild.
Pantographic metamaterials: an example of mathematically driven design and of its technological challenges.
Continuum Mechanics and Thermodynamics, 31(4):851–884, 2019.

[23] Francesco dell'Isola, Pierre Seppecher, Mario Spagnuolo, Emilio Barchiesi, François Hild, Tomasz Lekszycki, Ivan Giorgio, Luca Placidi, Ugo Andreaus, Massimo Cuomo, Simon R. Eugster, Aron Pfaff, Klaus Hoschke, Ralph Langkemper, Emilio Turco, Rizacan Sarikaya, Aviral Misra, Michele De Angelo, Francesco D'Annibale, Amine Bouterf, Xavier Pinelli, Anil Misra, Boris Desmorat, Marek Pawlikowski, Corinne Dupuy, Daria Scerrato, Patrice Peyre, Marco Laudato, Luca Manzari, Peter Göransson, Christian Hesch, Sofia Hesch, Patrick Franciosi, Justin Dirrenberger, Florian Maurin, Zacharias Vangelatos, Costas Grigoropoulos, Vasileia Melissinaki, Maria Farsari, Wolfgang Müller, Bilen Emek Abali, Christian Liebold, Gregor Ganzosch, Philip Harrison, Rafał Drobnicki, Leonid Igumnov, Faris Alzahrani, and Tasawar Hayat.
Advances in pantographic structures: design, manufacturing, models, experiments and image analyses.
Continuum Mechanics and Thermodynamics, 31(4):1231–1282, 2019.

[24] Justin Dirrenberger, Samuel Forest, and Dominique Jeulin.
Computational homogenization of architectured materials.
In Yuri Estrin, Yves Bréchet, John Dunlop, and Peter" Fratzl, editors, *Architectured materials in nature and engineering*, Springer Series in Materials Science, pages 89–139. Springer, 2019.

[25] F Dos Reis and JF Ganghoffer.
Construction of micropolar continua from the asymptotic homogenization of beam lattices.
Computers & Structures, 112:354–363, 2012.

[26] F Dos Reis and JF Ganghoffer.
Equivalent mechanical properties of auxetic lattices from discrete homogenization.
Computational Materials Science, 51(1):314–321, 2012.

[27] Khaled ElNady, Ibrahim Goda, and Jean-François Ganghoffer.
Computation of the effective nonlinear mechanical response of lattice materials considering geometrical nonlinearities.
Computational Mechanics, 58(6):957–979, 2016.

[28] Victor A Eremeyev.
On effective properties of materials at the nano-and microscales considering surface effects.
Acta Mechanica, 227(1):29–42, 2016.

[29] Victor A Eremeyev, Jean-François Ganghoffer, Violetta Konopińska-Zmysłowska, and Nikolay S Uglov.
Flexoelectricity and apparent piezoelectricity of a pantographic micro-bar.
International Journal of Engineering Science, 149:103213, 2020.

[30] Victor A Eremeyev, Sergey A Lurie, Yury O Solyaev, and Francesco dell'Isola.
On the well posedness of static boundary value problem within the linear dilatational strain gradient elasticity.
Zeitschrift für angewandte Mathematik und Physik, 71(6):1–16, 2020.

[31] Victor A Eremeyev, Giuseppe Rosi, and Salah Naili.
Comparison of anti-plane surface waves in strain-gradient materials and materials with surface stresses.
Mathematics and mechanics of solids, 24(8):2526–2535, 2019.

[32] A Cemal Eringen.
Theory of micropolar elasticity.
In *Microcontinuum field theories*, pages 101–248. Springer, 1999.

[33] Jacob Fish, Zhiqiang Yang, and Zifeng Yuan.
A second-order reduced asymptotic homogenization approach for nonlinear periodic heterogeneous materials.

International Journal for Numerical Methods in Engineering, 119(6):469–489, 2019.

[34] Samuel Forest.
Micromorphic media.
In *Generalized continua from the theory to engineering applications*, pages 249–300. Springer, 2013.

[35] Samuel Forest.
Continuum thermomechanics of nonlinear micromorphic, strain and stress gradient media.
Philosophical Transactions of the Royal Society A, 378(2170):20190169, 2020.

[36] Samuel Forest and Duy Khanh Trinh.
Generalized continua and non-homogeneous boundary conditions in homogenisation methods.
ZAMM-Journal of Applied Mathematics and Mechanics/Zeitschrift für Angewandte Mathematik und Mechanik, 91(2):90–109, 2011.

[37] JF Ganghoffer and H Reda.
A variational approach of homogenization of heterogeneous materials towards second gradient continua.
Mechanics of Materials, page 103743, 2021.

[38] Ivan Giorgio, Valerio Varano, Francesco dell'Isola, and Nicola L Rizzi.
Two layers pantographs: a 2D continuum model accounting for the beams' offset and relative rotations as averages in SO (3) lie groups.
International Journal of Solids and Structures, 2021.

[39] Ibrahim Goda, Mohamed Assidi, and Jean-François Ganghoffer.
Equivalent mechanical properties of textile monolayers from discrete asymptotic homogenization.
Journal of the Mechanics and Physics of Solids, 61(12):2537–2565, 2013.

[40] Ibrahim Goda and Jean-François Ganghoffer.
Construction of first and second order grade anisotropic continuum media for 3d porous and textile composite structures.
Composite Structures, 141:292–327, 2016.

[41] Stefano Gonella and Massimo Ruzzene.
Homogenization and equivalent in-plane properties of two-dimensional periodic lattices.
International Journal of Solids and Structures, 45(10):2897–2915, 2008.

[42] Behrooz Hassani and Ernest Hinton.
A review of homogenization and topology optimization I—homogenization theory for media with periodic structure.
Computers & Structures, 69(6):707–717, 1998.

[43] Scott J Hollister and Noboru Kikuchi.
A comparison of homogenization and standard mechanics analyses for periodic porous composites.
Computational mechanics, 10(2):73–95, 1992.

[44] Geralf Hütter.
Homogenization of a Cauchy continuum towards a micromorphic continuum.
Journal of the Mechanics and Physics of Solids, 99:394–408, 2017.

[45] Lukáš Jakabčin and Pierre Seppecher.
On periodic homogenization of highly contrasted elastic structures.
Journal of the Mechanics and Physics of Solids, 144:104104, 2020.

[46] Toufik Kanit, Samuel Forest, Isabelle Galliet, Valérie Mounoury, and Dominique Jeulin.
Determination of the size of the representative volume element for random composites: statistical and numerical approach.
International Journal of solids and structures, 40(13-14):3647–3679, 2003.

[47] Sergei Khakalo, Viacheslav Balobanov, and Jarkko Niiranen.
Modelling size-dependent bending, buckling and vibrations of 2d triangular lattices by strain gradient elasticity models: applications to sandwich beams and auxetics.
International Journal of Engineering Science, 127:33–52, 2018.

[48] Varvara Kouznetsova, Marc GD Geers, and WA Marcel Brekelmans.
Multi-scale constitutive modelling of heterogeneous materials with a gradient-enhanced computational homogenization scheme.
International journal for numerical methods in engineering, 54(8):1235–1260, 2002.

[49] VG Kouznetsova, Marc GD Geers, and WAM1112 Brekelmans.
Multi-scale second-order computational homogenization of multi-phase materials: a nested finite element solution strategy.
Computer methods in applied Mechanics and Engineering, 193(48-51):5525–5550, 2004.

[50] Rajesh S Kumar and David L McDowell.
Generalized continuum modeling of 2-D periodic cellular solids.
International Journal of solids and structures, 41(26):7399–7422, 2004.

[51] Siddhant Kumar, Stephanie Tan, Li Zheng, and Dennis M Kochmann.
Inverse-designed spinodoid metamaterials.
npj Computational Materials, 6(1):1–10, 2020.

[52] Jia Li.
A micromechanics-based strain gradient damage model for fracture prediction of brittle materials–part i: Homogenization methodology and constitutive relations.
International journal of solids and structures, 48(24):3336–3345, 2011.

[53] Jia Li and Xiao-Bing Zhang.
A numerical approach for the establishment of strain gradient constitutive relations in periodic heterogeneous materials.
European Journal of Mechanics-A/Solids, 41:70–85, 2013.

[54] Shutian Liu and Wenzheng Su.
Effective couple-stress continuum model of cellular solids and size effects analysis.
International Journal of Solids and Structures, 46(14-15):2787–2799, 2009.

[55] K. K. Mandadapu, B. E. Abali, and P. Papadopoulos.
On the polar nature and invariance properties of a thermomechanical theory for continuum-on-continuum homogenization.
Mathematics and Mechanics of Solids, pages 1–18, 2021.

[56] Nagham Mawassy, Hilal Reda, Jean-Francois Ganghoffer, Victor A Eremeyev, and Hassan Lakiss.
A variational approach of homogenization of piezoelectric composites towards piezoelectric and flexoelectric effective media.
International Journal of Engineering Science, 158:103410, 2021.

[57] Raymond David Mindlin and NN Eshel.
On first strain-gradient theories in linear elasticity.
International Journal of Solids and Structures, 4(1):109–124, 1968.

[58] Anil Misra and Payam Poorsolhjouy.
Identification of higher-order elastic constants for grain assemblies based upon granular micromechanics.
Mathematics and Mechanics of Complex Systems, 3(3):285–308, 2015.

[59] Vincent Monchiet, Nicolas Auffray, and Julien Yvonnet.
Strain-gradient homogenization: a bridge between the asymptotic expansion and quadratic boundary condition methods.
Mechanics of Materials, 143:103309, 2020.

[60] Wolfgang H Müller.
The experimental evidence for higher gradient theories.
In A Bertram and S Forest, editors, *Mechanics of Strain Gradient Materials*, volume 600 of *CISM International Centre for Mechanical Sciences*, pages 1–18. Springer, 2020.

[61] He Nassar, Q-C He, and Nicolas Auffray.
A generalized theory of elastodynamic homogenization for periodic media.
International Journal of Solids and Structures, 84:139–146, 2016.

[62] Muhammad Ridlo Erdata Nasution, Naoyuki Watanabe, Atsushi Kondo, and Arief Yudhanto.
A novel asymptotic expansion homogenization analysis for 3-D composite with relieved periodicity in the thickness direction.
Composites science and technology, 97:63–73, 2014.

[63] Lidiia Nazarenko, Rainer Glüge, and Holm Altenbach.
Positive definiteness in coupled strain gradient elasticity.
Continuum Mechanics and Thermodynamics, pages 1–13, 2020.

[64] Carlos M Portela, A Vidyasagar, Sebastian Krödel, Tamara Weissenbach, Daryl W Yee, Julia R Greer, and Dennis M Kochmann.
Extreme mechanical resilience of self-assembled nanolabyrinthine materials.
Proceedings of the National Academy of Sciences, 117(11):5686–5693, 2020.

[65] Y Rahali, I Giorgio, JF Ganghoffer, and F dell'Isola.
Homogenization à la Piola produces second gradient continuum models for linear pantographic lattices.
International Journal of Engineering Science, 97:148–172, 2015.

[66] Yosra Rahali, VA Eremeyev, and Jean-François Ganghoffer.
Surface effects of network materials based on strain gradient homogenized media.
Mathematics and Mechanics of Solids, 25(2):389–406, 2020.

[67] Ondřej Rokoš, Maqsood M Ameen, Ron HJ Peerlings, and Mark GD Geers.
Micromorphic computational homogenization for mechanical metamaterials with patterning fluctuation fields.
Journal of the Mechanics and Physics of Solids, 123:119–137, 2019.

[68] Giuseppe Rosi.
Waves and generalized continua.
In H Altenbach and A Öchsner, editors, *Encyclopedia of Continuum Mechanics*, pages 2756–2765. Springer, 2020.

[69] Giuseppe Rosi and Nicolas Auffray.
Anisotropic and dispersive wave propagation within strain-gradient framework.
Wave Motion, 63:120–134, 2016.

[70] Giuseppe Rosi, Luca Placidi, and Nicolas Auffray.
On the validity range of strain-gradient elasticity: a mixed static-dynamic identification procedure.
European Journal of Mechanics-A/Solids, 69:179–191, 2018.

[71] Andrzej Skrzat and Victor A Eremeyev.
On the effective properties of foams in the framework of the couple stress theory.
Continuum Mechanics and Thermodynamics, pages 1–23, 2020.

[72] Valery P Smyshlyaev and Kirill D Cherednichenko.
On rigorous derivation of strain gradient effects in the overall behaviour of periodic heterogeneous media.
Journal of the Mechanics and Physics of Solids, 48(6-7):1325–1357, 2000.

[73] Oliver Weeger.
Numerical homogenization of second gradient, linear elastic constitutive models for cubic 3d beam-lattice metamaterials.
International Journal of Solids and Structures, 2021.

[74] Hua Yang, Bilen Emek Abali, Dmitry Timofeev, and Wolfgang H Müller.
Determination of metamaterial parameters by means of a homogenization approach based on asymptotic analysis.
Continuum Mechanics and Thermodynamics, pages 1–20, 2019.

[75] Hua Yang, Dmitry Timofeev, Ivan Giorgio, and Wolfgang H Müller.
Effective strain gradient continuum model of metamaterials and size effects analysis.
Continuum Mechanics and Thermodynamics, pages 1–23, 2020.

[76] Marcus Yoder, Lonny Thompson, and Joshua Summers.
Size effects in lattice structures and a comparison to micropolar elasticity.
International Journal of Solids and Structures, 143:245–261, 2018.

[77] Wenbin Yu and Tian Tang.
Variational asymptotic method for unit cell homogenization of periodically heterogeneous materials.
International Journal of Solids and Structures, 44(11-12):3738–3755, 2007.

[78] J Yvonnet, Nicolas Auffray, and V Monchiet.
Computational second-order homogenization of materials with effective anisotropic strain-gradient behavior.
International Journal of Solids and Structures, 191:434–448, 2020.

Continuum Mech. Thermodyn.
https://doi.org/10.1007/s00161-020-00910-3

ORIGINAL ARTICLE

Hua Yang · Dmitry Timofeev · Ivan Giorgio · Wolfgang H. Müller

Effective strain gradient continuum model of metamaterials and size effects analysis

Received: 23 January 2020 / Accepted: 31 July 2020

Abstract In this paper, a strain gradient continuum model for a metamaterial with a periodic lattice substructure is considered. A second gradient constitutive law is postulated at the macroscopic level. The effective classical and strain gradient stiffness tensors are obtained based on asymptotic homogenization techniques using the equivalence of energy at the macro- and microscales within a so-called representative volume element. Numerical studies by means of finite element analysis were performed to investigate the effects of changing volume ratio and characteristic length for a single unit cell of the metamaterial as well as changing properties of the underlying material. It is also shown that the size effects occurring in a cantilever beam made of a periodic metamaterial can be captured with appropriate accuracy by using the identified effective stiffness tensors.

Keywords Effective continuum · Strain gradient elasticity · Asymptotic homogenization method · Finite element method

1 Introduction

The modeling of solids and structures in the framework of classical Cauchy mechanics has been widely used in diverse fields. However, experimental evidence increasingly shows limitations of this approach to predict the behavior of some materials at small scales (micro- or nanometer scales), where the intrinsic microstructure of the materials becomes crucial [11,26,54,61]. Heterogeneity inherited by microstructure leads to the so-called size effects, which cannot be captured by strain-based Cauchy mechanics. Particularly this is relevant to metamaterials whose effective properties are mainly determined by their microstructure [18,37,80,85]. When metamaterials are tested, small samples may show different deformation behaviors than larger ones [86]. In order to evaluate metamaterials with appropriate accuracy, a qualitative but also quantitative understanding of size effects needs to be included either in a physically feasible way or, as an alternative method, by

Communicated by Luca Placidi.

H. Yang (✉)· W. H. Müller
Chair of Continuum Mechanics and Constitutive Theory, Institute of Mechanics, Technische Universität Berlin, Einsteinufer 5, 10587 Berlin, Germany
E-mail: hua.yang@campus.tu-berlin.de

D. Timofeev · I. Giorgio
International Research Center for the Mathematics and Mechanics of Complex Systems, Università degli studi dell'Aquila, L'Aquila, Italy

I. Giorgio
Department of Civil, Construction-Architectural and Environmental Engineering, Università degli studi dell'Aquila, Via Giovanni Gronchi 18, 67100 L'Aquila, Italy

Published online: 28 August 2020

homogenization or identification of effective material properties. Indeed, size effects can be captured by using FEM and detailed modeling on a microstructural level with a relatively simple constitutive law [83,84], which means that the size of a mesh should be much smaller than that of the microstructure. The FEM model will readily overpower most of the modern computers. Such analysis is still very time-consuming and unmanageable. Indeed, in engineering practice, it is convenient to replace the heterogeneous material by an equivalent homogeneous material [14,47]. With the identified material parameters, engineers can efficiently design or optimize new structures or materials [24,55–57,71]. For this reason, different homogenization procedures have been proposed in the literature, including the well-known Voigt and Reuss bounds. For more examples, see [22,23,45,47].

Often, the so-called representative volume element (RVE) [42,46,50,74] is postulated. The topic of RVE definitions has been of interest in the scientific communities for over half a century. A recent review for this topic can be found in [19]. Such RVE-based methods divide the analysis into two scales: local and global scales. On the local scale, the microstructure is modeled in detail, and effective material properties are determined under boundary conditions. On the global scale, the material is treated as an equivalent homogeneous continuum with the aforementioned effective properties. There are a number of RVE-based methods, such as computational approaches [75], asymptotic homogenization methods [6,8,15,20,66], and variational-asymptotic methods [17,88]. However, these methods depend on the ratio, ϵ, of the unit size l to the size of the global region of interest L. Note that a unit cell can be different from an RVE. They are both constructed by considering an inclusion and the matrix of the material, but an RVE can be constituted by several unit cells. In general, the accuracy of RVE-based approaches increases as ϵ approaching zero. Nevertheless, for certain metamaterials, ϵ is fixed and sometimes significantly larger than zero. In this case, the size of the microstructure is comparable to the size of the whole structure, and the predicted effective properties will not be able to describe precisely the behavior of the material. In order to tackle these problems and capture these size-dependent phenomena, one possible way is to characterize and homogenize metamaterials in the framework of generalized continuum theories, also known as higher-order theories. Higher-order theories, including strain gradient theory, couple stress theory, micropolar theory, micromorphic theory, and so on, cover the microstructural information, and they are able to mimic the size effects. They have been studied by some researchers extensively, for example, see [5,30,35,36,38,52,59,62,76]. The main challenge for the higher-order continuum approach is to determine the corresponding additional constitutive parameters, which are difficult to measure experimentally. Many efforts have been made for the determination of metamaterial parameters [25,40,41,60,64,67,77] in the framework of generalized mechanics.

In [33,34,51], effective material parameters were derived in the framework of micropolar theory. In [58], an effective couple stress continuum was used for cellular solids. In a recent study [86], size effects occurring in lattice structures were studied and compared to micropolar elasticity. It is reported that the micropolar continuum model typically underpredicts the stiffness due to the size effects seen in the lattice model by an order of magnitude. In [49], the size-dependent bending, buckling, and vibration phenomena of 2D triangular lattices were investigated using simplified strain gradient theory. The effective elastic moduli, including classical moduli as well as additional moduli, were validated by matching the lattice response in benchmark problems. In [12,13,53,65,82], classical and higher-order elastic moduli were identified within the Toupin–Mindlin strain gradient theory due to its generality. In [53], the classical and higher-order elastic moduli were identified by means of the fast Fourier transform (FFT) method in the 2D case. In [13], FEM was used to identify these effective material parameters for materials of the so-called D4 as well as D6 symmetry. In [82], the effective material parameters were identified for square lattice structures. It is shown that the approach that was used in [13,53,82] guarantees a vanishing strain gradient stiffness tensor if the material is purely homogeneous, and it ensures that the resolved strain gradient parameters are not sensitive to choices of an RVE consisting in the repetition of smaller RVEs but depend upon the intrinsic size of the substructure. There are a few pieces of research in the literature validating the identified effective parameters, especially the higher-order moduli. For this reason, this work will focus on validations of effective materials parameters identified by a homogenization method proposed in [82]. Moreover, how the microstructures influence the effective material parameters is analyzed and discussed. It is also attempted in this work to answer the following question: Are the effective material parameters derived based on the homogenization method capable to capture size effects accurately? The paper is organized as follows: In Sect. 2, the homogenization method by means of asymptotic analysis by considering strain gradient effects is recalled. In Sect. 3, effective material parameters, including the classical as well as higher-order moduli, are obtained. The influences of the volume ratio between inclusions and matrices for a unit cell, of the properties of the solid material as well as of the unit cell sizes on the effective material parameters, are analyzed and discussed. In Sect. 4, three different types of computations, including

direct FEM simulation of metamaterials with a very fine mesh, an equivalent Cauchy homogenized model, as well as an equivalent strain gradient homogenized model, are conducted and used to validate the identified effective parameters. size effects presented in cantilever beam bending for a metamaterial are also analyzed. Discussions in Sect. 5 and concluding remarks in Sect. 6 end this paper.

2 Asymptotic homogenization method by considering strain gradient effects

A periodic heterogeneous structure with a 2D domain Ω is considered. Unlike the classical homogenization technique, where Ω is constituted by an infinite number of RVEs, here Ω is constructed with a finite number of RVEs Ω_P, namely:

$$\cup\, \Omega_P = \Omega, \quad \Omega_P \cap \Omega_Q = \emptyset, \quad P, Q = 1, 2, 3, \ldots M, P \neq Q \tag{1}$$

Assume that the equivalence of strain energy of an RVE at micro- Ω_P^{m} and macroscale Ω_P^{M} is possible by using different definitions of the microscale energy density w^{m} and the macroscale energy density w^{M}:

$$\begin{aligned} \int_{\Omega_P^{\mathrm{m}}} w^{\mathrm{m}}\, \mathrm{d}V^{\mathrm{m}} &= \int_{\Omega_P^{\mathrm{M}}} w^{\mathrm{M}}\, \mathrm{d}V^{\mathrm{M}}, \\ \int_{\Omega_P^{\mathrm{m}}} \frac{1}{2} C^{\mathrm{m}}_{ijkl} u^{\mathrm{m}}_{i,j} u^{\mathrm{m}}_{k,l}\, \mathrm{d}V^{\mathrm{m}} &= \int_{\Omega_P^{\mathrm{M}}} \frac{1}{2} \left(C^{\mathrm{M}}_{ijkl} u^{\mathrm{M}}_{i,j} u^{\mathrm{M}}_{k,l} + D^{\mathrm{M}}_{ijklmn} u^{\mathrm{M}}_{i,jk} u^{\mathrm{M}}_{l,mn} \right) \mathrm{d}V^{\mathrm{M}}, \end{aligned} \tag{2}$$

where C^{m}_{ijkl} is defined in each point of the heterogeneous continuum body Ω_P^{m}, and C^{M}_{ijkl} and D^{M}_{ijklmn} are the stiffness tensor and strain gradient stiffness tensor of the corresponding homogenized continuum Ω_P^{M}. It should be mentioned that Eq. (2) can be formulated in terms of the strain tensor and the strain gradient tensor as well. The present formulation is, however, equivalent to that in terms of strain tensors because of the symmetry properties of the stiffness tensors. For a discussion of the objectivity of the strain energy, we refer to [82].

The macro- and microscale energies for an RVE are derived by using the same quantity in order to find expressions for the C^{M}_{ijkl} and D^{M}_{ijklmn}. According to [82], the macroscale strain energy for an RVE can be expressed as:

$$\begin{aligned} &\int_{\Omega_P^{\mathrm{M}}} \frac{1}{2} \left(C^{\mathrm{M}}_{ijlm} u^{\mathrm{M}}_{i,j} u^{\mathrm{M}}_{l,m} + D^{\mathrm{M}}_{ijklmn} u^{\mathrm{M}}_{i,jk} u^{\mathrm{M}}_{l,mn} \right) \mathrm{d}V^{\mathrm{M}} \\ &\quad = \frac{1}{2} V^{\mathrm{M}} \Big(C^{\mathrm{M}}_{ijlm} \left\langle u^{\mathrm{M}}_{i,j} \right\rangle \left\langle u^{\mathrm{M}}_{l,m} \right\rangle + \left(C^{\mathrm{M}}_{ijlm} \bar{I}_{kn} + D^{\mathrm{M}}_{ijklmn} \right) \left\langle u^{\mathrm{M}}_{i,jk} \right\rangle \left\langle u^{\mathrm{M}}_{l,mn} \right\rangle \Big), \end{aligned} \tag{3}$$

where

$$\bar{I}_{kn} = \frac{1}{V^{\mathrm{M}}} \int_{\Omega_P^{\mathrm{M}}} \left(X_k - \overset{\mathrm{c}}{X}_k \right) \left(X_n - \overset{\mathrm{c}}{X}_n \right) \mathrm{d}V^{\mathrm{M}}, \quad \left\langle u^{\mathrm{M}}_{i,j} \right\rangle = u^{\mathrm{M}}_{i,j}\Big|_{\overset{\mathrm{c}}{\boldsymbol{X}}}, \quad \left\langle u^{\mathrm{M}}_{i,jk} \right\rangle = u^{\mathrm{M}}_{i,jk}\Big|_{\overset{\mathrm{c}}{\boldsymbol{X}}}, \tag{4}$$

$\overset{\mathrm{c}}{\boldsymbol{X}}$ is the geometric center of the RVE. Therefore, the macroscale strain energy for an RVE is expressed in terms of the macroscopic gradient and the second gradient of displacement. If the microscale strain energy can be expressed by using the same quantities, the expressions for C^{M}_{ijkl} and D^{M}_{ijklmn} can be found. For this reason, the asymptotic homogenization method is employed at the microscale when deriving the microscale strain energy.

Following the asymptotic homogenization method in [82], the left-hand side of Eq. (2) is reformulated. The asymptotic homogenization method defines two levels of length scales. One is the macroscopic level $\boldsymbol{X}$ to describe the global variation of a considered field, and the other one is the microscopic level $\boldsymbol{y}$, which associates with the RVE and represents the local fluctuation of such a field. The relationship between $\boldsymbol{X}$ and $\boldsymbol{y}$ is the following:

$$y_j = \frac{1}{\epsilon} \left(X_j - \overset{\mathrm{c}}{X}_j \right), \tag{5}$$

where ϵ is a scaling or homothetic ratio between the $\boldsymbol{X}$ and $\boldsymbol{y}$. Technically, ϵ can be set to be equal to l/L by magnifying the size of an RVE from l to L, as shown in Fig. 1. It should be noted that ϵ is regarded as zero

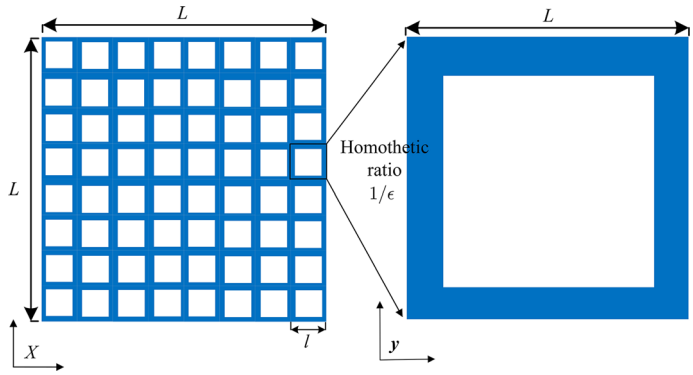

Fig. 1 A Cauchy heterogeneous metamaterial obtained by repeating unit cells periodically. The unit cell contains a square inclusion (white) within the matrix (blue). The unit cell is magnified $1/\epsilon$ times at local coordinate by using a homothetic ratio (color figure online)

in the classical homogenization technique since the macroscopic length L is infinite. However, in our case of finite macroscopic length L, ϵ has a finite value. We assume that field quantities, such as displacement, stress, and strain, vary as smoothly as required at the macroscopic level. At the microscopic level, the field quantities are assumed to be periodic, and their values fluctuate around the macroscopic values.

Following [82], the displacement field of an RVE at macroscopic coordinate $\boldsymbol{X}$ is expanded with respect to ϵ as a power series:

$$\boldsymbol{u}^{\mathrm{m}}(\boldsymbol{X}) = \overset{0}{\boldsymbol{u}}(\boldsymbol{X}, \boldsymbol{y}) + \epsilon \overset{1}{\boldsymbol{u}}(\boldsymbol{X}, \boldsymbol{y}) + \epsilon^2 \overset{2}{\boldsymbol{u}}(\boldsymbol{X}, \boldsymbol{y}) + \ldots, \tag{6}$$

where $\overset{n}{\boldsymbol{u}}(\boldsymbol{X}, \boldsymbol{y})$ ($n = 0, 1, 2, \ldots$) are assumed to be $\boldsymbol{y}$-periodic. The first term $\overset{0}{\boldsymbol{u}}(\boldsymbol{X}, \boldsymbol{y})$ depends only on $\boldsymbol{X}$ [82], and thus, $\overset{0}{\boldsymbol{u}}(\boldsymbol{X})$ is assumed to be the macroscopic displacement field.

Within an RVE, the governing equation reads

$$\left(C^{\mathrm{m}}_{ijkl} u^{\mathrm{m}}_{k,l}\right)_{,j} + f_i = 0 \quad \forall \boldsymbol{X} \in \Omega^{\mathrm{m}}_P, \tag{7}$$

where $\boldsymbol{f}$ is the body force field. By substituting Eq. (6) into Eq. (7) and after solving partial differential equations, Eq. (6) can be rewritten as

$$u^{\mathrm{m}}_i(\boldsymbol{X}, \boldsymbol{y}) = u^{\mathrm{M}}_i(\boldsymbol{X}) + \epsilon \varphi_{abi}(\boldsymbol{y}) u^{\mathrm{M}}_{a,b}(\boldsymbol{X}) + \epsilon^2 \psi_{abci}(\boldsymbol{y}) u^{\mathrm{M}}_{a,bc}(\boldsymbol{X}) + \ldots, \tag{8}$$

where $\varphi_{abi}(\boldsymbol{y})$ and $\psi_{abci}(\boldsymbol{y})$ are both $\boldsymbol{y}$-periodic. They are the solutions of the following two partial differential equations,

$$\frac{\partial}{\partial y_j}\left(C^{\mathrm{m}}_{ijkl}\left(\frac{\partial \varphi_{abk}}{\partial y_l} + \delta_{ak}\delta_{bl}\right)\right) = 0, \tag{9}$$

$$\frac{\partial}{\partial y_j}\left(C^{\mathrm{m}}_{ijkl}\left(\frac{\partial \psi_{abck}}{\partial y_l} + \varphi_{abk}\delta_{lc}\right)\right) + C^{\mathrm{m}}_{ickl}\left(\frac{\partial \varphi_{abk}}{\partial y_l} + \delta_{ka}\delta_{lb}\right) - C^{\mathrm{M}}_{icab} = 0. \tag{10}$$

The derivation of Eqs. (9) and (10) can be found in the appendix of [82]. By writing the gradient of the microscale displacement by neglecting terms higher than second gradients, we obtain

$$u^{\mathrm{m}}_{i,j} = L_{abij}\left\langle u^{\mathrm{M}}_{a,b}\right\rangle + \epsilon M_{abcij}\left\langle u^{\mathrm{M}}_{a,bc}\right\rangle + \ldots, \tag{11}$$

where

$$\begin{aligned} L_{abij} &= \delta_{ia}\delta_{jb} + \frac{\partial \varphi_{abi}}{\partial y_j}, \\ M_{abcij} &= y_c\left(\delta_{ia}\delta_{jb} + \frac{\partial \varphi_{abi}}{\partial y_j}\right) + \left(\varphi_{abi}\delta_{jc} + \frac{\partial \psi_{abci}}{\partial y_j}\right). \end{aligned} \tag{12}$$

By using the latter on the left-hand side of Eq. (2), the microscale energy becomes

$$\int_{\Omega_P^{\mathrm{m}}} \frac{1}{2} C^{\mathrm{m}}_{ijkl} u^{\mathrm{m}}_{i,j} u^{\mathrm{m}}_{k,l} \,\mathrm{d}V^{\mathrm{m}} = \frac{V^{\mathrm{M}}}{2} \left(\bar{C}_{abcd} \left\langle u^{\mathrm{M}}_{a,b} \right\rangle \left\langle u^{\mathrm{M}}_{c,d} \right\rangle + \bar{D}_{abcdef} \left\langle u^{\mathrm{M}}_{a,bc} \right\rangle \left\langle u^{\mathrm{M}}_{d,ef} \right\rangle + \bar{G}_{abcde} \left\langle u^{\mathrm{M}}_{a,b} \right\rangle \left\langle u^{\mathrm{M}}_{c,de} \right\rangle \right) \tag{13}$$

with

$$\begin{aligned} \bar{C}_{abcd} &= \frac{1}{V^{\mathrm{M}}} \int_{\Omega_P^{\mathrm{m}}} C^{\mathrm{m}}_{ijkl} L_{abij} L_{cdkl} \,\mathrm{d}V^{\mathrm{m}}, \\ \bar{D}_{abcdef} &= \frac{\epsilon^2}{V^{\mathrm{M}}} \int_{\Omega_P^{\mathrm{m}}} C^{\mathrm{m}}_{ijkl} M_{abcij} M_{defkl} \,\mathrm{d}V^{\mathrm{m}}, \\ \bar{G}_{abcde} &= \frac{2\epsilon}{V^{\mathrm{M}}} \int_{\Omega_P^{\mathrm{m}}} C^{\mathrm{m}}_{ijkl} L_{abij} M_{cdekl} \,\mathrm{d}V^{\mathrm{m}}. \end{aligned} \tag{14}$$

In the case of centrosymmetric materials, the rank 5 tensor vanishes, $\bar{\boldsymbol{G}} = 0$. By comparing with Eq. (3), the expressions for C^{M}_{ijlm} and D^{M}_{ijklmn} can be obtained as:

$$\begin{aligned} C^{\mathrm{M}}_{ijlm} &= \bar{C}_{ijlm}, \\ C^{\mathrm{M}}_{ijlm} \bar{I}_{kn} + D^{\mathrm{M}}_{ijklmn} &= \bar{D}_{ijklmn}, \end{aligned} \tag{15}$$

where

$$\bar{I}_{kn} = \frac{1}{V^{\mathrm{M}}} \int_{\Omega_P^{\mathrm{M}}} \left(X_k - \overset{\mathrm{c}}{X}_k \right) \left(X_n - \overset{\mathrm{c}}{X}_n \right) \mathrm{d}V^{\mathrm{M}} = \frac{\epsilon^2}{V^{\mathrm{M}}} \int_{\Omega_P^{\mathrm{m}}} y_k y_n \,\mathrm{d}V^{\mathrm{M}}. \tag{16}$$

They can also be rewritten as:

$$\begin{aligned} C^{\mathrm{M}}_{abcd} &= \frac{1}{V^{\mathrm{M}}} \int_{\Omega_P^{\mathrm{m}}} C^{\mathrm{m}}_{ijkl} L_{abij} L_{cdkl} \,\mathrm{d}V^{\mathrm{m}}, \\ D^{\mathrm{M}}_{abcdef} &= \frac{\epsilon^2}{V^{\mathrm{M}}} \left(\int_{\Omega_P^{\mathrm{m}}} C^{\mathrm{m}}_{ijkl} M_{abcij} M_{defkl} \,\mathrm{d}V^{\mathrm{m}} - C^{\mathrm{M}}_{abef} \int_{\Omega_P^{\mathrm{m}}} y_c y_d \,\mathrm{d}V^{\mathrm{M}} \right). \end{aligned} \tag{17}$$

3 Determination of effective material parameters

The set of factors influencing the effective properties contains the volume fraction of the matrix, the properties of the underlying material, and the size of unit cells. The way they affect the effective material properties is investigated quantitatively in this section. The computations for the identification process are performed by means of FEM using the FEniCS computing platform. For the implemented weak forms, we refer to [82]. A metamaterial constituted with square inclusions is studied. The constituents of the metamaterial (inclusions and matrix) are linear elastic isotropic materials characterized by two independent parameters (Young's modulus and Poisson's ratio). After homogenization, the continuum model is not isotropic at the macroscale of observation. Indeed, it is of D4-invariant symmetry [9,10,67]. The inclusions can be voids, with their material parameters being zero. Indeed, small values for these material parameters are used numerically. In this case, the metamaterial can also be regarded as a lattice structure. The effective moduli of the metamaterial are plotted as the functions of volume fraction of matrix, sizes of the unit cell as well as the properties of underlying material. The plots are shown in Figs. 2, 3 and 4, respectively. The Voigt notations used in this paper are shown in Tables 1 and 2. There are 3 independent parameters in the classical stiffness tensor, and there are 6 independent parameters in the strain gradient stiffness tensor as shown in what follows.

$$\begin{bmatrix} C_{1111} & C_{1122} & 0 \\ & C_{1111} & 0 \\ \text{sym} & & C_{1212} \end{bmatrix},$$

Table 1 Voigt notation used for 2D strain tensors

I	1	2	3
ij	11	22	12

Table 2 Voigt notation used for 2D strain gradient tensors

I	1	2	3	4	5	6
ijk	111	221	122	222	112	121

Table 3 Varying the volume ratio of the matrix

	1	2	3	4	5
Unit cell	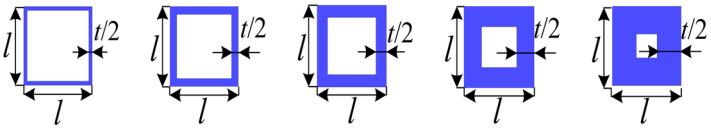				
V_f	19%	36%	51%	75%	91%
t (mm)	0.1	0.2	0.3	0.5	0.7
l (mm)	1	1	1	1	1

$$\begin{bmatrix} D_{111111} & D_{111221} & D_{111122} & 0 & 0 & 0 \\ & D_{221221} & D_{221122} & 0 & 0 & 0 \\ & & D_{122122} & 0 & 0 & 0 \\ & & & D_{111111} & D_{111221} & D_{111122} \\ & \text{sym} & & & D_{221221} & D_{221122} \\ & & & & & D_{122122} \end{bmatrix}.$$

3.1 Influence of the volume fraction of matrix

A metamaterial whose microstructure is constructed with square voids inside a matrix, which is shaped like a lattice structure, is studied. The material parameters used for matrix are Young's modulus $E = 100$ MPa and Poisson's ratio $\nu = 0.3$. The material properties of the inclusions are all zero. The size of the unit cell l is set to 1 mm. The thickness of the cell wall t varies from 0.1 to 1.0 mm, leading to a change of the volume fraction V_f of the matrix from 19 to 100% as indicated in Table 3. As shown in Fig. 2, with the increasing of the volume ratio of the matrix, the effective classical stiffness parameters increase accordingly. However, effective strain gradient parameters increase at first, and then, they decrease. When the volume ratio is 100%, the material is homogeneous, and the effective strain gradient parameters become zero. This is consistent with intuitive understandings.

3.2 Influence of the size of a unit cell

In this section, the size of the unit cell l varies in the set of values: 1 mm, 0.5 mm, and 0.2 mm. The thickness of the cell wall t is kept at 0.2 mm meaning the volume fraction of the matrix is fixed as 36% as indicated in Table 4. The material parameters used for the matrix entail Young's modulus $E = 100$ MPa and Poisson's ratio $\nu = 0.3$, while the inclusions are voids. The results are shown in Fig. 3. Corresponding to the variation of the size of the unit cell, it is found that the effective classical stiffness parameters are unchanged due to the fact that they have the same topology and volume fraction of matrix. However, the effective strain gradient stiffness parameters are sensitive to it. When decreasing the size of the unit cell, the effective stiffness parameters decrease as well. Indeed, when the size of the unit cell vanishes, the material tends to be homogeneous and in

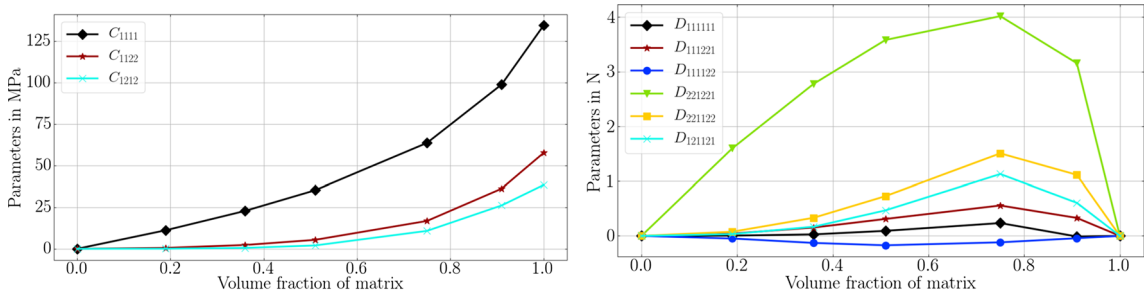

(a) Effective classical stiffness parameters.

(b) Effective strain gradient stiffness parameters.

Fig. 2 Effective material parameters versus volume ratio of matrix

Table 4 Varying the size of unit cell

	1	2	3
Unit cell	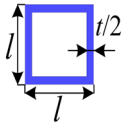		
V_f	36%	36%	36%
t (mm)	0.2	0.2	0.2
l (mm)	1	0.5	0.2

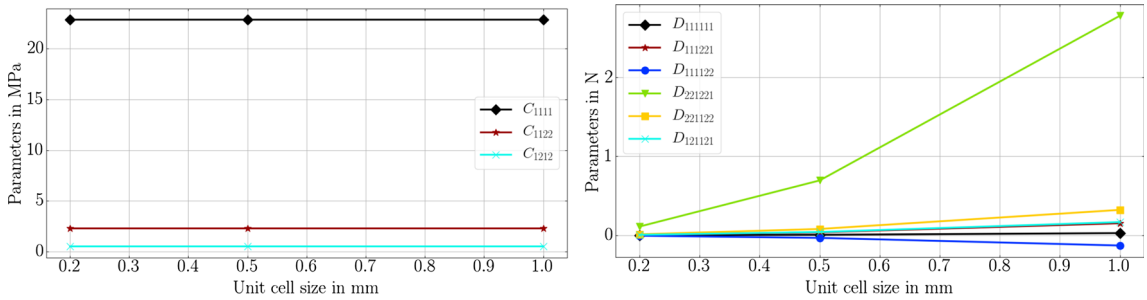

(a) Effective classical stiffness parameters.

(b) Effective strain gradient stiffness parameters.

Fig. 3 Effective material parameters versus size of a unit cell

this case, the effective strain gradient stiffness parameters tend to be zero. Actually, the values of the effective strain gradient parameters are linearly dependent on ϵ^2. This can also be observed in Eq. (17).

3.3 Influence of the properties of base materials

In this section, Young's modulus of the base material for inclusions is set to 0 MPa, 10 MPa, 30 MPa, 50 MPa, 70 MPa, 90 MPa. The Poisson's ratio of the inclusions is the same for all cases studied here, $\nu = 0.3$. The properties of the base material for the matrix are kept at 100 MPa for Young's modulus and Poisson's ratio $\nu = 0.3$. The sizes of the unit cell l are all 1 mm. The thickness of the cell wall t is kept at 0.2 mm, which means the volume fraction of the matrix is fixed at 36% as indicated in Table 5. The results are shown in Fig. 4. It is indicated that with increasing Young's modulus of the inclusions, the effective classical stiffness parameters monotonously increase. Although not every effective, the strain gradient parameter shows a monotonous trend, the dominant one, D_{221221} (with the biggest absolute value), shows a monotonously decreasing trend. All the

Table 5 Varying the properties of base materials

	1	2	3	4	5	6
Unit cell	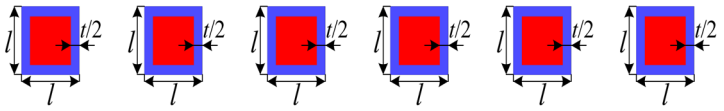					
V_f	36%	36%	36%	36%	36%	36%
t (mm)	0.2	0.2	0.2	0.2	0.2	0.2
l (mm)	1	1	1	1	1	1
E_{inc} (MPa)	0	10	30	50	70	90
E_{mat} (MPa)	100	100	100	100	100	100

(a) Effective classical stiffness parameters. **(b)** Effective strain gradient stiffness parameters.

Fig. 4 Effective material parameters versus properties of base materials

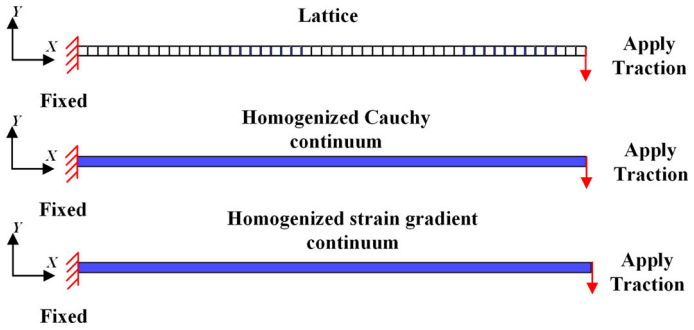

Fig. 5 Three types of conducted simulations and boundary conditions applied

effective strain gradient parameters reach zero when the material is homogeneous. (Young's modulus ratio between the matrix and inclusion is 1.)

4 Investigations of size effects by using the identified parameters

In order to investigate size effects and validate the identified parameters, comparisons are made employing FEM computations among a direct calculation of heterogeneous metamaterial, an equivalent Cauchy homogeneous continuum, as well as an equivalent strain gradient homogeneous continuum. Bending tests for a cantilever beam are modeled and studied for these three cases. The left edge of the beam is fixed in both x and y directions. Traction from 0 to 100 Pa (0.0001 MPa) is applied incrementally at the right edge of the beam along the vertical direction as shown in Fig. 5.

A Lagrange element with quadratic shape function is used for the direct computation and in case of the equivalent Cauchy homogeneous continuum. It is known that for the numerical implementation of strain gradient elasticity, at least C^1 continuity is mandatory. In order to fulfill this requirement, isogeometric FEM

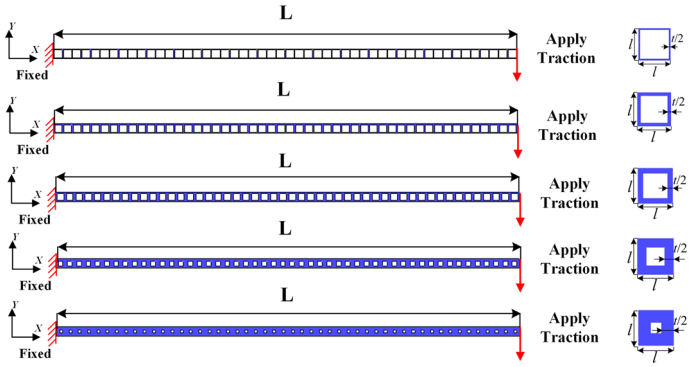

Fig. 6 Cantilever beam: geometry and boundary conditions

Table 6 Identified effective parameters $V_f = 19\%$

Unit cell	V_f	t (mm)	l (mm)	C (MPa)	D (N)
	19%	0.1	1.0	$\begin{bmatrix} 11.177 & 0.555 & 0 \\ 0.555 & 11.177 & 0 \\ 0 & 0 & 0.060 \end{bmatrix}$	$\begin{bmatrix} 0.005 & 0.042 & -0.048 \\ 0.042 & 1.598 & 0.076 \\ -0.048 & 0.076 & 0.033 \end{bmatrix}$

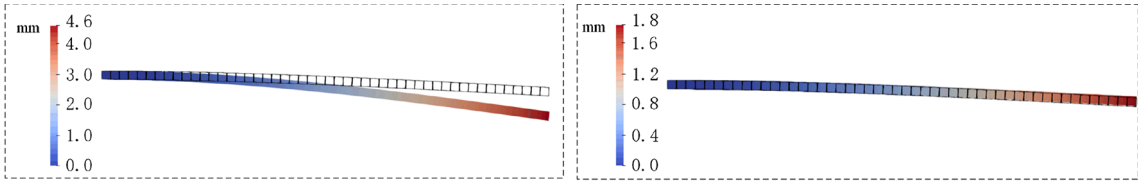

(a) Total displacement plot of lattice and Cauchy continuum in current configuration.

(b) Total displacement plot of lattice and strain gradient continuum in current configuration.

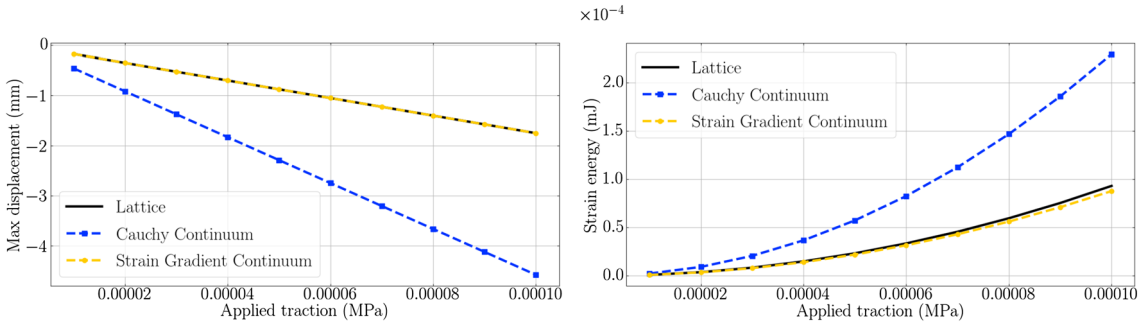

(c) Maximum deflection $\boldsymbol{u}_y$ versus applied traction.

(d) Strain energy versus applied traction.

Fig. 7 Comparisons of lattice, Cauchy continuum, and strain gradient continuum for RVE with volume ratio 19%

Table 7 Identified effective parameters $V_f = 36\%$

Unit cell	V_f	t (mm)	l (mm)	C (MPa)	D (N)
	36%	0.2	1.0	$\begin{bmatrix} 22.849 & 2.293 & 0 \\ 2.293 & 22.849 & 0 \\ 0 & 0 & 0.534 \end{bmatrix}$	$\begin{bmatrix} 0.028 & 0.153 & -0.129 \\ 0.153 & 2.779 & 0.322 \\ -0.129 & 0.322 & 0.168 \end{bmatrix}$

Table 8 Identified effective parameters $V_f = 51\%$

Unit cell	V_f	t (mm)	l (mm)	C (MPa)	D (N)
	51%	0.3	1.0	$\begin{bmatrix} 35.254 & 5.386 & 0 \\ 5.386 & 35.254 & 0 \\ 0 & 0 & 2.009 \end{bmatrix}$	$\begin{bmatrix} 0.092 & 0.310 & -0.172 \\ 0.310 & 3.582 & 0.727 \\ -0.172 & 0.727 & 0.467 \end{bmatrix}$

Table 9 Identified effective parameters $V_f = 75\%$

Unit cell	V_f	t (mm)	l (mm)	C (MPa)	D (N)
	75%	0.5	1.0	$\begin{bmatrix} 63.704 & 16.798 & 0 \\ 16.798 & 63.704 & 0 \\ 0 & 0 & 10.792 \end{bmatrix}$	$\begin{bmatrix} 0.235 & 0.556 & -0.118 \\ 0.556 & 4.018 & 1.506 \\ -0.118 & 1.506 & 1.128 \end{bmatrix}$

Table 10 Identified effective parameters $V_f = 91\%$

Unit cell	V_f	t (mm)	l (mm)	C (MPa)	D (N)
	91%	0.7	1.0	$\begin{bmatrix} 98.958 & 36.238 & 0 \\ 36.238 & 98.958 & 0 \\ 0 & 0 & 26.149 \end{bmatrix}$	$\begin{bmatrix} -0.011 & 0.329 & -0.043 \\ 0.329 & 3.156 & 1.113 \\ -0.043 & 1.113 & 0.605 \end{bmatrix}$

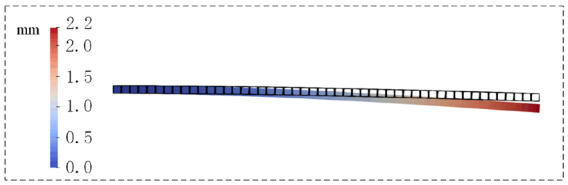

(a) Total displacement plot of lattice and Cauchy continuum in current configuration.

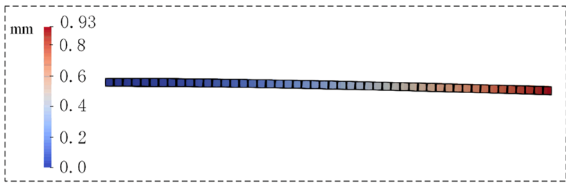

(b) Total displacement plot of lattice and strain gradient continuum in current configuration.

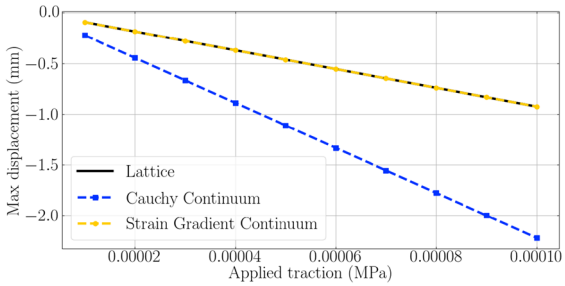

(c) Maximum deflection $\boldsymbol{u}_y$ versus applied traction.

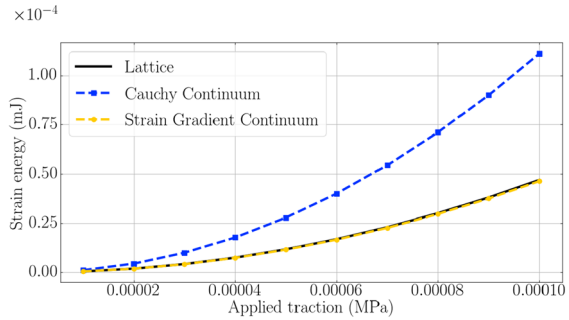

(d) Strain energy versus applied traction.

Fig. 8 Comparisons of lattice, Cauchy continuum, and strain gradient continuum for RVE with volume ratio 36%

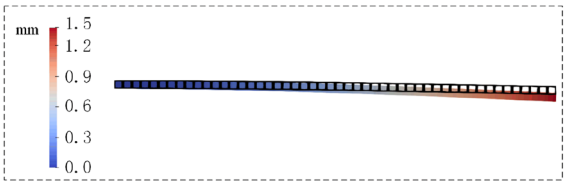

(a) Total displacement plot of lattice and Cauchy continuum in current configuration.

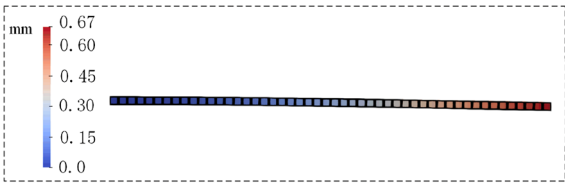

(b) Total displacement plot of lattice and strain gradient continuum in current configuration.

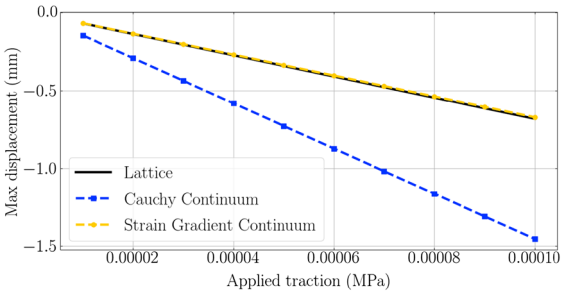

(c) Maximum deflection $\boldsymbol{u}_y$ versus applied traction.

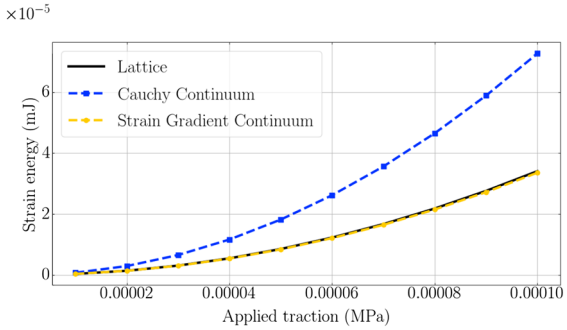

(d) Strain energy versus applied traction.

Fig. 9 Comparisons of lattice, Cauchy continuum, and strain gradient continuum for RVE with volume ratio 51%

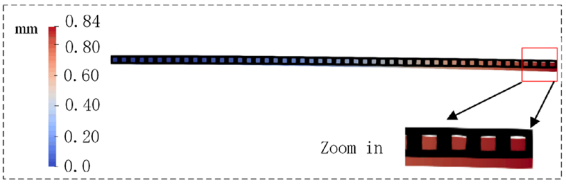

(a) Total displacement plot of lattice and Cauchy continuum in current configuration.

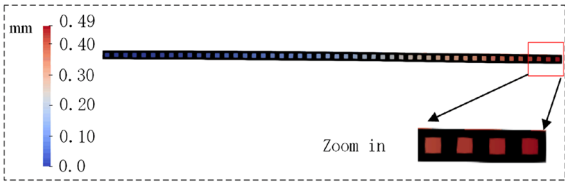

(b) Total displacement plot of lattice and strain gradient continuum in current configuration.

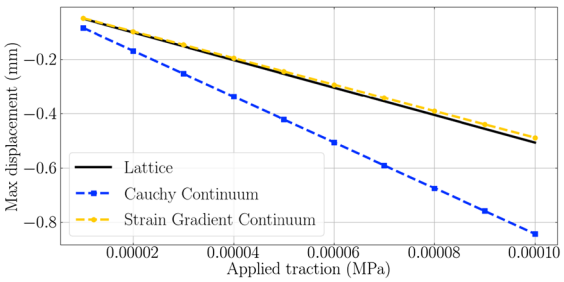

(c) Maximum deflection $\boldsymbol{u}_y$ versus applied traction.

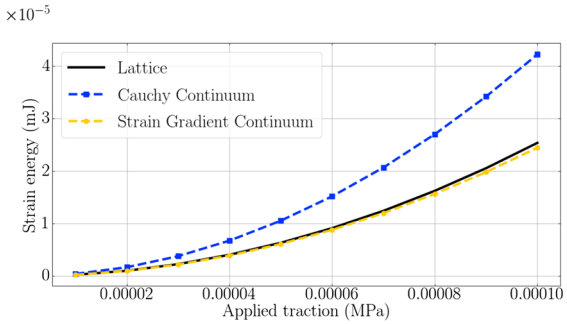

(d) Strain energy versus applied traction.

Fig. 10 Comparisons of lattice, Cauchy continuum, and strain gradient continuum for RVE with volume ratio 75%

is employed with non-uniform rational Bezier spline (NURBS)-based shape functions in the computations of the equivalent strain gradient homogeneous continuum case [21,39,43,44,48,63,69]. A derivation of the weak form of the strain gradient elasticity can be found in [1,81]. The maximum deflection $\boldsymbol{u}_y$ and deformation energies in the computations are calculated for comparison.

Simulations are carried out as follows:

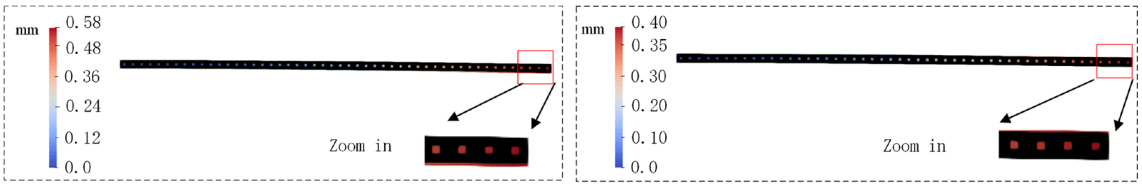

(a) Total displacement plot of lattice and Cauchy continuum in current configuration.

(b) Total displacement plot of lattice and strain gradient continuum in current configuration.

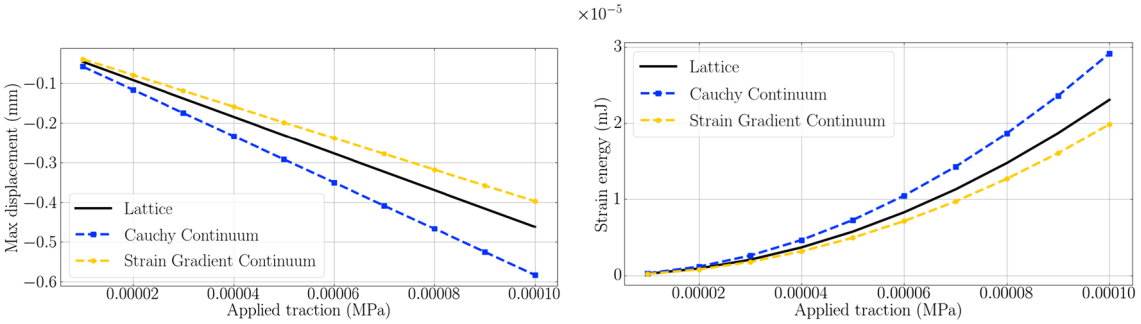

(c) Maximum deflection $\boldsymbol{u}_y$ versus applied traction.

(d) Strain energy versus applied traction.

Fig. 11 Comparisons of lattice, Cauchy continuum, and strain gradient continuum for RVE with volume ratio 91%

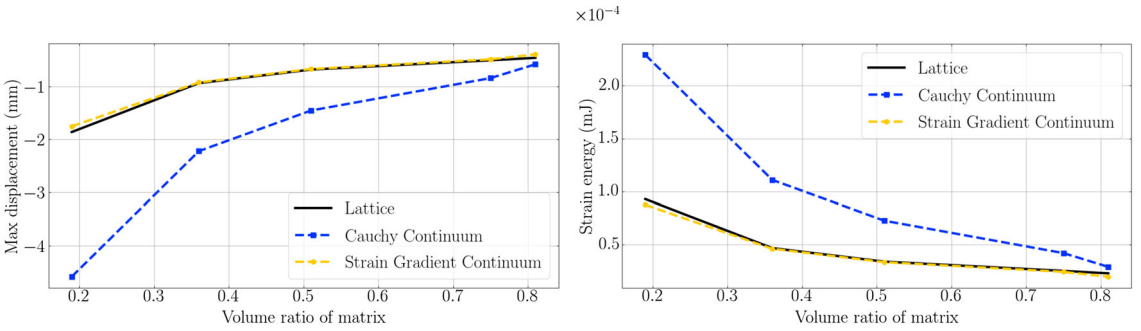

(a) Maximum deflection $\boldsymbol{u}_y$ versus volume fraction of matrix.

(b) Strain energy versus volume fraction of matrix.

Fig. 12 Comparisons of maximum deflection $\boldsymbol{u}_y$ and strain energy versus volume fraction of matrix

- Five bending tests of cantilever beams constructed by RVEs for different volume fractions of the matrix, 19%, 36%, 51% , 75%, 91%.
- Three bending tests of cantilever beams constructed by RVEs with different unit cell sizes, 1 mm , 0.5 mm, 0.2 mm.
- Three bending tests of cantilever beams with different macrolengths (50 mm, 40 mm, 30 mm) but unchanged microstructures.
- Six bending tests of cantilever beams constructed by RVEs with different properties of base materials.

4.1 Different volume fractions of matrix

In this section, five bending tests of cantilever beams constructed by RVEs with volume fraction of matrix 19%, 36%, 51%, 75%, 91% are examined, as shown in Fig. 6. The macrolength L of beams is set to be 50 mm. The microlength l of the RVE is the same $l = 1$ mm in all five cases. The thickness t of the wall of the RVE is changing between 0.1 mm, 0.2 mm, 0.3 mm, 0.5 mm, 0.7 mm. These geometry parameters as

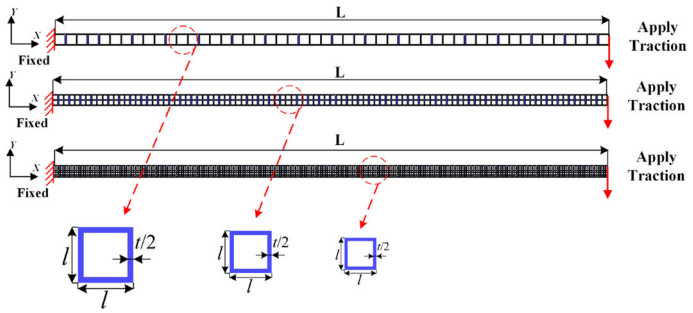

Fig. 13 Cantilever beam: geometry and boundary conditions

Table 11 Identified effective parameters $l = 0.5$ mm

Unit cell	V_f	t (mm)	l (mm)	C (MPa)	D (N)
	36%	0.1	0.5	$\begin{bmatrix} 22.849 & 2.293 & 0 \\ 2.293 & 22.849 & 0 \\ 0 & 0 & 0.534 \end{bmatrix}$	$\begin{bmatrix} 0.007 & 0.038 & -0.032 \\ 0.038 & 0.695 & 0.081 \\ -0.032 & 0.081 & 0.042 \end{bmatrix}$

Table 12 Identified effective parameters $l = 0.2$ mm

Unit cell	V_f	t (mm)	l (mm)	C (MPa)	D (N)
	36%	0.04	0.2	$\begin{bmatrix} 22.849 & 2.293 & 0 \\ 2.293 & 22.849 & 0 \\ 0 & 0 & 0.534 \end{bmatrix}$	$\begin{bmatrix} 0.001 & 0.006 & -0.005 \\ 0.006 & 0.111 & 0.013 \\ -0.005 & 0.013 & 0.007 \end{bmatrix}$

well as the identified effective parameters can be found from Tables 6, 7, 8, 9, and 10. It can be observed from the figures (Figs. 7, 8, 9, 10, 11) that the results of homogenized strain gradient continua show a good quantitative match with direct computations of lattice structures both for the displacement field and for the strain energy. When the volume fraction of matrix V_f becomes larger and larger, the discrepancy between the direct computations of lattice structures and homogenized Cauchy continuum becomes smaller and smaller. When the volume fraction of the matrix is equal to 91%, the results of the homogenized Cauchy continuum show a good agreement with direct computations, as depicted in Fig. 12.

4.2 Different unit cell sizes

In this section, three bending tests of cantilever beams constructed by RVEs with different unit cell sizes 1 mm, 0.5 mm, 0.2 mm are compared, as shown in Fig. 13. The effective material parameters identified are shown in Tables 7, 11, and 12. We conclude that the homogenized strain gradient continua match well with the direct computations of lattice structures as indicated in Figs. 14, 15, and 16. With decreasing unit cell size, the results (strain energy and displacement field) of homogenized strain gradient continua are gradually converging to the results of the homogenized Cauchy continua, as shown in Fig. 16. The difference between the results (strain energy and displacement field) with a few unit cells and many unit cells must be attributed to a size-effect. This size-effect is largest when there are few unit cells. In other words, if the microstructure is comparable to macroscopic structures, size effects cannot be ignored.

4.3 Different macrolengths

In this section, three bending tests of cantilever beams with different macrolengths ($L = 50$ mm, 40 mm, 30 mm) but the same microstructure ($l = 1$ mm, $V_f = 36\%$, $t = 0.2$ mm) are compared, as shown in Fig. 17. The identified effective material parameters can be found in Table 7. As indicated in Figs. 8, 18, and 19, homogenized strain gradient continua results match well with direct computations of lattice structures. It

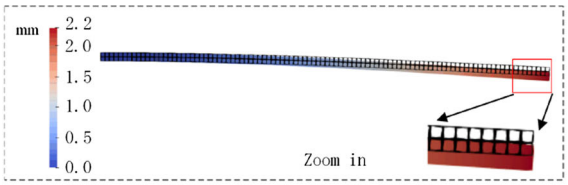

(a) Total displacement plot of lattice and Cauchy continuum in current configuration.

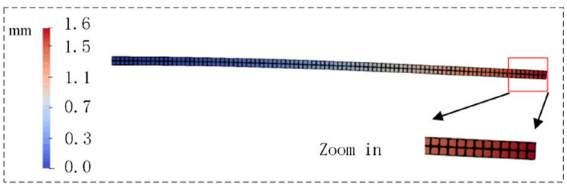

(b) Total displacement plot of lattice and strain gradient continuum in current configuration.

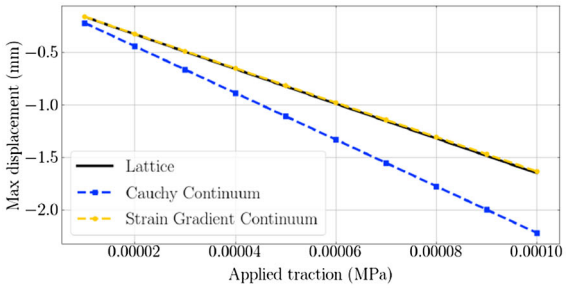

(c) Maximum deflection $\boldsymbol{u}_y$ $\boldsymbol{u}_y$ versus applied traction.

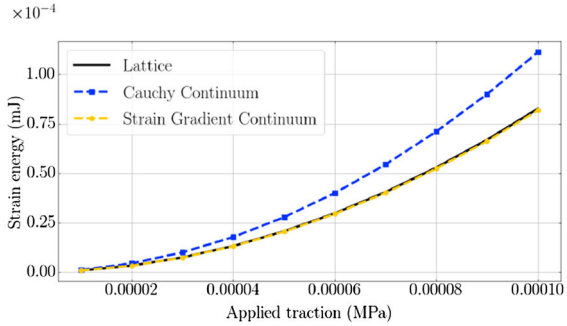

(d) Strain energy versus applied traction.

Fig. 14 Comparisons of lattice, Cauchy continuum, and strain gradient continuum for unit cell with $l = 0.5$ mm

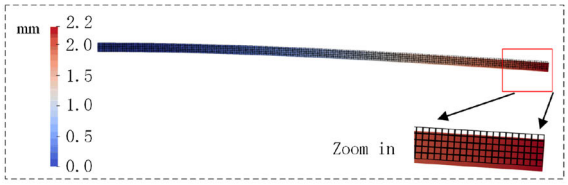

(a) Total displacement plot of lattice and Cauchy continuum in current configuration.

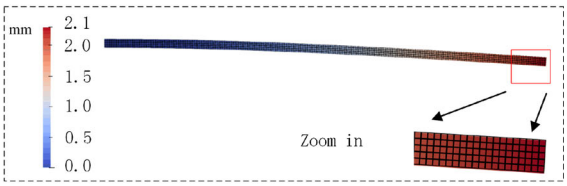

(b) Total displacement plot of lattice and strain gradient continuum in current configuration.

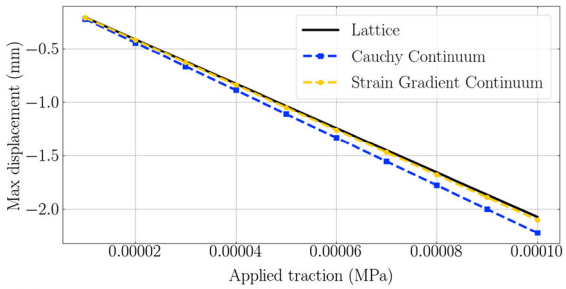

(c) Maximum deflection $\boldsymbol{u}_y$ versus applied traction.

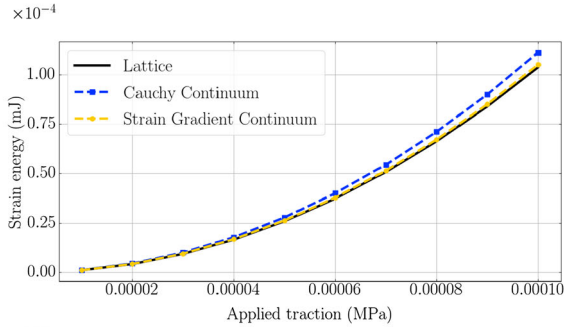

(d) Strain energy versus applied traction.

Fig. 15 Comparisons of lattice, Cauchy continuum, and strain gradient continuum for unit cell with $l = 0.2$ mm

should be remarked that (see Fig. 20) with increasing macrolength L of the beams, the differences between the Cauchy continua and the lattice structures increase. This occurs because if L increases, the beam will be softer, which leads to a larger deflection. This will conduct an increase in the bending energy resulting in the aforementioned large differences (Fig. 21).

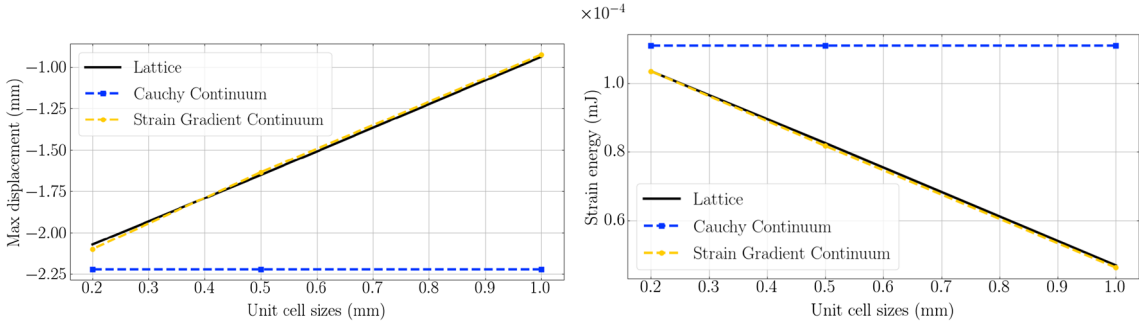

(a) Maximum deflection $\boldsymbol{u}_y$ versus unit cell size l.

(b) Strain energy versus unit cell size l.

Fig. 16 Comparisons of maximum deflection $\boldsymbol{u}_y$ and strain energy with regard to microstructure size l

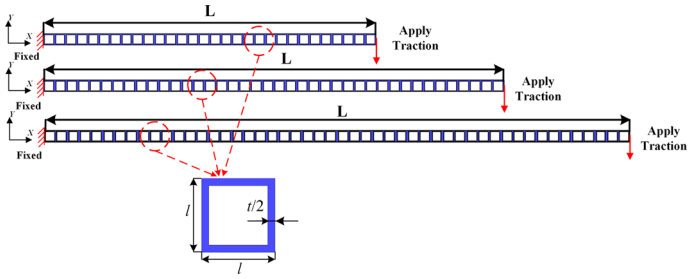

Fig. 17 Cantilever beams with the different macrolength L and the same microstructures

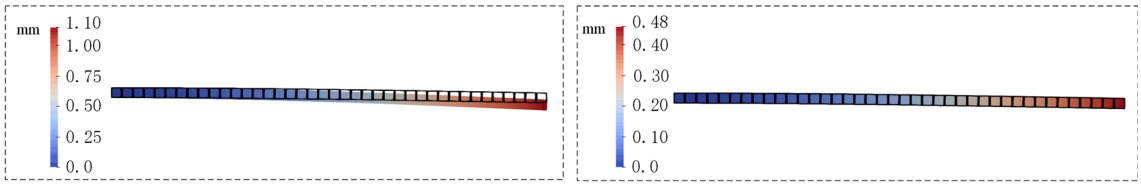

(a) Total displacement plot of lattice and Cauchy continuum in current configuration.

(b) Total displacement plot of lattice and strain gradient continuum in current configuration.

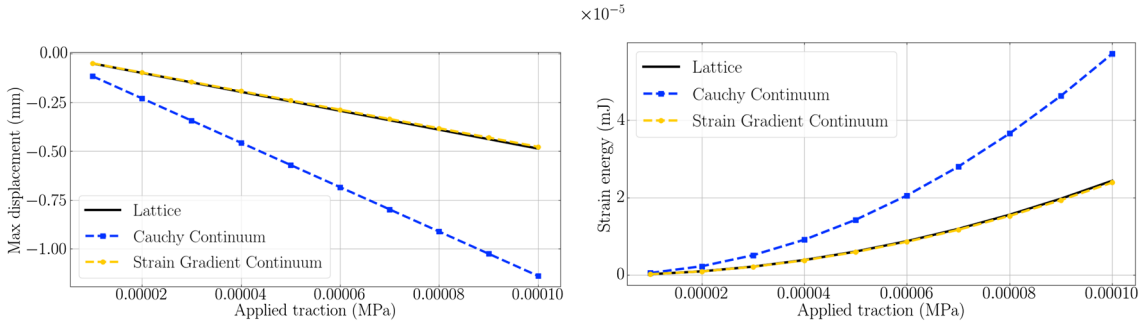

(c) Maximum deflection $\boldsymbol{u}_y$ versus applied traction.

(d) Strain energy versus applied traction.

Fig. 18 Comparisons of lattice, Cauchy continuum, and strain gradient continuum for $L = 40$ mm

4.4 Different material properties

Six bending tests of cantilever beams constructed by RVEs with different properties of underlying material are compared in this section. The Young's modulus of the inclusions changes between 0, 10 MPa, 30 MPa,

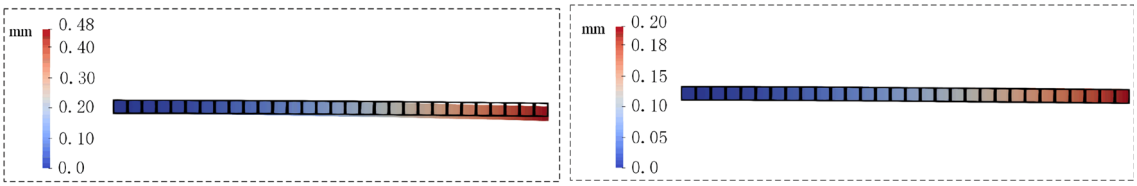

(a) Total displacement plot of lattice and Cauchy continuum in current configuration.

(b) Total displacement plot of lattice and strain gradient continuum in current configuration.

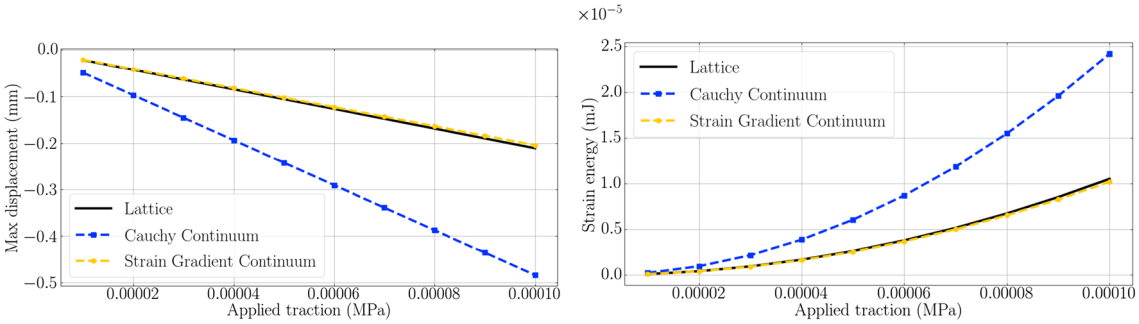

(c) Maximum deflection $\boldsymbol{u}_y$ versus applied traction.

(d) Strain energy versus applied traction.

Fig. 19 Comparisons of lattice, Cauchy continuum, and strain gradient continuum for $L = 30$ mm

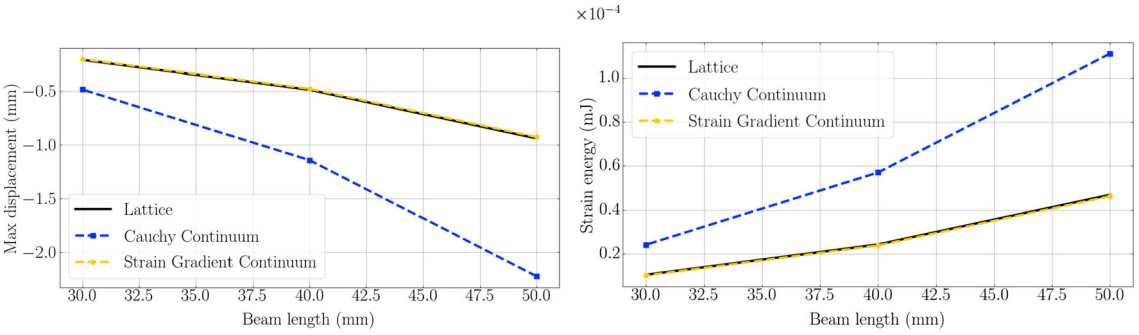

(a) Maximum deflection $\boldsymbol{u}_y$ versus macro length of the beam.

(b) Strain energy versus macro length of the beam.

Fig. 20 Comparisons of maximum deflection $\boldsymbol{u}_y$ and strain energy with regard to the macrolength L

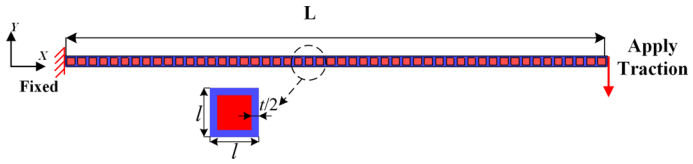

Fig. 21 Cantilever beams constructed by RVEs with inclusions (red) and matrices (blue) (color figure online)

50 MPa, 70 MPa, 90 MPa. The Young's modulus of the matrix is kept at 100 MPa. The Poisson ratios for the inclusions and the matrix are equal to 0.3. The macrolengths L of the beams and the microlengths l of the microstructures are equal to 50 mm and 1 mm, respectively, in all cases. The other microstructure-related parameters, t, V_f, as well as the identified effective material parameters can be found in Tables 7, 13, 14, 15, 16, and 17.

The figures (Figs. 22, 23, 24, 25, 26) reveal that the results of homogenized strain gradient continua agree well with the results for heterogeneous continua. The differences between the homogenized Cauchy

Table 13 Identified effective parameters

Unit cell	E_{mat} (MPa)	E_{inc} (MPa)	C (MPa)	D (N)
	100.0	10.0	$\begin{bmatrix} 37.167 & 10.185 & 0 \\ 10.185 & 37.167 & 0 \\ 0 & 0 & 6.145 \end{bmatrix}$	$\begin{bmatrix} 0.070 & 0.142 & 0.034 \\ 0.142 & 2.428 & 0.449 \\ 0.034 & 0.449 & 0.159 \end{bmatrix}$

Young's modulus for the inclusion is 10 MPa

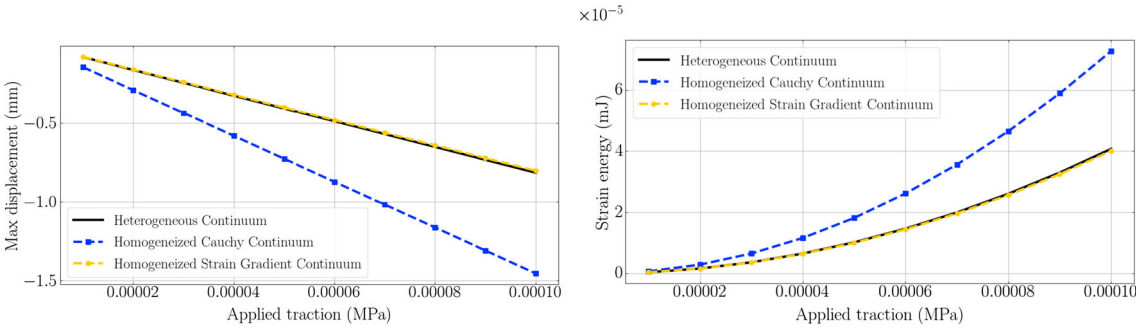

(a) Maximum deflection $\boldsymbol{u}_y$ versus applied traction. **(b)** Strain energy versus applied traction.

Fig. 22 Comparisons of heterogeneous continuum, homogenized Cauchy continuum, and homogenized strain gradient continuum for $E_{\text{inc}} = 10$ MPa

Table 14 Identified effective parameters

Unit cell	E_{mat} (MPa)	E_{inc} (MPa)	C (MPa)	D (N)
	100.0	30.0	$\begin{bmatrix} 63.085 & 23.886 & 0 \\ 23.886 & 63.085 & 0 \\ 0 & 0 & 15.699 \end{bmatrix}$	$\begin{bmatrix} 0.066 & 0.089 & 0.071 \\ 0.089 & 1.784 & 0.534 \\ 0.071 & 0.534 & 0.109 \end{bmatrix}$

Young's modulus for the inclusion is 30 MPa

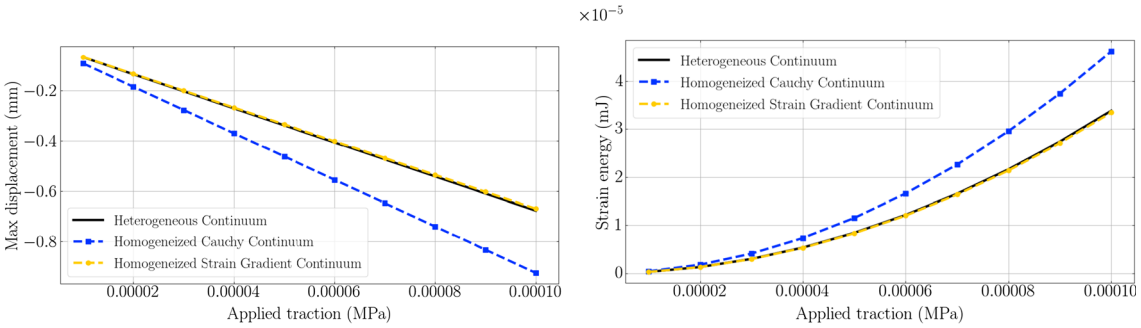

(a) Maximum deflection $\boldsymbol{u}_y$ versus applied traction. **(b)** Strain energy versus applied traction.

Fig. 23 Comparisons of heterogeneous continuum, homogenized Cauchy continuum, and homogenized strain gradient continuum for $E_{\text{inc}} = 30$ MPa

continuum and the heterogeneous continuum are due to size effects. It can also be observed from Fig. 27 that for an increasing ratio of Young's modulus between the inclusions and the matrices ($E_{\text{inc}}/E_{\text{mat}}$), the size effects decay and the homogenized Cauchy continua show a satisfactory agreement with the heterogeneous continua.

Table 15 Identified effective parameters

Unit cell	E_{mat} (MPa)	E_{inc} (MPa)	C (MPa)	D (N)
	100.0	50.0	$\begin{bmatrix} 86.160 & 35.456 & 0 \\ 35.456 & 86.160 & 0 \\ 0 & 0 & 23.584 \end{bmatrix}$	$\begin{bmatrix} 0.042 & 0.046 & 0.092 \\ 0.046 & 1.207 & 0.476 \\ 0.092 & 0.476 & 0.058 \end{bmatrix}$

Young's modulus for the inclusion is 50 MPa

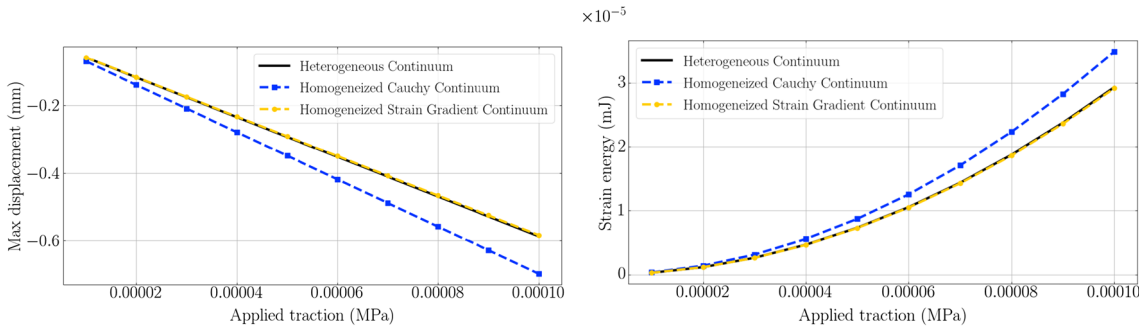

(a) Maximum deflection $\boldsymbol{u}_y$ versus applied traction.

(b) Strain energy versus applied traction.

Fig. 24 Comparisons of heterogeneous continuum, homogenized Cauchy continuum, and homogenized strain gradient continuum for $E_{\text{inc}} = 50$ MPa

Table 16 Identified effective parameters

Unit cell	E_{mat} (MPa)	E_{inc} (MPa)	C (MPa)	D (N)
	100.0	70.0	$\begin{bmatrix} 106.941 & 45.345 & 0 \\ 45.345 & 106.941 & 0 \\ 0 & 0 & 30.227 \end{bmatrix}$	$\begin{bmatrix} 0.017 & 0.016 & 0.071 \\ 0.016 & 0.686 & 0.327 \\ 0.071 & 0.327 & 0.021 \end{bmatrix}$

Young's modulus for the inclusion is 70 MPa

5 Discussions

It should be noted that in this work, the periodicity of the microstructures and the linear elastic constituents of the metamaterial are required. The presented results show how the effective material properties change when varying the unit cell properties (volume fraction of matrix V_f, unit cell length l, and the material properties of base material E_{inc} and E_{mat}). It was demonstrated that when the size of the microstructure of some metamaterial is comparable to the size of the whole structure, size effects become clearly visible. For instance, when V_f decreases, the resistance to curvature of the microstructures tends to grow, but the normal and shear strains remain relatively constant, which leads to a size-effect. The homogenized strain gradient continua are able to model such size effects because the strain gradient energies cover the deformation energies resulting from local curvatures, which are not taken into account by homogenized Cauchy continua.

The size effects can also be examined by making use of the homogenization method for different metamaterials under different boundary conditions, for example, metamaterials of D4-invariant, D6-invariant, Z2-invariant, etc., as shown in [9] under stretching, shearing, transverse bending [86]. In a specific case, the pantographic metamaterial which has been largely studied by dell'Isola and his colleagues [7,29,31,32,68,70,72,73,78,79] is a so-called higher gradient material [2–4,16,27,28]. It is also possible to determine the effective material parameters of a pantographic metamaterial by using this method. Note that the investigated size effects result from the bending deformation of the cantilever beam. Nevertheless, it should be mentioned that the mechanism of size effects could also be the result of the so-called edge effects [58,87], which lead to a softer response of structures. Therefore, in order to understand size effects, softening effects must be studied, and this will be left for the future.

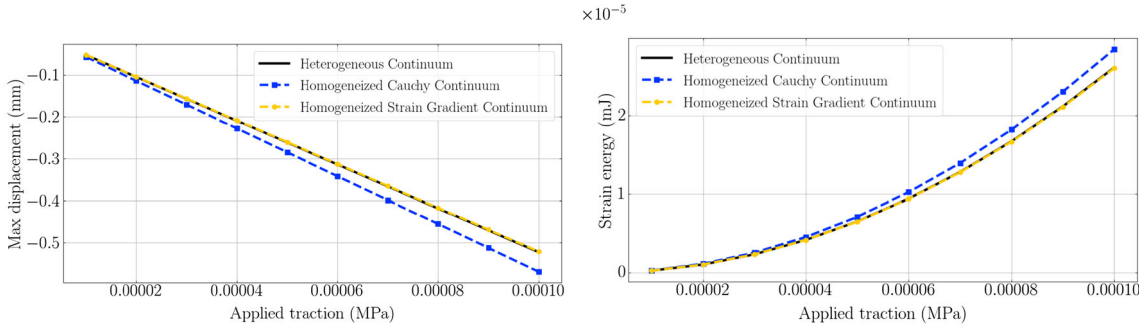

(a) Maximum deflection $\boldsymbol{u}_y$ versus applied traction.

(b) Strain energy versus applied traction.

Fig. 25 Comparisons of heterogeneous continuum, homogenized Cauchy continuum, and homogenized strain gradient continuum for $E_{\text{inc}} = 70$ MPa

Table 17 Identified effective parameters

Unit cell	E_{mat} (MPa)	E_{inc} (MPa)	C (MPa)	D (N)
	100.0	90.0	$\begin{bmatrix} 125.807 & 53.867 & 0 \\ 53.867 & 125.807 & 0 \\ 0 & 0 & 35.912 \end{bmatrix}$	$\begin{bmatrix} 0.002 & 0.002 & 0.027 \\ 0.002 & 0.216 & 0.119 \\ 0.027 & 0.119 & 0.002 \end{bmatrix}$

Young's modulus for the inclusion is 90 MPa

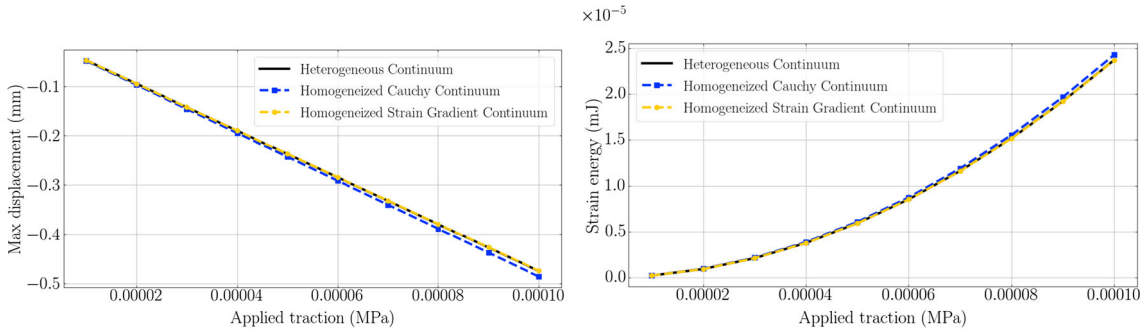

(a) Maximum deflection $\boldsymbol{u}_y$ versus applied traction.

(b) Strain energy versus applied traction.

Fig. 26 Comparisons of heterogeneous continuum, homogenized Cauchy continuum, and homogenized strain gradient continuum for $E_{\text{inc}} = 90$ MPa

As can be observed from previous sections, some negative values in the strain gradient stiffness tensor result. It is physically allowed as long as the strain gradient stiffness tensor is positive semi-definite. Indeed, an equivalence of strain energies for one RVE was used. At the microscale, the constituents of the RVE are linear elastic, which means that the strain energy (please see Eq. (2)) is always positive when specifying a specific Young's modulus and Poisson's ratio. Therefore, the corresponding strain energy for the RVE is always positive with the identified effective parameters at the macroscale. In the case of FEM, if the size of the FEM element is larger than or equal to that of RVE, an outcome of positive energy for the FEM computation is ensured. This was demonstrated also in [13,53]. Fortunately, in the present work isogeometric analysis was utilized, and it is possible to specify a relatively big size of elements, and convergence of computations is assured by setting a higher polynomial degree of NURBS. Please note that choosing a bigger size of elements than RVE in FEM is a sufficient but not a necessary condition to ensure the positive-definite of the effective material parameters.

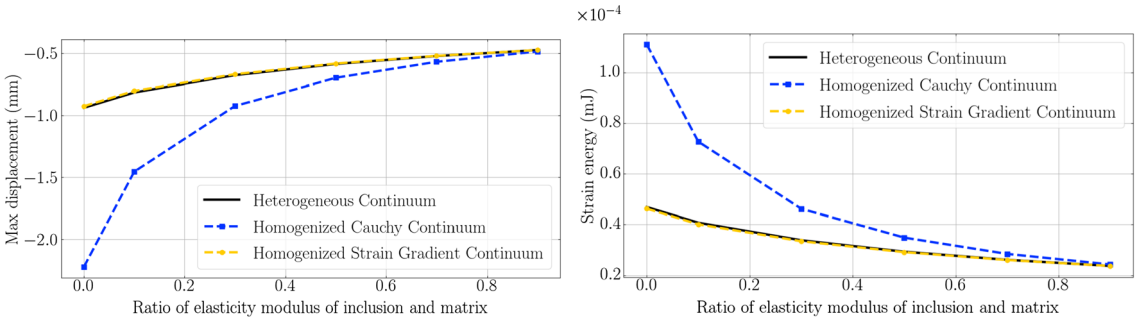

(a) Maximum deflection $\boldsymbol{u}_y$ versus ratio of Young's modulus of the inclusion and the matrix.

(b) Strain energy versus ratio of Young's modulus of inclusion and matrix .

Fig. 27 Comparisons of maximum deflection $\boldsymbol{u}_y$ and strain energy with regard to the ratio of Young's modulus of inclusion and matrix

6 Conclusions

A homogenization method based on asymptotic analysis considering higher-order terms is utilized in this paper to identify the effective classical and strain gradient material parameters. A metamaterial of the so-called D4 invariant symmetry was investigated. The mathematical form of identified material parameters is in perfect agreement with the rigorous theoretical predictions of the results in [9]. The influences of the volume fraction of the matrix, the unit cell sizes, as well as the properties of the underlying material on the effective material properties, were investigated quantitatively. The size effects manifesting in a cantilever beam were investigated by using the identified effective material parameters. It is found that the homogenized Cauchy continua cannot capture the size effects, and the homogenized strain gradient continua match well with the size-dependent phenomena. This is due to the fact that the microstructural information is contained in the higher-order moduli. In addition, an investigation of critical buckling load, as well as eigenfrequencies based on the effective material parameters, is possible. An extension to the 3D case of this work is natural, which will be carried out in the future as well.

Funding Open Access funding provided by Projekt DEAL.

References

1. Abali, B.E., Müller, W.H., dell'Isola, F.: Theory and computation of higher gradient elasticity theories based on action principles. Arch. Appl. Mech. **87**(9), 1495–1510 (2017)
2. Abdoul-Anziz, H., Seppecher, P.: Strain gradient and generalized continua obtained by homogenizing frame lattices. Math. Mech. Complex Syst. **6**(3), 213–250 (2018)
3. Abdoul-Anziz, H., Seppecher, P., Bellis, C.: Homogenization of frame lattices leading to second gradient models coupling classical strain and strain-gradient terms. Math. Mech. Solids **24**(12), 3976–3999 (2019)
4. Alibert, J.J., Seppecher, P., dell'Isola, F.: Truss modular beams with deformation energy depending on higher displacement gradients. Math. Mech. Solids **8**(1), 51–73 (2003)
5. Altenbach, H., Eremeyev, V.: On the linear theory of micropolar plates. ZAMM J. Appl. Math. Mech. Z. Angew. Math. Mech. **89**(4), 242–256 (2009)
6. Ameen, M.M., Peerlings, R., Geers, M.: A quantitative assessment of the scale separation limits of classical and higher-order asymptotic homogenization. Eur. J. Mech. A/Solids **71**, 89–100 (2018)
7. Andreaus, U., Spagnuolo, M., Lekszycki, T., Eugster, S.R.: A Ritz approach for the static analysis of planar pantographic structures modeled with nonlinear Euler–Bernoulli beams. Contin. Mech. Thermodyn. **30**(5), 1103–1123 (2018)

8. Arabnejad, S., Pasini, D.: Mechanical properties of lattice materials via asymptotic homogenization and comparison with alternative homogenization methods. Int. J. Mech. Sci. **77**, 249–262 (2013)
9. Auffray, N., Bouchet, R., Brechet, Y.: Derivation of anisotropic matrix for bi-dimensional strain-gradient elasticity behavior. Int. J. Solids Struct. **46**(2), 440–454 (2009)
10. Auffray, N., Dirrenberger, J., Rosi, G.: A complete description of bi-dimensional anisotropic strain-gradient elasticity. Int. J. Solids Struct. **69**, 195–206 (2015)
11. Avella, M., Dell'Erba, R., Martuscelli, E.: Fiber reinforced polypropylene: Influence of iPP molecular weight on morphology, crystallization, and thermal and mechanical properties. Polym. Compos. **17**(2), 288–299 (1996)
12. Bacigalupo, A., Paggi, M., Dal Corso, F., Bigoni, D.: Identification of higher-order continua equivalent to a Cauchy elastic composite. Mech. Res. Commun. **93**, 11–22 (2018)
13. Barboura, S., Li, J.: Establishment of strain gradient constitutive relations by using asymptotic analysis and the finite element method for complex periodic microstructures. Int. J. Solids Struct. **136**, 60–76 (2018)
14. Barchiesi, E., dell'Isola, F., Hild, F., Seppecher, P.: Two-dimensional continua capable of large elastic extension in two independent directions: asymptotic homogenization, numerical simulations and experimental evidence. Mech. Res. Commun. **103**, 103466 (2020)
15. Barchiesi, E., Eugster, S.R., dell'Isola, F., Hild, F.: Large in-plane elastic deformations of bi-pantographic fabrics: asymptotic homogenization and experimental validation. Math. Mech. Solids **25**(3), 739–767 (2020)
16. Barchiesi, E., Eugster, S.R., Placidi, L., Dell'Isola, F.: Pantographic beam: a complete second gradient 1D-continuum in plane. Z. Angew. Math. Phys. **70**(5), 135 (2019)
17. Barchiesi, E., Khakalo, S.: Variational asymptotic homogenization of beam-like square lattice structures. Math. Mech. Solids **24**(10), 3295–3318 (2019)
18. Barchiesi, E., Spagnuolo, M., Placidi, L.: Mechanical metamaterials: a state of the art. Math. Mech. Solids **24**, 212–234 (2019)
19. Bargmann, S., Klusemann, B., Markmann, J., Schnabel, J.E., Schneider, K., Soyarslan, C., Wilmers, J.: Generation of 3D representative volume elements for heterogeneous materials: a review. Prog. Mater. Sci. **96**, 322–384 (2018)
20. Cai, Y., Xu, L., Cheng, G.: Novel numerical implementation of asymptotic homogenization method for periodic plate structures. Int. J. Solids Struct. **51**(1), 284–292 (2014)
21. Cazzani, A., Malagù, M., Turco, E., Stochino, F.: Constitutive models for strongly curved beams in the frame of isogeometric analysis. Math. Mech. Solids **21**(2), 182–209 (2016)
22. Chen, Q., Pindera, M.J.: Homogenization and localization of elastic–plastic nanoporous materials with Gurtin–Murdoch interfaces: an assessment of computational approaches. Int. J. Plast. **124**, 42–70 (2020)
23. Chen, Q., Wang, G., Pindera, M.J.: Homogenization and localization of nanoporous composites—a critical review and new developments. Compos. Part B Eng. **155**, 329–368 (2018)
24. Chiaia, B., Barchiesi, E., De Biagi, V., Placidi, L.: A novel structural resilience index: definition and applications to frame structures. Mech. Res. Commun. **99**, 52–57 (2019)
25. De Angelo, M., Barchiesi, E., Giorgio, I., Abali, B.E.: Numerical identification of constitutive parameters in reduced-order bi-dimensional models for pantographic structures: application to out-of-plane buckling. Arch. Appl. Mech. **89**, 1333–1358 (2019)
26. Dell'Erba, R.: Rheo-mechanical and rheo-optical characterisation of ultra high molecular mass poly(methylmethacrylate) in solution. Polymer **42**(6), 2655–2663 (2001)
27. dell'Isola, F., Andreaus, U., Placidi, L.: At the origins and in the vanguard of peridynamics, non-local and higher-gradient continuum mechanics: an underestimated and still topical contribution of Gabrio Piola. Math. Mech. Solids **20**(8), 887–928 (2015)
28. dell'Isola, F., Giorgio, I., Pawlikowski, M., Rizzi, N.: Large deformations of planar extensible beams and pantographic lattices: heuristic homogenization, experimental and numerical examples of equilibrium. Proc. R. Soc. A Math. Phys. Eng. Sci. **472**(2185), 20150790 (2016)
29. dell'Isola, F., Lekszycki, T., Pawlikowski, M., Grygoruk, R., Greco, L.: Designing a light fabric metamaterial being highly macroscopically tough under directional extension: first experimental evidence. Z. Angew. Math. Phys. **66**(6), 3473–3498 (2015)
30. dell'Isola, F., Sciarra, G., Vidoli, S.: Generalized Hooke's law for isotropic second gradient materials. Proc. R. Soc. Lond. A Math. Phys. Eng. Sci. **465**, 2177–2196 (2009)
31. dell'Isola, F., Seppecher, P., Alibert, J.J., Lekszycki, T., Grygoruk, R., Pawlikowski, M., Steigmann, D., Giorgio, I., Andreaus, U., Turco, E., Gołaszewski, M., Rizzi, N., Boutin, C., Eremeyev, V.A., Misra, A., Placidi, L., Barchiesi, E., Greco, L., Cuomo, M., Cazzani, A., Corte, A.D., Battista, A., Scerrato, D., Eremeeva, I.Z., Rahali, Y., Ganghoffer, J.F., Müller, W., Ganzosch, G., Spagnuolo, M., Pfaff, A., Barcz, K., Hoschke, K., Neggers, J., Hild, F.: Pantographic metamaterials: an example of mathematically driven design and of its technological challenges. Contin. Mech. Thermodyn. **31**(4), 851–884 (2019)
32. dell'Isola, F., Seppecher, P., Spagnuolo, M., Barchiesi, E., Hild, F., Lekszycki, T., Giorgio, I., Placidi, L., Andreaus, U., Cuomo, M., Eugster, S.R., Pfaff, A., Hoschke, K., Langkemper, R., Turco, E., Sarikaya, R., Misra, A., Angelo, M.D., D'Annibale, F., Bouterf, A., Pinelli, X., Misra, A., Desmorat, B., Pawlikowski, M., Dupuy, C., Scerrato, D., Peyre, P., Laudato, M., Manzari, L., Göransson, P., Hesch, C., Hesch, S., Franciosi, P., Dirrenberger, J., Maurin, F., Vangelatos, Z., Grigoropoulos, C., Melissinaki, V., Farsari, M., Müller, W., Abali, B.E., Liebold, C., Ganzosch, G., Harrison, P., Drobnicki, R., Igumnov, L., Alzahrani, F., Hayat, T.: Advances in pantographic structures: design, manufacturing, models, experiments and image analyses. Contin. Mech. Thermodyn. **31**(4), 1231–1282 (2019)
33. Dos Reis, F., Ganghoffer, J.: Equivalent mechanical properties of auxetic lattices from discrete homogenization. Comput. Mater. Sci. **51**(1), 314–321 (2012)
34. ElNady, K., Goda, I., Ganghoffer, J.F.: Computation of the effective nonlinear mechanical response of lattice materials considering geometrical nonlinearities. Comput. Mech. **58**(6), 957–979 (2016)
35. Eremeyev, V.A.: A nonlinear model of a mesh shell. Mech. Solids **53**(4), 464–469 (2018)

36. Eremeyev, V.A.: Two-and three-dimensional elastic networks with rigid junctions: modeling within the theory of micropolar shells and solids. Acta Mech. **230**(11), 3875–3887 (2019)
37. Eremeyev, V.A., Turco, E.: Enriched buckling for beam-lattice metamaterials. Mech. Res. Commun. **103**, 103458 (2020)
38. Eringen, A.C.: Mechanics of micromorphic continua. In: Kröner, E. (ed.) Mechanics of Generalized Continua, pp. 18–35. Springer, Berlin (1968)
39. Fischer, P., Klassen, M., Mergheim, J., Steinmann, P., Müller, R.: Isogeometric analysis of 2D gradient elasticity. Comput. Mech. **47**(3), 325–334 (2011)
40. Forest, S., Pradel, F., Sab, K.: Asymptotic analysis of heterogeneous Cosserat media. Int. J. Solids Struct. **38**(26–27), 4585–4608 (2001)
41. Giorgio, I.: Numerical identification procedure between a micro-Cauchy model and a macro-second gradient model for planar pantographic structures. Z. Angew. Math. Phys. **67**(4), 95 (2016)
42. Gitman, I., Askes, H., Sluys, L.: Representative volume: existence and size determination. Eng. Fract. Mech. **74**(16), 2518–2534 (2007)
43. Greco, L., Cuomo, M., Contrafatto, L.: A quadrilateral G1-conforming finite element for the Kirchhoff plate model. Comput. Methods Appl. Mech. Eng. **346**, 913–951 (2019)
44. Greco, L., Cuomo, M., Contrafatto, L., Gazzo, S.: An efficient blended mixed B-spline formulation for removing membrane locking in plane curved Kirchhoff rods. Comput. Methods Appl. Mech. Eng. **324**, 476–511 (2017)
45. Hashin, Z.: Analysis of composite materials—a survey. J. Appl. Mech. **50**(3), 481–505 (1983)
46. Hill, R.: Elastic properties of reinforced solids: some theoretical principles. J. Mech. Phys. Solids **11**(5), 357–372 (1963)
47. Hollister, S.J., Kikuchi, N.: A comparison of homogenization and standard mechanics analyses for periodic porous composites. Comput. Mech. **10**(2), 73–95 (1992)
48. Kamensky, D., Bazilevs, Y.: tIGAr: automating isogeometric analysis with FEniCS. Comput. Methods Appl. Mech. Eng. **344**, 477–498 (2019)
49. Khakalo, S., Balobanov, V., Niiranen, J.: Modelling size-dependent bending, buckling and vibrations of 2D triangular lattices by strain gradient elasticity models: applications to sandwich beams and auxetics. Int. J. Eng. Sci. **127**, 33–52 (2018)
50. Kouznetsova, V.G., Geers, M., Brekelmans, W.: Size of a representative volume element in a second-order computational homogenization framework. Int. J. Multiscale Comput. Eng. **2**(4), 575–598 (2004)
51. Kumar, R.S., McDowell, D.L.: Generalized continuum modeling of 2-D periodic cellular solids. Int. J. Solids Struct. **41**(26), 7399–7422 (2004)
52. Lam, D.C., Yang, F., Chong, A.C.M., Wang, J., Tong, P.: Experiments and theory in strain gradient elasticity. J. Mech. Phys. Solids **51**(8), 1477–1508 (2003)
53. Li, J., Zhang, X.B.: A numerical approach for the establishment of strain gradient constitutive relations in periodic heterogeneous materials. Eur. J. Mech. A/Solids **41**, 70–85 (2013)
54. Liebold, C., Müller, W.H.: Comparison of gradient elasticity models for the bending of micromaterials. Comput. Mater. Sci. **116**, 52–61 (2016)
55. Liu, H., Li, B., Tang, W.: Manufacturing oriented topology optimization of 3D structures for carbon emission reduction in casting process. J. Clean. Prod. **225**, 755–770 (2019)
56. Liu, H., Li, B., Yang, Z., Hong, J.: Topology optimization of stiffened plate/shell structures based on adaptive morphogenesis algorithm. J. Manuf. Syst. **43**, 375–384 (2017)
57. Liu, J., Fei, Q., Jiang, D., Zhang, D., Wu, S.: Experimental and numerical investigation on static and dynamic characteristics for curvilinearly stiffened plates using DST–BK model. Int. J. Mech. Sci. **169**, 105286 (2020)
58. Liu, S., Su, W.: Effective couple-stress continuum model of cellular solids and size effects analysis. Int. J. Solids Struct. **46**(14–15), 2787–2799 (2009)
59. Mindlin, R.D., Eshel, N.: On first strain-gradient theories in linear elasticity. Int. J. Solids Struct. **4**(1), 109–124 (1968)
60. Misra, A., Poorsolhjouy, P.: Identification of higher-order elastic constants for grain assemblies based upon granular micromechanics. Math. Mech. Complex Syst. **3**(3), 285–308 (2015)
61. Nejadsadeghi, N., De Angelo, M., Drobnicki, R., Lekszycki, T., dell'Isola, F., Misra, A.: Parametric experimentation on pantographic unit cells reveals local extremum configuration. Exp. Mech. **59**(6), 927–939 (2019)
62. Nejadsadeghi, N., Misra, A.: Extended granular micromechanics approach: a micromorphic theory of degree n. Math. Mech. Solids **25**(2), 407–429 (2020)
63. Niiranen, J., Khakalo, S., Balobanov, V., Niemi, A.H.: Variational formulation and isogeometric analysis for fourth-order boundary value problems of gradient-elastic bar and plane strain/stress problems. Comput. Methods Appl. Mech. Eng. **308**, 182–211 (2016)
64. Ostoja-Starzewski, M., Boccara, S.D., Jasiuk, I.: Couple-stress moduli and characteristic length of a two-phase composite. Mech. Res. Commun. **26**(4), 387–396 (1999)
65. Peerlings, R., Fleck, N.: Computational evaluation of strain gradient elasticity constants. Int. J. Multiscale Comput. Eng. **2**(4), 599–619 (2004)
66. Pinho-da Cruz, J., Oliveira, J., Teixeira-Dias, F.: Asymptotic homogenisation in linear elasticity. Part I: mathematical formulation and finite element modelling. Comput. Mater. Sci. **45**(4), 1073–1080 (2009)
67. Placidi, L., Andreaus, U., Giorgio, I.: Identification of two-dimensional pantographic structure via a linear D4 orthotropic second gradient elastic model. J. Eng. Math. **103**(1), 1–21 (2017)
68. Placidi, L., Barchiesi, E., Turco, E., Rizzi, N.L.: A review on 2D models for the description of pantographic fabrics. Z. Angew. Math. Phys. **67**(5), 121 (2016)
69. Rudraraju, S., Van der Ven, A., Garikipati, K.: Three-dimensional isogeometric solutions to general boundary value problems of Toupin's gradient elasticity theory at finite strains. Comput. Methods Appl. Mech. Eng. **278**, 705–728 (2014)
70. Scerrato, D., Zhurba Eremeeva, I.A., Lekszycki, T., Rizzi, N.L.: On the effect of shear stiffness on the plane deformation of linear second gradient pantographic sheets. ZAMM Z. Angew. Math. Mech. **96**(11), 1268–1279 (2016)
71. Solyaev, Y., Lurie, S., Barchiesi, E., Placidi, L.: On the dependence of standard and gradient elastic material constants on a field of defects. Math. Mech. Solids **25**(1), 35–45 (2020)

72. Spagnuolo, M., Barcz, K., Pfaff, A., Dell'Isola, F., Franciosi, P.: Qualitative pivot damage analysis in aluminum printed pantographic sheets: numerics and experiments. Mech. Res. Commun. **83**, 47–52 (2017)
73. Steigmann, D., dell'Isola, F.: Mechanical response of fabric sheets to three-dimensional bending, twisting, and stretching. Acta Mech. Sin. **31**(3), 373–382 (2015)
74. Sun, C., Vaidya, R.: Prediction of composite properties from a representative volume element. Compos. Sci. Technol. **56**(2), 171–179 (1996)
75. Terada, K., Hori, M., Kyoya, T., Kikuchi, N.: Simulation of the multi-scale convergence in computational homogenization approaches. Int. J. Solids Struct. **37**(16), 2285–2311 (2000)
76. Toupin, R.A.: Elastic materials with couple-stresses. Arch. Ration. Mech. Anal. **11**(1), 385–414 (1962)
77. Trinh, D.K., Janicke, R., Auffray, N., Diebels, S., Forest, S.: Evaluation of generalized continuum substitution models for heterogeneous materials. Int. J. Multiscale Comput. Eng. **10**(6), 527–549 (2012)
78. Turco, E., Barchiesi, E.: Equilibrium paths of Hencky pantographic beams in a three-point bending problem. Math. Mech. Complex Syst. **7**(4), 287–310 (2019)
79. Turco, E., dell'Isola, F., Cazzani, A., Rizzi, N.L.: Hencky-type discrete model for pantographic structures: numerical comparison with second gradient continuum models. Z. Angew. Math. Phys. **67**(4), 85 (2016)
80. Vangelatos, Z., Komvopoulos, K., Grigoropoulos, C.: Vacancies for controlling the behavior of microstructured three-dimensional mechanical metamaterials. Math. Mech. Solids **24**(2), 511–524 (2019)
81. Yang, H., Abali, B.E., Müller, W.H.: On finite element analysis in generalized mechanics. In: Indeitsev, D., Krivtsov, A. (eds.) International Summer School-Conference "Advanced Problems in Mechanics", pp. 233–245. Springer, Berlin (2019)
82. Yang, H., Abali, B.E., Timofeev, D., Müller, W.H.: Determination of metamaterial parameters by means of a homogenization approach based on asymptotic analysis. Contin. Mech. Thermodyn. **32**, 1251–1270 (2019)
83. Yang, H., Ganzosch, G., Giorgio, I., Abali, B.E.: Material characterization and computations of a polymeric metamaterial with a pantographic substructure. Z. Angew. Math. Phys. **69**(4), 105 (2018)
84. Yang, H., Müller, W.H.: Computation and experimental comparison of the deformation behavior of pantographic structures with different micro-geometry under shear and torsion. J. Theor. Appl. Mech. **57**, 421–434 (2019)
85. Yildizdag, M.E., Tran, C.A., Barchiesi, E., Spagnuolo, M., dell'Isola, F., Hild, F.: A multi-disciplinary approach for mechanical metamaterial synthesis: a hierarchical modular multiscale cellular structure paradigm. In: Altenbach, H., Öchsner, A. (eds.) State of the Art and Future Trends in Material Modeling, pp. 485–505. Springer, Berlin (2019)
86. Yoder, M., Thompson, L., Summers, J.: Size effects in lattice structures and a comparison to micropolar elasticity. Int. J. Solids Struct. **143**, 245–261 (2018)
87. Yoder, M., Thompson, L., Summers, J.: Size effects in lattice-structured cellular materials: edge softening effects. J. Mater. Sci. **54**(5), 3942–3959 (2019)
88. Yu, W., Tang, T.: Variational asymptotic method for unit cell homogenization of periodically heterogeneous materials. Int. J. Solids Struct. **44**(11–12), 3738–3755 (2007)

Computation of brittle fracture propagation in strain gradient materials by the FEniCS library

E. Barchiesi[a], H. Yang*[b], C. A. Tran[a], L. Placidi[c] and W. H. Müller[b]

[a] *Università degli Studi dell'Aquila, L'Aquila (Italy)*
[b] *Technische Universität Berlin , Berlin (Germany)*
[c] *International Telematic University Uninettuno , Rome (Italy)*

Abstract

Strain gradient continuum damage modeling has been applied to quasi-static brittle fracture within an approach based on a maximum energy-release rate principle. The model was implemented numerically making use of the FEniCS open-source library. The considered model introduces non-locality by taking into account the strain gradient in the deformation energy. This allows for stable computations of crack propagation in differently notched samples. The model can take wedges into account, so that fracture onset can occur at wedges. Owing to the absence of a damage gradient term in the dissipated energy, the normal part of the damage gradient is not constrained on boundaries. Thus, non-orthogonal and non-parallel intersections between cracks and boundaries can be observed.

Keywords: Strain gradient elasticity, brittle fracture, FEniCS, variational principles, regularization

1 Introduction

Continuum mechanics has been used widely to study damage phenomena [10, 4, 28, 45, 51, 52, 57, 59, 60, 66]. In continuum damage models the studied system is described not only by a displacement field, but also by a damage field. Thus there is one more independent variable when compared to the usual elasticity models. In the present work such a damage field is considered to take the local deterioration of the material into account. Furthermore, healing mechanisms are not considered, so that damage is assumed to be non-decreasing in time.

Localization phenomena in damage mechanics Continuum damage models usually involve localization phenomena [40, 48, 49, 76]: the stress and the strain concentrate in small regions. This phenomenon must be taken into account by the numerical model to avoid instability or mesh-dependence. The size of such regions of concentration can be considered as a length scale characterizing the studied material. As such, it must also be acknowledged by the mathematical model. This is the aim of non-local damage models: the length scale is introduced in order to control how much the deformation varies in space. In a variational framework, that means regularizing the solution by penalizing the candidate displacements which are too localized.

For example, in damage gradient models the elastic strain energy depends on the gradient of the damage field, allowing to deal with localization and mesh-dependence. In the present work, the non-locality is based on the dependence of the deformation energy on strain gradient instead of damage gradient [45].

Damage may also be considered as a micro-structure having macroscopic effects. Materials showing such structures have at least been known since the 19$^{\text{th}}$ century [15, 12, 13] and were widely studied during the last decades [38, 26, 20, 18, 21, 19, 77]. In particular, strain gradient models have been applied extensively to micro-structured materials [23, 32, 2, 36, 37, 3, 46].

*Corresponding author. E-mail: hua.yang@campus.tu-berlin.de

Maximum energy-release principle to model damaging phenomena In the present work, the mathematical problem to be solved is derived from the maximum energy-release principle, which is a variational inequality [53, 58] aimed at modeling dissipative systems, and generalizing the least action principle. Using a variational approach has many advantages [16], one being that it is possible to derive the boundary conditions ensuring well-posedness of the problem [14, 86]. Furthermore, the weak form can be simply recovered [1, 69, 70, 71, 72, 74], this being convenient if the problem is solved by using a numerical method based on weak forms, such as finite element methods [50, 54, 55, 56, 61, 62, 63, 64, 65, 67, 68, 73]. The maximum energy-release principle used in the present work requires the specification of the energy released in damaging, as in [45, 29, 31].

Strain gradient damage model for quasi-static brittle fracture The model studied in the present work considers an isotropic two-dimensional continuum, showing geometrically non linear elastic behavior, and undergoing quasi-static brittle fracture. The kinematic description relies on a displacement and on a damage field, where the latter is assumed to be non-decreasing in time. The application of the maximum energy-release principle yields both balance equations and Karush–Kuhn–Tucker conditions. The considered energy terms include a dissipated energy depending on damage (but not on its gradient), and a deformation energy depending on both strain and strain gradient. Moreover, the deformation energy involves elastic coefficients which are assumed to depend on the local damage.

Plan of the work The paper is structured as follows. In Section 2, the mathematical model is presented. The frameworks of elasticity and damage are introduced followed by the variational derivation of the problem to be solved. The numerical model is then presented in Section 3 by explaining the solution algorithm and the software implementation. Numerical results are given in Section 4 for two applications on notched samples. Finally, Section 5 presents concluding remarks.

2 Strain gradient modeling of brittle fracture

The reference configuration of the studied two-dimensional body is represented by an open set $\Omega \subset \mathbb{R}^2$ and its boundary $\partial\Omega$. A Cartesian coordinate system $(O, (e_1, e_2))$ is defined, in which any generic point $X \in \Omega$ has the coordinates (X_1, X_2).

By using a Lagrangian framework, the kinematics of the model, as well as the different energy quantities that are used to derive the equations of the problem from the maximum energy-release principle, will be defined in this section.

2.1 Elasticity framework

The modeling of an undamaged elastic body is described first. Damage effects are left to the next Subsection 2.2.

2.1.1 Kinematics – first independent variable

The placement $\chi : \Omega \to \mathbb{R}^2$ is defined to be the map that relates to any point $X \in \Omega$ its current position $\chi(X)$. Thus, $\chi(\Omega)$ is the current configuration. The displacement is then defined as $u(X) = \chi(X) - X$. It is the first independent variable of the problem.

At this point, the gradient of placement $F = \nabla\chi$ with respect to the space variable in the reference configuration, as well as the gradient of displacement $\nabla u = F - I$[1], shall be introduced. The local deformation of the body is described by the Green-Lagrange strain tensor $G = \frac{1}{2}(F^T F - I)$. As in brittle fracture only small zones in proximity of the crack tip undergo large deformations, it is generally accepted the so-called small strain hypothesis, where quadratic terms in ∇u are neglected, i.e. $G = \epsilon = \frac{1}{2}(\nabla u + \nabla u^T)$. Henceforth, we will make use of such an assumption.

2.1.2 Strain gradient internal energy

The studied system is assumed to be isotropically elastic. Its deformation energy (when undamaged, i.e. recoverable elastic energy) W_{def} is defined as the integration in space of a quadratic form of the strain and its gradient:

$$W_{\text{def}} = \int_\Omega \Big(\frac{1}{2}\epsilon_{ij} C_{ijkl} \epsilon_{kl} + \frac{1}{2}\epsilon_{ij,k} D_{ijklmn} \epsilon_{lm,n} \Big) \mathrm{d}A \tag{1}$$

[1] where I may be represented by the identity matrix in the previously defined Cartesian basis.

with:

$$\begin{aligned} &C_{ijkl} = c_1\delta_{ij}\delta_{kl} + c_2(\delta_{ik}\delta_{jl} + \delta_{il}\delta_{jk}),\\ &D_{ijklmn} = c_3(\delta_{ij}\delta_{kl}\delta_{mn} + \delta_{in}\delta_{jk}\delta_{lm} + \delta_{ij}\delta_{km}\delta_{ln} + \delta_{ik}\delta_{jn}\delta_{lm})\\ &+ c_4\delta_{ij}\delta_{kn}\delta_{ml} + c_5(\delta_{ik}\delta_{jl}\delta_{mn} + \delta_{im}\delta_{jk}\delta_{ln} + \delta_{ik}\delta_{jm}\delta_{ln} + \delta_{il}\delta_{jk}\delta_{mn})\\ &+ c_6(\delta_{il}\delta_{jm}\delta_{kn} + \delta_{im}\delta_{jl}\delta_{kn}) + c_7(\delta_{il}\delta_{jn}\delta_{mk} + \delta_{im}\delta_{jn}\delta_{lk} + \delta_{in}\delta_{jl}\delta_{km} + \delta_{in}\delta_{jm}\delta_{kl}) \end{aligned} \tag{2}$$

Note that, when dealing with 2D isotropic materials, there are only four independent parameters out of the five parameters c_3, c_4, c_5, c_6, c_7 in in D_{ijklmn}, see a discussion in [30]. The first gradient coefficients (Lamé coefficients) can be expressed by Young's modulus E and Poisson's ratio ν:

$$c_1 = \frac{E\nu}{(1+\nu)(1-2\nu)}\ ,\ c_2 = \frac{E}{2(1+\nu)}\ . \tag{3}$$

2.1.3 Exterior work

The considered external effects are modelled as the works of a bulk force b and a bulk double force m per unit area, a contact force t and a contact double force s per unit length:

$$W_{ext} = \int_\Omega \Big(b_i u_i + m_{ij}u_{i,j}\Big)\mathrm{d}A + \int_{\partial\Omega}\Big(t_i u_i + s_{ij}u_{i,j}\Big)\mathrm{d}l \tag{4}$$

2.2 Damage modeling

It will now be presented how damage is taken into account in both the deformation and dissipation occurring in the system. More details about the chosen model can be found in [45].

2.2.1 Kinematics – second independent variable

Damage is modelled as a scalar field $\omega : \Omega \to [0,1]$, which is the second independent variable of the problem. Although the elastic model takes into account both the first and second gradient of deformation, we assume that there is only one damage field in the present work, instead of considering one damage field acting on first-gradient deformation mechanisms and another field for the second gradient. This assumption is made first for simplification, and shall be investigated in future works.

For every $X \in \Omega$, $\omega(X)$ it represents the local damage state of the particle that was at point X in the reference configuration. The damage values go from 0, for a non-damaged material, to 1 for a totally damaged material. Since no healing mechanism is considered, the damage field is assumed to be non-decreasing in time.

2.2.2 Apparent stiffness loss and energy dissipation

The damage field has two effects on the energy of the system. First, every damaged area undergoes an apparent loss of stiffness. This phenomenon is taken into account by assuming that the stiffness coefficients C_{ijkl} and D_{ijklmn} depend on the local damage. Thus, the deformation energy depends not only on the strain and strain gradient, but also on the damage field. Second, the energy lost in damaging phenomena is also taken into account as a dissipation term W_{diss}, which is added to the deformation energy as part of the internal energy $W_{\text{int}} = W_{\text{def}} + W_{\text{diss}}$.

Deformation energy for the damaged material As stated above, the effectiveness of the stiffness coefficients C_{ijkl} and D_{ijklmn} must correlate with the damage field ω. Two parameters $n, m \in]-\infty, 1]$ are introduced for this purpose as follows:

$$W_{\text{int}} = \int_\Omega \Big((1-m\omega)\frac{1}{2}\epsilon_{ij}C_{ijkl}\epsilon_{kl} + (1-n\omega)\frac{1}{2}\epsilon_{ij,k}D_{ijklmn}\epsilon_{lm,n}\Big)\mathrm{d}A. \tag{5}$$

The n and m parameters allow to model the behaviour of the damaged material. More specifically,

- if $n, m > 0$, then the more damaged the material is, the more its stiffness decreases locally. For the limit value $n = 1$ or $m = 1$, the corresponding stiffness vanishes when the material is locally totally damaged.
- if $n, m < 0$, then an increasing damage also increases the local stiffness. This may happen for example when the damage changes the microstructure of the material, resulting in an effective stiffening.

One should note that for the limit value $n = 1$ or $m = 1$, the problem is not well posed anymore, since the corresponding stiffnesses vanish. It is thus preferable to stop at a lower value, for example $n = 0.999$ and $m = 0.999$.

Dissipated energy The dissipated energy is modelled by a functional W_{diss}. It involves two parameters $K_1, K_2 \in \mathbb{R}_+$. The former represents a threshold ruling the appearance and increase of damage, while the latter models the resistance of the material to damaging phenomena:

$$W_{\text{diss}} = \int_\Omega \Big(K_1 \omega + \frac{1}{2} K_2 \omega^2 \Big) \mathrm{d}A. \tag{6}$$

It is added to the internal energy W_{int}, along with the deformation term:

$$\begin{aligned} W_{\text{int}} &= W_{\text{def}} + W_{\text{diss}} \\ &= \int_\Omega \Big((1 - m\omega) \frac{1}{2} \epsilon_{ij} C_{ijkl} \epsilon_{kl} + (1 - n\omega) \frac{1}{2} \epsilon_{ij,k} D_{ijklmn} \epsilon_{lm,n} \Big) \mathrm{d}A + \int_\Omega \Big(K_1 \omega + \frac{1}{2} K_2 \omega^2 \Big) \mathrm{d}A. \end{aligned} \tag{7}$$

2.3 Discrete-time maximum energy-release principle

So far, the model has been presented by considering a reference configuration Ω and one current configuration $\chi(\Omega)$. The load parameter $\lambda \in \mathbb{R}$ shall now be introduced, so that one may consider a sequence of configurations $\chi^\lambda(\Omega)$.

2.3.1 Potential energy

At this point, the total potential energy $\mathcal{E}^\lambda$ associated to the configuration $\chi^\lambda(\Omega)$ of the system, defined for every admissible motion $\hat{u}$ and non-decreasing admissible damage $\hat{\omega}$, is introduced as:

$$\begin{aligned} \mathcal{E}^\lambda(\hat{u}, \hat{\omega}) &= W^\lambda_{\text{int}}(\hat{\epsilon}_{ij}, \hat{\epsilon}_{ij,k}, \hat{\omega}) - W^\lambda_{\text{ext}}(\hat{u}, \nabla \hat{u}) \\ &= W^\lambda_{\text{def}}(\hat{\epsilon}_{ij}, \hat{\epsilon}_{ij,k}, \hat{\omega}) + W^\lambda_{\text{diss}}(\hat{\omega}) - W^\lambda_{\text{ext}}(\hat{u}, \nabla \hat{u}). \end{aligned} \tag{8}$$

Under the hypothesis of a quasi-static evolution, the kinetic energy is negligible with respect to that potential energy. By applying the maximum energy-release principle similarly as in [45], every solution $(u^\lambda, \omega^\lambda)$ has to satisfy[2]:

$$\delta\mathcal{E}^\lambda(u^\lambda, \omega^\lambda)(\Delta u^\lambda, \Delta\omega^\lambda) \geqslant \delta\mathcal{E}^\lambda(u^\lambda, \omega^\lambda)(\delta u, \delta\omega) \tag{9}$$

for all admissible displacement and damage variations, δu and $\delta\omega \geqslant 0$, respectively, with $\Delta u^\lambda = u^\lambda - u^{\lambda - \Delta\lambda}$ and $\Delta\omega^\lambda = \omega^\lambda - \omega^{\lambda-\Delta\lambda} \geqslant 0$, $\Delta\lambda \to 0$ being the step between λ and the previous load parameter.

2.3.2 Equilibrium for a fixed damage field

For a null damage variation $\delta\omega = 0$, Eq. (9) yields the stationarity condition usually met for undamaged elastic behavior,

$$\delta\mathcal{E}^\lambda(u^\lambda, \omega^\lambda)(\delta u, 0) = 0. \tag{10}$$

This is when simplifying the notations,

$$\delta W_{\text{int}} - \delta W_{\text{ext}} = 0, \tag{11}$$

where the variation of internal energy reads:

$$\delta W_{\text{int}} = \frac{\partial W_{\text{int}}}{\partial \epsilon_{ij}} \delta\epsilon_{ij} + \frac{\partial W_{\text{int}}}{\partial \epsilon_{ij,k}} \delta\epsilon_{ij,k} + \frac{\partial W_{\text{int}}}{\partial \omega} \delta\omega. \tag{12}$$

Hence the stationarity condition can be rewritten as:

$$\frac{\partial W_{int}}{\partial \epsilon_{ij}} \delta\epsilon_{ij} + \frac{\partial W_{int}}{\partial \epsilon_{ij,k}} \delta\epsilon_{ij,k} - \delta W_{ext} + \frac{\partial W_{int}}{\partial \omega} \delta\omega = 0, \tag{13}$$

i.e.,

$$\begin{aligned} &\int_\Omega \Big((1 - m\omega) \epsilon_{ij} C_{ijkl} \delta\epsilon_{kl} + (1 - n\omega) \epsilon_{ij,k} D_{ijklmn} \delta\epsilon_{lm,n} \Big) \mathrm{d}A \\ &- \int_\Omega \Big(b_i \delta u_i + m_{ij} \delta u_{i,j} \Big) \mathrm{d}A - \int_{\partial\Omega} \Big(t_i \delta u_i + s_{ij} \delta u_{i,j} \Big) \mathrm{d}l \\ &+ \int_\Omega \Big(- \frac{m}{2} \epsilon_{ij} C_{ijkl} \epsilon_{kl} \delta\omega - \frac{n}{2} \epsilon_{ij,k} D_{ijklmn} \epsilon_{lm,n} \delta\omega + K_1 \delta\omega + K_2 \omega \delta\omega \Big) \mathrm{d}A = 0 \end{aligned} \tag{14}$$

[2] where $\delta\mathcal{E}(u, \omega)(\delta u, \delta\omega)$ denotes the Gateaux derivative of $\mathcal{E}$ at (u, ω) along the direction $(\delta u, \delta\omega)$.

2.3.3 Karush–Kuhn–Tucker conditions for a fixed displacement field

For a null displacement variation $\delta u = 0$, one can derive the Karush–Kuhn–Tucker conditions from Eq. (9) (see [45]), namely:

$$\begin{cases} \omega^{\lambda} = \left(\dfrac{m}{2}\epsilon_{ij}C_{ijkl}\epsilon_{kl} + \dfrac{n}{2}\epsilon_{ij,k}D_{ijklmn}\epsilon_{lm,n} - K_1\right)/K_2, \\ \text{or} \\ \omega^{\lambda} = \omega^{\lambda-1}. \end{cases}$$

3 Numerical modeling: Alternate minimization algorithm

The model presented previously showed a separation between the elastic behavior for a fixed damage field on the one hand, and the evolution of damage for a fixed displacement field on the other. This distinction is exploited to implement the studied model numerically through a version of an alternate minimization algorithm (also presented in [45]).In this algorithm, two minimization problems are solved one after the other for each load parameter λ.

- First, while keeping the damage field $\omega^{\lambda-\Delta\lambda}$ of the previous step, the new displacement field u^{λ} is computed as the solution of the minimization of the potential energy,

$$\mathcal{E}(u^{\lambda}, \omega^{\lambda-\Delta\lambda}) = \min\left\{\mathcal{E}(\hat{u}, \omega^{\lambda-\Delta\lambda}), \hat{u} \text{ admissible displacement}\right\}. \tag{15}$$

  A standard mixed finite element method for strain gradient mechanics has been employed [44, 47, 87, 88] , thus introducing extra independent variables during the discretization of the weak form. The extra independent variables were constrained by using Lagrange multipliers.

- Second, the new damage field ω^{λ} is computed by checking the Karush–Kuhn–Tucker conditions with the previously computed displacement field u^{λ},

$$\omega^{\lambda} = \max\left[\min\left(\overline{\omega}(u^{\lambda}), 1\right), \omega^{\lambda-\Delta\lambda}\right], \tag{16}$$

  where $\overline{\omega}(u^{\lambda})$ is the damage threshold value,

$$\overline{\omega}(u^{\lambda}) = \left(\frac{m}{2}\epsilon_{ij}C_{ijkl}\epsilon_{kl} + \frac{n}{2}\epsilon_{ij,k}D_{ijklmn}\epsilon_{lm,n} - K_1\right)/K_2. \tag{17}$$

  In the undamaged state, the condition above means that two events may happen. First, the deformation energy may locally exceed the damage initiation level K_1, in which case the local damage assumes the (non-zero) difference value divided by K_2. Second, damage remains unchanged, thus being equal to zero.

This algorithm is summarized in Figure 1.

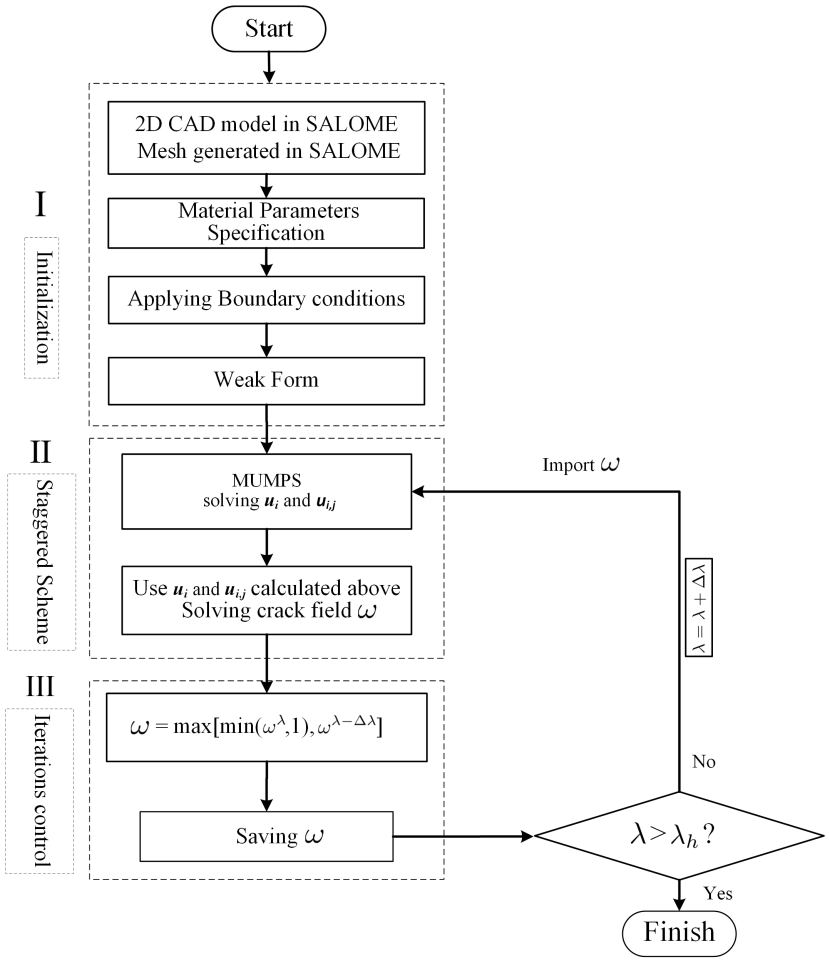

Figure 1: Flowchart for the numerical implementation. Here, the load parameter is denoted by λ. The quantity λ_h denotes the time horizon.

4 Numerical results

In what follows, numerical simulations of extension tests for two different samples will be presented. Both samples have initial crack(s) implemented as an absence of matter (elements), outside of which the material is initially undamaged ($\omega^0 = 0$).

4.1 Case 1: oblique notch

4.1.1 Case 1: Geometry and numerical data

The geometry is a rectangle (see Fig. 2) of width W and length L, in which emerges a straight notch. As one can see in the figure, the notch starts from the middle of the bottom side with a 45° angle, has width w and length l.

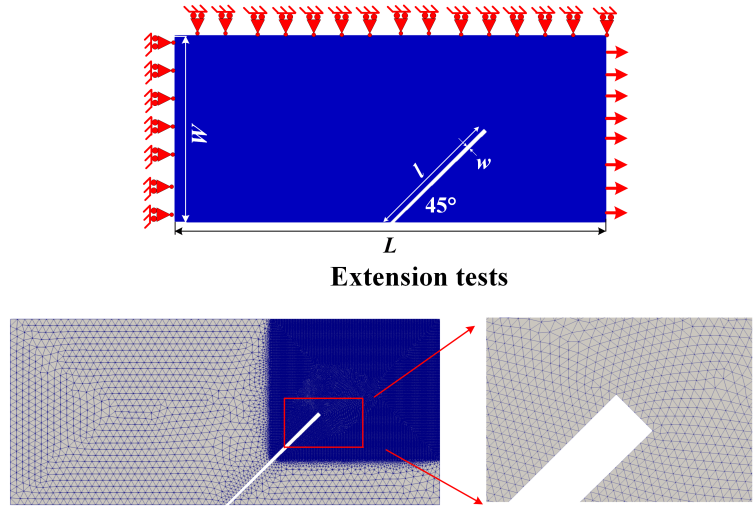

Figure 2: The geometry, boundary conditions, and mesh for an obliquely notched sample.

The boundary conditions are fixed as follows:

- left-hand side: null horizontal displacement
- top: null vertical displacement
- bottom: free displacement
- right-hand side: imposed displacement (extension).

It shall also be recalled that in the considered model it is meaningless to set boundary conditions for damage, since the energy to be minimized does not involve a damage gradient. As a consequence, there is no boundary term involving damage. This may also be seen in the numerical procedure, since the displacement field u^λ is computed by keeping the previous damage $\omega^{\lambda-\Delta\lambda}$.

Numerically, the mesh is made of triangular elements. It is finer around the crack, and even more so in the top-right of the sample, where fracture is expected to appear. In Table 1 the values chosen for the parameters in the simulations are shown. Note that the parameters n and m have been chosen in such a way that, when the damage field $\omega(X)$ is equal to 1, then a physically negligible, yet non-zero, amount of elastic energy is still stored at point X of the continuum. This standard remedy is adopted aiming at keeping well-posedness of the elastic problem during crack propagation as mentioned above.

Table 1: Data used for numerical simulations.

Young's modulus (GPa)	Poisson's ratio (1)	c_3, c_4, c_5, c_6, c_7 (N)	L (mm)	W (mm)	l (mm)	w (mm)	m,n (1)
75	0.32	1	30	13	10	0.3	0.999

4.1.2 Case 1: Results

Total displacement The total displacement is plotted in Figure 3. The propagating crack is visible as a line through which the displacement norm is discontinuous. The last picture shows the final step, when the crack reaches the superior side.

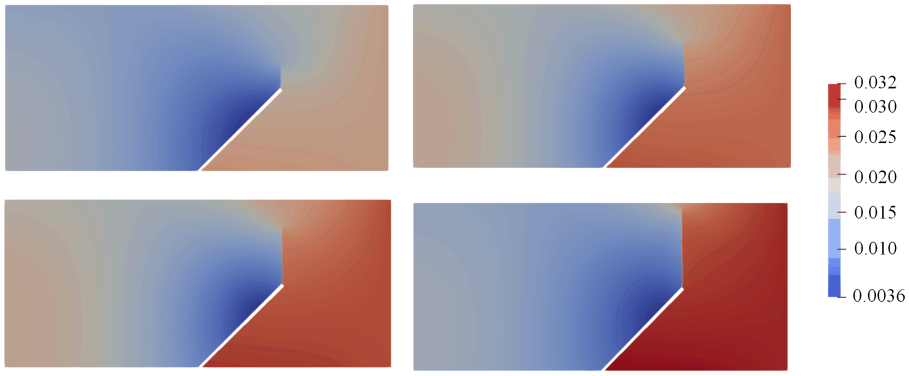

Figure 3: Case 1 – Evolution of total displacement.

Damage The propagation of the crack is more apparent when plotting the damage field (Fig. 4). More specifically, two interesting observations can be made:

- the width of the propagating crack is much smaller than the width of the initial notch;
- consequently, it is clear that the crack appears at a wedge, and that its propagation is not orthogonal to the sides of the notch.

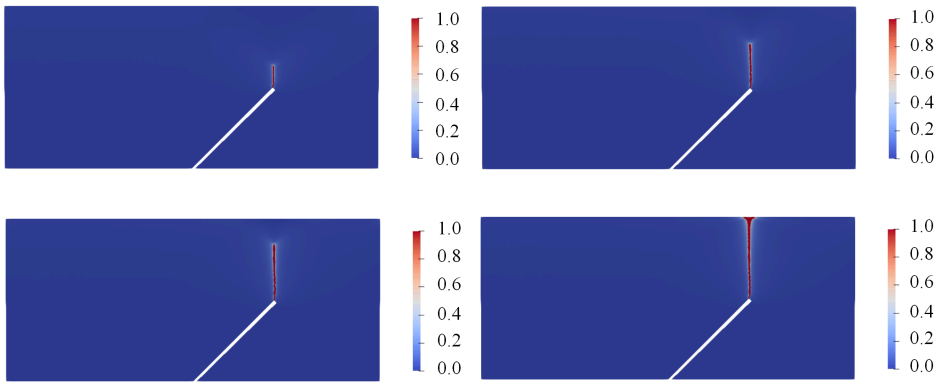

Figure 4: Case 1 – Evolution of damage field.

Stress The evolution of the three stress components is plotted in Figure 5. Once again, the propagation of the crack is clearly apparent. Two interesting results are worth noticing:

- every stress component is zero inside the propagating crack;
- outside of the crack, the stress is much higher around the propagating crack-tip than far from it.

4.2 Case 2: notch and hole

4.2.1 Case 2: Geometry and numerical data

The geometry is again a rectangle (see Fig. 6) of width W and length L, but the initial cracks are different. Indeed, as it can be seen in the figure, there are now:

- a horizontal notch starting from the left-hand side, of length l and width w;
- a hole of diameter 20 mm, whose center is 28.5 mm from the right-hand side and 51 mm from the bottom.

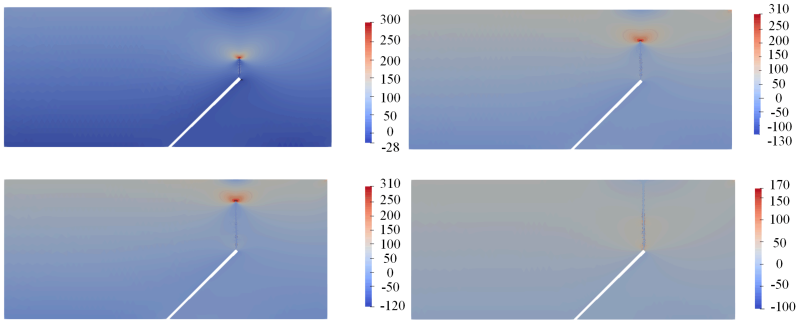

(a) Horizontal extension stress σ_{xx}.

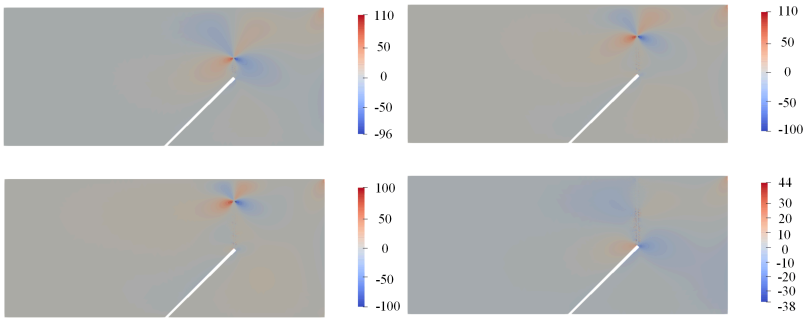

(b) Shear stress σ_{xy}.

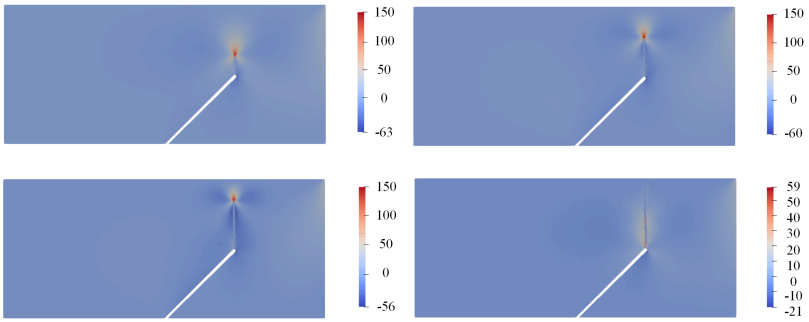

(c) Vertical extension stress σ_{yy}.

Figure 5: Case 1 – Evolution of stress components.

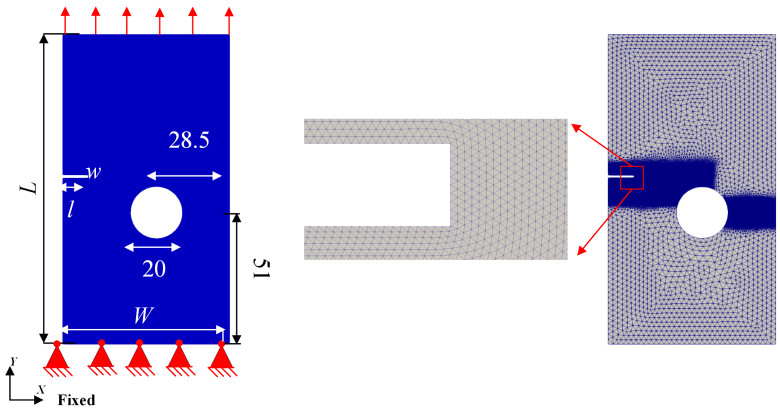

Figure 6: The geometry, boundary conditions and mesh for a notched sample with a hole.

Concerning the boundary conditions,

- bottom: null displacement;
- lateral sides: free displacement;
- top: imposed displacement (extension).

The mesh visible in Fig. 6 is much finer around the initial notches, where cracks are expected to propagate. The numerical values are gathered in Table 2.

Table 2: Data used for numerical simulations.

Young's modulus (GPa)	Poisson's ratio (1)	c_3, c_4, c_5, c_6, c_7 (N)	L (mm)	W (mm)	l (mm)	w (mm)	m,n
75	0.32	1	120	65	10	1	0.999

4.2.2 Case 2: Results

Damage and total displacement The evolution of both damage and displacement fields are plotted in Figure 7, where a crack is propagating from the left-hand side notch towards the central hole. As in Case 1,

- the width of the propagating crack is small enough to see that it starts from a wedge
- in the final step, the crack clearly reaches the central hole non-orthogonally.

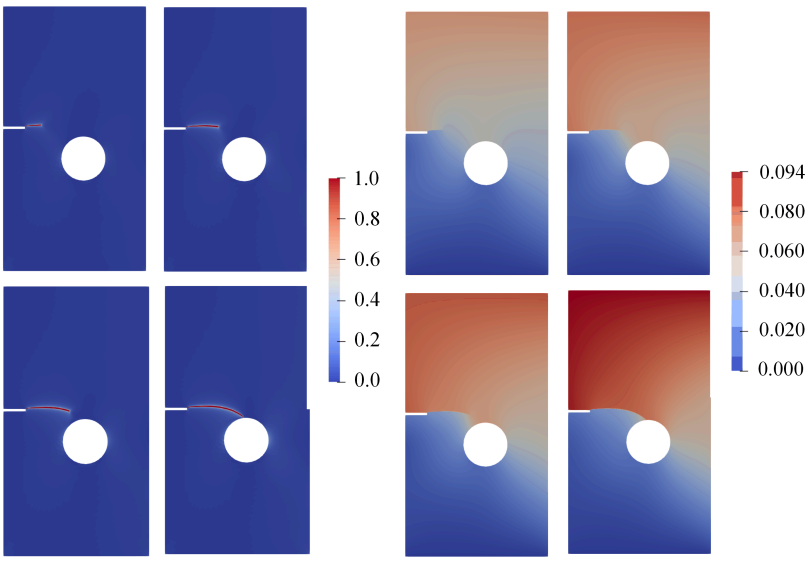

(a) Damage field. (b) Total displacement field.

Figure 7: Case 2 – Evolution of damage and total displacement.

Stress The stress components are plotted in Figure 8. As in the previous case, the stress is concentrated around the propagating crack-tip, while being vanishing within the crack.

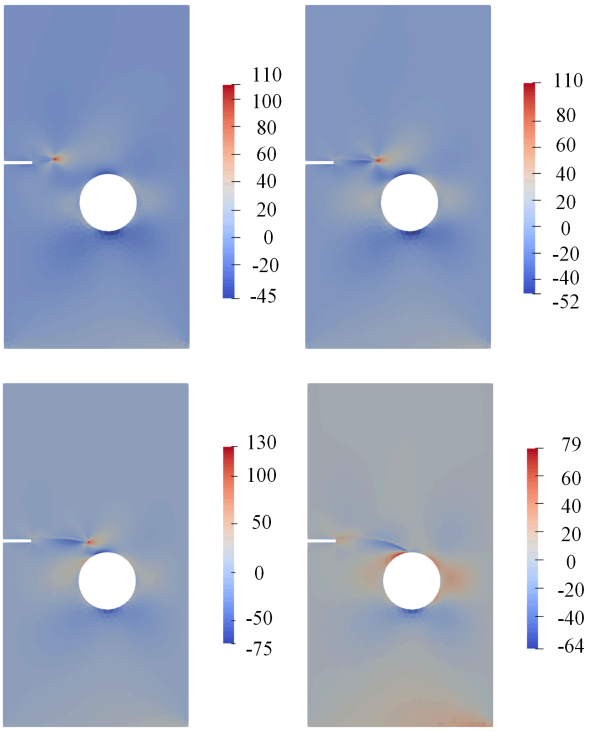

(a) Horizontal extension stress σ_{xx}.

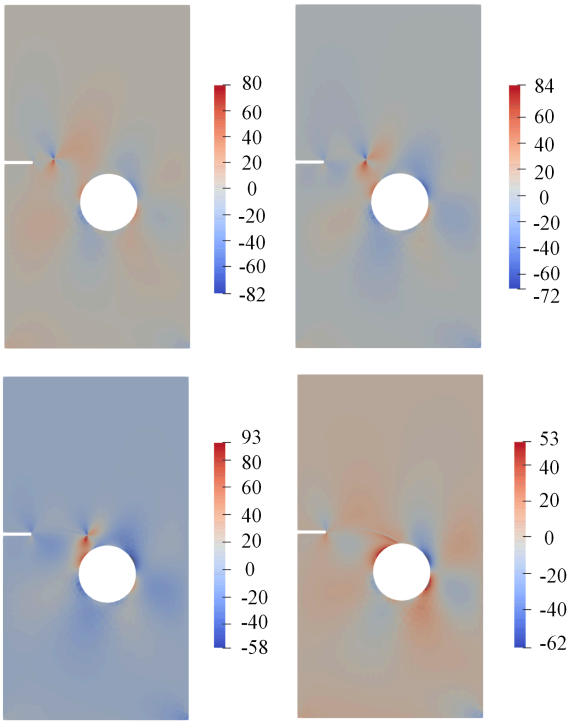

(b) Shear stress σ_{xy}.

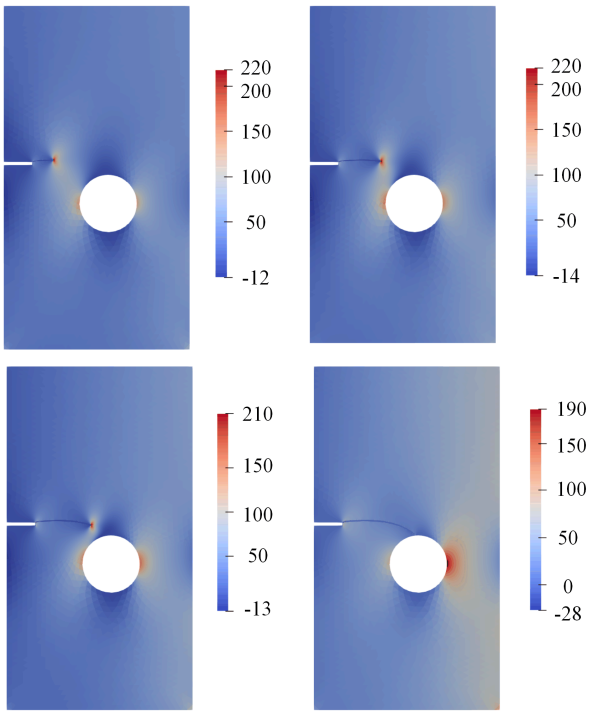

(c) Vertical extension stress σ_{yy}.

Figure 8: Case 2 – Evolution of stress components.

4.3 Interpretation: advantages of the considered model

The numerical results give an interesting insight on how damage and stress fields behave in the considered model.

Stress results There were no numerical instabilities due to the concentration of stress around the propagating crack: it was always significantly high close to the crack-tip, while being vanishing inside the crack itself. This is due to the parameters m and n in Equation 5, which had values close to 1 in the presented applications (see Tables 1 and 2). The rational behind this choice is that no elastic energy should be stored within a crack.

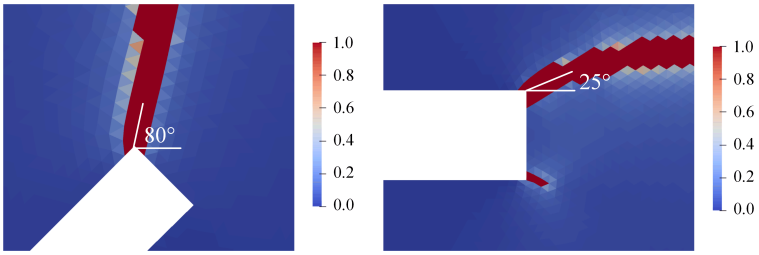

Figure 9: A close look at the crack near the notches.

Crack propagation The numerical results show that the width of the propagating crack is much smaller than the initial notches. This can be clearly observed in Figure 9. Kinking angles of the cracks departing from the notch tip are for the first and second test approximately 80° and 25°, respectively. A comparison with predictions of the kinking angles as predicted by other means, such as criteria based on stress intensity factors ([22], [75]), would potentially be beneficial. However, note that these criteria are strictly valid for sharp cracks under external load and not for notches. So, they should be compared when the internal phase-field approximation length introduced to approximate the crack is greater than the width of the initial notch, i.e. when fracture onset within the notch is not resolved, as it is usually done in damage gradient phase-field theories. A detailed analysis is therefore left to future research. However, it is worth to remark here that the dependence of the deformation energy on the strain gradient enables to go further in the integration by parts when deriving the weak form for the elastic problem, i.e. up to point contributions in the two-dimensional case. Consequently, cracks can start at wedges, which is not possible in damage gradient theories if damage second gradient is not considered [84, 86, 85]. Remark that, in damage gradient phase field theories[3], essential boundary conditions on the damage field, which are not usually considered as a datum in fracture problems, or natural boundary conditions enforcing the normal damage gradient to vanish, should be given. The latter condition implies that cracks must intersect boundaries either orthogonally or parallelly, which is rather limiting in the description of some real cracking phenomena. When damage gradient theories are applied, the regularization length is chosen sufficiently large so that the phase-field approximation of the propagating crack can "surround" the initial notch. In this way, there is no more any constraint in terms of, e.g., kinking angle. Clearly, this remedy prevents from taking into account the effect of the notch-tip geometry on the crack propagation. Such an effect could be non-negligible when the ratio between the notch width and the total size of the specimen is appreciably greater than zero. Finally, recall that in the second test the propagating crack reaches the central hole non-orthogonally. Aimed at resolving the intersection of the propagating crack with the central hole, the regularization length introduced by the phase-field approach should be clearly smaller than the diameter of the hole. In a damage gradient approach the crack would intersect the central hole (as well as any other boundary resolved by the regularization length) orthogonally (see, e.g., [78, 79, 80, 81, 82, 83]).

5 Concluding remarks

Work done In the present work quasi-static brittle fracture of a strain gradient elastic continuum has been modelled and numerically simulated by using the finite element method through the utilization of the FEniCS library. The displacement field and the damage field were considered as the independent variables of the problem. Several energy functionals were defined. First, a deformation energy was defined depending on strain, strain gradient and damage fields. The involved effective stiffness coefficients were assumed to depend on damage. Second, the energy dissipated by damage was taken into account through a dissipative term depending on the damage field. Last, the interaction with the external world was modelled by an external work term. Then, the solution of the weak form elasticity problem, for a fixed damage, and of the Karush–Kuhn–Tucker conditions, obtained as a result of the maximum energy-release rate principle, has been addressed aimed at finding the evolution of the two independent variables. Setup this way, the problem was solved by using the alternate minimization algorithm. Every iteration had two steps: First, the displacement field at equilibrium was computed while the damage field of the previous iteration was kept. Second, the

[3] A single damage variable shall be considered to better elucidate the question.

damage field was updated by applying the Karush–Kuhn–Tucker conditions. The displacement field was computed by means of a finite element method mixed formulation, which was implemented numerically by using the FEniCS library. Simulation results have then been presented for two test cases on notched samples.

Results The main outcomes of this work are the implementation itself, which is to authors' best knowledge the first computational implementation by an open-source library of the strain gradient energy approach to phase-field brittle fracture, and the validation of results obtained in [45] by using a commercial software. Results obtained in the two test cases that were considered, addressing crack onset and propagation from an initial notch, hint to the fact that using strain gradient modeling has many advantages, also in terms of physical accuracy, over existing approaches which are not including strain gradient effects:

- there is no instability when computing the stress, and the resulting fields vanish within the crack, while being high around its tip and very much lower far from it;
- crack onset can be resolved within the notches, i.e. cracks do not necessarily have to surround the notch-tip to get realistic results, and cracks can depart from notch wedges;
- cracks can intersect non-orthogonally the boundaries.

Thanks to the highly customisable computational platform that has been developed, it is possible to envision for the next future the following extensions of this work:

- passing from a mixed formulation to a non-mixed one by, e.g., isogeometric analysis;
- implementing tip-following adaptive meshing, aimed at increasing the computational efficiency;
- addressing dynamic analyses for studying crack propagation velocity, crack branching, etc.;
- addressing anisotropic damaging;
- exploiting strain splits, aimed at being able of differentiating (locally) damage occurring in extension from that occurring in compression, or damage occurring in dilation from that occurring in shearing;
- addressing ductile fracture;
- running three-dimensional analyses.

References

[1] B.E. Abali, W.H. Müller, and F. dell'Isola. Theory and computation of higher gradient elasticity theories based on action principles. *Archive of Applied Mechanics*, pages 1–16, 2017.

[2] B.E. Abali, W.H. Müller, and V. A Eremeyev. Strain gradient elasticity with geometric nonlinearities and its computational evaluation. *Mechanics of Advanced Materials and Modern Processes*, 1(1):4, 2015.

[3] U. Andreaus, F. dell'Isola, I. Giorgio, L. Placidi, T. Lekszycki, and N.L. Rizzi. Numerical simulations of classical problems in two-dimensional (non) linear second gradient elasticity. *International Journal of Engineering Science*, 108:34–50, 2016.

[4] B. Bourdin, G.A. Francfort, and J.-J. Marigo. The variational approach to fracture. *J.Elast.*, 91:5–148, 2008.

[5] A. Cazzani, M. Malagù, and E. Turco. Isogeometric analysis of plane-curved beams. *Mathematics and Mechanics of Solids*, 21(5):562–577, 2016.

[6] A. Cazzani, M. Malagù, E. Turco, and F. Stochino. Constitutive models for strongly curved beams in the frame of isogeometric analysis. *Mathematics and Mechanics of Solids*, 21(2):182–209, 2016.

[7] L. Contrafatto and M. Cuomo. A framework of elastic–plastic damaging model for concrete under multiaxial stress states. *International Journal of Plasticity*, 22(12):2272–2300, 2006.

[8] L. Contrafatto, M. Cuomo, and F. Fazio. An enriched finite element for crack opening and rebar slip in reinforced concrete members. *International journal of fracture*, pages 1–18, 2012.

[9] L. Contrafatto, M. Cuomo, and S. Gazzo. A concrete homogenisation technique at meso-scale level accounting for damaging behaviour of cement paste and aggregates. *Computers and Structures*, 173:1–18, 2016.

[10] M. Cuomo, L. Contrafatto, and L. Greco. A variational model based on isogeometric interpolation for the analysis of cracked bodies. *International Journal of Engineering Science*, 80:173–188, 2014.

[11] M. Cuomo and L. Greco. Isogeometric analysis of space rods: Considerations on stress locking. 2012.

[12] F. dell'Isola, U. Andreaus, and L. Placidi. At the origins and in the vanguard of peridynamics, non-local and higher-gradient continuum mechanics: an underestimated and still topical contribution of Gabrio Piola. *Mathematics and Mechanics of Solids*, 20(8):887–928, 2015.

[13] F. dell'Isola, A. Della Corte, and I. Giorgio. Higher-gradient continua: The legacy of Piola, Mindlin, Sedov and Toupin and some future research perspectives. *Mathematics and Mechanics of Solids*, 2016.

[14] F. dell'Isola, A. Madeo, and P. Seppecher. Cauchy tetrahedron argument applied to higher contact interactions. *Archive for Rational Mechanics and Analysis*, 219(3):1305–1341, 2016.

[15] F. dell'Isola, G. Maier, U. Perego, U. Andreaus, R. Esposito, and S. Forest. The complete works of Gabrio Piola: volume I. *Cham, Switzerland: Springer*, 2014.

[16] F. dell'Isola and L. Placidi. Variational principles are a powerful tool also for formulating field theories. In *Variational models and methods in solid and fluid mechanics*, pages 1–15. Springer, 2011.

[17] F. dell'Isola, P. Seppecher, and A. Della Corte. The postulations á la d'Alembert and á la Cauchy for higher gradient continuum theories are equivalent: a review of existing results. In *Proc. R. Soc. A*, volume 471. The Royal Society, 2015.

[18] V.A. Eremeyev and H. Altenbach. Equilibrium of a second-gradient fluid and an elastic solid with surface stresses. *Meccanica*, 49(11):2635–2643, 2014.

[19] V.A. Eremeyev, F. dell'Isola, C. Boutin, and D. Steigmann. Linear pantographic sheets: existence and uniqueness of weak solutions. *Journal of Elasticity*, 132(2):175–196, 2018.

[20] V.A. Eremeyev, L.P. Lebedev, and H. Altenbach. *Foundations of micropolar mechanics*. Springer Science & Business Media, 2012.

[21] V.A. Eremeyev and W. Pietraszkiewicz. Material symmetry group and constitutive equations of micropolar anisotropic elastic solids. *Mathematics and Mechanics of Solids*, 21(2):210–221, 2016.

[22] Erdogan, F., & Sih, G. C. (1963). On the crack extension in plates under plane loading and transverse shear. J. of Basic engineering. Transactions of the American Society of Mechanical Engineering, ASME, 519-527.

[23] I. Giorgio. Numerical identification procedure between a micro-Cauchy model and a macro-second gradient model for planar pantographic structures. *Zeitschrift für angewandte Mathematik und Physik*, 67(4):95, 2016.

[24] L. Greco and M. Cuomo. B-spline interpolation of Kirchhoff-Love space rods. *Computer Methods in Applied Mechanics and Engineering*, 256:251–269, 2013.

[25] L. Greco and M. Cuomo. An implicit G1 multi patch B-spline interpolation for Kirchhoff–Love space rod. *Computer Methods in Applied Mechanics and Engineering*, 269:173–197, 2014.

[26] R.D. Mindlin and H.F. Tiersten. Effects of couple-stresses in linear elasticity. *Archive for Rational Mechanics and analysis*, 11(1):415–448, 1962.

[27] A. Misra and V. Singh. Thermomechanics-based nonlinear rate-dependent coupled damage-plasticity granular micromechanics model. *Continuum Mechanics and Thermodynamics*, 27(4-5):787–817, 2015.

[28] K. Pham, J.-J. Marigo, and C. Maurini. The issues of the uniqueness and the stability of the homogeneous response in uniaxial tests with gradient damage models. *Journal of the Mechanics and Physics of Solids*, 59(6):1163–1190, 2011.

[29] L. Placidi. A variational approach for a nonlinear 1-dimensional second gradient continuum damage model. *Continuum Mechanics and Thermodynamics*, 27(4-5):623, 2015.

[30] Placidi, L., Andreaus, U., Della Corte, A., and Lekszycki, T. (2015). Gedanken experiments for the determination of two-dimensional linear second gradient elasticity coefficients. *Zeitschrift für angewandte Mathematik und Physik 66*, 6, 3699–3725.

[31] L. Placidi. A variational approach for a nonlinear one-dimensional damage-elasto-plastic second-gradient continuum model. *Continuum Mechanics and Thermodynamics*, 28(1-2):119, 2016.

[32] L. Placidi, U. Andreaus, and I. Giorgio. Identification of two-dimensional pantographic structures via a linear D4 orthotropic second gradient elastic model. *Journal of Engineering Mathematics*, 103(1007):1–21, 2017.

[33] Placidi, L., Barchiesi, E., & Misra, A. (2018). A strain gradient variational approach to damage: a comparison with damage gradient models and numerical results. *Mathematics and Mechanics of Complex Systems*, 6(2), 77-100..

[34] L. Placidi and A.R. El Dhaba. Semi-inverse method à la Saint-Venant for two-dimensional linear isotropic homogeneous second-gradient elasticity. *Mathematics and Mechanics of Solids*, 22(5):919–937, 2017.

[35] Placidi, L., Misra, A., & Barchiesi, E. (2018). Two-dimensional strain gradient damage modeling: a variational approach. *Zeitschrift für angewandte Mathematik und Physik*, 69(3), 56.

[36] L. Placidi, G. Rosi, I. Giorgio, and A. Madeo. Reflection and transmission of plane waves at surfaces carrying material properties and embedded in second-gradient materials. *Mathematics and Mechanics of Solids*, 19(5):555–578, 2014.

[37] Y. Rahali, I. Giorgio, J.F. Ganghoffer, and F. dell'Isola. Homogenization à la Piola produces second gradient continuum models for linear pantographic lattices. *International Journal of Engineering Science*, 97:148–172, 2015.

[38] R.A. Toupin. Elastic materials with couple-stresses. *Archive for Rational Mechanics and Analysis*, 11(1):385–414, 1962.

[39] E. Turco and M. Aristodemo. A three-dimensional B-spline boundary element. *Computer methods in applied mechanics and engineering*, 155(1-2):119–128, 1998.

[40] Y. Yang and A. Misra. Higher-order stress-strain theory for damage modeling implemented in an element-free Galerkin formulation. *CMES-Computer modeling in engineering & sciences*, 64(1):1–36, 2010.

[41] Y. Yang and A. Misra. Micromechanics based second gradient continuum theory for shear band modeling in cohesive granular materials following damage elasticity. *International Journal of Solids and Structures*, 49(18):2500–2514, 2012.

[42] M. Cuomo and M. Fagone. Model of anisotropic elastoplasticity in finite deformations allowing for the evolution of the symmetry group.*Nanomechanics Science and Technology: An International Journal*, 6(2), 2015.

[43] M. Cuomo. Forms of the dissipation function for a class of viscoplastic models. *Mathematics and Mechanics of Complex Systems*, 5(3):217–237, 2017.

[44] Phunpeng, V., and Baiz, P. Mixed finite element formulations for strain-gradient elasticity problems using the fenics environment. *Finite Elements in Analysis and Design* 96 (2015), 23–40.

[45] Placidi, L., and Barchiesi, E. Energy approach to brittle fracture in strain-gradient modelling. *Proceedings of the Royal Society A: Mathematical, Physical and Engineering Sciences* 474, 2210 (2018).

[46] Yang, H., Abali, B. E., Timofeev, D., and Müller, W. H. Determination of metamaterial parameters by means of a homogenization approach based on asymptotic analysis. *Continuum Mechanics and Thermodynamics* (2019), 1–20.

[47] Zybell, L., Mühlich, U., Kuna, M., and Zhang, Z. A three-dimensional finite element for gradient elasticity based on a mixed-type formulation. *Computational materials science* 52, 1 (2012), 268–273.

[48] Misra, A., & Singh, V. (2013). Micromechanical model for viscoelastic materials undergoing damage. *Continuum Mechanics and Thermodynamics*, 25(2-4), 343-358.

[49] Misra, A., & Poorsolhjouy, P. (2015). Granular micromechanics model for damage and plasticity of cementitious materials based upon thermomechanics. *Mathematics and Mechanics of Solids*.

[50] De Angelo, M., Spagnuolo, M., D'annibale, F., Pfaff, A., Hoschke, K., Misra, A., et al. (2019). The macroscopic behavior of pantographic sheets depends mainly on their microstructure: experimental evidence and qualitative analysis of damage in metallic specimens. *Continuum Mechanics and Thermodynamics*, 31(4), 1181-1203.

[51] Bilotta, A., Morassi, A., & Turco, E. (2018). The use of quasi-isospectral operators for damage detection in rods. *Meccanica*, 53(1-2), 319-345.

[52] Bilotta, A., Morassi, A., & Turco, E. Damage identification in longitudinally vibrating rods based on quasi-isospectral operators.

[53] Placidi, L., Barchiesi, E., Misra, A., & Andreaus, U. (2020). Variational methods in continuum damage and fracture mechanics. Encylopedia of continuum mechanics. Berlin: Springer-Verlag.

[54] Misra, A., Singh, V., & Darabi, M. K. (2019). Asphalt pavement rutting simulated using granular micromechanics-based rate-dependent damage-plasticity model. *International Journal of Pavement Engineering*, 20(9), 1012-1025.

[55] Misra, A., & Sarikaya, R. (2019). Computational analysis of tensile damage and failure of mineralized tissue assisted with experimental observations. *Proceedings of the Institution of Mechanical Engineers, Part H: Journal of Engineering in Medicine*, 0954411919870650.

[56] Placidi, L., Misra, A., & Barchiesi, E. (2019). Simulation results for damage with evolving microstructure and growing strain gradient moduli. *Continuum Mechanics and Thermodynamics*, 31(4), 1143-1163.

[57] Misra, A. (2002). Effect of asperity damage on shear behavior of single fracture. *Engineering Fracture Mechanics*, 69(17), 1997-2014.

[58] dell'Isola, F., Seppecher, P., Placidi, L., Barchiesi, E., & Misra, A. (2020). 8 Least Action and Virtual Work Principles for the Formulation of Generalized Continuum Models. Discrete and Continuum Models for Complex Metamaterials, 327.

[59] Volkov, I. A., Igumnov, L. A., dell'Isola, F., Litvinchuk, S. Y., & Eremeyev, V. A. (2020). A continual model of a damaged medium used for analyzing fatigue life of polycrystalline structural alloys under thermal–mechanical loading. *Continuum Mechanics and Thermodynamics*, 32(1), 229-245.

[60] Nasedkina, A., Eremeyev, V., & Nasedkin, A. Finite Element Simulation of Transient Axisymmetric Thermoelastic Problems for Heterogeneous Media with Physical Nonlinearities and Circular Fractures.

[61] Khakalo, S., & Niiranen, J. (2020). Anisotropic strain gradient thermoelasticity for cellular structures: plate models, homogenization and isogeometric analysis. *Journal of the Mechanics and Physics of Solids*, 134, 103728.

[62] Khakalo, S., & Niiranen, J. (2019). Lattice structures as thermoelastic strain gradient metamaterials: Evidence from full-field simulations and applications to functionally step-wise-graded beams. *Composites Part B: Engineering*, 177, 107224.

[63] Turco, E., Golaszewski, M., Cazzani, A., & Rizzi, N. L. (2016). Large deformations induced in planar pantographic sheets by loads applied on fibers: experimental validation of a discrete Lagrangian model. *Mechanics Research Communications*, 76, 51-56.

[64] Cazzani, A., Malagù, M., & Turco, E. (2016). Isogeometric analysis: a powerful numerical tool for the elastic analysis of historical masonry arches. *Continuum Mechanics and thermodynamics*, 28(1-2), 139-156.

[65] Grillanda, N., Chiozzi, A., Bondi, F., Tralli, A., Manconi, F., Stochino, F., & Cazzani, A. (2019). Numerical insights on the structural assessment of historical masonry stellar vaults: the case of Santa Maria del Monte in Cagliari. *Continuum Mechanics and thermodynamics*, 1-24.

[66] Della Corte, A., Battista, A., dell'Isola, F., & Giorgio, I. (2017). Modeling deformable bodies using discrete systems with centroid-based propagating interaction: fracture and crack evolution. In Mathematical Modelling in Solid Mechanics (pp. 59-88). Springer, Singapore.

[67] Cazzani, A., Stochino, F., & Turco, E. (2016). An analytical assessment of finite element and isogeometric analyses of the whole spectrum of Timoshenko beams. *ZAMM-Journal of Applied Mathematics and Mechanics/Zeitschrift für Angewandte Mathematik und Mechanik*, 96(10), 1220-1244.

[68] Schulte, J., Dittmann, M., Eugster, S. R., Hesch, S., Reinicke, T., dell'Isola, F., & Hesch, C. (2020). Isogeometric analysis of fiber reinforced composites using Kirchhoff–Love shell elements. *Computer Methods in Applied Mechanics and Engineering*, 362, 112845.

[69] Spagnuolo, M., Franciosi, P., & dell'Isola, F. (2020). A Green operator-based elastic modeling for two-phase pantographic-inspired bi-continuous materials. *International Journal of Solids and Structures*, 188, 282-308.

[70] dell'Isola, F., Lekszycki, T., Spagnuolo, M., Peyre, P., Dupuy, C., Hild, F., ... & Dirrenberger, J. (2020). 6 Experimental Methods in Pantographic Structures. Discrete and Continuum Models for Complex Metamaterials, 263.

[71] dell'Isola, F., Turco, E., & Barchiesi, E. (2020). 5 Lagrangian Discrete Models: Applications to Metamaterials. Discrete and Continuum Models for Complex Metamaterials, 197.

[72] dell'Isola, F., Spagnuolo, M., Barchiesi, E., Giorgio, I., & Seppecher, P. (2020). 3 Pantographic Metamaterial: A (Not So) Particular Case. Discrete and Continuum Models for Complex Metamaterials, 103.

[73] Barchiesi, E., dell'Isola, F., Hild, F., & Seppecher, P. (2020). Two-dimensional continua capable of large elastic extension in two independent directions: asymptotic homogenization, numerical simulations and experimental evidence. *Mechanics Research Communications*, 103, 103466.

[74] Placidi, L., dell'Isola, F., & Barchiesi, E. (2020). Heuristic Homogenization of Euler and Pantographic Beams. In Mechanics of Fibrous Materials and Applications (pp. 123-155). Springer, Cham.

[75] Sih, George C. (1973). Handbook of stress-intensity factors: Stress-intensity factor solutions and formulas for reference. Bethlehem, Pa., Lehigh University.

[76] Chen, Q. & Wang, G. (2020). Computationally-efficient homogenization and localization of unidirectional piezoelectric composites with partially cracked interface. *Composite Structures*, 232, 111452.

[77] Tu, W. & Chen, Q. (2020). Evolution of Interfacial Debonding of a Unidirectional Graphite/Polyimide Composite under Off-Axis Loading. *Engineering Fracture Mechanics*, 106947.

[78] Miehe, C., Schaenzel, L.-M., & Ulmer, H. (2015). Phase field modeling of fracture in multi-physics problems. part i. balance of crack surface and failure criteria for brittle crack propagation in thermo-elastic solids. *Computer Methods in Applied Mechanics and Engineering*, 449–485.

[79] Nagaraja, S., Elhaddad, M., Ambati, M., Kollmannsberger, S., De Lorenzis, L., & Rank, E. (2019). Phase-field modeling of brittle fracture with multi-level hp-fem and the finite cell method. *Computational Mechanics*, 6, 1283–1300.

[80] Miehe, C., Hofacker, M., & Welschinger, F. (2010). A phase field model for rate-independent crack propagation: Robust algorithmic implementation based on operator splits. *Computer Methods in Applied Mechanics and Engineering 199*, 45-48, 2765–2778.

[81] Huynh, G., Zhuang, X., & Nguyen-Xuan, H. (2019). Implementation aspects of a phase-field approach for brittle fracture. *Frontiers of Structural and Civil Engineering 13*, 2, 417–428.

[82] Chakraborty, P., Sabharwall, P., & Carroll, M. C. (2016). A phase-field approach to model multi-axial and microstructure dependent fracture in nuclear grade graphite. *Journal of Nuclear Materials 475*, 200–208.

[83] Hentati, H., Dhahri, M., & Dammak, F. (2016). A phase-field model of quasistatic and dynamic brittle fracture using a staggered algorithm. *Journal of Mechanics of Materials and Structures 11*, 3, 309–327.

[84] Alibert, J.-J., Seppecher, P., and Dell'Isola, F. (2003). Truss modular beams with deformation energy depending on higher displacement gradients. *Mathematics and Mechanics of Solids 8*, 1, 51–73.

[85] dell'Isola, F., and Seppecher, P. (1997). Edge contact forces and quasi-balanced power. *Meccanica 32*, 1, 33–52.

[86] dell'Isola, F., Seppecher, P., and Corte, A. D. (2015). The postulations á la d'alembert and á la cauchy for higher gradient continuum theories are equivalent: a review of existing results. *Proceedings of the Royal Society A: Mathematical, Physical and Engineering Sciences 471*, 2183, 20150415.

[87] Reiher, J. C., Giorgio, I., and Bertram, A. Finite-element analysis of polyhedra under point and line forces in second-strain gradient elasticity. *Journal of Engineering Mechanics 143*, 2 (2017), 04016112.

[88] Scerrato, D., Zhurba Eremeeva, I. A., Lekszycki, T., and Rizzi, N. L. On the effect of shear stiffness on the plane deformation of linear second gradient pantographic sheets. *ZAMM-Journal of Applied Mathematics and Mechanics/Zeitschrift für Angewandte Mathematik und Mechanik 96*, 11 (2016), 1268–1279.